ISSUES IN DEEP-UV LITHOGRAPHY USING PULSED LASER LIGHT SOURCES

by

William Norman Partlo

Memorandum No. UCB/ERL M92/14

20 January 1992

ISSUES IN DEEP-UV LITHOGRAPHY USING PULSED LASER LIGHT SOURCES

by

William Norman Partlo

Memorandum No. UCB/ERL M92/14

20 January 1992

ELECTRONICS RESEARCH LABORATORY

College of Engineering
University of California, Berkeley
94720

Issues in Deep-UV Lithography using Pulsed Laser Light Sources

by

William Partlo

Abstract

Pulsed lasers are investigated as possible radiation sources for deep-UV lithography. A KrF excimer laser (248.4nm) is used to test long term transmission stability of deep-UV optical materials. A quintupled Nd-YAG laser (212.8nm) is used to investigate problems associated with using a highly coherent pulsed laser as a lithographic radiation source.

Pellicles and fluids are two important classes of materials used in lithography systems. The large photon energy and high peak power of the KrF excimer laser degrades most pellicle materials and optical fluids. An exposure system with *in situ* transmission and optical thickness monitoring is used to test candidate materials. A flouropolymer pellicle material is shown to have a stable transmission lifetime up to exposures of 10,000J/cm^2. Several candidate optical fluids are described with long transmission lifetimes and suitable refractive index values; including Dupont Krytox (n=1.319), deionized water (n=1.374), Dow 200 (n=1.467), and ethylene glycol (n=1.484).

The relevant characteristics of an 0.25W, 10Hz quintupled Nd-YAG laser, such as energy stability, spectral linewidth, and coherence length, are described. This laser exhibits a spectral linewidth of 0.035pm, well within the requirements of the all-fused silica deep-UV lenses. The narrow linewidth, combined with single transverse mode operation, causes high-contrast speckle intensity variations, severely degrading illumination uniformity.

Two novel speckle reduction schemes are employed. One scheme uses two closely spaced counter-rotating diffusers. A diffuser-speckle model is developed to determine the speckle reduction capabilities of a given diffuser. Significant speckle reduction is produced during a single 4.2ns laser pulse with rotation speeds less than 30,000RPM. A second speckle reduction scheme that uses no moving parts nor employs any special optics is demonstrated. This scheme produces several sub-pulses from a single incident pulse, each delayed by an amount greater than the coherence length. The delayed sub-pulses do not interfere, thus reducing speckle contrast by $1/\sqrt{(N)}$, where N is the number of sub-pulses.

An all-refractive 20:1 reduction lens, designed for use at 212.8nm, is used in combination with the speckle reduction schemes to print speckle-free 0.2μm line/space patterns in PMMA. These line/space patterns represent $0.56\frac{\lambda}{NA}$ features for this 0.6NA objective.

W G Oldham

Prof. W.G. Oldham

Committee Chairman

Dedicated to my family: Donald, Vivian, Fred, and Dominique

In memory of my Grandmother

Table of Contents

Chapter 1: Introduction 1
Excimer Lithography 1
Quintupled Nd-YAG Lithography 3
Chapter 2: Transmission Lifetime Measurements of Pellicles for Deep-UV Lithography 7
2.1: Introduction 7
2.2: Theory 8
2.3: Experimental Apparatus 9
2.4: Nitrocellulose Test Results 11
2.5: Polyvinyl Butyral Test Results 12
2.6: Reciprocity Tests on Polyvinyl Butyral 14
2.7: Fluoropolymer Pellicle Material Test Results 17
2.8: Conclusions 18
Chapter 3: Transmission Lifetime and Refractive Index Measurements of Fluids for Deep-UV Lithography 35
3.1: Introduction 35
3.2: Fluid Properties 37
3.3: Measurement Techniques 38
3.4: Results 43
3.5: Conclusions 45
Chapter 4: Synthesis and Characteristics of 213nm Quintupled Nd-YAG Radiation 63
4.1: Introduction 63
4.2: Laser System 65
4.3: BBO Crystal Heating 68
4.4: 5th Harmonic Energy Output and Beam Profiles 71
4.5: Spectral Characteristics of Quintupled Nd-YAG Radiation 73
4.6: Conclusions 76
Chapter 5: Speckle Reduction via Multiple Rotating Diffusers 94
5.1: Introduction 94
5.2: Diffuser Model 95
5.3: Single Rotation Diffuser 96
5.4: Two Counter Rotating Diffusers 100
5.5: Noise Reduction for a Single Laser Pulse 102
5.6: Simulation 103
5.7: Experiment 105

5.8: Conclusions 107
Chapter 6: Speckle Reduction via Multiple Pulse Generation 123
6.1: Introduction 123
6.2: Previous Multiple Pulse Generation Schemes 124
6.3: Novel Polarization and Delay Scheme 128
6.4: Cascading Polarization and Delay Stages 131
6.5: Conclusions 132
Chapter 7: 213nm Lithography 145
7.1: Introduction 145
7.2: Schwarzschild Objective 146
7.3: 213nm BOLD Objective 149
7.4: PMMA as a 213nm Photoresist 152
7.5: Schwarzschild Imaging Results 157
7.6: BOLD Imaging Results 158
7.7: Conclusions and Future Work 159
Chapter 8: Conclusions and Future Work 188
8.1: Conclusions 188
8.2: Second Generation 5th Harmonic Source 189

Acknowledgements

I would like to express my gratitude to Professor William G. Oldham for the opportunity to work in his group. His guidance has been clear and true through my five years here at UC-Berkeley. Professor Andrew R. Neureuther has had equal effect on me as a student and as a researcher, I thank him. Finally, I would like to thank Professors Stone and Lau for sitting on my qualifying committee. SEMATECH, its member companies, and the Federal Government deserve a humble thank you for their financial assistance.

The many students that served as my mentors and peers fall into three generations: those before me, those with me, and those after me. Gino Addiego, Rich Fergusen, Carl Galewski, and Nelson Tam all served as guiding lights when I had no idea what was going on. Gino's practical knowledge of optics was a tremendous help to me. Carl's well practiced discipline concerning experimental work helped me acquire good habits in the microlab. Rich and Nelson both offered precious assistance with the group's computer systems and programs, never again will I call them CAD weenies or bit heads.

The students who began their graduate work at the same time as me also had a significant impact. Though Dean Drako and Don Lyons were my coworkers for only two years, they remain social companions to this day. Two lucky guys, Ed Scheckler and Alex Wong, had the dubious honor of trying to earn a Ph.D. while I was hanging around. They put up me with good humor and were of great assistance on many occasions. Anton Pfau, a post-doc in our group for the last two years, was invaluable as a sounding board for ideas.

Last but not least, the students who joined our group after me have added to my experience more than they will ever know. I can not remember a single day when Diane Hoffstetter was down or in a bad mood, sharing a cubical with her was like spending time in a bar with your best drinking buddy. John Hutchinson made me feel like I had learned something in the past few years. He always seemed to be asking the same questions that I had, and boy what an ego trip to be able to answer them.

Finally, I am indebted to the staff of the microlab and the machine shop. Jose Rivera in the machine shop could make anything that I asked for, even when I described it in less than precise terms. Richard Hsu in the microlab should get combat pay for having to work in the same room with me. His tolerance of my obnoxious behavior in *GL4* was often tested.

Chapter 1
Introduction

1.1 Excimer Lithography

Deep-UV lithography using pulsed laser sources has enjoyed a brief history with rapid advancement during the past decade (1980's). Initial work to produce images in photoresist using a deep-UV laser source was done by Hawryluk and Smith in 1982.[1,2] This work consisted of forming interference fringes from two incident laser beams. The photoresist patterns formed using this method were line/space gratings. This method is limited to line/space patterns and thus can not be used to print the arbitrary patterns needed for IC fabrication.

The first work to print arbitrary patterns using a pulsed laser source was done by Jain et. al in 1982.[3] Contact printing was demonstrated using both a XeCl excimer laser (308nm) and a KrF excimer laser (248nm). Resolution of 1μm line/space patterns was achieved. The drawbacks of contact printing, 1X masks and mask damage caused by wafer contact, prevent this method from becoming a high volume low cost method of deep-UV microlithography.

The mask damage problem is eliminated by projection lithography systems. Jain et. al. modified a Perkin-Elmer projection printer for use with a XeCl excimer laser source and succeeded in obtaining 1μm line/space resolution.[4,5,6,7] Since the Perkin-Elmer projection printer is an all-reflective system, there was no need to reduce the spectral width of the XeCl laser source. Though eliminating the mask/wafer contact problem, 1:1 lithography systems still require a 1X mask. The requirement for 1X masks can only be avoided with the use of reduction optics.

Full field projection printing using reduction optics and a pulsed laser source was first demonstrated by Pol et. al. in 1986.[8,9] The projection lens used in this system was an all-

fused silica refractive optic with 5:1 reduction ratio. Fused silica is the only optical glass with sufficient transparency in the deep-UV. The lack of alternative optical glasses with dispersion properties complementary to fused silica force deep-UV lens designs to be nearly monochromatic. The KrF excimer laser used in this first demonstration system was line-narrowed to 5pm spectral linewidth. The greatest difficulty encountered in this work was poor control of the spectral content and line center stability of the line-narrowed KrF excimer laser.

Great improvements in line-narrowed excimer laser design and fabrication have been achieved since the first work by Pol. Numerous systems have been proposed and described in the literature.[10,11,12,13] The excimer laser installed in the Berkeley Microfabrication facility and used in the experiments described in this thesis is a Cymer Laser Technologies Model CX-2LS line-narrowed KrF laser. This laser has proven to be highly reliable and routinely produces 3W of 248nm power with a spectral linewidth less than 3pm.

Deep-UV lens design and fabrication have also advanced since the first deep-UV lens in 1986. Today (1991) there are five manufacturers of deep-UV lithography systems using 248nm radiation: ASM Lithography, Canon, GCA/Troppel, Nikon, and SVG Lithography. All of these systems except for the SVG system use a line-narrowed KrF excimer laser as the radiation source. The SVG system uses a filtered mercury-arc lamp at 250nm. These systems are gaining acceptance in the IC industry as production-worthy lithographic tools.

248nm deep-UV lithography will be continuously advanced in incremental steps and focus on extending the lifetimes and reliabilities of each component in a deep-UV stepper system. Chapters 2 and 3 of this thesis describe work on lifetime testing for pellicles and fluids for use in 248nm excimer lithography. Using pellicles and fluids in a deep-UV stepper can improve performance by protecting reticles, reducing unwanted reflections, and improving lens performance. These materials must be thoroughly tested to ensure that they do not degrade after accumulating large doses of deep-UV radiation, else their degradation will

effect the performance of a deep-UV stepper.

1.2 Quintupled Nd-YAG Lithography

Now that KrF excimer lithography has been established as a practical technology, stepper manufacturers are looking for a deep-UV source with a shorter wavelength than the KrF excimer laser. Two laser sources are currently available: ArF excimer (193nm) and Quintupled Nd-YAG (213nm). The ArF excimer laser would be the logical next step after the KrF excimer laser except for the safety and high periodic maintenance of excimer lasers. The quintupled Nd-YAG laser, with its small size, solid state lasing medium, and low maintenance level, is a viable alternative to the ArF excimer laser. An additional point in favor of the Quintupled Nd-YAG is the potential extension to even higher harmonics. The only remaining excimer line after ArF is F_2 at 157nm. The F_2 line is weak and offers little hope of generating high enough average power needed for microlithography. In contrast, the higher harmonics of the Nd-YAG laser can be produced by means of four wave mixing in nonlinear gasses, producing the needed amounts of average power. Stepping downward along the harmonics of the Nd-YAG laser represents a possible technological road map to 0.1μm lithography.

Chapters 4 through 7 of this thesis investigate the problems involved in using the Quintupled Nd-YAG laser in microlithography. High average power 213nm radiation has only recently become available through the use of frequency quintupling in beta Barium Borate crystal.[14, 15, 16, 17] The problems involved with producing 213nm radiation include thermal effects in the BBO crystal, BBO crystal damage, and damage to other optical components due the high peak power and short wavelength of 213nm radiation. These problems can be overcome with a properly designed laser system.

The greatest impediment to using the quintupled Nd-YAG laser for microlithography is the high speckle contrast owing to the highly coherent nature of this laser source. Several

methods of speckle reduction have been investigated with two promising methods described in chapters 5 and 6. High quality, speckle-free images have been obtained using a 213nm version of the BOLD family of small field projection lenses.[18] The performance of this lens is nearly diffraction limited, producing high contrast aerial images of 0.2μm line/space patterns over a 950μm field. Chapter 7 describes the optical system consisting of the 213nm source and the BOLD projection lens.

References

1. A.M. Hawryluk and H.I Smith, "Deep-Ultraviolet spatial-period division using an excimer laser," *Optics Letters*, vol. 7, no. 9, pp. 402-404, Sept. 1982.

2. A.M. Hawryluk and H.I Smith, "Deep-UV spatial-frequency doubling by combining multilayer mirros with diffrection gratings," *J Vac. Sci. Technol. B.*, vol. 1, no. 4, pp. 1200-1203, Oct. 1983.

3. K. Jain, C.G. Willson, and B.J. Lin, "Ultrafast Deep UV Lithography with Excimer Lasers," *Elec. Dev. Lett.*, vol. EDL-3, no. 3, pp. 53-55, March 1982.

4. K. Jain, "Laser Applications in Semiconductor Microlithography," *Microcircuit Engineering*, pp. 181-190, 1983.

5. K. Jain and R.T. Kerth, "Excimer Laser Projection Lithography," *Apllied Optics*, vol. 23, no. 5, pp. 648-649, March 1984.

6. K. Jain, "Advances in Excimer Laser Lithography," *SPIE Proc. on Excimer Lasers and Optics*, vol. 710, pp. 35-42, March 1986.

7. R.T. Kerth, K. Jain, and M.R. Latta, "Excimer Laser Projection Lithography on a Full-Field Scanning Projection System," *IEEE Elec. Dev. Lett.*, vol. EDL-7, no. 5, pp. 299-301, May 1986.

8. V. Pol, J.H. Bennewitz, G.C. Ecsher, M. Fieldman, V.A. Firtion, T.E. Jewell, B.E. Wilcomb, and J.T. Clemens, "Excimer Laser-Based Lithography: a Deep Ultraviolet Wafer Stepper," *SPIE Proc. on Opt. Microlith.*, vol. 633, pp. 6-16, March 1986.

9. T.E. Jewell, J.H. Bennewitz, G.C. Escher, and V. Pol, "Effect of Laser Characteristics on the Performance of a Deep UV Projection System," *SPIE Proc. on Lasers in Microlith.*, vol. 774, pp. 124-132, March 1987.

10. T.A. Znotins, T.J. McKee, S.J. Gutz, K.O. Tan, and W.B. Norris, "The Design of Excimer Lasers for Use in Microlithography," *SPIE Proc. on Optical/Laser Microlith.*,

vol. 922, pp. 454-460, 1988.

11. B. Ruckle, P. Lokai, H. Rosenkranz, B. Nukolaus, H.J. Kahlert, B. Burghardt, D. Basting, and W. Muckenheim, "Computerized Wavelength Stabilized 248.4nm Excimer Laser for Stepper," *SPIE Proc. on Optical/Laser Microlith.*, vol. 922, pp. 450-453, 1988.

12. R.L. Sandstrom, R.P. Akins, U.K. Sengupta, C. Reiser, D.G. Larson, and S.L. Anderson, "Krpton Fluoride Excimer Laser for Microlithography," *SPIE Proc. on Microlith.*, 1989.

13. R. Sandstrom, "Measurements of Beam Characteristics Relevant to DUV Microlithography on a KrF Excimer Laser," *SPIE Proc. on Microlith.*, 1990.

14. C. Chen, B. Wu, G. You, A. Jiang, and Y. Haung, "High Efficiency and Wide-Band Single-Harmonic-Generation Properties of the New Crystal beta-BaB2O4," *Thirteenth Int. Quant. Elec. Conf.*, pp. 20-21, June 1984.

15. K. Miyazaki, H. Sakai, and T. Sato, "Efficient Deep-ultraviolet Generation by Frequency Doubling in beta-BaB2O4 Crystals," *Optics Lett.*, vol. 11, no. 12, pp. 797-799, Dec. 1986.

16. W.L. Glab and J.P. Hessler, "Efficient Generation of 200-nm Light in beta-BaB2O4," *Applied Optics*, vol. 26, no. 16, pp. 3181-3182, Aug. 1987.

17. D. Eimerl, L. Davis, and S. Velsko, "Optical, Mechanical, and Thermal Properties of Barium Borate," *J. Appl. Phys.*, vol. 62, no. 5, pp. 1968-1983, Sept. 1987.

18. J.H. Bruning and W.G. Oldham, "A Compact Optical Imaging System for Resist Process and Lithography Research," *SPIE proc. of Optical/Laser Microlith.*, vol. 992, pp. 471-475, 1988.

Chapter 2
Transmission Lifetime Measurements of Pellicles for Deep-UV Lithography

Abstract -Candidate deep-UV pellicle materials have been tested for transmission stability under deep-UV exposure. Measurements were made with an exposure apparatus using a KrF excimer laser and a light pipe illuminator. Increased absorption and thickness reduction caused by deep-UV exposure have been found in polyvinyl butyral(PVB)-based pellicles. The thickness of the PVB pellicles has been monitored *in situ* and a "dark reaction" is found to occur long after the deep-UV exposure is complete. Pellicles made from a second, fluoropolymer, material have also been tested and found to be stable up to exposures of 10,000J/cm^2.

2.1 Introduction

The beneficial effects of pellicles on manufacturing yield in the semiconductor industry have been well demonstrated.[1,2] Ideally, a pellicle is an invisible, zero thickness membrane placed above the surface of a mask used in photolithography. This membrane prevents any airborne particles from landing on the patterned surface of the mask. The pellicle is suspended far enough above the mask surface so that the particles are held well outside the depth of focus. This required standoff distance depends on the depth of focus at the mask plane for a given lithography system. A 1:1 projection system would require less standoff than a reduction system because of the inherently higher numerical aperture(NA) at the mask.[3,4] The thickness of the quartz mask is usually enough to "pelliclize" the back side of the reticle used in a 1:1 system, where as a pellicle is often required for both sides of a mask used in a reduction system.

A key property of pellicles is uniformity of transmission, lest the nonuniformity affect the linewidth-control error-budget. It is straightforward to show that any aging of transmission would lead to pattern dependent exposure dose variations; thus candidate pellicle materials must be carefully tested to verify negligible aging during the intended pellicle life. Few materials are stable under deep-UV exposure, and several mechanisms can lead to transmission changes.

2.2 Theory

A pellicle that interacts with the laser beam will have a nonzero absorption coefficient. If the pellicle surfaces possess perfect anti-reflective(AR) coatings, then its transmission is given simply by:

$$T_1 = e^{-\alpha h} \tag{1}$$

where α is the absorption coefficient and h is the pellicle thickness. Most pellicles have either imperfect AR-coatings or no AR-coatings at all and thus have a transmission that depends on the thickness in a complex periodic fashion. The pellicle functions as an etalon because of the constructive or destructive interference of radiation reflected from the two surfaces of the pellicle membrane. If the absorption coefficient is small the pellicle transmission is given by:

$$T = T_1 T_2 \tag{2}$$

with T_1 from Eqn. (1) and T_2 given by:

$$T_2 = \frac{1}{1 + \frac{4R_{surf}}{(1-R_{surf})^2} \sin^2\left(\frac{2\pi n(\lambda) h}{\lambda}\right)} \tag{3}$$

where R_{surf} is the single surface reflection. For a pellicle with out AR-coatings, R_{surf} is

given by:

$$R_{surf} = \frac{(n(\lambda)-1)^2}{(n(\lambda)+1)^2} \tag{4}$$

and:

$n(\lambda)$ film refractive index

h film thickness

λ wavelength of light

Equation (3) ignores film absorption and a more rigorous derivation is straightforward. However the simple formula in (3) is preferred in this application since it differs from the more rigorous result by at most 2% over the full range of parameters studied.

The reduction of R_{surf} with AR-coatings reduces the amplitude of the transmission variation caused by the etalon effect, and thus good AR-coatings will make the pellicle transmission less sensitive to variations in physical thickness and refractive index.[5] There are four physical parameters that can affect the pellicle transmission: absorption coefficient (α), single surface reflection (R_{surf}), refractive index (n), and thickness (h). In this study, pellicle performance is shown to degrade with 248nm exposure owing to significant changes in all these parameters except refractive index.

2.3 Experimental Apparatus

Since many pellicles were to be examined, a semiautomated exposure and *in situ* transmission measurement apparatus was constructed. A schematic is shown in Fig. 1. High efficiency is required to permit large doses to be accumulated in reasonable time and good exposure uniformity is essential for data integrity. Both are obtained by using a quartz light pipe as the main illuminator element. Radiation from a line-narrowed KrF excimer laser (linewidth = 3pm) is concentrated onto a diffuser plate placed against the entrance of the light pipe. The scattered rays from the diffuser create many virtual sources at the entrance

plane of the light pipe that combine at the exit to form a uniform plane of illumination. The system produces an exposure uniformity of +/-5% over an area 0.5cm by 1.0cm (see Figs. 2 and 3).

The uniformity of exposure is improved as the number of internal reflections is increased. The number of virtual sources created by the lightpipe is directly related to the number of internal reflections suffered by the light rays as they travel the length of the light-pipe. To increase the number of internal reflections, one could use a diffuser with a large scattering angle or one could use a light pipe with a large length to width ratio. The first method has a drawback in that a large NA lens must be used to collect the light traveling at high angles from the exit plane. High NA lenses made from the simple quartz elements used in this system are highly aberrated and produce poor uniformity. Using a long narrow light-pipe combined with a weak diffuser produces excellent uniformity while allowing the use of lower NA optics. This exposure system uses a lightpipe with a length to width ratio of 70:1 and a length to height ratio of 35:1.

The exit plane of the light pipe is imaged onto a rectangular mask constructed from four knife edges. The use of a knife edge mask instead of a standard quartz mask is needed because volatile material leaving a pellicle under test might deposit on the quartz mask, permanently altering the system transmission. A small portion of the incident light is split off by a beamsplitter and passes through a mask identical to the first to provide a reference beam. After passing through the exposure mask and the pellicle under test, another beam-splitter deflects some of the radiation into the transmitted energy detector. Both optical paths in this system (incident and transmitted) were constructed as identical as possible. In this way any intensity dependent effects on the detectors or optical components would be ratioed thus improving the linearity of the transmitted energy measurement.

Both the incident and transmitted energy detectors are large area silicon photodiodes with quartz window packaging. The large are of the diodes helps to sample from all points

in the exposure area and not limiting the transmission measurement to a small area on the pellicle. The detector electronics consist of a current to voltage converter with an RC time constant of 0.5 seconds. Since the laser has a pulse rate of 200pps, this RC time constant gives an output voltage that is the average energy reading of several hundred pulses. This pulse averaging smooths the +/-20% pulse to pulse energy variation from the excimer laser. Fig. 4 shows the system transmission stability, it is a graph of transmission versus dose with no pellicle in place. This exposure system demonstrates a long term exposure stability of +/-1%.

The data is processed and stored on a IBM PC using the same software written for the Berkeley large area exposure station.[6] The incident energy and pellicle transmission are then stored to a text file for easy manipulation.

2.4 Nitrocellulose Test Results

A nitrocellulose pellicle was tested even though this material is highly absorbing at 248nm. The transmission versus wavelength for a nitrocellulose pellicle is shown in Fig. 5. The failure mechanisms of this pellicle give insight into those of the deep-UV pellicle materials. Fig. 6. shows the transmission of this pellicle versus dose. The initial transmission is low and varies sinusoidally with dose. This sinusoidal behavior is evidence of a change in thickness during exposure. The pellicle changes thickness so quickly in the beginning of the exposure that the sine wave varies too rapidly for the system sample rate to fully resolve. Near a dose of 250 J/cm^2 the rate of thickness change slows so that the sinusoid can be resolved. The pellicle finally breaks at 800 J/cm^2 as evidenced by the sharp change in transmission. The erratic transmission variations between 800 and 1500 J/cm^2 are the result of further pellicle breakage. Visual inspection of the pellicle after exposure shows wrinkles in the unexposed pellicle film near the exposure area. This wrinkling is evidence of stress in the film created during the exposure.

2.5 Polyvinyl Butyral Test Results

Polyvinyl butyral(PVB)-based resin has been advanced as a candidate deep-UV pellicle material.[7,8,9,10,11] Fig. 7a shows the transmission versus wavelength for a typical 2.3μm thick uncoated PVB pellicle. The oscillations with wavelength agree with Eqns. (1)-(4). For wavelengths shorter than 300nm absorption is evident. The material has excellent transmission at 248nm, about 98%.

This pellicle transmission versus dose is displayed in Fig. 8. The transmission of this pellicle begins to change immediately on exposure and forms a sinusoidal pattern superimposed on a gradual decrease in transmission. The gradual reduction in the "DC" transmission of the pellicle is caused by an increase in absorption of the bulk material. The sinusoidal shape may be ascribed to a change in the optical thickness during exposure. In this instance, the effect on transmission owing to optical thickness change is much more pronounced than that caused by absorption. (In Fig. 8, 1000J/cm^2 would correspond to about 250,000 equivalent exposures, assuming a 5X reduction stepper and 100mJ/cm^2 sensitive resist. This number is reduced by a factor of 25 for a unity magnification system.)

A change in optical thickness can be caused by either a physical thickness change or a change in refractive index. To determine the mechanism, a measurement of transmission versus wavelength is made before and after a deep-UV exposure. A fit is then made to these two curves using Eqns. (3) and (4). To find the best fit, both the pellicle physical thickness, h, and refractive index, n(λ), are allowed to vary. The form for the real part of the refractive index was chosen as the simple Cauchy equation:

$$n(\lambda) = n_0 + \frac{n_1}{\lambda^2} \tag{5}$$

where n_0 is the long wavelength index and n_1 is the strength of the pole at $\lambda = 0$. Thus, three parameters are allowed to vary while searching for the best fit: h, n_0, and n_1. Once this best fit is found, the transmission values at each peak in the curve are used to find the absorption

coefficient versus wavelength of the bulk material. These values of the absorption coefficient are then used in Eqn. (2) to find a new fit for n_0, n_1, and h. This process is iterated until the best fit for all the variables is found. Once the best fit is obtained, the absorption coefficient is calculated from the imaginary part of the refractive index, $k(\lambda)$, by the relation:

$$k(\lambda) = \frac{4\pi\lambda\alpha(\lambda)}{n(\lambda)}. \qquad (6)$$

Figs. 7a and 7b show the measured transmission versus wavelength data and the theoretical fit before and after the deep-UV exposure.

Fig. 9 is a plot of the real and imaginary parts of the film refractive index versus wavelength before and after exposure. The imaginary part of the refractive index shows a significant increase in absorption for all wavelengths below 300nm. L little change in the real part of the refractive index occurs during deep-UV exposure. We must conclude that the sinusoidal variation in transmission during exposure arises from a change in the physical thickness of the pellicle. This interpretation is further supported by the theoretical fit for the physical thickness change. The theoretical fit for the pellicle thickness, h, gives a pre-exposure thickness of 2.29μm and a post-exposure thickness of 2.09μm. A 0.2μm thickness change is about five quarter-wavelengths (divided by the film refractive index) at 248nm, which should lead to 5 transmission maxima-minima (minima-maxima) shifts. Fig. 8 shows the five shifts that indeed occur within this exposure dose.

The application of an AR-coating to the surfaces of the pellicle film can greatly reduce the amplitude of the sinusoidal variation in transmission during exposure. Tests on pellicles with several proprietary organic and inorganic AR-coatings have been performed. The organic AR-coatings that we tested tested failed after only a small exposure dose, less than 100J/cm^2. After testing many pellicles, examples were found of stable AR-coatings, all were inorganic according to the pellicle vendors. A measurement of transmission versus wavelength for a PVB pellicle with an inorganic AR-coating (Fig. 10) demonstrates the

effectiveness of an AR-coating in reducing the dependence of transmission on optical thickness. The sinusoidal variation in transmission near 248nm has been reduced from a range of 14% to less than 2%. This graph is for different wavelengths, but according to eqn. (3) changes in thickness and wavelength have the same effect.

Fig. 11 shows the transmission versus dose for this pellicle. Clearly the periodic variation in transmission has been greatly reduced from that of Fig. 8. For pellicles with such AR-coatings, the dominant aging mechanism is a simple increase in the bulk absorption, and the useful life is much improved. Finally, to show that the AR-coating did survive the 1500J/cm^2 exposure, Fig. 12 is a graph of transmission versus wavelength for this pellicle after the exposure. The periodic variations near 248nm are still greatly damped while the bulk absorption has markedly increased from that shown in Fig. 10.

2.6 Reciprocity Tests on Polyvinyl Butyral

In a production environment, a pellicle would not be exposed to continuous deep-UV radiation, since wafer loading and alignment interrupt the exposure step. A rough idea of production exposure conditions may be obtained by assuming the following manufacturing environment:

exposures per wafer	100
wafers per hour	25
hours per week	100
total exposures per week	250,000
weekly dose at wafer for 100mJ/cm^2 resist	25,000J/cm^2
weekly dose at mask for 100mJ/cm^2 resist and 5X stepper	1000J/cm^2

Our pellicle exposure system can deliver this equivalent dose in about 2 hours. The exposure time is reduced, compared to a stepper, both because of a larger energy per pulse and a higher duty cycle. If one assumes a reasonable intensity of 1.0mJ/cm^2 per pulse at the wafer

plane of a 5X stepper, this corresponds to 0.04mJ/cm^2 per pulse at the pellicle plane. Our exposure system uses a 1.0mJ/cm^2 intensity at the pellicle. This 25 times increase leads to questions about peak-power reciprocity. Do the results at our high fluence conditions carry over to the low intensity exposure conditions found in production?

To test for failure of peak-power reciprocity, we exposed two identical pellicles, one to 1.0mJ/cm^2 at 20 pulses per second (pps) and the other to 0.1mJ/cm^2 at 200pps. Each exposure produces the same average power, but the first uses 10 times the peak intensity of the second. The resultant aging rates showed only a small difference between the two pulse energies, less than 2%. This small difference may even be due in part to some nonlinearity in the detection system. Because most reciprocity failure mechanisms are highly nonlinear, such as ablation, this small difference is most likely not caused by a failure of peak power reciprocity. It is also reasonable to assume than even lower peak powers will have the same effect since the peak powers currently used are below the ablation threshold of PVB.

The second difference between our test conditions and those experienced in a production environment is the exposure duty cycle. A production stepper exposes for a short duration then pauses while moving to the next field. Our test system performs a continuous exposure. To test for duty cycle effects, two identical pellicles were exposed with identical pulse power, but this time with different pulse frequency. The first pellicle received 200mW/cm^2 average power while the second received 20mW/cm^2 average power. Both pellicles were exposed using a 200hz pulse rate. This 10 times reduction in average exposure rate leads to a 10 times increase in the time needed to accumulate a given dose. The transmission measurements for these two experiments is shown in Fig. 13. The pellicle tested with the lower average exposure rate aged significantly more at a given dose than did the film exposed at the higher average rate.

To gain greater insight into the source of this failure of average power reciprocity, the thickness of the pellicle was monitored during exposure and for a time after the exposure

was complete. This *in situ* thickness monitoring was performed by the system shown in Fig. 14. A HeNe laser beam is reflected off the back side of the pellicle under test. The ratio of the reflected to incident 633nm energy varies sinusoidally with changes in the thickness of the pellicle. This technique is much like that used in resist development-rate monitoring systems.[12] This sinusoidal variation can be derived from eqn. (3), the reflectance of the pellicle is given by $R_{totoal} = 1 - T_{total}$:

$$R_{total} = \frac{\frac{4R_{surf}}{(1-R_{surf})^2}\sin^2(\frac{2\pi n(\lambda)h}{\lambda})}{1+\frac{4R_{surf}}{(1-R_{surf})^2}\sin^2(\frac{2\pi n(\lambda)h}{\lambda})}, \tag{7}$$

which can be approximated by:

$$R_{total} \approx \frac{4R_{surf}}{(1-R_{surf})^2}\sin^2(\frac{2\pi n(\lambda)h}{\lambda}). \tag{8}$$

The thickness of the pellicle is then given by:

$$h \approx \frac{\lambda}{2\pi n(\lambda)}\arcsin\left[\sqrt{\frac{(1-R_{surf})^2}{4R_{surf}}R_{total}}\right]. \tag{9}$$

This equation is periodic with period $\frac{1}{2}\frac{\lambda}{n(\lambda)}$. As each period of the reflectance in repeated, an additional $\frac{1}{2}\frac{\lambda}{n(\lambda)}$ of thickness must be added or subtracted. Eqns. (7) through (9) make the assumption of a constant refractive index at the wavelength used for thickness monitoring. This assumption is valid for the PVB pellicle material as was shown in the previous section, since the index of PVB does not change at the HeNe wavelength, 633nm.

The experiment performed was to expose the pellicle under the two different average powers shown in Fig. 13 while monitoring the pellicle thickness. The monitoring continued for 2 hours after completion of the exposure. The results of these measurements are shown in Figs. 15 and 16. Fig. 15 shows the pellicle thickness during exposure for the two different average exposure powers. The lower average power shows a greater loss of thickness versus

dose than does the higher average power. Fig. 16 shows the pellicle thickness versus time after the exposure has been completed at the two different exposure rates. In both cases the pellicle continues to lose thickness after the exposure is complete, but the pellicle that received the exposure using the higher average power exhibits a greater thickness change during the dark period. This suggests that a greater potential thickness change is built up in the pellicle during the exposure at higher average power.

Clearly, a "dark reaction" occurs, and is the source of average power reciprocity failure. We may speculate about the mechanism leading to the dark reaction. Because of the long time constants, diffusion-limited processes are suggested. For example, out-diffusion of destructed polymer by-products, or in-diffusion of an atmospheric reactant are possible mechanisms. In-diffusion is unlikely since that would lead to swelling and is contrary to the loss in thickness measured in the previous section. During the deep-UV exposure, the concentration of these diffusing components reach a steady state inside the pellicle. This steady state concentration depends on the diffusion rate of the components involved and the deep-UV exposure rate. Higher exposure rates lead to higher steady state concentrations and thus reciprocity fails. Since the time constant of this dark reaction is so long (several hours), and the exposure rate in a production stepper is still an 10 times slower than these experiments, it would be prudent to further reduce the estimated useful lifetime for PVB pellicles from the value suggested in Figs. 11, 15, and 16. Without a greater understanding of the reciprocity failure mechanism, we can not give a quantitative value for the amount of reduction in useful lifetime beyond our present estimate.

2.7 Fluoropolymer Pellicle Material Test Results

A proprietary deep-UV pellicle material was also made available to us for testing. This material is manufactured by Dupont Semiconductor Products and is described as a Teflon AF amorphous fluoropolymer. Fig. 17 shows the transmission versus wavelength of this material with no AR-coating. The thickness has been well tuned to achieve maximum

transmission at 248nm as evidenced by the 98% transmission peak at 248nm. Fig. 18 shows the result of transmission versus dose measurements for an uncoated sample and Fig. 19 shows the results for an AR-coated sample. The AR-coated pellicle has a slightly lower transmission at 248nm apparently owing to some absorption in the AR-coating, but neither type showed any evidence of aging up to 1500J/cm^2.

Because of the high stability of this pellicle material, an experiment was performed with a much higher exposure dose. The AR-coated pellicle was exposed to an integrated fluence of 10,000J/cm^2, corresponding to some 2,500,000 equivalent 5X stepper exposures, or 10 weeks of use in our simple manufacturing model. Within the +/-1% stability of our measurement system, the pellicle material and the AR-coating remained stable after this large exposure dose (Fig. 20).

2.8 Conclusions

For comparison, the results for 10 uncoated and AR-coated pellicles supplied by 6 different vendors are shown in Figs. 21 and 22. As these graphs show, the performance of each pellicle within a given material class is similar. Great variations exist among the AR-coatings, with the inorganic coatings performing far superior to the organic coatings.

The PVB based pellicle material shows a fundamental thickness loss during exposure, which continues even after the exposure is complete. This "dark reaction" leads to an average power reciprocity failure. Consequently our high exposure rates give lifetime results that are optimistic when extrapolated to production test conditions. A derating of the useful PVB pellicle lifetime presented here would be prudent. Unfortunately, our present analysis can not give a quantitative value for the amount of derating.

All lifetime tests performed on the Dupont Teflon AF material, both uncoated and AR-coated, showed no degradation with exposure. Large doses equivalent to 2,500,000 die exposures have been applied to this material with no observable increase in absorption or

optical thickness change.

References

1. A. Rangappan and C. Rao, "Yield Improvement with Pellicalised masks in Projection Printing Technology," *SPIE Proc. on Optical Microlithography*, vol. 334, pp. 52-57, 1982.

2. R. Winn and R. Turnager, "Pellicles-An Industry Overview," *Solid State Technology*, pp. 41-43, June 1982.

3. R. Hershel, "Pellicle Protection of Integrated Circuit (IC) Masks," *Proc. SPIE*, vol. 275, pp. 23-28, 1981.

4. T.A. Brunner, C.P. Auschnitt, and D.L. Duly, "Pellicle Mask Protection for 1:1 Projection Lithography," *Solid State Tech.*, no. 5, pp. 135-143, 1983.

5. R. Winn, "Coated Versus Uncoated Pellicles THe Pros and Cons," *MICROlithography News*, pp. 11-18, May 1989.

6. D.M. Drako, W.N. Partlo, and W.G. Oldham, "Characterization System for Deep-UV Resists," *Proc. SPIE*, vol. 1086, pp. 471-482, 1989.

7. I. Ward, "Pellicle Compositions and Pellciles Thereof for Projection Printing," *U.S. Patent #4,476,172*, Oct. 1984.

8. I. Ward, "Polyvinyl Butyrate Pellicle Compositions and Pellicles Thereof for Projection Printing," *U.S. Patent #4,482,591*, Nov. 1984.

9. I. Ward and D.L. Duly, "A Broadband Deep UV Pellicle for 1:1 Scanning Projection and Step and Repeat Lithography," *SPIE Proc. on Optical Microlithography*, vol. 470, pp. 147-156, 1984.

10. I.E. Ward and P.M. Papoojian, "Pellicle Compositions and Pellicles Thereof for Projection Printing," *U.S. Patent #4,499,231*, Feb. 1985.

11. P. Yan and H. Gaw, "Lifetime and Transmittance Stability of Pellicles for I-line and KrF Excimer Laser Lithography," *Proc. KTI Microelec. Seminar*, pp. 261-277, Nov.

1989.

12. D.J. Kim, "Caracterization and Modeling of Positive Photoresist," *UCB/ERL Memorandum No. M84/65*, Aug. 1984.

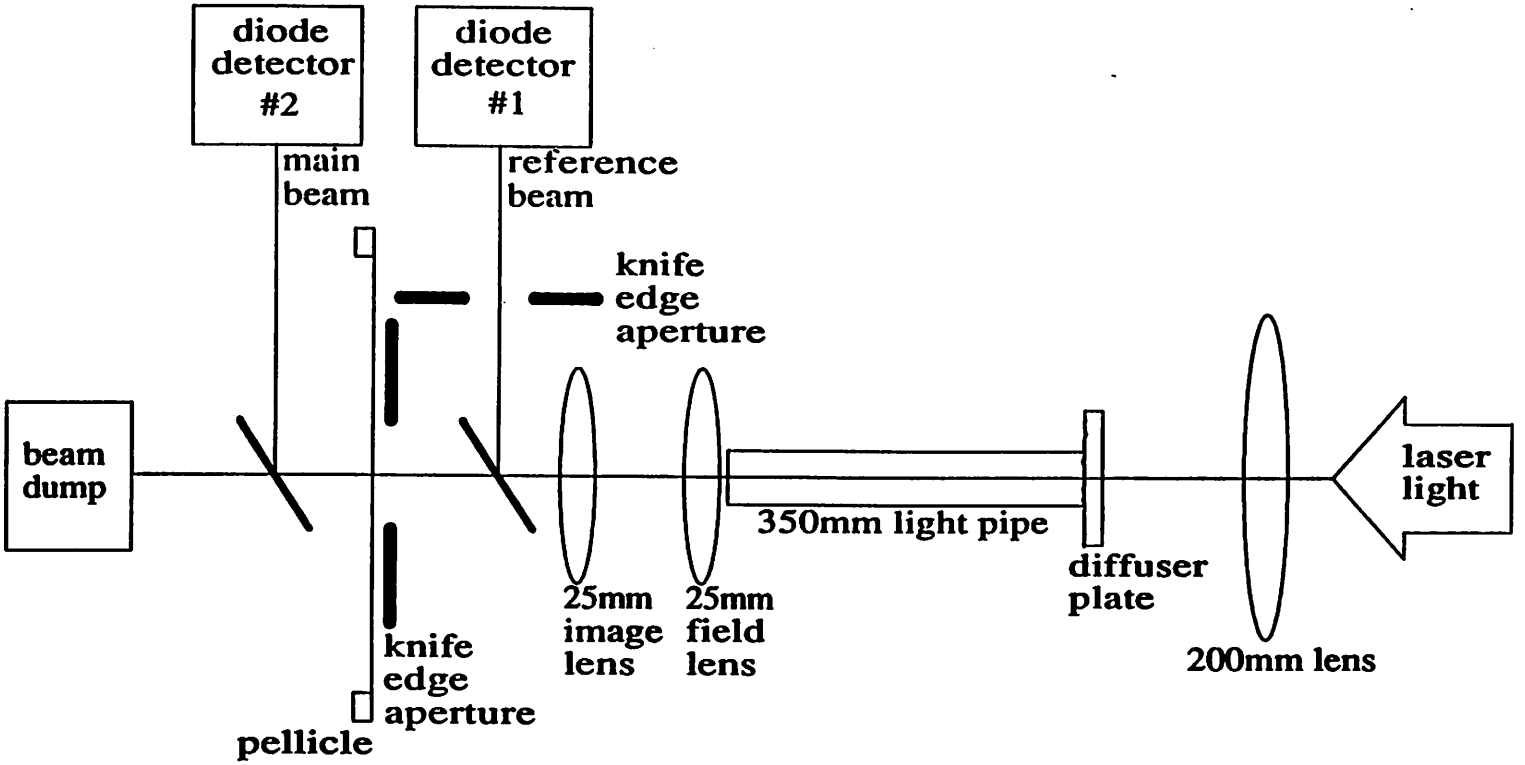

Fig. 1. Exposure apparatus used to measure transmission during deep-UV exposure.

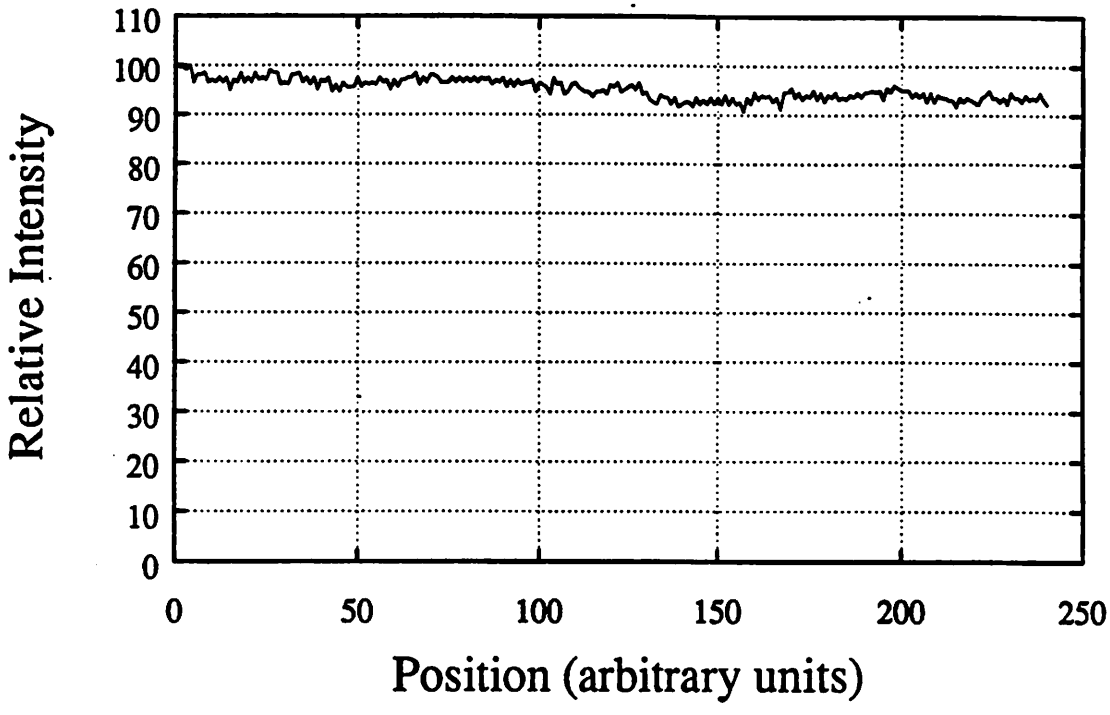

Fig. 2. Exposure uniformity in the horizontal direction for the system shown in Fig. 1.

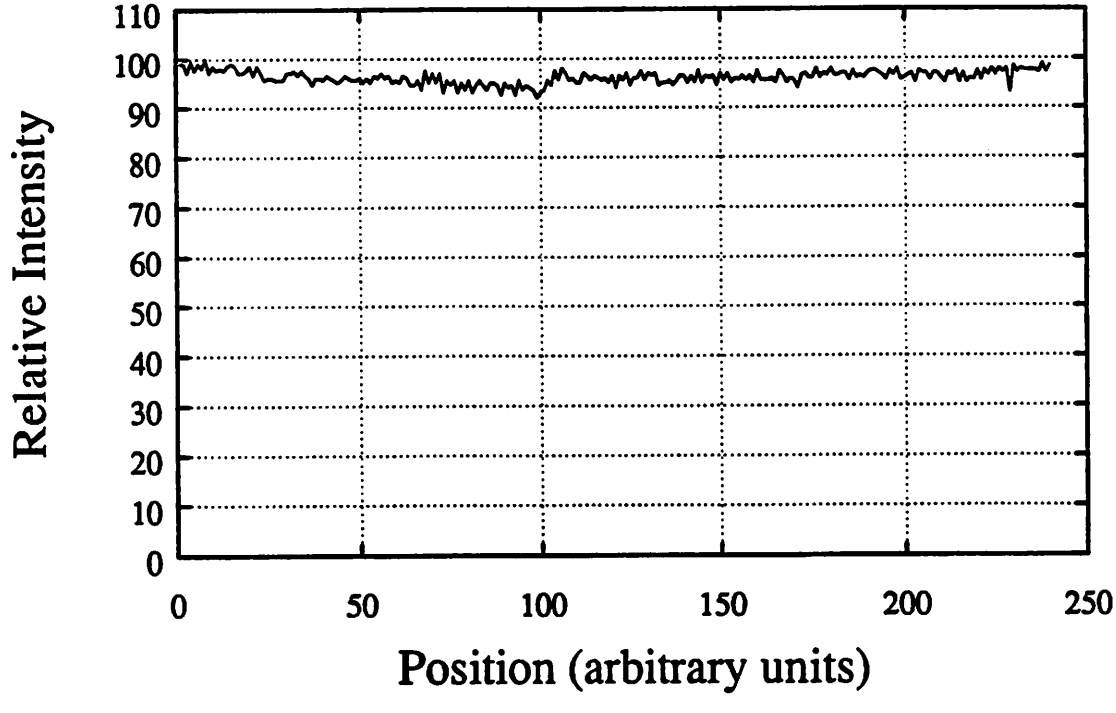

Fig. 3. Exposure uniformity in the vertical direction for the system shown in Fig. 1.

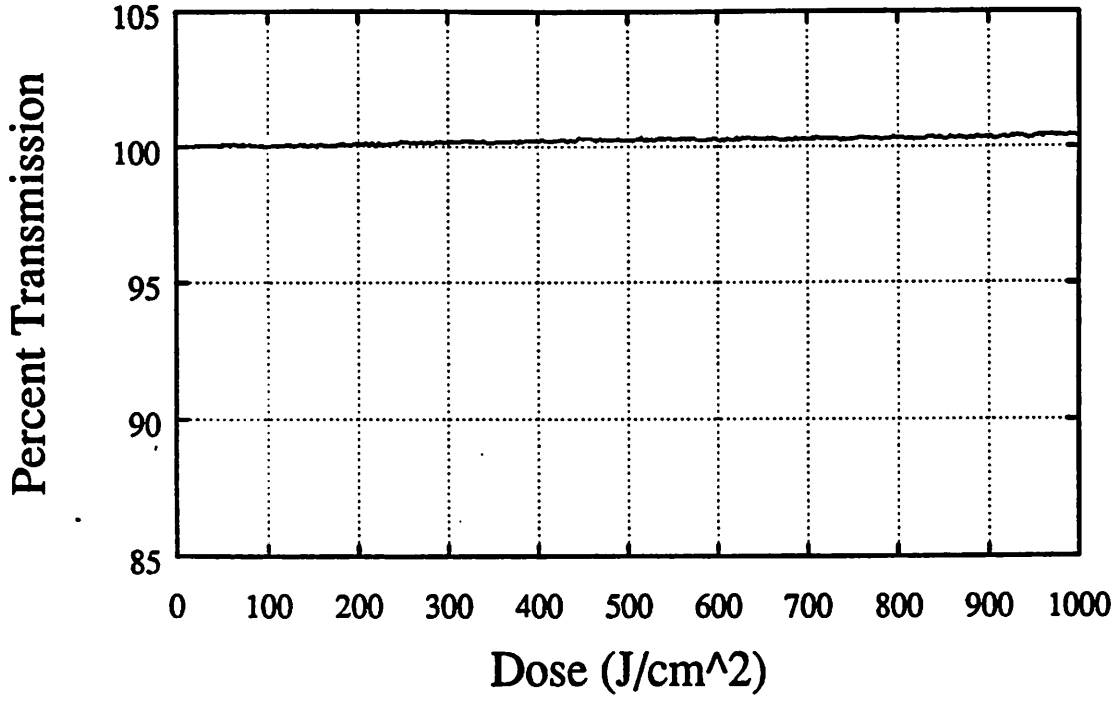

Fig. 4. System stability test (no pellicle in place).

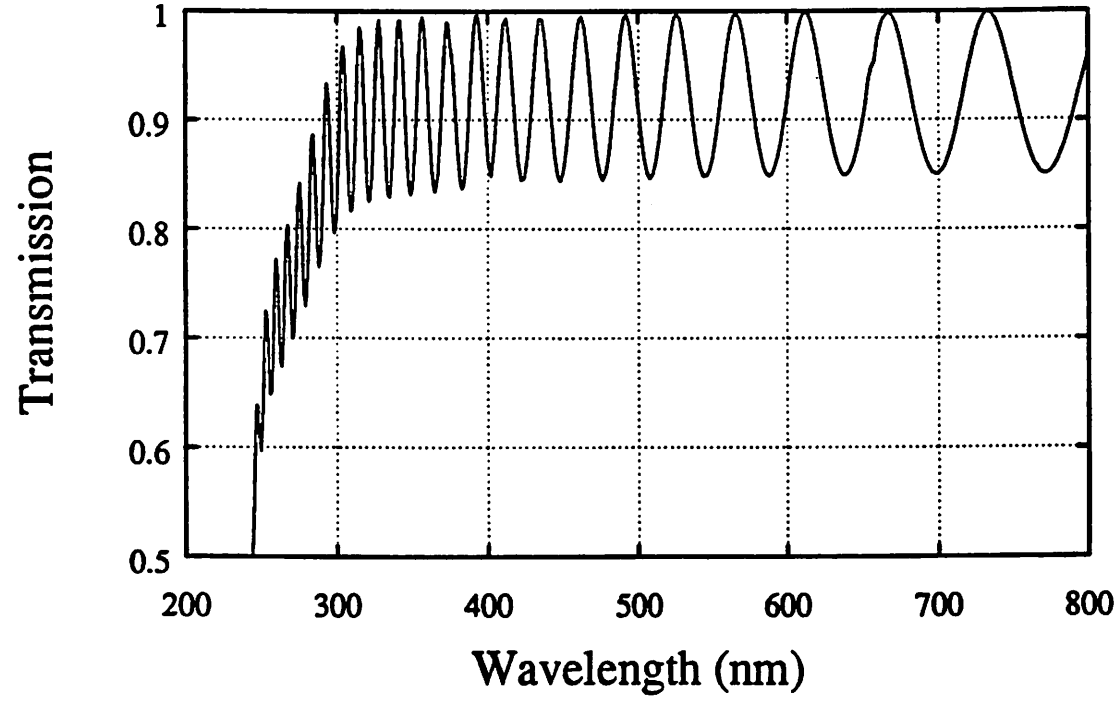

Fig. 5. Transmission vs. wavelength for a nitrocellulose pellicle before exposure.

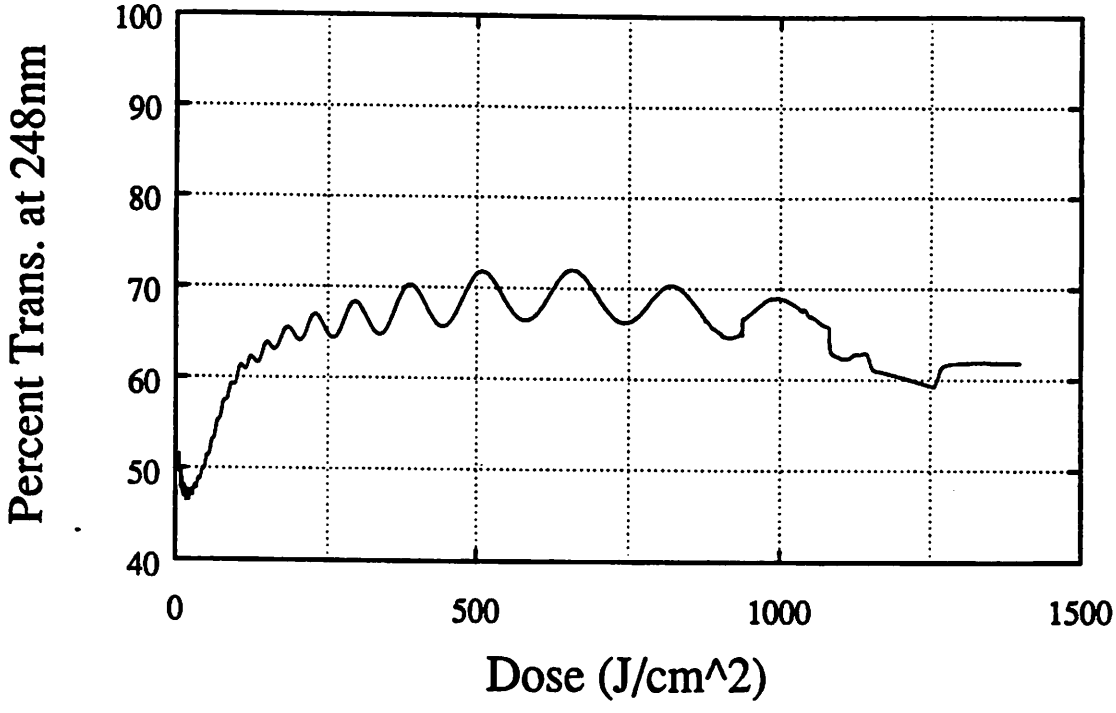

Fig. 6. Percent transmission at 248nm vs. dose for a nitrocellulose pellicle.

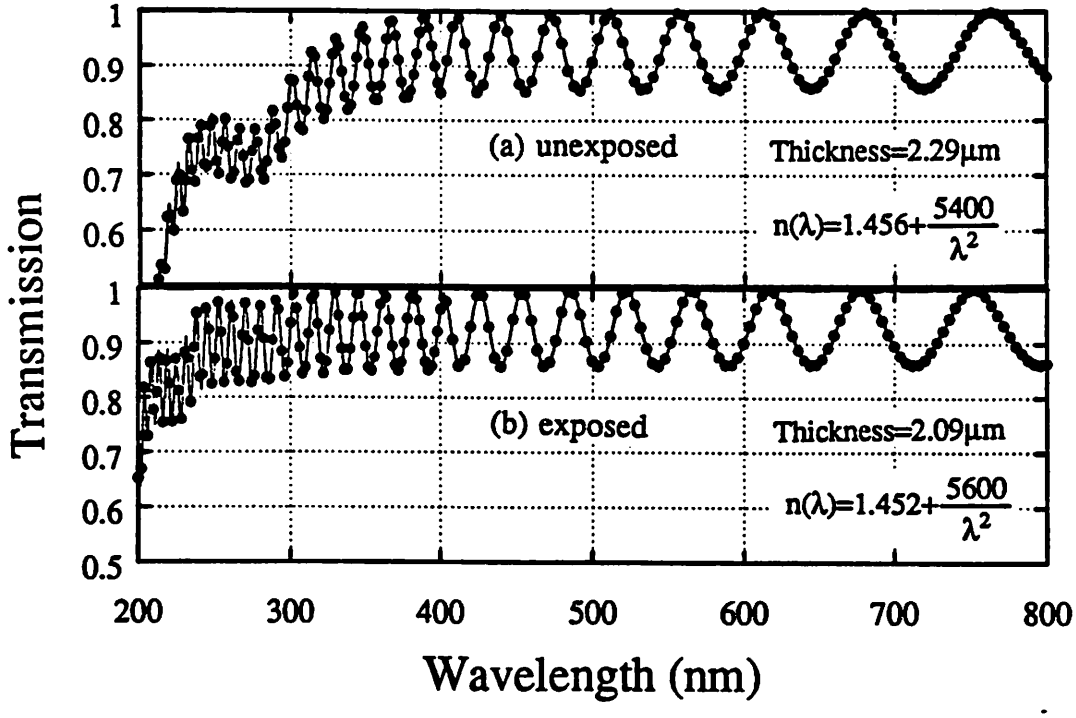

Fig. 7. Transmission vs. wavelength for an uncoated PVB pellicle:
a) unexposed b) exposed (1500J/cm^2).

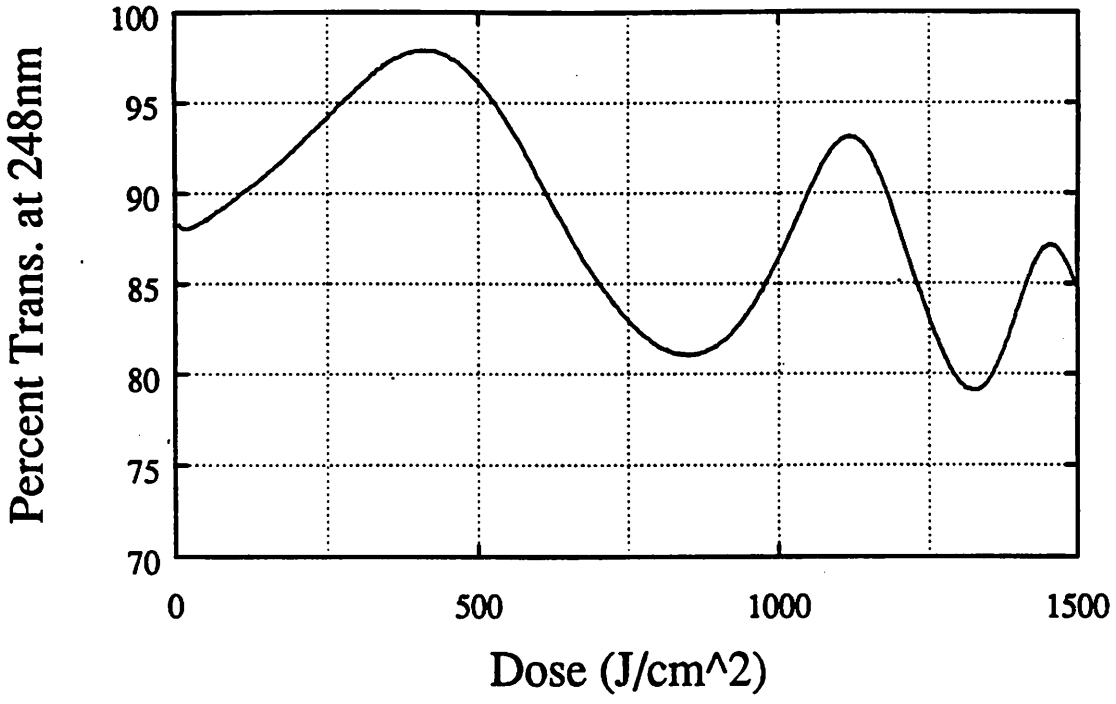

Fig. 8. Percent transmission at 248nm vs. dose for an uncoated PVB pellicle.

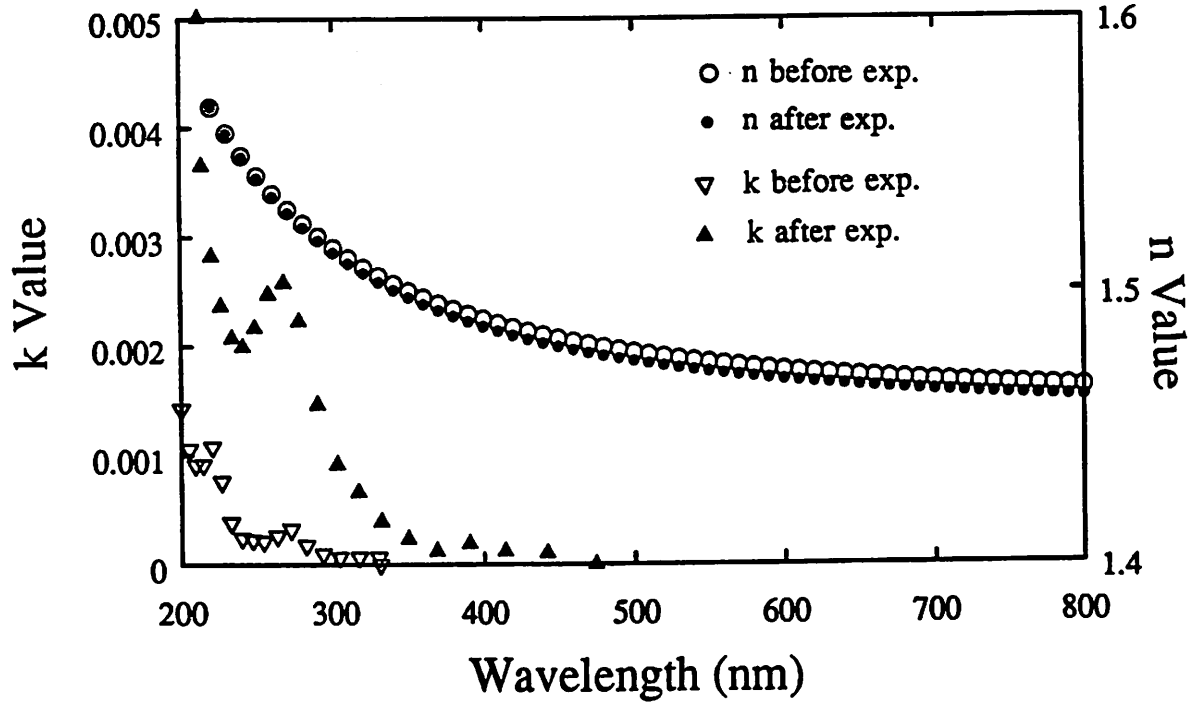

Fig. 9. Real (n) and imaginary (k) parts of the refractive index for a PVB pellicle before and after an exposure of 1500J/cm^2.

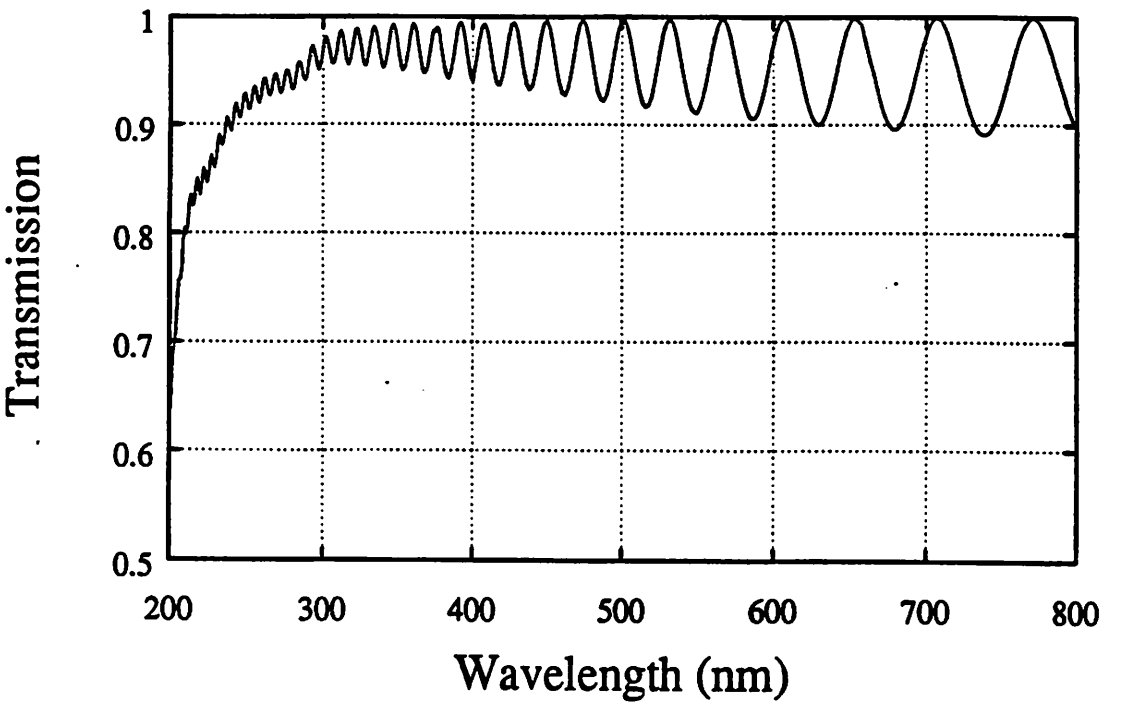

Fig. 10. Transmission vs. wavelength for an AR-coated PVB pellicle before exposure.

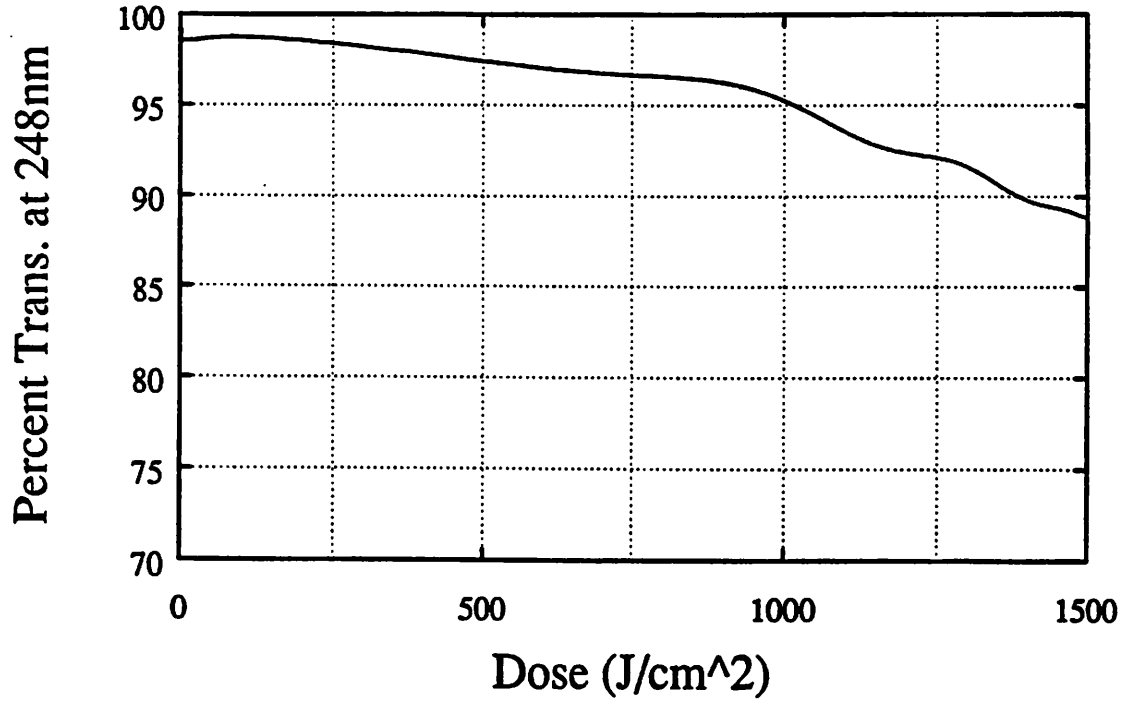

Fig. 11. Percent transmission at 248nm vs. dose for an AR-coated PVB pellicle.

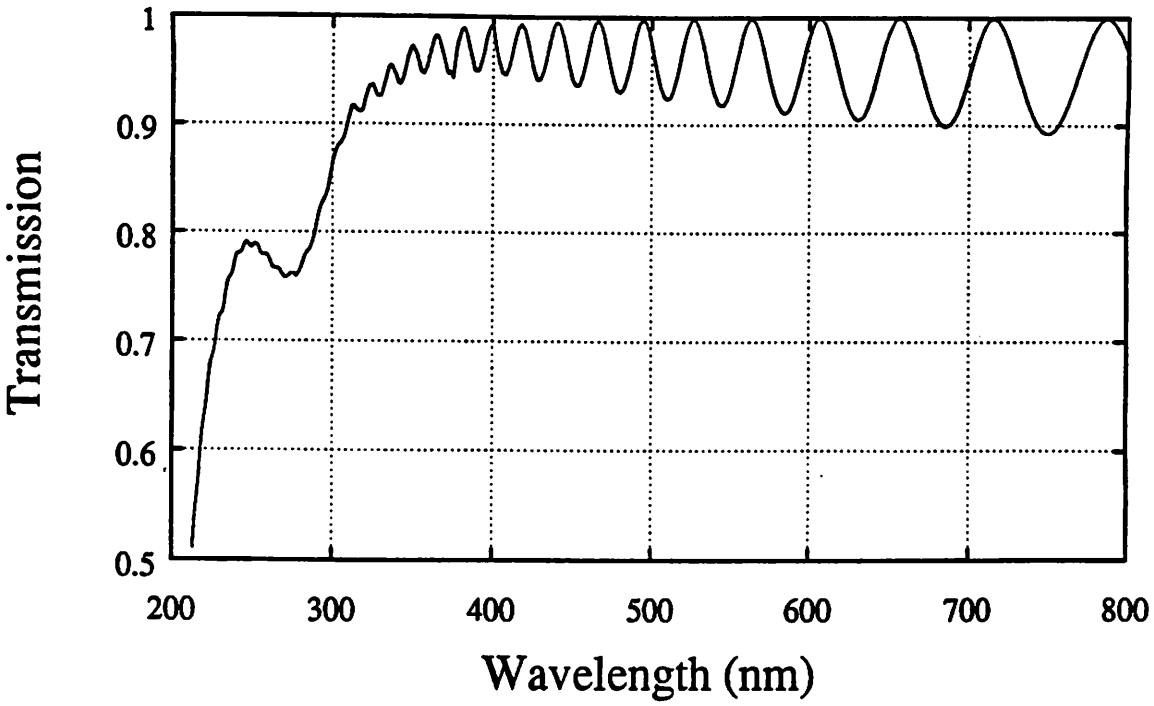

Fig. 12. Transmission vs. wavelength for an AR-coated pellicle after an exposure of 1500J/cm^2.

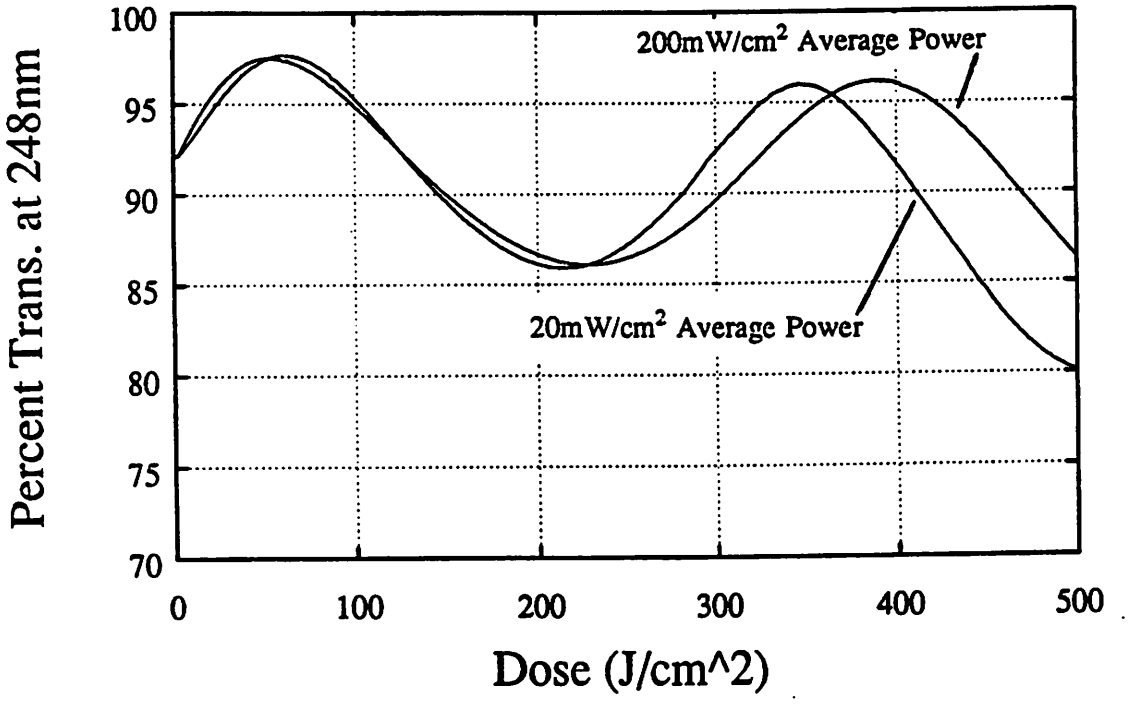

Fig. 13. Percent transmission at 248nm vs. dose using two different average powers to test for average power reciprocity.

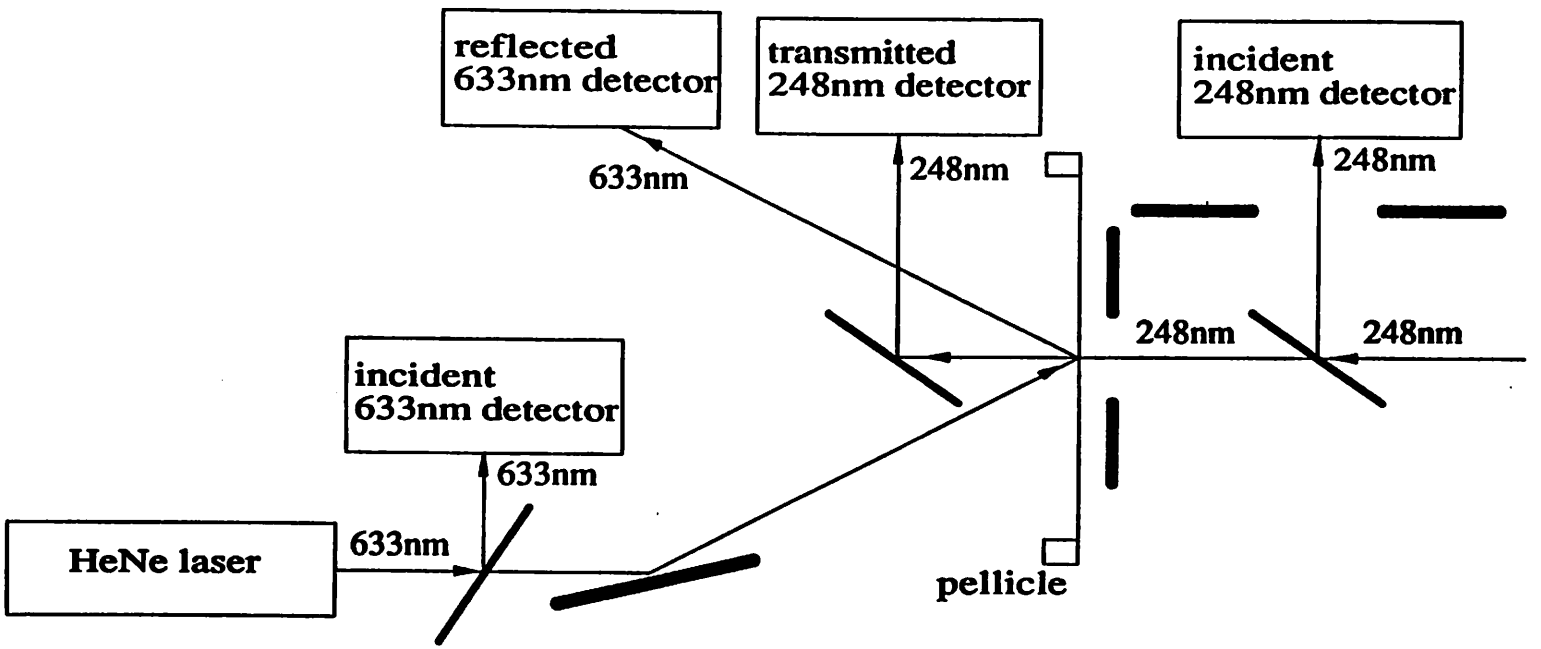

Fig. 14. In situ thickness monitoring system used in conjunction with exposure aparatus.

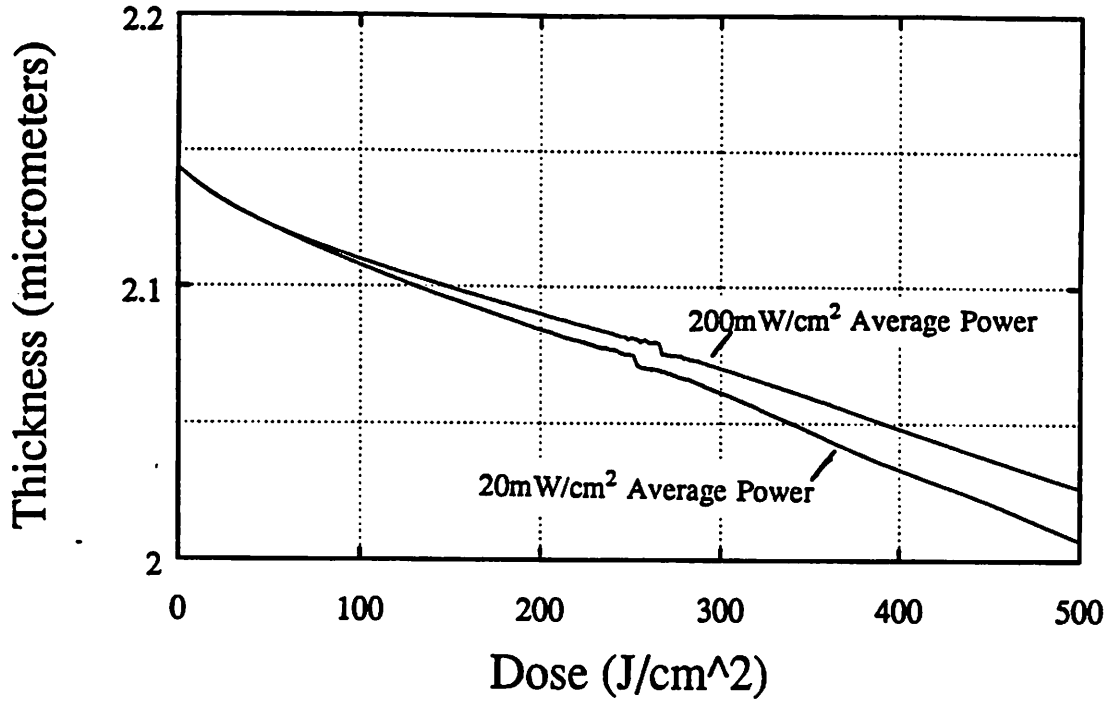

Fig. 15. PVB pellicle thickness vs. dose, exposed using two different average powers.

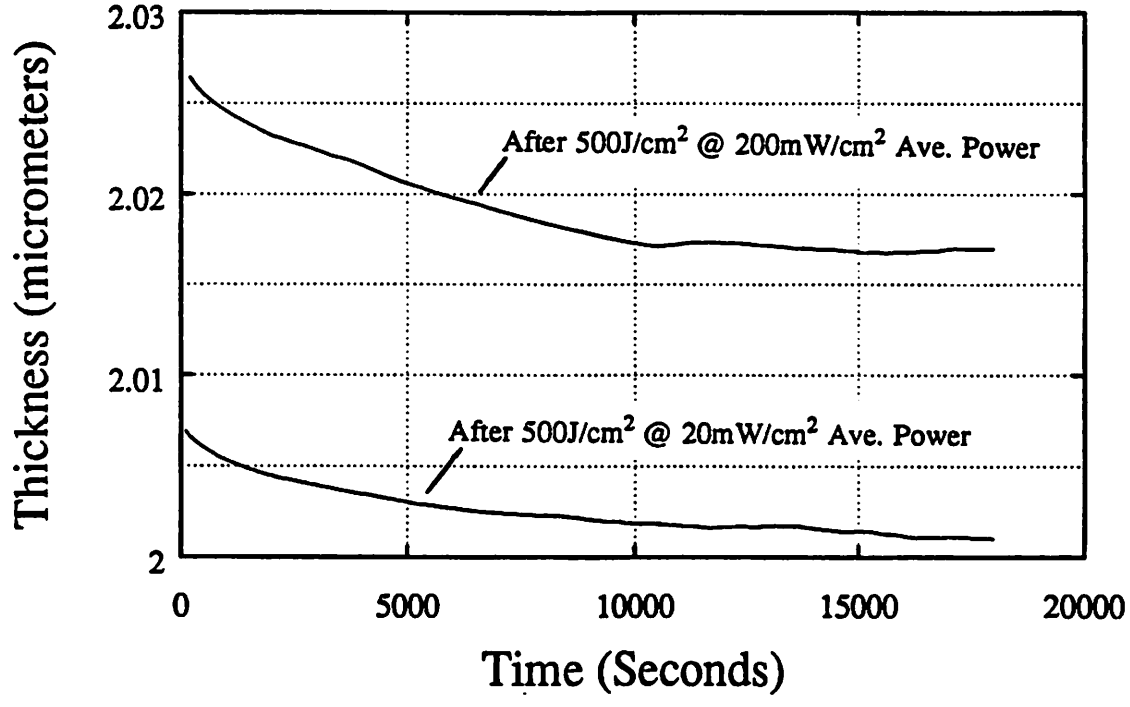

Fig. 16. PVB pellicle thickness vs. time after exposure is complete. Results for both average powers shown in Fig. 15 are displayed.

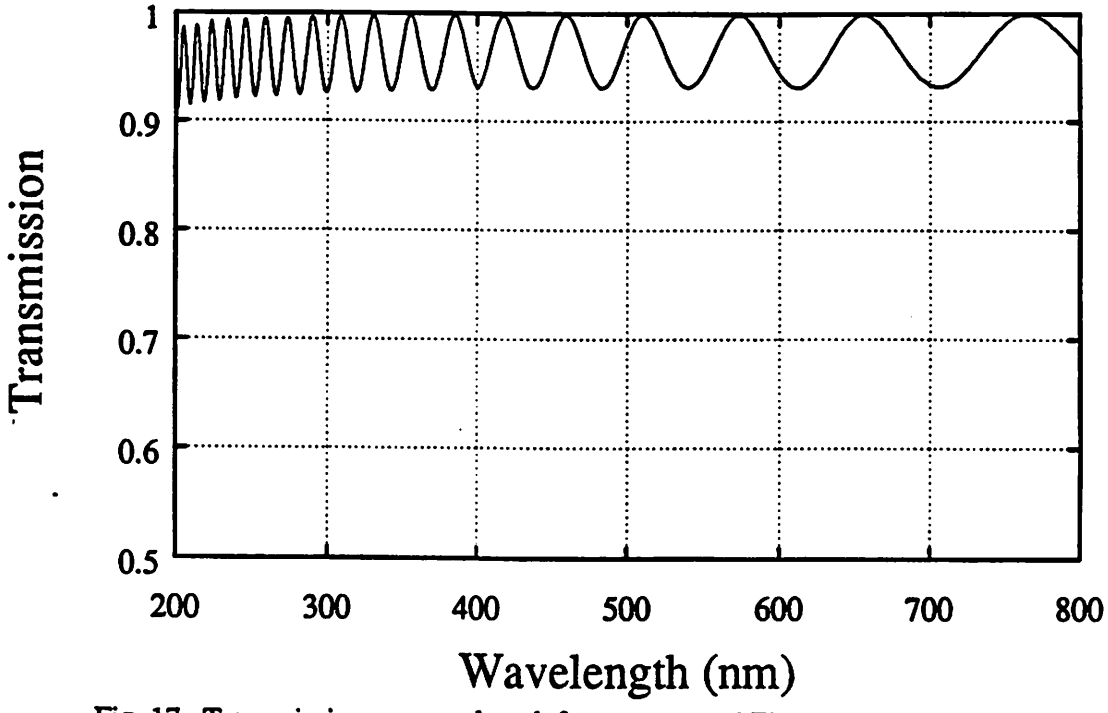

Fig. 17. Transmission vs. wavelength for an uncoated Fluoropolymer pellicle.

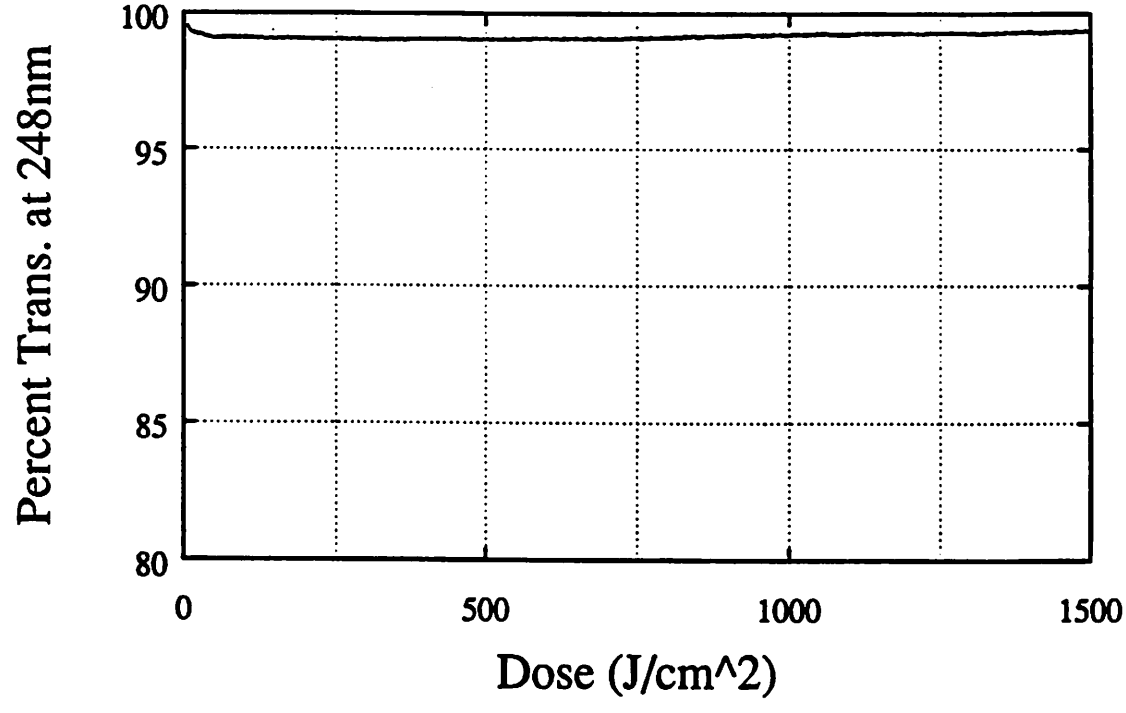

Fig. 18. Percent transmission at 248nm vs. dose for an uncoated fluoropolymer pellicle.

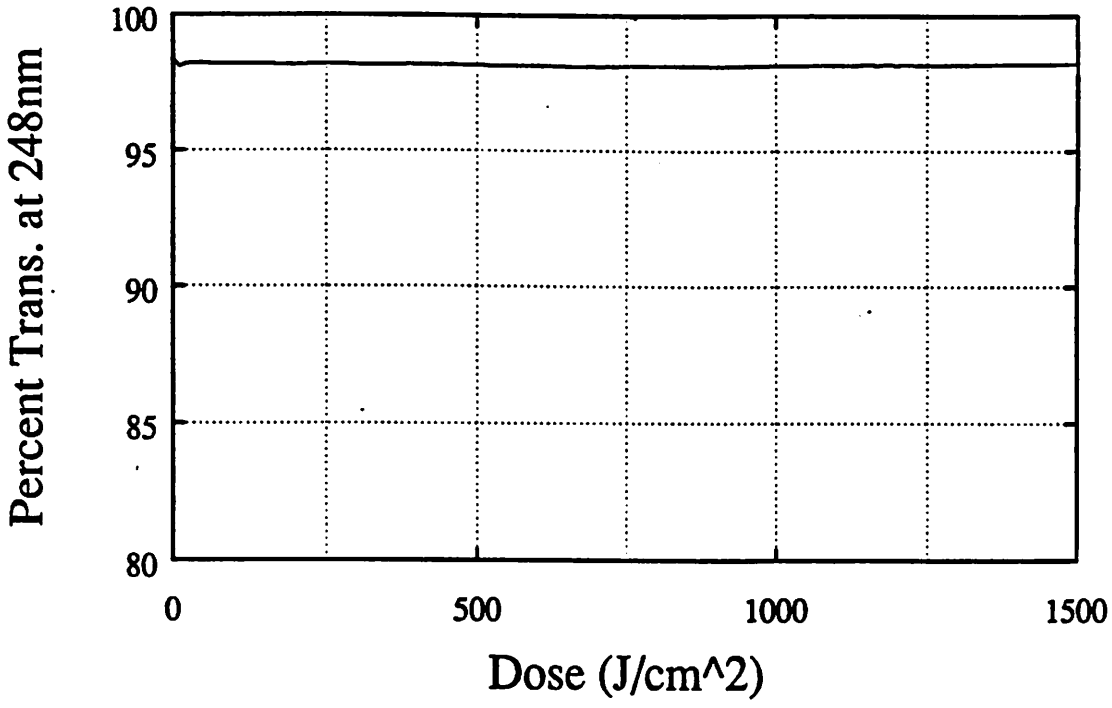

Fig. 19. Percent transmission at 248nm vs. dose for an AR-coated Fluoropolymer pellicle.

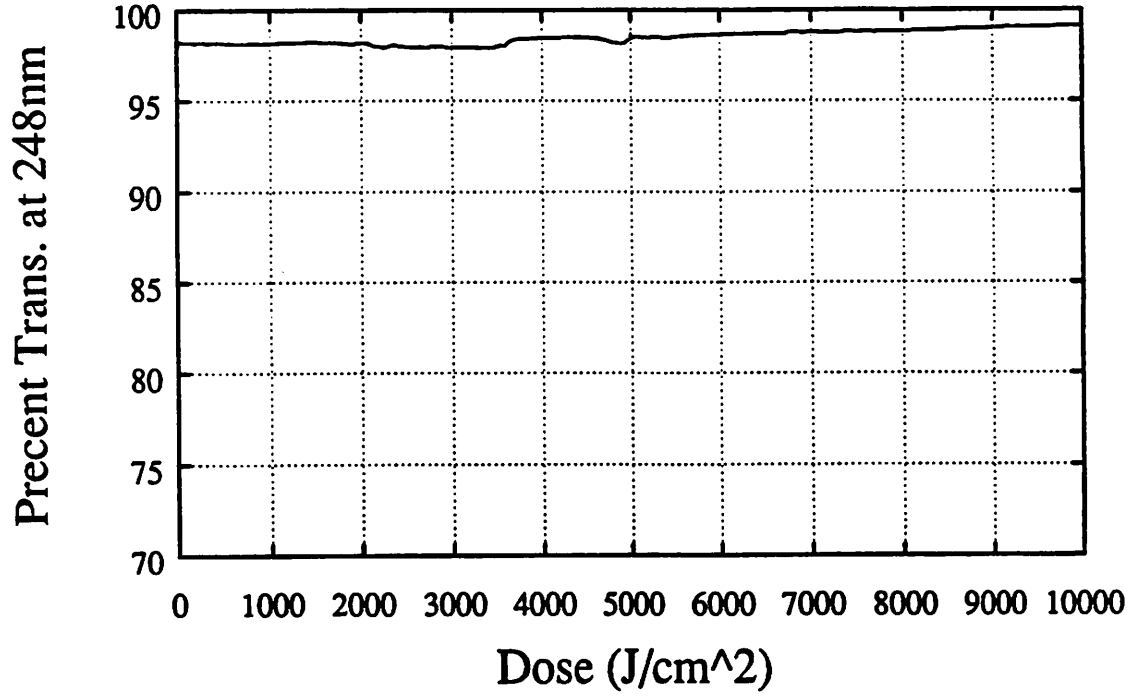

Fig. 20. Long exposure test of an AR-coated Fluoropolymer pellicle, total exposure equivalent to 2,500,000 die exposures.

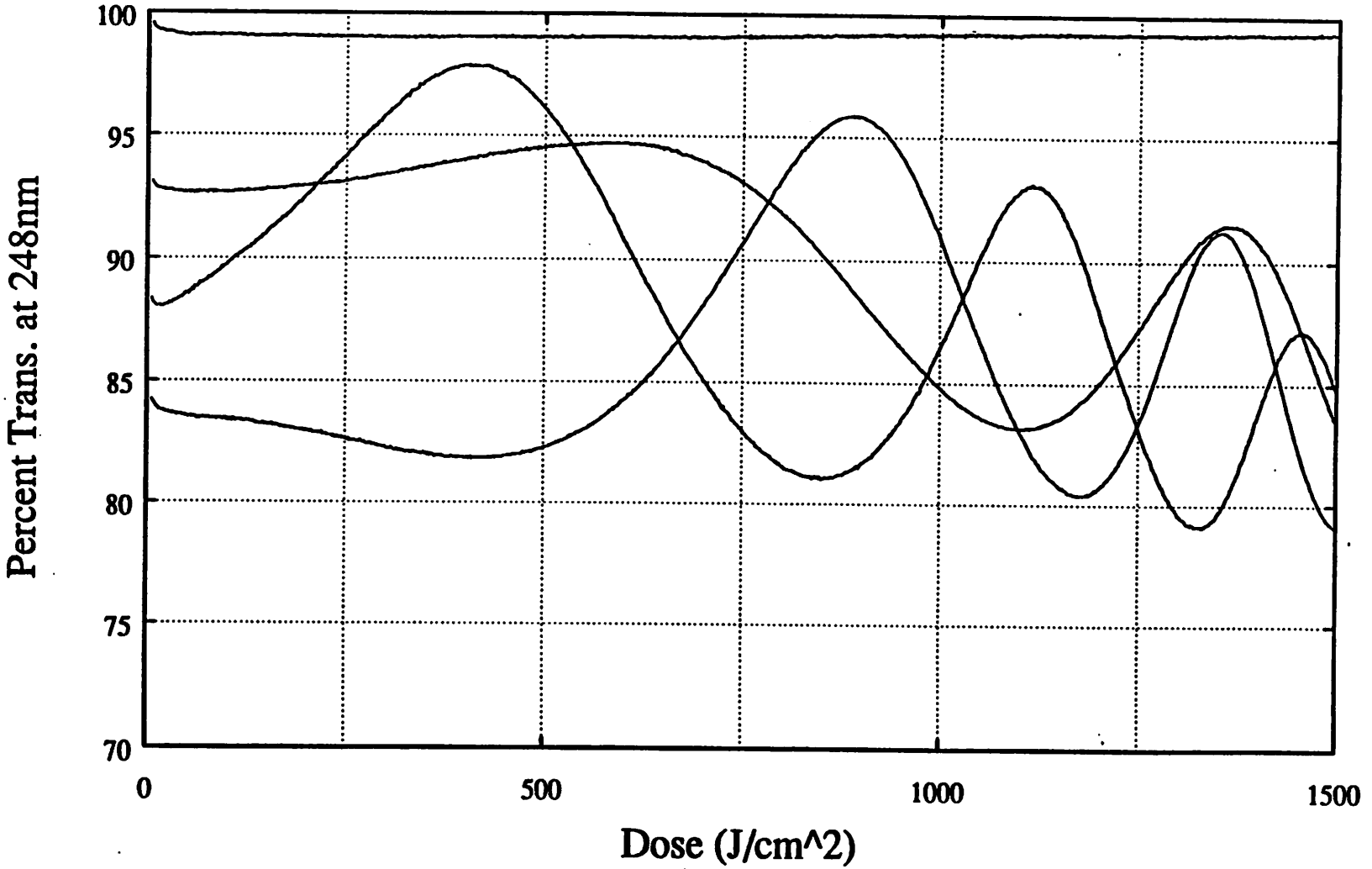

Fig. 21. Four uncoated candidate deep-UV pellicles from different vendors plotted together for comparison.

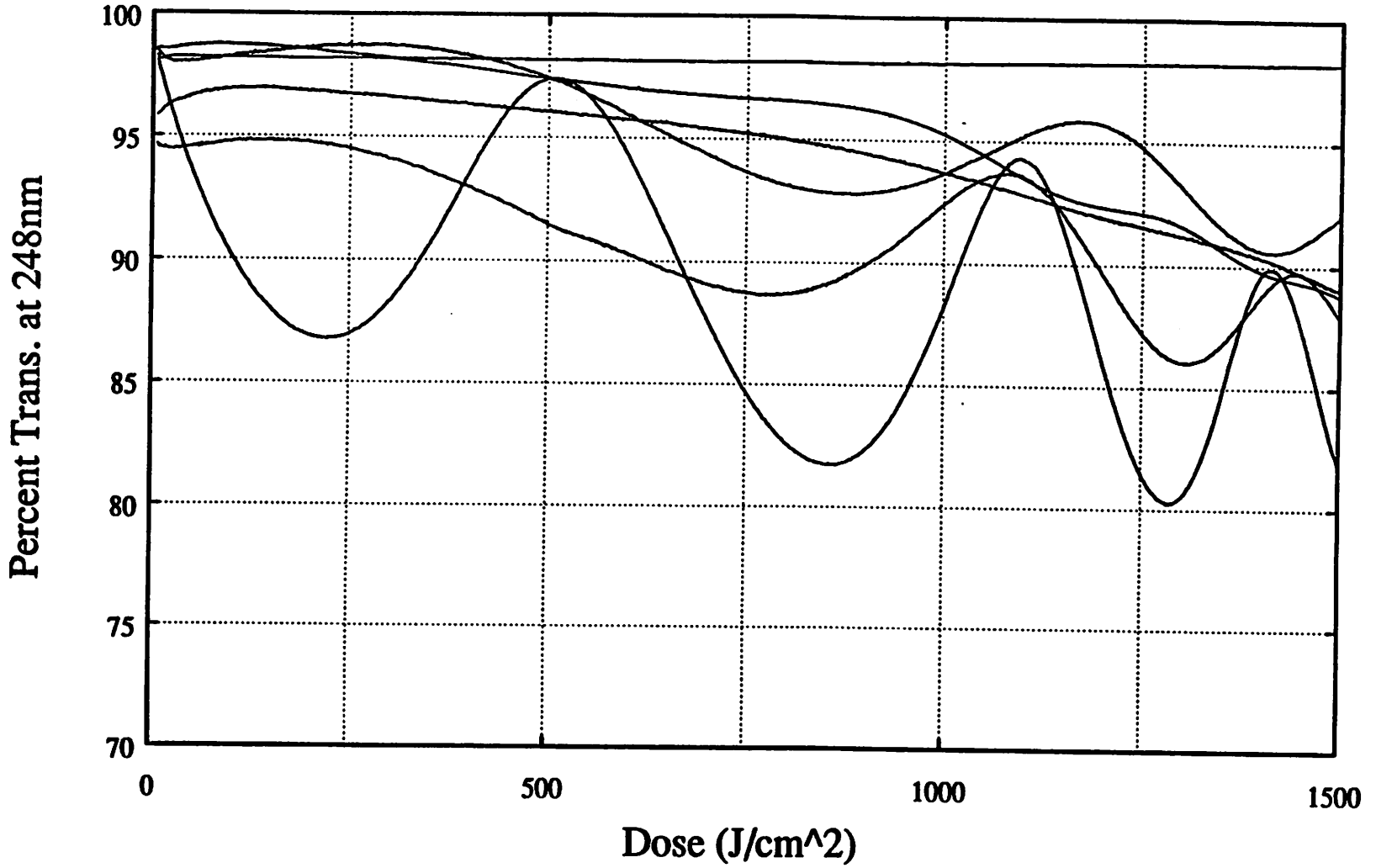

Fig. 22. Six AR-coated candidate deep-UV pellicles from different vendors plotted together for comparison.

Chapter 3
Transmission Lifetime and Refractive Index Measurements of Fluids for Deep-UV Lithography

Abstract- Candidate optical fluids for use in deep-UV lithographic systems have been tested for transmission lifetime and refractive index value. Examples of fluids found with stable, high transmission at 248nm are: Dupont Krytox, deionized water, Dow 200, and ethylene glycol.

Two methods for measuring the refractive index of a fluid have been developed. A simple fringe counting method gives quick but inaccurate measurements. A more accurate but more difficult prism method possesses an accuracy of +/-0.001. The refractive index values obtained for the above mentioned fluids are: Dupont Krytox (1.319), deionized water (1.374), Dow 200 (1.467), and ethylene glycol (1.484). These fluids cover a wide range of refractive index values and are useful for mask coverplate systems, reducing lens figuring tolerances, antireflective coatings, and increasing projection lens numerical apertures.

3.1 Introduction

The classic use of optical fluids is in the construction of lens systems using individual elements of differing optical properties. For use in visible wavelength systems the fluids are designed to harden like a cement between the lens elements. A crown element is cemented to its corresponding flint element to form a color corrected doublet. The glue used to cement the two elements together is chosen so that it has the same index of refraction as one element, assume the flint element. In this configuration, the glue will mold itself to the surface of the flint element making this surface "disappear" optically. The glue will also mold itself to the surface of the crown element and thus there will be only one optical surface, the interface between the crown element and the optical glue.

This method of cementing greatly reduces the requirements on the surface figure of the flint element. Because the optical glue has the same refractive index as the flint element and forms to the surface of the crown, there are no wavefront aberrations introduced by the flint surface. For typical optical materials the surface finish on both elements will be of high quality and the improvement in wavefront aberration will be no more than a factor of two. If one element is fabricated from a material that is difficult to polish, the improvement wavefront aberration can be large. Fig. 1 shows the cemented doublet configuration with fused silica and lithium fluoride (LiF) as the two materials. Lithium fluoride is one optical material besides fused silica with adequate transparency in the deep-UV. Lithium fluoride is difficult to polish because it is a soft crystalline material. Fused silica is both hard and amorphous. Fused silica can be figured to $\lambda/200$ with present technology while LiF can only be figured to $\lambda/4$.[1] Use of an optical fluid with the same refractive index as LiF will greatly reduce the wavefront aberrations introduced by the LiF element.

The second example of a use of optical fluids in deep-UV lithography is in a mask coverplate system. Chapter 2 discussed the problems associated with using a pelliclized mask in deep-UV lithography, such as the fragile nature of pellicles and their aging with exposure to deep-UV radiation. In place of a pellicle, a fused silica coverplate is placed over the chrome side of a mask. The coverplate is made thick enough to hold off any dust particles that might land on the mask.[2]

The optical performance of such coverplates can be improved by placing a fluid between the mask and the coverplate. This arrangement is shown in Fig. 2. The fluid would have a refractive index equal to the fused silica mask and coverplate. This fluid would eliminate the surface reflections that occur in the small gap between the mask substrate and the coverplate. These surface reflections can create a low finesse etalon that would vary in transmission as the gap distance changed by one quarter of the exposure wavelength. Maintaining a constant gap distance is difficult and would require optically flat mask substrates and coverplates. Use of an optical fluid in the gap reduces the required tolerance on the gap

distance and the flatness of the mask and coverplate. An additional advantage of using an optical fluid is an increase in the optical throughput by removing the two inside surface reflections and thus increasing the transmission of the mask coverplate system.

A final example of optical fluid use in deep-UV lithography is shown in Fig. 3. This is a diagram of the Half-Field Dyson lithography system. It is a unity magnification high numerical aperture projection system employing a reflective mask. The gap between the final lens element and the mask would require an optical fluid because of surface figure considerations. The gap between the mask and the wafer would also require an optical fluid for an additional reason besides surface figure and reflective losses. As designed, this lens system forms the best image at the surface of the mask just above the wafer. The transition from the fused silica mask to air for light rays incident on the wafer causes spherical aberration and degrades image quality. If a fluid with the same index as fused silica were placed in the gap between the mask and the wafer, this spherical aberration would be eliminated leading to improved image quality.

3.2 Fluid Properties

There are many desired properties of optical fluids. Some of the desired nonoptical properties include chemical stability, low thermal expansion, easy handling, low or no toxicity, and compatibility with materials in contact with the fluid. This last property is extremely important when using fluids with optical materials like LiF since it is soluble in water and thus would dissolve in any water based fluid.

The most critical optical properties that a fluid must satisfy are stable deep-UV transmission and proper refractive index. Since these fluids are used as a thin film, some deep-UV absorption may be acceptable since it would lead to small losses only. If the amount of absorption changes with time though, the overall transmission of the optical system will be affected and have detrimental effects on exposure control. The fluid refractive index need

not be exact. Correct index matching to three or four decimal places will produce all the desired positive effects described in the previous paragraphs.[1]

3.3 Measurement Techniques

A system used to measure the transmission stability of a material was described in Fig. 1 of chapter 2. Instead of placing a pellicle at the exposure plane, a sample holder filled with the fluid under test can be placed at the exposure plane. The fluid holder can be a simple UV-quartz cubette. In our case a 1cm thick cubette is used. This large thickness helps to exaggerate any change in transmission during exposure. In this way, we can obtain a more accurate estimate of the absorption coefficient. For example, a fluid that exhibited 13.2% transmission through a 1cm thick sample would be 98% transmitting through a 100μm thick film. Accurately measuring the difference between 97% and 98% is difficult using our life-time exposure system (the absorption coefficient for 97% would give only 4.8% transmission in a 1cm thick sample, easily differentiated from 13.2%).

If the fluid is only slightly absorbing, the amount of exposure per unit volume remains the same throughout the fluid volume. If the fluid is highly absorbing so that an appreciable fraction of the exposure radiation is absorbed, then the amount of exposure applied to the latter portion of the fluid will be less than that received by the forward portion of the fluid volume. For a free flowing fluid it becomes difficult to calculate the total exposure dose received by a given molecule of the fluid. If the fluid is a solid glue or a highly viscous gel, then a simple exponential decay through the sample will give a good estimate of the total dose received by each portion of the fluid volume. In this way a reasonable estimate of the thin film aging characteristics can be made.

For free flowing fluids we can assume that the fluid is continuously mixing and thus will possess uniform optical absorption properties. An estimate of the average amount of exposure applied to the fluid can be found by calculating the average intensity throughout

the thickness of the sample:

$$<I> = \frac{1}{D}\int_0^D I_{inc} e^{-\alpha x} dx, \qquad 1$$

where D is the sample thickness, I_{inc} is the incident intensity, and α is the absorption coefficient. This integral can be calculated, giving:

$$<I> = \frac{I_{inc}}{\alpha D}\left[1 - e^{-\alpha D}\right]. \qquad 2$$

In the limit of $\alpha = 0$ the average intensity goes to I_{inc} as it should. As α becomes large this equation simplifies to $<I> = \frac{I_{inc}}{\alpha D}$, which physically means that all the radiation is absorbed in a fraction of the fluid volume equal to $\frac{1}{\alpha D}$. Knowing the amount of radiation absorbed by each region of the fluid is important for estimating the change in absorption with exposure. Once the change in absorption with exposure is known for a thick sample, uniform characteristics can be assumed in the very thin films used in optical systems.

The second important optical fluid parameter is the index of refraction at the wavelength of use. Some fluids have published index information in the visible wavelength range, but little information is available in the deep-UV region. A second complication is that many of the fluids tested, such as the synthetic vacuum pump oils, were never intended for optical use and thus no optical information is available regardless of wavelength. The index properties of many thin films used in the semiconductor industry have been determined by use of a method called variable-angle monochromatic fringe observation.[3] This method is highly accurate but only practical for thin films of 10μm or less. Two methods for determining the refractive index of a bulk fluid have been developed. The first, a variation on the fringe counting method, is simple to execute but imprecise. The second, a prism refraction method, has longer setup time but yields greater precision.

The fringe counting method consists of counting the change in the interference fringes between two optical flats as the space between the flats is filled with the fluid under test. The

setup used in the fringe method is shown in Fig. 4. The basic components are two fused silica wedges and a beam collimation system. The wedges are held by five axis lens positioners and are positioned nearly parallel to each other. Their spacing is kept to less than 100μm though this distance is not critical. A collimated beam of 248nm radiation is made incident on the wedges and the reflections from the inside surfaces is monitored by a linear diode array. The degree of tilt between the wedges is adjusted so that the fringe pattern created by the two reflected beams has a low enough spatial frequency to be monitored by the diode array. Because the precision of this method depends on the number of fringes across the diode array, we attempt to produce as many fringes across the array as possible without surpassing the spatial frequency of the diode array.

The fringe pattern owing to interference between the reflections from the inside surfaces of the wedges can be written:

$$I(x) = I_0 \cos\left[2\frac{2\pi n_{gap}}{\lambda} h(x)\cos(\theta_{inc})\right], \qquad 3$$

where I_0 is the fringe peak intensity, n_{gap} is the refractive index of the material in the gap, h(x) is the gap distance, and θ_{inc} is the angle of incidence for the illuminating beam. If the wedges are held at some small angle to each other, call it θ_{wedge}, then the gap distance is $h(x) = h_0 + \tan(\theta_{wedge})x$, where h_0 is some initial wedge distance. The fringe intensity can then be written:

$$I(x) = I_0 \cos\left[2\frac{2\pi n_{gap}}{\lambda}\cos(\theta_{in})h_0 + 2\frac{2\pi n_{gap}}{\lambda}\cos(\theta_{in})\tan(\theta_{wedge})x\right]. \qquad 4$$

The first part inside the cosine function is a constant phase while the second part varies with x across the diode array. The number of fringes on the diode array can be written:

$$\text{fringes} = \frac{2n_{gap}\cos(\theta_{in})\tan(\theta_{wedge})x_{width}}{\lambda}, \qquad 5$$

where x_{width} is the total width of the diode array.

The procedure for measuring refractive index is as follows: Adjust the wedge spacing and tilt as described in the previous paragraph with air in the gap between the wedges, then record the fringe pattern across the diode array. Fill the gap between the wedges with the fluid and again record the fringe pattern across the diode array. We can now use Eqn. 5 twice with the two different values of n_{gap}:

$$\text{fringes}_{air} = \frac{2n_{air}\cos(\theta_{in})\tan(\theta_{wedge})x_{width}}{\lambda}$$

$$\text{fringes}_{fluid} = \frac{2n_{fluid}\cos(\theta_{in})\tan(\theta_{wedge})x_{width}}{\lambda}. \qquad 6$$

The measurement with air in the gap can be used to eliminate all the unknowns in the measurement with the fluid in the gap, giving:

$$n_{fluid} = n_{air}\frac{\text{fringes}_{fluid}}{\text{fringes}_{air}}. \qquad 7$$

The refractive index of the fluid is related to the refractive index of air by the ratio of the two fringe counts. We take the index of air to be equal to one.

The largest error in this measurement stems from the inability to count the fractions of fringe across the diode array with high precision. Because of the limited pixels per fringe period (usually 10 pixels per period) one can not determine the number of fringes on the array to greater than two digits of precision. The other large error in this method is the assumption that the gap spacing and tilt angle remain constant when the fluid is poured between the wedges. Capillary forces can pull the wedges together and thus alter the fringe spacing independent of a change in refractive index.

The more precise but more difficult prism approach for index measurement is shown in Fig. 5. In this method a hollow prism is constructed of fused silica windows and filled with the fluid under test. This "fluid prism" refracts a collimated beam of light according to Snell's law allowing one to obtain index information by measuring angles. Fig. 5 shows a collimated beam of light, created by passing through a 100μm slit, made incident on the

prism. The angle of the prism, which is nominally 30 degrees, is measured by observing the reflected light from both of the faces of the prism as imaged back through the slit. By measuring the amount of prism rotation required to back reflect from both prism faces we can obtain a value for the angle of the prism. The second measurement is the angle required to back reflect the beam through the fluid and off the back side of the prism. These angles are shown in Fig. 6.

The disadvantage with this method is the time consuming adjustments required to autocollimate the 1000mm focal length lens and the 100μm wide slit. The slit must be placed at the back focal plane of the lens so that a sharp image of the slit is formed when reflecting from the prism surfaces. A further difficulty is fabricating the hollow prism. An aluminum base is used with fused silica plates glued to form a sealed chamber. Because most of the fluids tested are not easily dissolved, the prism must be destroyed and remade after each test. The wedges used in the fringe method could be disassembled and wiped clean, making for a much quicker turn around time.

Using Snell's law we can relate the refractive index of air to that of the fluid by the following equation:

$$n_{fluid} = n_{air} \frac{\sin(\theta_m)}{\sin(\theta_p)}, \qquad 8$$

where θ_p is the prism angle, and θ_m is the refracted angle shown in step 3 of Fig. 6. The prism angle was chosen to be 30 degrees because of the need to avoid total internal reflection inside the prism. Fig. 7 shows the maximum allowed prism angle for a given fluid index. Since the range of index values was expected to be between 1 and 2, and the sensitivity to errors increases as the prism angle is decreased, we chose a prism angle of 30 degrees.

The precision of this method is limited by the width of the slit and our measurement of the two angles. The rotation stage used in these experiments was capable of measuring angles to arcminutes, 2.9e-4 radians. The collimating lens is operated at an f-number of 100

and results in a diffraction limited width (distance to first null) equal to 50μm.[4] After convolving with the 100m slit, the angular width of the lens/slit system is 1.1e-4 radians. Summing the errors from the stage and optics ($\sqrt{E_1^2 + E_2^2}$) gives a system precision of 3.1e-4 radians. We can calculate the effect on the index by taking the partial derivative of Eqn. 8 with respect to the two angles:

$$\Delta n_{fluid} = \Delta\theta_m \sqrt{\frac{n_{air}^2}{\sin^2(\theta_p)} - n_{fluid}^2}$$

$$\Delta n_{fluid} = \Delta\theta_p \cot(\theta_p) \sqrt{\frac{n_{air}^2}{\sin^2(\theta_p)} - n_{fluid}^2} \qquad 9$$

Evaluating Eqn. 9 with $\theta_p = 30$ degrees and assuming $n_{fluid} = 1.5$ gives:

$$\Delta n_{fluid} = 1.32\Delta\theta_m$$

$$\Delta n_{fluid} = 2.28\Delta\theta_p, \qquad 10$$

which results in a total error in the index value of 8.1e-4. Thus, using the present equipment, this method gives three digits of precision for the refractive index.

3.4 Results

Many fluids were tested using the lifetime exposure test system. Figs. 8 through 17 show the results for most of the fluids tested. These transmission values are relative to an empty cubette. Some fluids show greater than 100% transmission owing to the reduction of Fresnel reflection losses at the inside surfaces of the cubette. Additional fluids were tested but they showed near zero transmission in a 1cm thick sample. These highly absorbing fluids were rejected. Two fluids intended for use in optical systems were made available to us for testing. These fluids were the J.P. Banks fluid (Fig. 16) and the Cargile #3421 fluid (Fig. 12). Neither of these samples showed high transmission at 248nm, with the Cargile fluid possessing a moderate transmission of 60% and the J.P. Banks material less than 10%. In a

thin film both of these fluids may suffice if no other fluid with the same refractive index can be found. It is interesting to note that many of the fluids that show high and stable transmission under 248nm exposure are synthetic pump oils and lubricants. Their inert chemical nature makes for an optical absorption band higher than the 5eV photons produced by the KrF excimer laser.

The measured refractive index values of these fluids are shown in table 1. There are several fluids with index values close to that of fused silica, 1.508.[5] The J.P. Banks fluid matches to 3 decimal places, but has poor transmission characteristics. The fluid nearest in index and possessing high transmission is Ethylene Glycol. This fluid is highly stable, easy to obtain, and has no handling restrictions. The small mismatch in index of 0.024 produces only a 0.0068% Fresnel reflection and thus would be an excellent index matching fluid for the mask coverplate system.

Lithium Fluoride has a refractive index of 1.419 at 248nm.[5] None of the fluids tested had a refractive index sufficiently close to LiF for use as a surface finish. The Cargile #3421 fluid is the closest with a mismatch of 0.018. To test the compatibility of this fluid with LiF, a second lifetime test exposure of the Cargile fluid was made but this time a small piece of LiF was placed in the cubette. The LiF was fully submerged in the fluid and positioned so that it was exposed to the 248nm radiation. The result of this experiment is shown in Fig. 18. When compared to the Cargile test alone (Fig. 12), the aging characteristics of the LiF/Cargile sample are much degraded. Some interaction between the two materials must have occurred reducing the overall transmission. Because of this interaction the Cargile fluid is a poor candidate to index matching to LiF.

In an attempt to produce a fluid with long transmission lifetime and a suitable refractive index for LiF, we mixed two fluids, one with an index below that of LiF and the other with an index above LiF. These fluids must be miscible so that the mixture will maintain uniform optical properties. Two candidates for such a mixture are deionized water and

ethylene glycol. Fig. 19 shows the refractive index of various percent mixtures of these two fluids. The mixture exhibits a nearly linear relationship between the refractive index and the fraction of ethylene glycol in water. The mixture with 30% ethylene glycol in water nearly matches the index of LiF. The results of the transmission stability of this mixture is shown in Fig. 20. A test of compatibility with LiF is shown in Fig. 21. Both Figs. 20 and 21 shown that this mixture is a promising candidate for use as an index matching fluid with LiF.

3.5 Conclusions

Many candidate optical fluids with stable transmission lifetimes under deep-UV exposure have been found. The range of refractive index covered by these materials includes most of the common deep-UV optical glasses such as fused silica and LiF. This inventory of optical fluids should provide a broad range of options for choosing the appropriate fluid for use in many optical systems. The most promising of the candidate fluids are deionized water, Dupont Krytox, Demnum S-65, and ethylene glycol.

To further this work, these fluids should be tested at even shorter exposure wavelengths, such as the quintupled Nd-YAG (213nm) and the ArF excimer (193nm). Higher photon energies and higher peak powers from these laser sources will be more likely to cause damage during exposure. The present 213nm system at Berkeley, though producing high pulse energies (28mj/pulse), is a low repetition rate system and thus produces only a limited amount of average power. With such low average power it is difficult to make suitable lifetime measurements in a reasonable time.

This work could be expanded to include lifetime testing of optical glasses at these wavelengths. Currently, we have tested fused silica and LiF. Both have shown high and stable transmission characteristics at 248nm. A great amount of exposure testing has been done on fused silica at 193nm.[6,7,8] The results show an increase in absorption near 210nm when exposed to 193nm radiation. Exposure tests at 213nm would be interesting since this may

lead to a run away process with increased absorption leading to accelerated damage. Again, these tests are best postponed for the second generation Berkeley 213nm source that will produce much higher average power.

References

1. D.A. Markle, *Private communication*, 1990.

2. E.L. Banks, "Glass Coverplates for Photomasks," *BACUS News*, pp. 6-9, Feb. 1987.

3. A.J. Warnecke and P.J. LoPresti, "Refractive Index Dispersion in Semiconductor-related Thin Films," *IBM J. Res. Develop.*, pp. 256-262, May 1973.

4. J.W. Goodman, in *Itroduction to Fourier Optics*, McGraw-Hill, New York, 1968.

5. E.D. Palik, in *Handbook of Optical Constants of Solids*, Academic Press, Orlando, 1985.

6. J. Reif, "High Power Laser Interaction with the Surface of Wide Bandgap Materials," *Opt. Eng.*, vol. 28, no. 10, pp. 1122-1132, Oct. 1989.

7. M. Rothschild, D.J. Ehrlich, and D.C. Shaver, "Effects of Excimer Laser Radiation on the Transmission, Index of Refraction, and Density of Ultraviolet Grade Fused Silica," *Appl. Phys. Lett.*, vol. 55, no. 13, pp. 1276-1278, Sept. 1989.

8. N. Leclerc, C. Pfleiderer, H. Hitzler, J. Wolfrum, K. Greulich, S. Thomas, H. Fabian, R. Takke, and W. Englisch, "Transient 210nm Absorption in Fused Silica Induced by High-power UV Laser Irradiation," *Opt. Soc. Am.*, vol. 16, no. 12, pp. 940-942, June 1991.

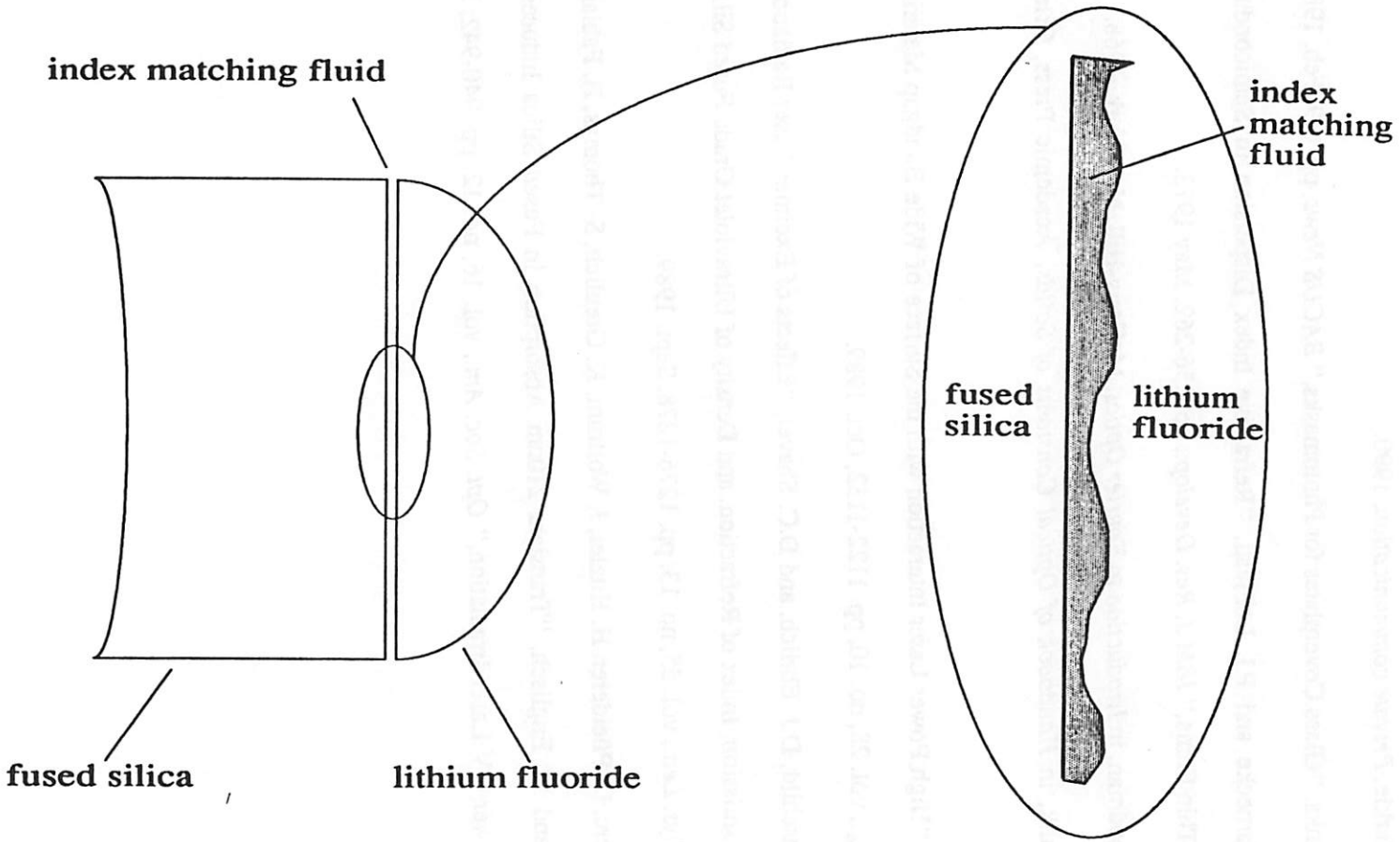

Fig. 1 Use of an index matching fluid to reduce surface figure requirements.

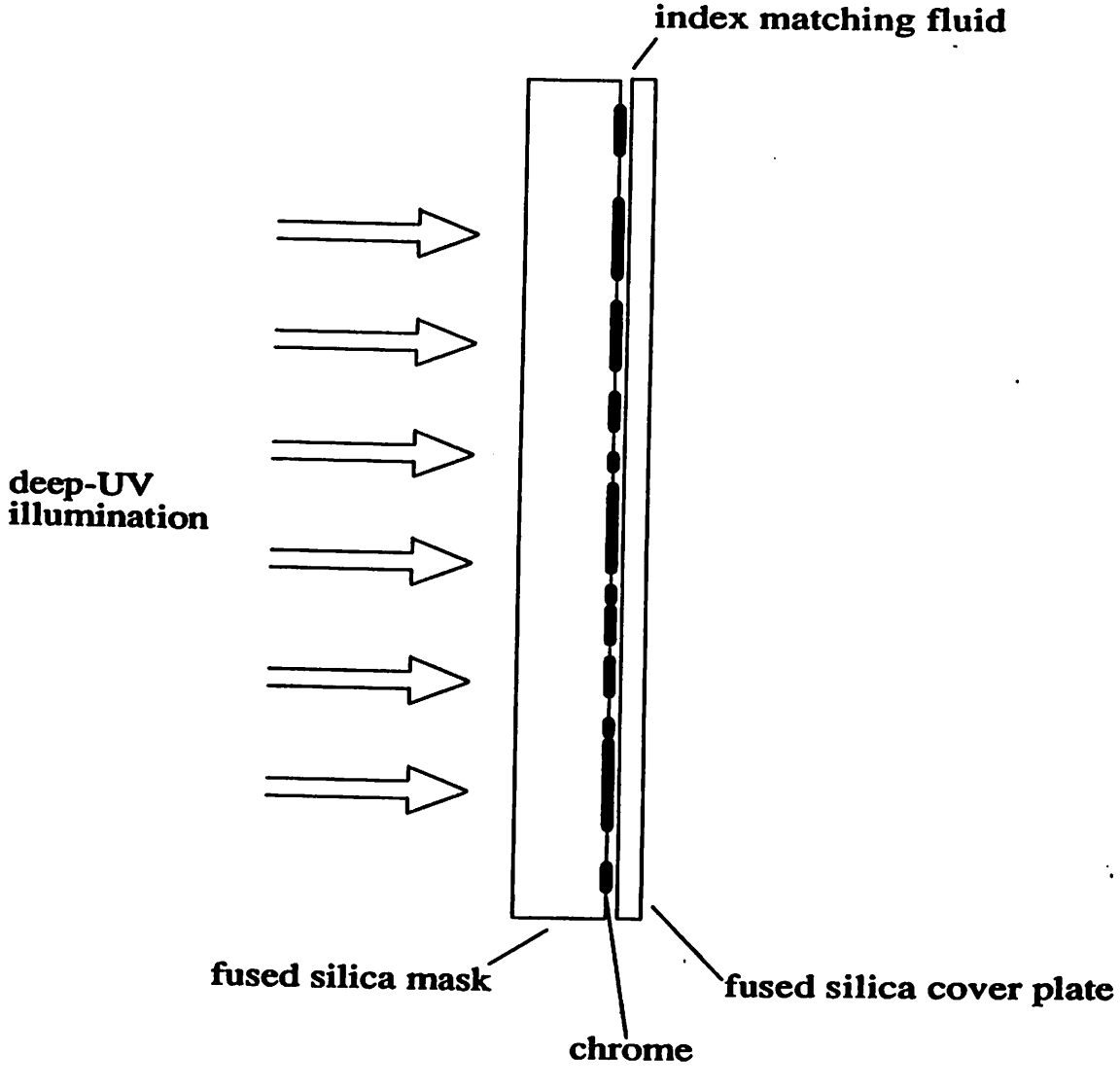

Fig. 2 Index matching fluid used to reduce reflections from a mask coverplate.

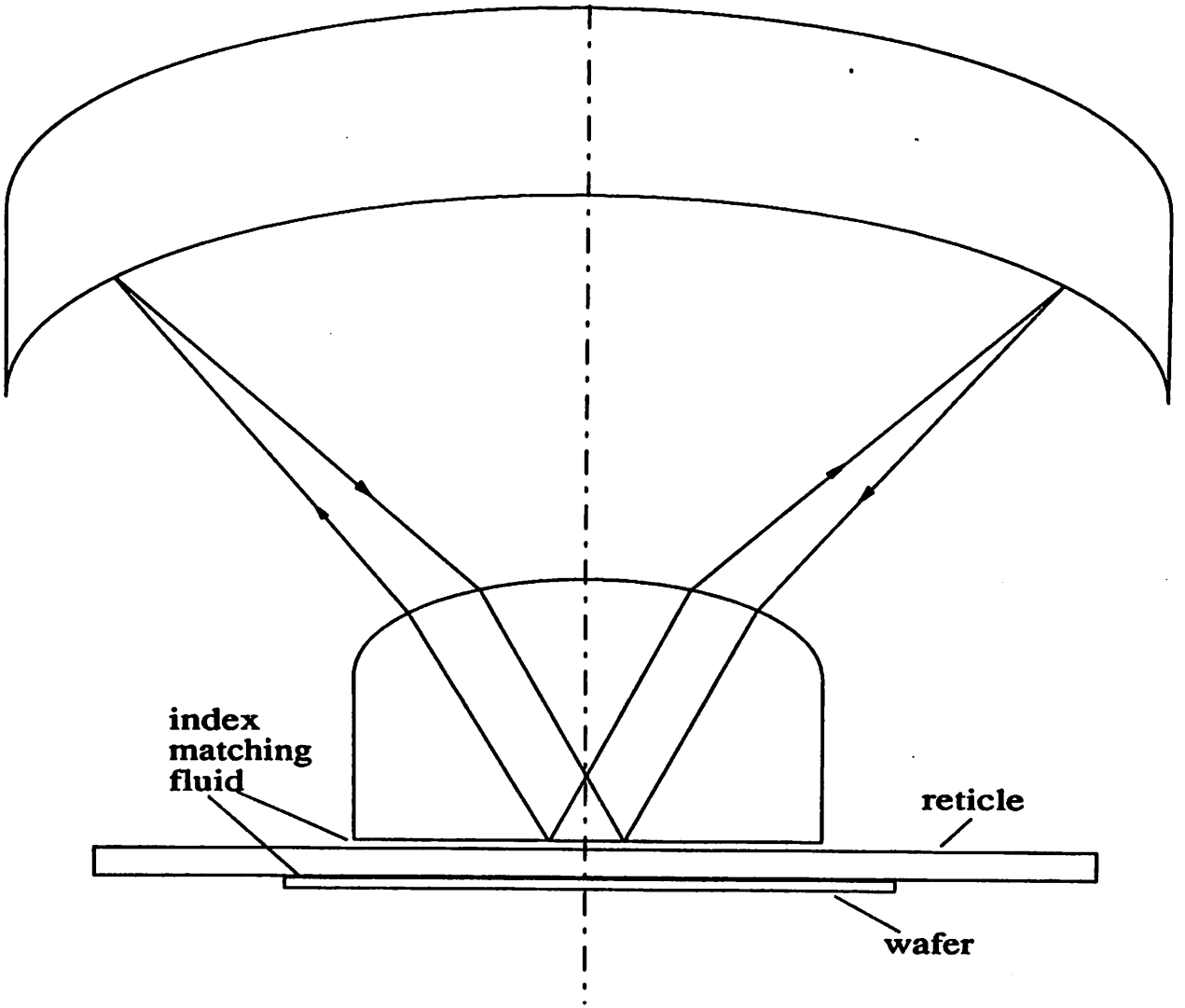

Fig. 3 Half-Field Dyson imaging system using index matching fluids.

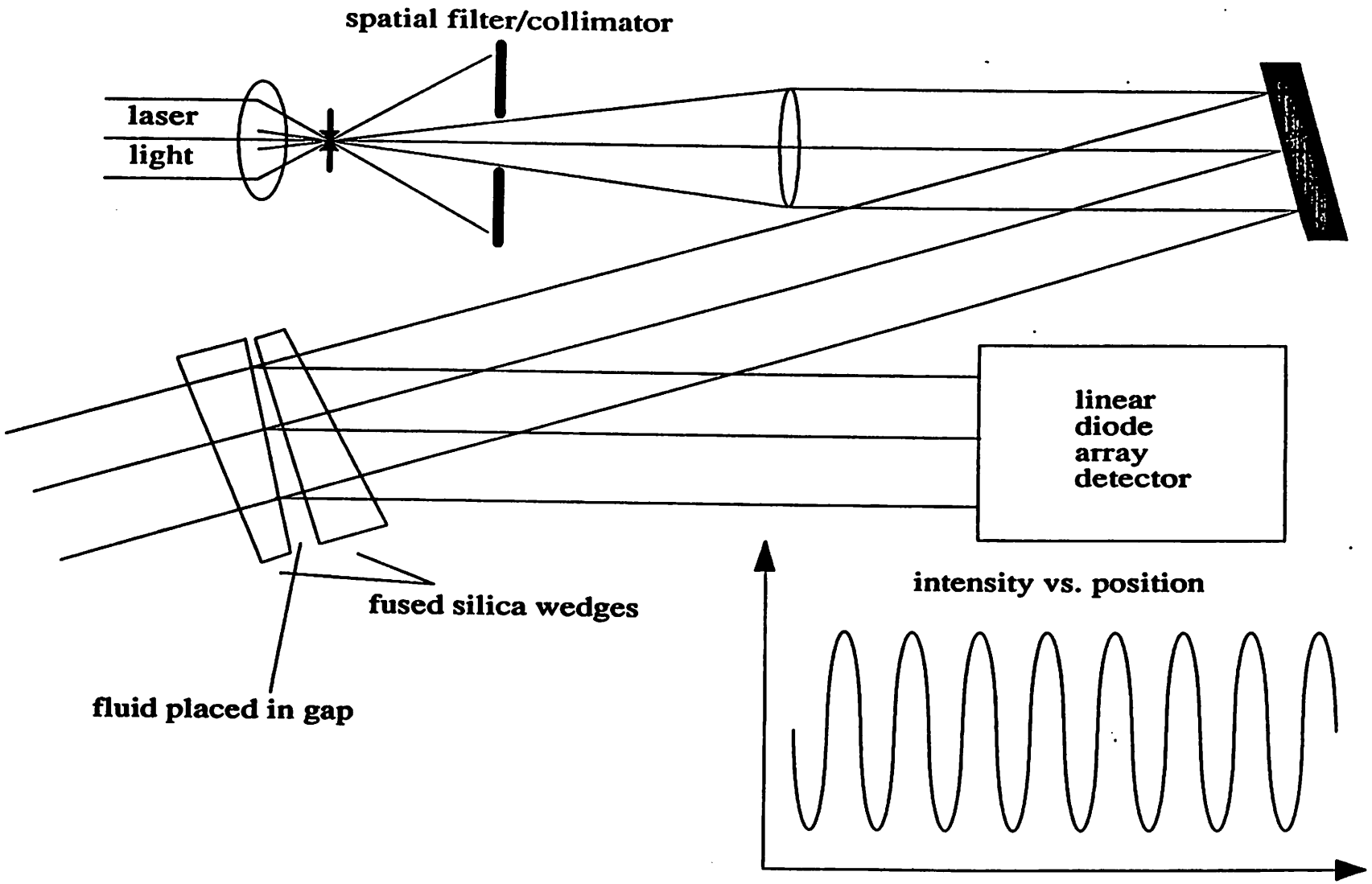

Fig. 4. Fringe counting method of determining a fluid's refractive index.

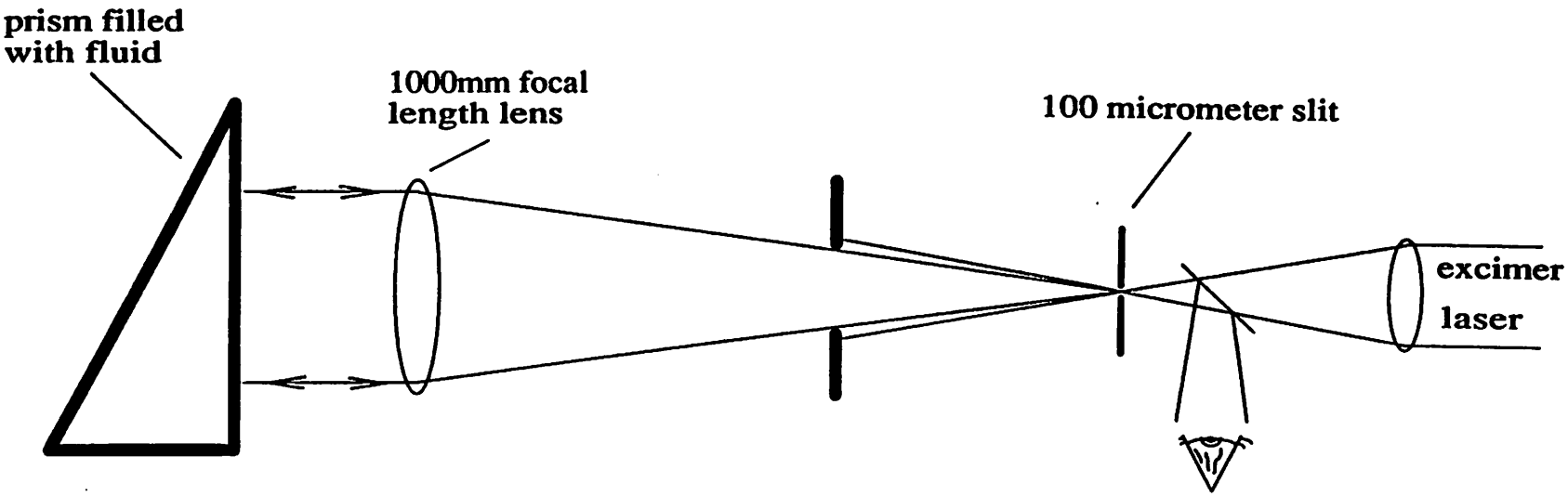

Fig. 5 Prism method of measuring a fluid's refractive index at 248nm.

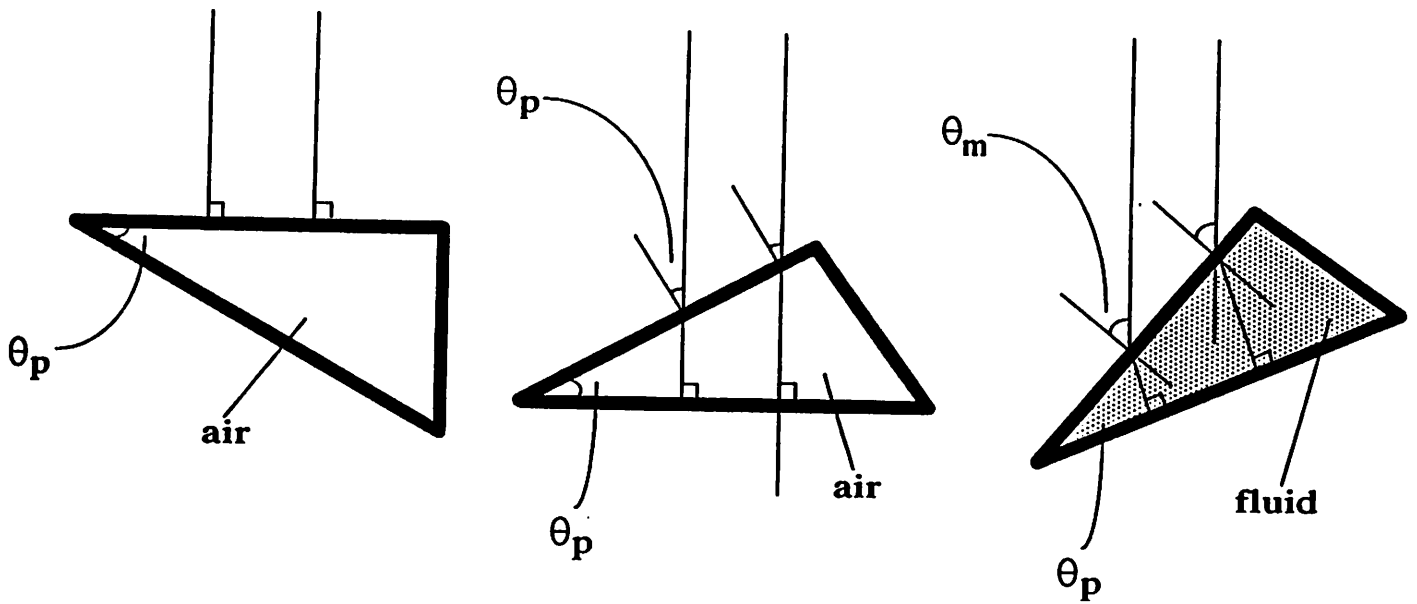

Fig. 6 Three angle measurements used to calculate a fluid's refractive index.

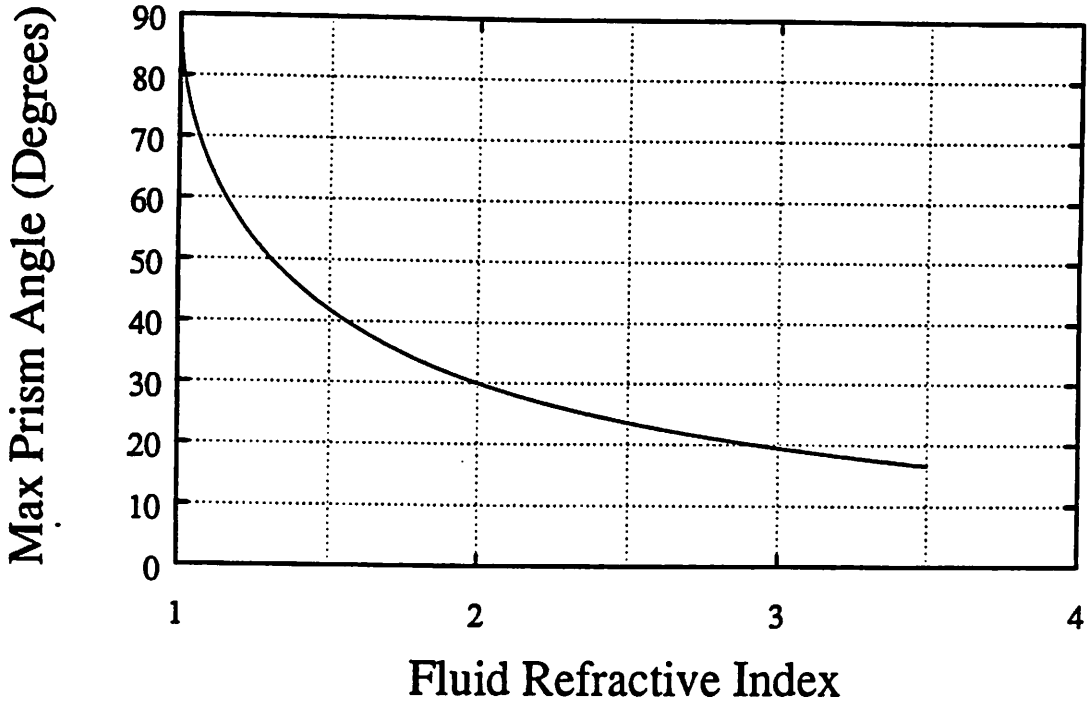

Fig. 7. Maximum allowed prism angle versus fluid refractive index.

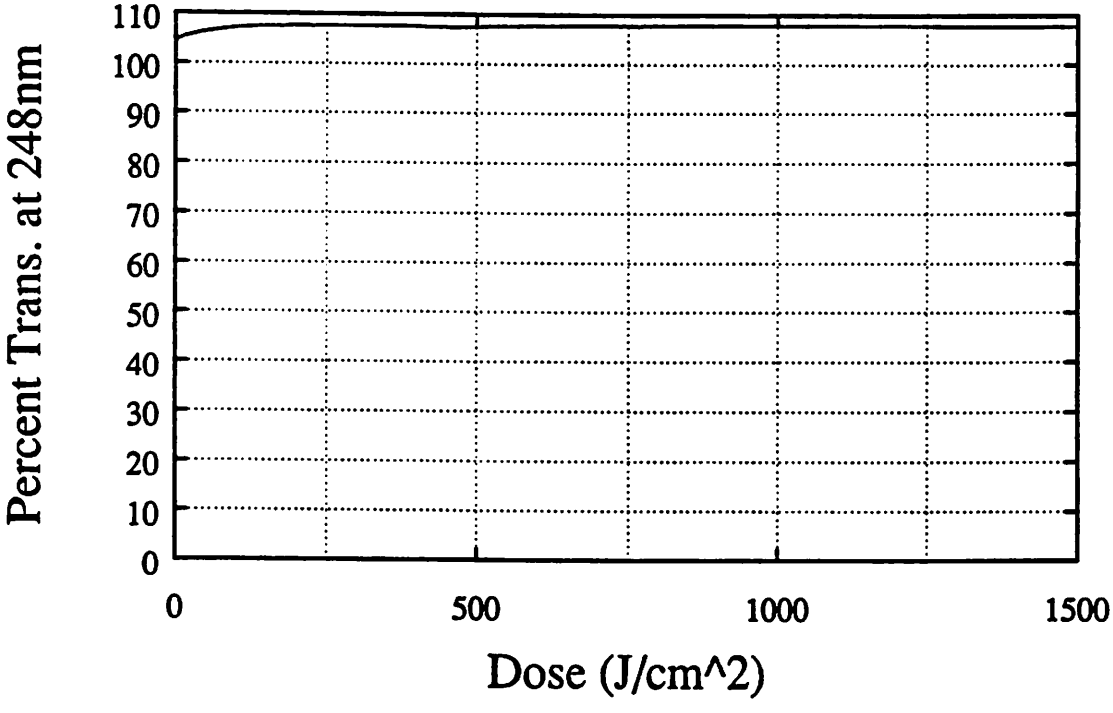

Fig. 8. Transmission at 248nm versus dose for a 1cm thick sample of Dupont Krytox.

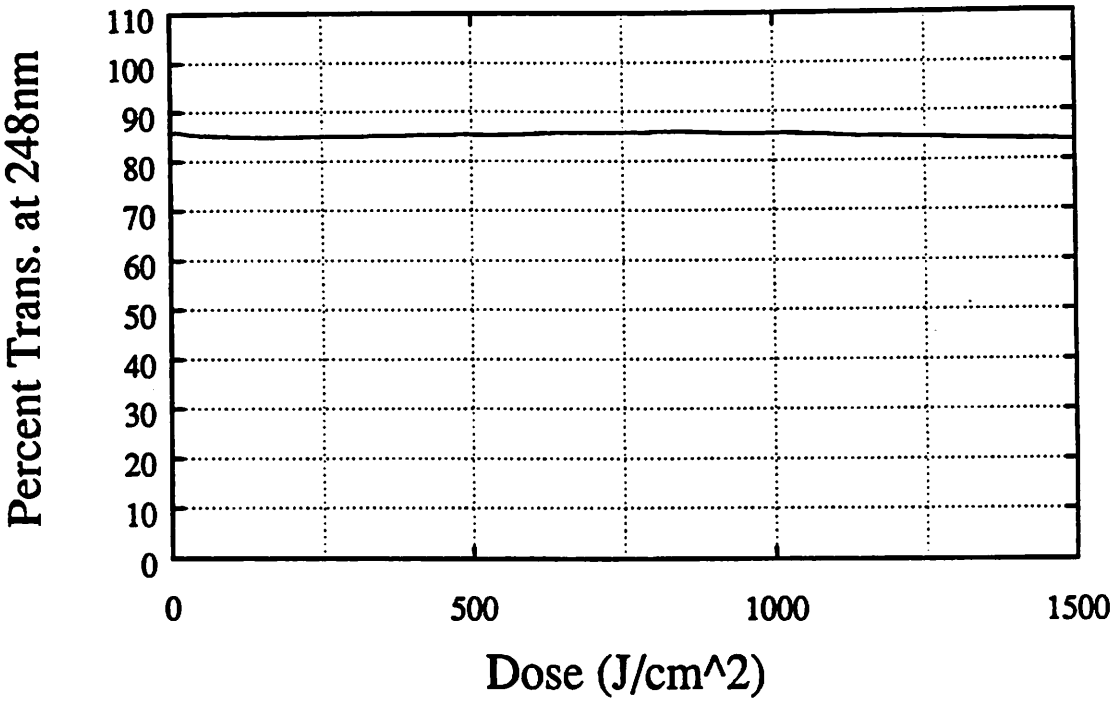

Fig. 9. Transmission at 248nm versus dose for a 1cm thick sample of Fomblin VT-219.

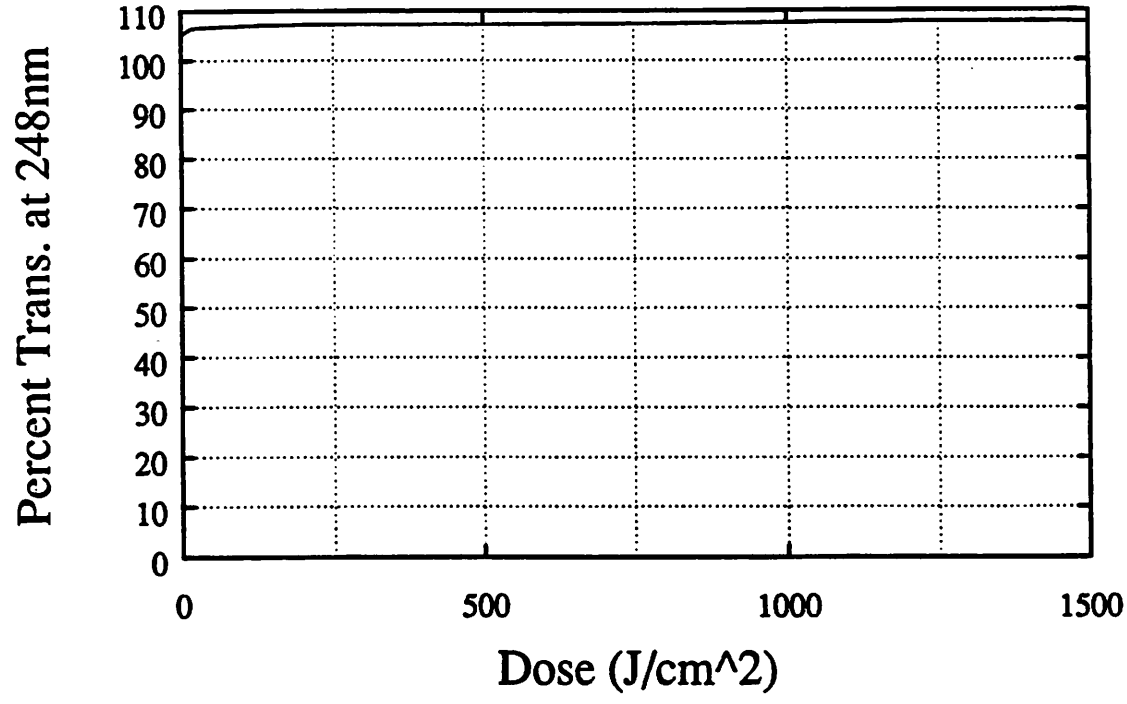

Fig. 10. Transmission at 248nm versus dose for a 1cm thick sample of Demnum S-65.

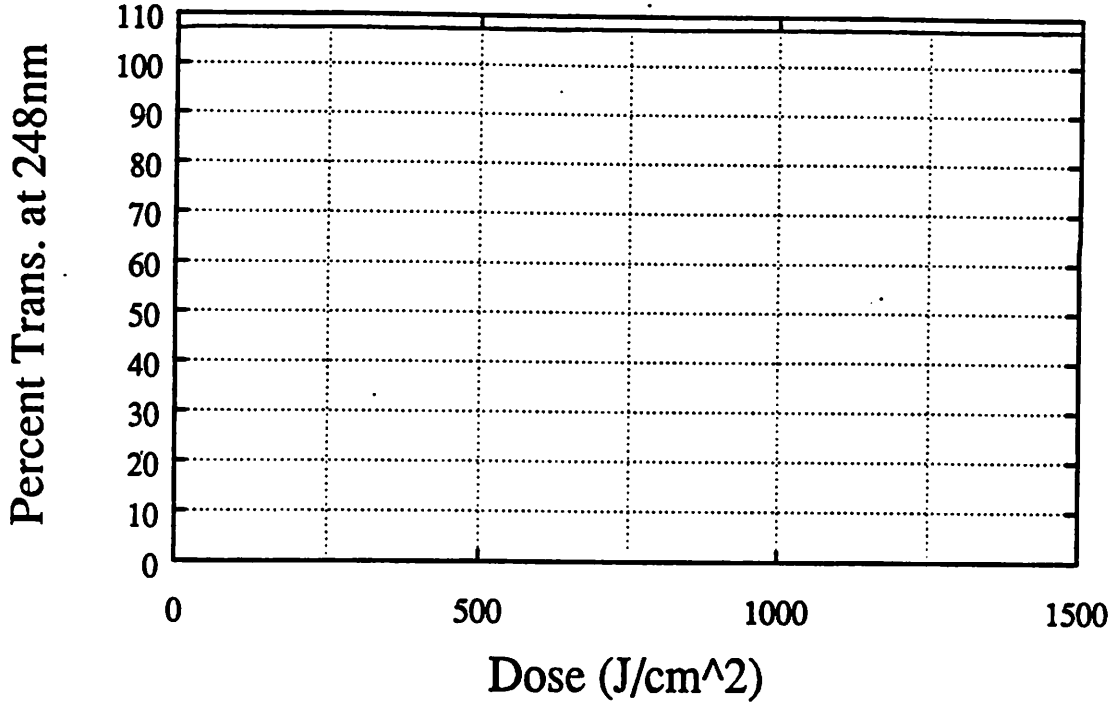

Fig. 11. Transmission at 248nm versus dose for a 1cm thick sample of deionized water.

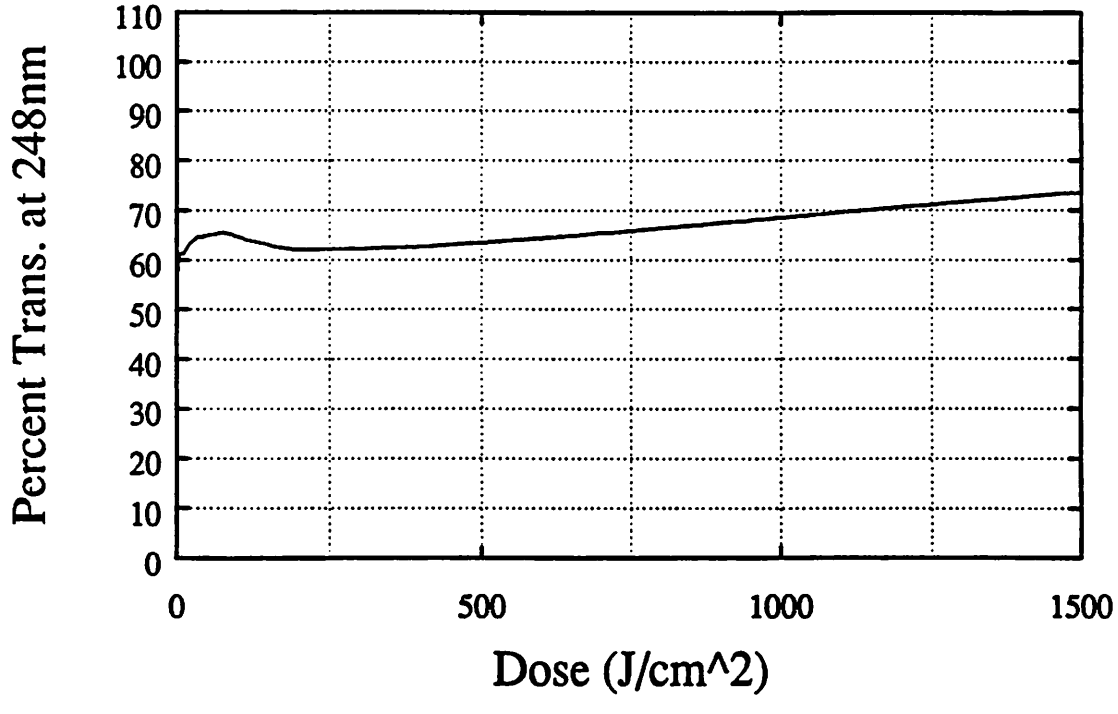

Fig. 12. Transmission at 248nm versus dose for a 1cm thick sample of Cargile laser liquid #3421.

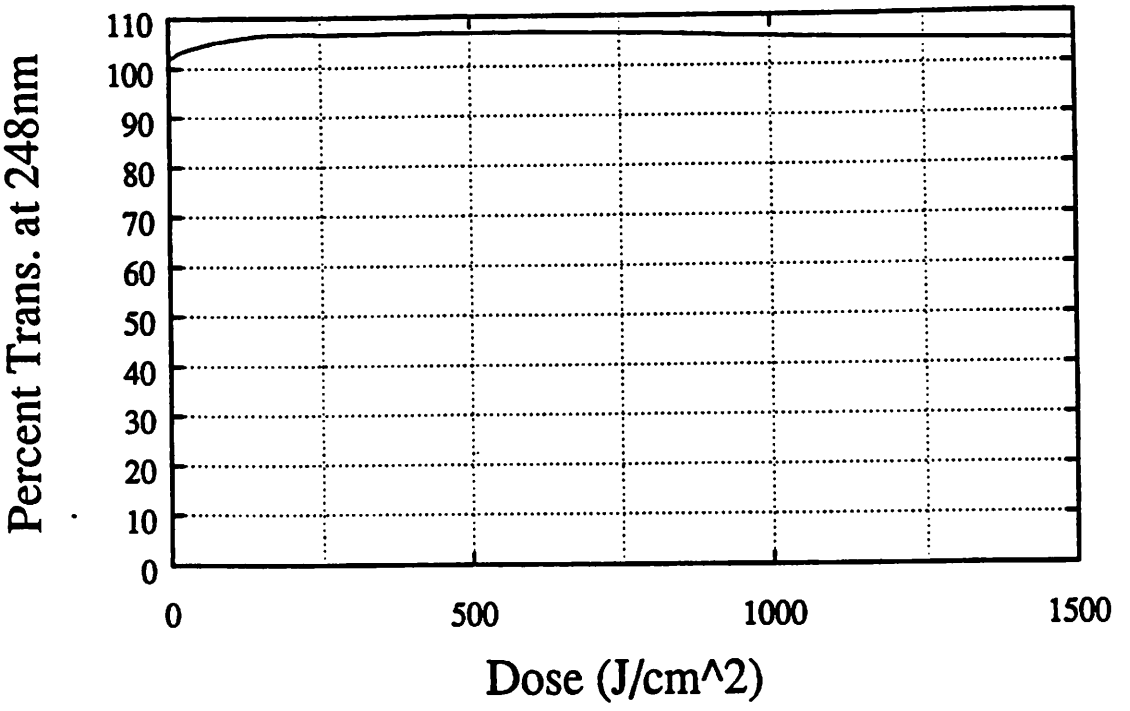

Fig. 13. Transmission at 248nm versus dose for a 1cm thick sample of DOW 200.

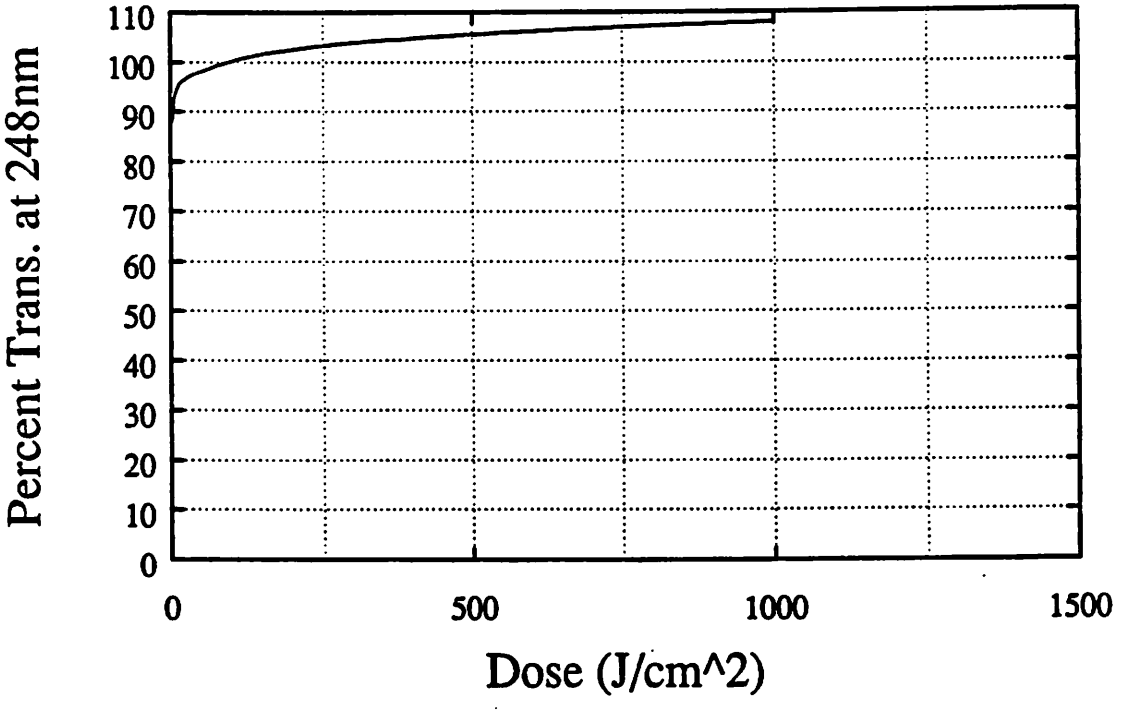

Fig. 14. Transmission at 248nm versus dose for a 1cm thick sample of ethylene glycol.

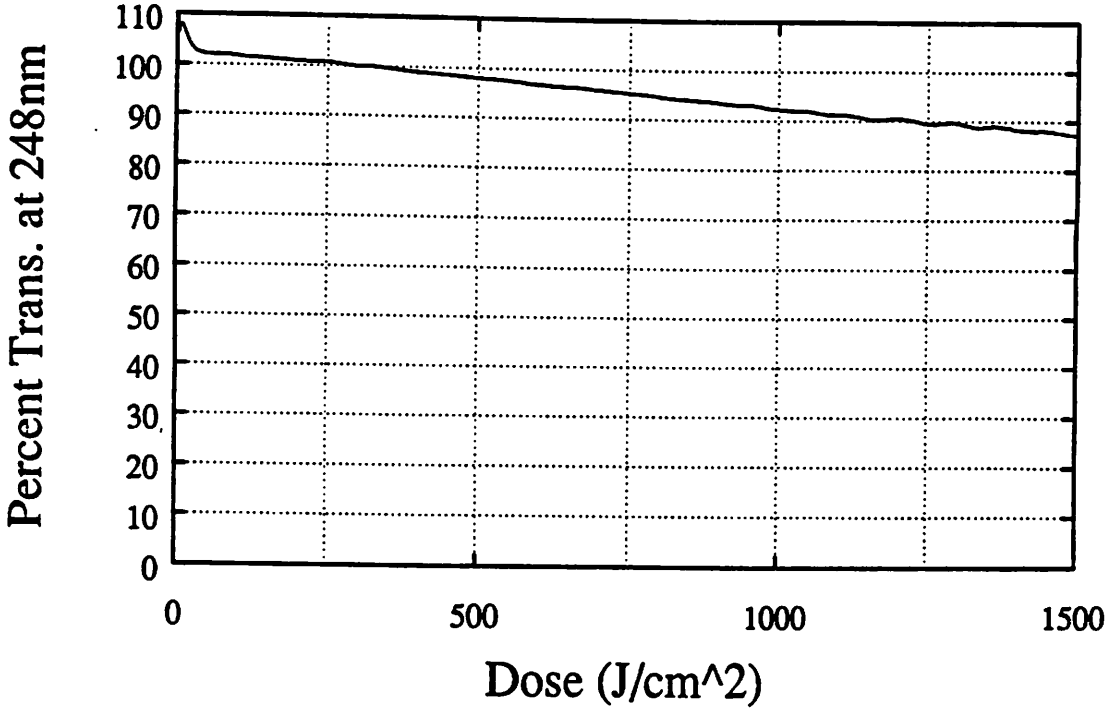

Fig. 15. Transmission at 248nm versus dose for a 1cm thick sample of propylene glycol.

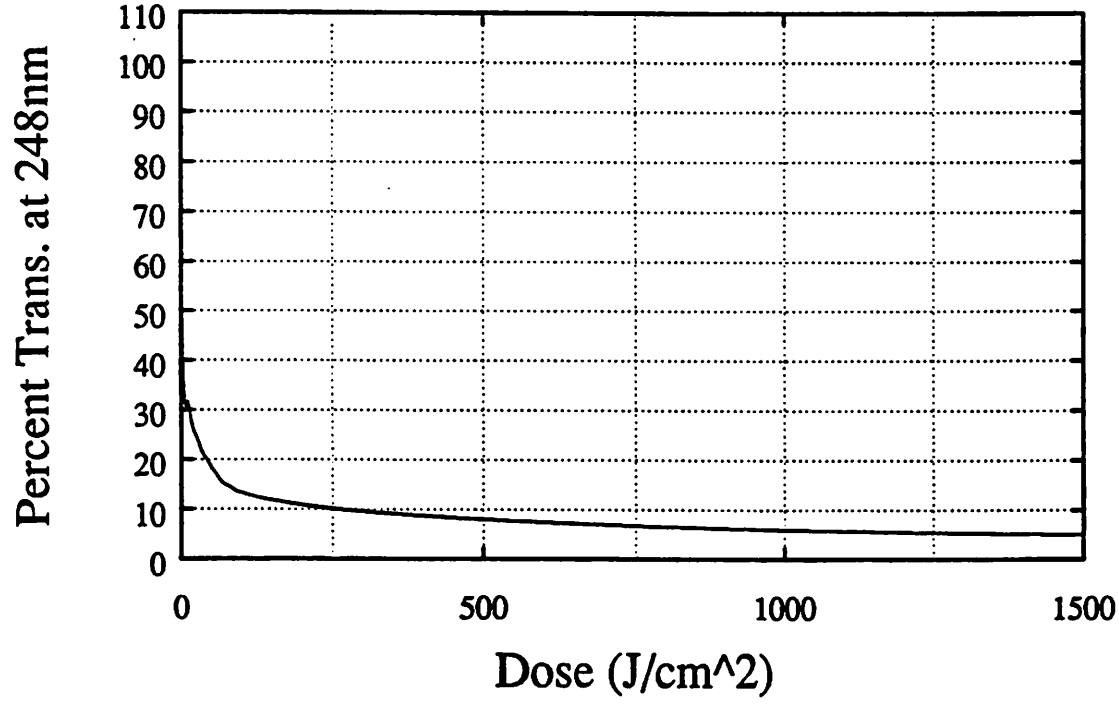

Fig. 16. Transmission at 248nm versus dose for a 1cm thick sample of J.P. Banks optical fluid.

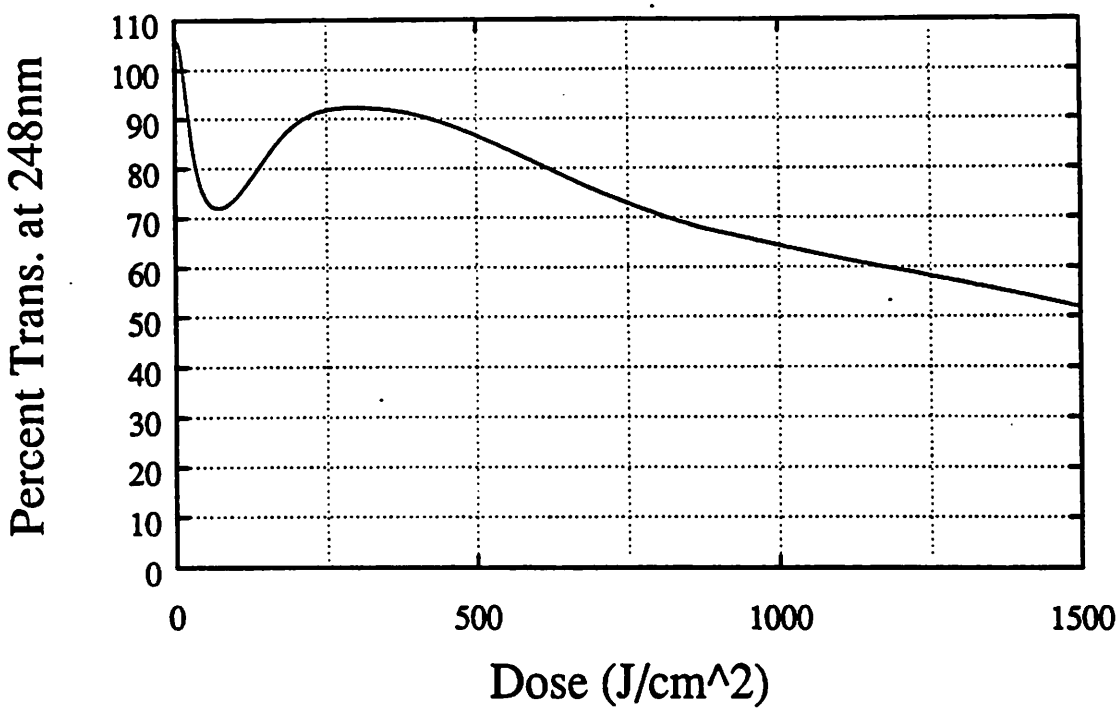

Fig. 17. Transmission at 248nm versus dose for a 1cm thick sample of glycerine 99.7 USP.

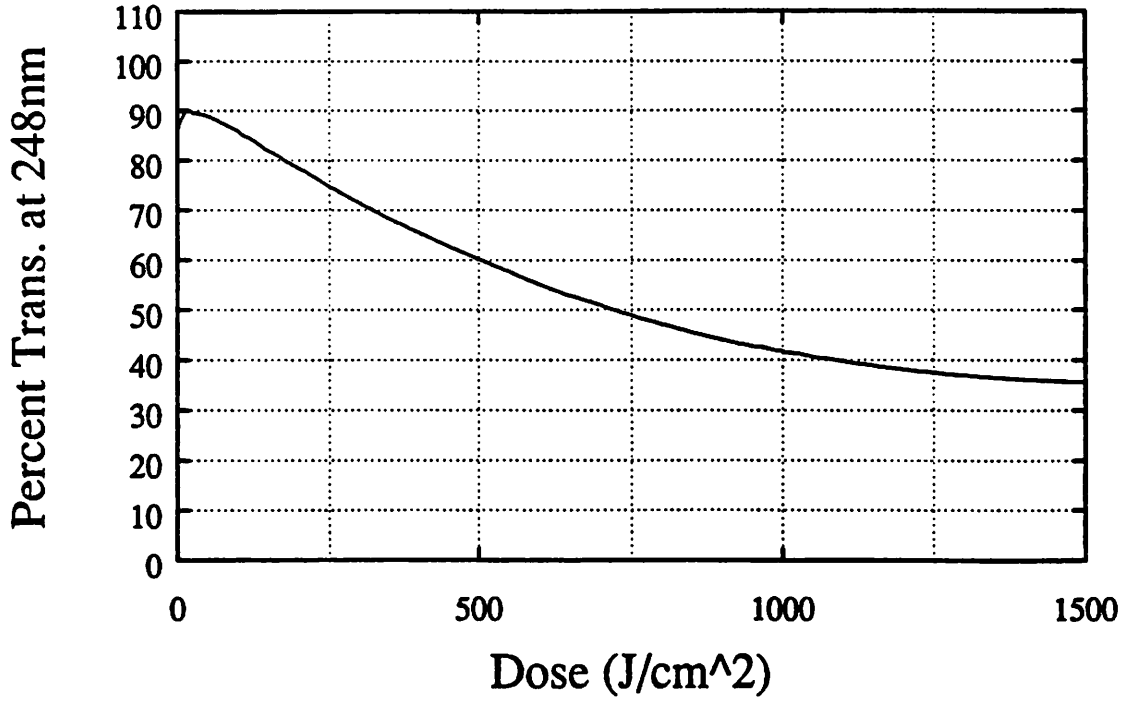

Fig. 18. Transmission at 248nm versus dose for Cargile #3421 with a piece of LiF submerged.

Index Matching Fluids @ 248nm		
Fluid Name	Refractive Index (+/-0.001)	Transmission
Dupont Krytox	1.319	Good
Fomblin VT-219	1.322	Good
Demnum S-65	1.337	Good
Deionized Water	1.374	Good
Cargile #3421	1.436	Poor
Dow 200 50 cst	1.467	Good
Dow 200 100 cst	1.467	Good
Dow 200 200 cst	1.467	Good
Ethylene Glycol	1.484	Good
Propylene Glycol	1.486	Poor
J.P. Banks Fluid	1.508	Bad
Polyglycol	1.511	Bad
Glycerine 99.7USP	1.533	Poor

Table 1. Index of refraction at 248nm for several candidate optical fluids.

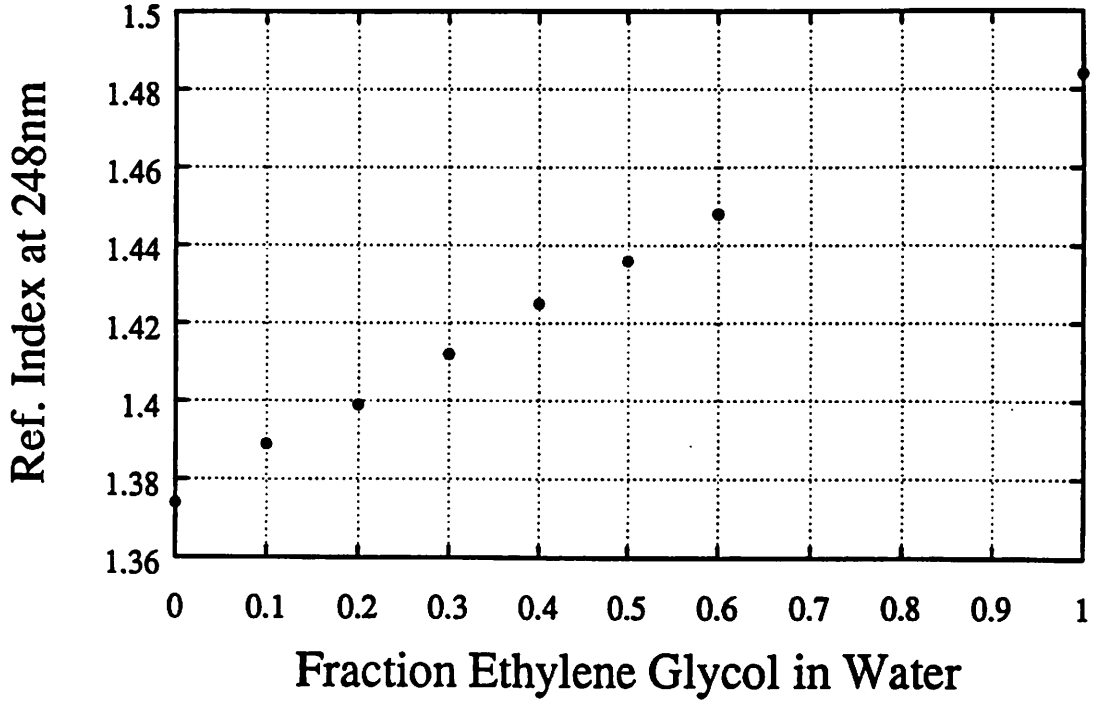

Fig. 19. Refractive index at 248nm of DI water/ethylene glycol mixture for various percent mixtures of ethylene glycol.

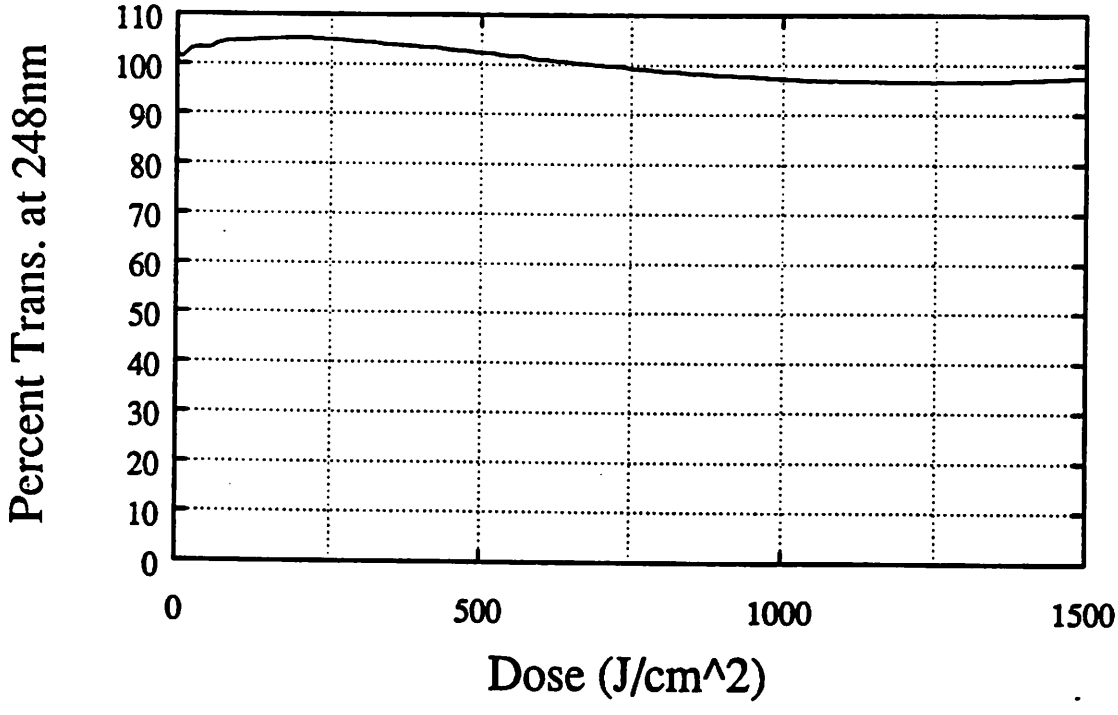

Fig. 20. Transmission at 248nm versus dose for a 1cm thick sample of 70% DI water/30% ethylene glycol.

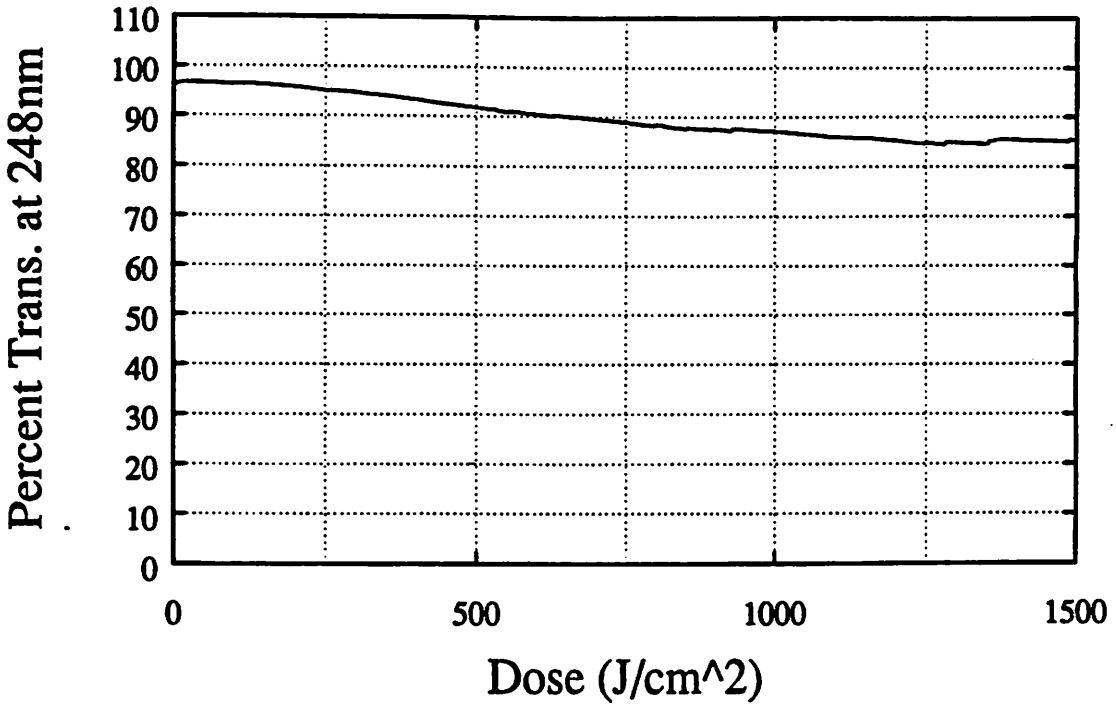

Fig. 21. Transmission at 248nm versus dose for 70% DI water/30% ethylene glycol with a piece of LiF submerged.

Chapter 4
Synthesis and Characteristics of 213nm Quintupled Nd-YAG Radiation

Abstract- A quintupled Nd-YAG (213nm) laser source has been constructed to investigate the use of highly coherent pulsed lasers in deep-UV microlithography. The relevant characteristics of this 10Hz, 0.25W laser have been measured.

This laser can be operated in two modes: free running and injection seeded. The spectral linewidth while free running is 47pm with a coherence length of 0.95mm. Injection seeding results in single-mode Fourier-transform limited pulses with spectral linewidth of 0.035pm and coherence length of 1.3m. The injection seeded linewidth is well within the 1pm requirements of today's monochromatic all-fused silica microlithography lenses. The coherent nature of this source leads to high contrast speckle. The speckle is characterized by 100% contrast intensity variations in the far-field scattering of the quintupled Nd-YAG laser.

4.1 Introduction

The first demonstration of frequency upconversion was published in 1961.[1] This first demonstration used quartz as the nonlinear material and only a tiny fraction of the incident ruby laser pulse (694.3nm) was converted to the second harmonic (347.2nm). The small conversion efficiency was caused by a difference in the refractive index of quartz for the two wavelengths. This dispersion caused a difference in propagation velocity and thus a loss of phase between to the wavelengths as the two colors traveled through the quartz.

The introduction of biaxial nonlinear crystals[2,3] solved the problem of dispersion between the incident and resultant wavelengths. The biaxial property was exploited by making the resultant wave possess a polarization orthogonal to the incident wave. The angle of the crystal axis could then be tilted such that the refractive index for both waves was

matched. This results in a long length over which the two waves are in phase and thus energy can transfer from the incident to the resultant wave with high efficiences. Conversion efficiences of greater than 80% have been reported for frequency doubling of the Nd-YAG laser.[4]

The amount of average power produced in the deep-UV region by nonlinear upconversion had been limited by the lack of a nonlinear crystal that was highly transmitting in the deep-UV. The development of beta Barium Borate (BBO)[5,6] has sparked new investigations into the production of high average power deep-UV radiation because of the high deep-UV transparency of BBO. Recent work with BBO has shown deep-UV generation down to 204.8nm.[7,8,9] 204.8nm is the short wavelength cutoff for type I SHG phase matching in the BBO crystal.

The shortest wavelength obtainable from the harmonics of the ND-YAG laser is the 5th harmonic at 213nm. The 5th harmonic can be obtained in two ways: 1) Produce the 2nd harmonic, double this to the 4th harmonic, and finally mix the 4th harmonic with the fundamental to produce the 5th. 2) Produce the 2nd harmonic, mix the 2nd harmonic with the fundamental to produce the 3rd, and finally mix the 2nd and 3rd harmonic to produce the 5th. Both of these methods result in radiation at 212.8nm and each method has its advantages and disadvantages. The first method is more straightforward. No waveplates are needed to rotate the polarizations of the harmonics into proper angle. The disadvantage with this method is the difficulty with producing the 4th harmonic (266nm). This wavelength is far into the deep-UV and only a BBO crystal can reasonably be used for its production. The second method is more complicated in that the resulting polarizations of the 2nd and 3rd harmonics are orthogonal and must be rotated into parallelism by a waveplate. The advantage of this method is the ease of producing the 3rd harmonic. Commonly available crystals such as KDP can be used and lead to stable high power 3rd harmonic output.

4.2 Laser System

This original optical layout for production of 213nm radiation is shown in Fig. 1. This system was purchased from Continuum Corp. The detailed operation of the Nd-YAG laser is described in the *Operation and Maintenance Manual for the Model YG661-10 YAG Laser.* This Nd-YAG laser is a 10Hz pulse repetition rate system capable of producing 600mJ per pulse. Our system has been adjusted to produce about 400mJ per pulse at 10Hz. The fundamental pulse energy was lowered to prevent damage to the 5th harmonic crystal. Several 5th harmonic crystals were damaged during the initial installation using the higher pulse energy. The 5th harmonic is produced by mixing the 2nd and 3rd harmonics. Although mixing the 1st and 4th harmonics has a higher nonlinearity coefficient, at the time this system was constructed producing the 4th harmonic was difficult and resulted in an unstable 4th harmonic output.

In the original configuration, this system produced 5mJ per pulse at 213nm at 10hz for an average power of 50mW. There were several simple improvements possible with the original configuration that led to much increased 213nm power. The first improvement was to remove the uncoated windows around the 5th harmonic crystal. Each surface of these windows accounted for a 4% loss owing to Fresnel reflection. Removal of the output window increased the 213nm output by 8% because of the elimination of two Fresnel reflections. Removal of the input window caused a greater than 8% increase because of the nonlinear operation that occurs after the input window in the BBO crystal. 5th harmonic radiation produced by the mixing of 2nd and 3rd harmonic is given by:

$$P(5\omega) = \gamma P(2\omega)P(3\omega), \qquad 1$$

where $P(5\omega)$, $P(3\omega)$, and $P(2\omega)$ are the average powers in the 5th harmonic, 3rd harmonic, and 2nd harmonic. The constant, γ, is a proportionality constant that contains all the nonlinearity coefficients and phase matching parameters for a given crystal and configuration. As one can see from Eqn. 1, the 5th harmonic output goes as the square of the total input power.

The 5th harmonic output is thus increased by a factor of 1.17 on removal of the input window (1.08*1.08=1.17). To compensate for the loss of protection provided by the windows the entire laser enclosure was sealed and purged with dry nitrogen.

The aperture shown in Fig. 1 is required because the original crystal diameter was less than the laser beam diameter. This 4.3mm diameter aperture blocked nearly 50% of the beam area. Replacing the BBO original crystal with a new BBO crystal with dimensions 9X9mm and 5mm long allowed the use of the full beam diameter. Additionally, the input face of the BBO crystal was AR-coated for the incident 2nd and 3rd harmonic wavelengths. The increase in beam area leads to a 50% increase in 213nm power while the AR-coating leads to a 8% increase (1.04*1.04=1.08).

Further improvements in 213nm power were achieved by eliminating the turning prism and the windows around the 2nd and 3rd harmonic crystals. All these components contributed to a reduction of one or more of the harmonics needed in the synthesis of 213nm radiation. Combining these improvements should have increased the 213nm output power by a factor of 5.11. This much increased 213nm power damaged the Pellin Broca prism used for wavelength separation. In place of the prism, four dielectric mirrors coated for maximum reflection at 213nm are used to separate the 213nm radiation from the other remaining harmonics. These mirrors have a measured reflectivity near 99% at 213nm and thus contribute at most a loss of 4%. This arrangement is an improvement over the Pellin Broca prism since the prism was not AR-coated and exhibited some absorption of the 213nm radiation.

The final optical configuration is shown in Fig. 2. The record to date is 28mJ per pulse at 213nm at 10Hz giving 280mW of average 213nm power. This is a 560% increase over the original configuration, most of which is accounted for in the previous paragraphs. The additional improvement is most likely owing to the shorter BBO crystal used in the final configuration. The original BBO crystal was 7mm long while the new crystal is 5mm long.

The formula for the ideal crystal length requires knowledge of incident beam size, power density, spectral linewidth, beam divergence, crystal nonlinear coefficient, and absorption.[10] We have good estimates of all these factors except for incident beam divergence and crystal absorption. We do know that the crystal exhibits more absorption than expected and that the divergence of the Nd-YAG beam is most likely not as low as the original specifications. Since the ideal crystal length becomes shorter for both higher crystal absorption and higher beam divergence, we chose a length for the replacement crystal shorter than the original by 2mm. Better results might be obtained with an even shorter crystal.

Further gains in 213nm output could be obtained by applying an AR-coating to the waveplate and the 2nd and 3rd harmonic crystals. The output from the Nd-YAG laser itself could also be increased up to its rated value of 600mJ per pulse. Now that no crystal damage has been experienced with the new crystal, it is reasonable to assume that further increases are safe. This is also supported by the literature, where 600mJ 1064nm pulses at 10Hz have been upconverted to 70.0mJ 213nm pulses with no crystal damage.[4] Increasing the Nd-YAG output power would require a change in the collimating lens positioned at the output of the oscillator cavity. This lens removes the beam divergence caused by the thermal profile within the Nd-YAG rod. Increasing the flashlamp voltage would change this profile, necessitating a different focal length lens at the oscillator output. One final change in the present system might lead to a further increase 213nm power. As stated in the previous paragraph, the BBO crystal length used in the present system in most likely not optimum. An effort to measure the pertinent properties of the laser and BBO crystal would lead to a properly calculated crystal length. A more straightforward but more expensive solution would be to purchase several crystal lengths and measure their conversion efficiency when used in our present setup.

4.3 BBO Crystal Heating

As delivered, the 5th harmonic BBO crystal was not held inside any type of temperature controlled oven. As the BBO crystal absorbed some of the 213nm radiation it changed temperature causing the crystal to become detuned. The heating effect inside the BBO crystal created a large amount of hysteresis in the tuning angle. Any loss of tuning would reduce the amount of 213nm energy and thus reduce the amount of crystal heating, leading to a run away process. Thus if the best tuning angle was lost even briefly the crystal had to be rotated all the way back to the cold position and the tuning process had to be repeated. To alleviate this problem we built a temperature controlled oven around the BBO crystal. Fig. 3 shows schematically the effect of the oven. Without the oven, the overall crystal temperature must increase to expel the excess heat into the air. With the oven in direct contact with the crystal, the excess heat is swiftly carried away by the highly conducting aluminum oven. The oven can help prevent a change in the average temperature of the crystal but nothing short of changing the crystal shape can change the temperature profile within the crystal. Fig. 3 shows the profile within the crystal is the same with and without the oven.

This temperature profile causes a loss in conversion efficiency because the crystal is not properly angle tuned throughout the volume of the crystal. As an example of this loss in conversion, Matthews[11] showed reduction in 4th harmonic conversion from 58% to 46% when the repetition rate was increased from 1Hz to 10Hz. This is a 21% loss in 4th harmonic energy per pulse and is attributed to a transverse thermal gradient caused by absorption of 266nm energy. For creation of 5th harmonic from 2nd and 3rd the FWHM temperature bandwidth of our crystal is 7.4°C.[12] The thermal conductivity of BBO has been measured for the 11 and 33 crystal orientations and are 0.08W/m/K and 0.8W/m/K respectively.

To estimate the temperature rise at the center of the crystal we will use an approximation for the thermal profile of a crystal illuminated with a Gaussian distributed laser beam:[13]

$$T(r) = \frac{qw_0^2}{4k} e^{\frac{-r^2}{w_0^2}}, \qquad 2$$

where T(r) is the radial temperature, q is the absorbed power per unit volume, w_0 is the beam waist and K is the crystal thermal conductivity. Our incident beam is not Gaussian in shape but we will make this assumption to simplify the calculations (see section 4.4 for 213nm beam profile). To estimate the absorbed power per unit volume, we will assume that the 213nm intensity is uniform along the crystal length and equal to half of the output intensity. We will also use an estimation of the absorption coefficient at 213nm obtained from Eimerl[12] of 0.52 cm^{-1}. Okada[13] also gives an estimate of the power per volume absorbed by the crystal:

$$q \approx \frac{2W\alpha}{\pi w_0^2}, \qquad 3$$

where α is the absorption coefficient and W is the incident beam power. Combining Eqn. 2 and 3 gives:

$$T(r) \approx \frac{W\alpha}{2\pi K} e^{\frac{-r^2}{w_0^2}}. \qquad 4$$

The temperature at the center is simply:

$$T_{center} \approx \frac{W\alpha}{2\pi K}. \qquad 5$$

Using the assumptions stated above the the thermal conductivity in the 11 direction (this is the direction toward the oven walls) gives a center temperature 29°C higher than the edge.

This crude estimate of the temperature rise at the center may be off by a large factor, but it demonstrates the severity of the heating problem involved with producing high average power 213nm radiation. The crystal heating can affect the stability of the output energy, as well as a cause reduction in conversion efficiency. Fig. 4. shows schematically two regions of tuning within the temperature range of the crystal. Adjusting the crystal angle such that

the crystal is on the low side of the temperature profile with no incident radiation leads to a detrimental positive feedback situation. On application of the incident laser beam the crystal will heat up moving the tuning angle toward higher conversion, causing more heating, greater conversion and so on. This runaway process in not desired since this feedback works on the down slope as well. If, for some reason, there is a momentary reduction in 213nm power, the crystal will cool reducing its conversion efficiency and thus lowering the amount of 213nm power further cooling the crystal, etc. Thus, positioning the crystal on the lower temperature side of the tuning curve will lead to unstable operation. This effect is demonstrated in Fig. 5. This is a plot of 213nm energy versus time with crystal tuned to the low side of the tuning curve. The incident energy is applied at 20sec and the 213nm output rises by a factor 10 before leveling off.

Tuning to the high temperature side of the tuning curve leads to a negative feedback situation. If the 213nm output is perturbed higher, raising the crystal temperature, the conversion efficiency will drop returning the output to the previous level. Likewise the lower 213nm out, the efficiency will raise returning the output to the steady state level. Fig. 6 shows the output energy versus time with the crystal tuned to the high temperature side. On application of the incident laser beam the 213nm output is high, heating the crystal and reducing the conversion efficiency until the steady state point is reached. It is interesting to note that the steady state output is one half of the initial. Retuning the crystal can regain some of this loss, returning the output to about 75% of the initial level. This inability to regain all the lost conversion efficiency is consistent with Matthews.[11] Fig. 6 also gives us an estimate of the time constant involved in the heating and cooling of the crystal. The exponential approach to steady state has an e^{-1} value of 15sec. This long time constant shows that the crystal does not react on the time scale of the pulse repetition rate of 10Hz and thus it is reasonable to calculate crystal heating on an average power basis and not on a per pulse basis.

4.4 5th Harmonic Energy Output and Beam Profiles

Once a stable operating point has been found, the 213nm output still shows considerable variation in pulse to pulse energy output. Fig. 7 shows the 213nm output energy versus pulse number for a representative 2000 pulses. The crystal was tuned to the negative feedback side of the temperature curve to achieve best energy stability. Fig. 8 is a histogram of the energy measurements shown in Fig 7. The standard deviation of the 213nm pulse energy is 7.6% and the total included range is +/-20%. Exposures with +/-1% dose control (TIR) would require a minimum of 400 pulses. This pulse count equates to a 40sec exposure using the 10Hz pulse rate. If the second generation 213nm source exhibits the same energy variation with its much higher 2000Hz pulse rate, only 200ms would be required for +/-1% exposure dose control.

We used the measurement setup shown in Fig. 9 to measure the beam profile of the 213nm output and each of the harmonics. For the 213nm measurement, six dielectric mirrors were used to insure that none of the other wavelengths contributed to the beam profile. For the other harmonics only two dielectric mirrors were needed to reduce the other colors sufficiently below the desired color. Four quartz wedges are placed after the dielectric mirrors to reduce the intensity of each beam profile below the level of camera saturation. Intensity variations are made by changing the angle of incidence on the quartz wedges.

Figs. 10 through 13 show the beam profiles for the 1st, 2nd, 3rd, and 5th harmonics. The profile for the 1st harmonic is nearly flat top. A flat top profile is expected since the amplifier rod is operated in the saturation condition. The variation in intensity across the flat top region is mostly owing to differences in the level of inversion across the amplifier rod. Since the rod is pumped by a flashlamp and mirror arrangement, some nonuniform pumping is expected. The profiles for each successive harmonic show a further degradation in the profile uniformity. Each nonlinear operation exaggerates the nonuniformities of the input beam. The smooth drop off in intensity in the vertical direction in the 2nd harmonic profile

is evidence of beam "walk off" caused by different k-vector directions for the incident 1st harmonic wave and the resulting 2nd harmonic wave. The difference in k-vectors for SHG of 1064nm in KDP cannot be eliminated since non-critical phase matching in this crystal can only be achieved over a small wavelength range near 520nm. This small walk off effect is accepted rather than replacing the KDP crystal with another type because of the high conversion efficiency and rebust nature of the KDP crystal. The 3rd harmonic operation is close to non-critical phase matching, thus the 3rd harmonic beam profile is not significantly degraded.

The 5th harmonic beam profile shown in Fig. 13 possesses severe nonuniformities. These nonuniformities are caused by three factors. The first factor is the uniformities of the incident 2nd and 3rd harmonic beams. The second factor is beam "walk off". The BBO crystal is not operated close to non-critical phase matching. In the case of the 5th harmonic crystal, the "walk off" is in the horizontal direction. The third and most important factor causing the 5th harmonic beam nonuniformities is the temperature profile across the crystal. This temperature variation causes a difference in conversion efficiency across the face of the crystal. Fig. 13 shows that the tuning angle is such that maximum conversion occurs at the top of the crystal. When tuned for best conversion in this region the 213nm output is maximized. Changing the tuning angle can produce higher intensities near the middle or even at the lower portion of the crystal but at the expense of total 213nm energy output.

To test the stability of the 5th harmonic beam profile from pulse to pulse, 16 sequential pulses were recorded by the camera and the variation from pulse to pulse was analyzed. The measure of variation used was the correlation coefficient between two profiles defined by:

$$\rho_n = \frac{\sum_{\text{allpixels}} (I_n(x,y) - < I_n >)(I_1(x,y) - < I_1 >)}{\sqrt{\text{var}(I_n)}\sqrt{\text{var}(I_1)}}, \qquad 6$$

where ρ_n is the correlation coefficient between pulse number n and pulse number 1, I(x, y) is the camera intensity at position (x, y), < I > is the average pixel intensity, and var(I) is the

variance of the pixel intensity for a single pulse. The variance is given by:

$$\mathrm{var}(I) = \sum_{\mathrm{allpixels}} (I(x,y) - \langle I \rangle)^2. \qquad 7$$

Eqns. 6 and 7 were applied to the pixel data after each picture was normalized so that variations in total energy were eliminated. After normalization only changes in shape will reduce the correlation coefficient. The result of this measurement is shown in Fig. 14. The correlation coefficient for the first pulse is 1 since it correlates perfectly with itself. The correlation of the following pulses decreases with pulse number. Unfortunately the camera system can only record 16 pulses at one time, making it impossible to measure the long term stability of the pulse profile.

4.5 Spectral Characteristics of Quintupled Nd-YAG Radiation

The single most important characteristic of any radiation source for lithography is its spectral content. The Nd-YAG source employed in these experiments can be operated with two different spectral linewidth specifications. In normal operation the Nd-YAG oscillator cavity lases in many longitudinal modes and several transverse modes. By folding a small single-frequency CW laser source into the main oscillator cavity, the laser can be operated in a single longitudinal and transverse mode. This method of line-narrowing is called injection seeding and is available as an option on our Nd-YAG laser. By the simple opening and closing of a shutter the ND-YAG can be operated multimode or single mode. A change in properties of the fundamental harmonic has a dramatic affect on the higher harmonics, particularly the 5th harmonic.

Since the spectral linewidth produced by the quintupled Nd-YAG laser is less than a few 100pm for both seeded and unseeded operation, a grating or prism spectrometer has insufficient resolution to measure these narrow linewidths. We measured the laser coherence length and used the relation between coherence length and spectral linewidth given by:[14]

$$\Delta\lambda = \frac{\lambda^2}{\Delta L}, \qquad 8$$

where $\Delta\lambda$ is the spectral linewidth, λ is the center wavelength, and ΔL is the coherence length. To measure the coherence length of our laser we used the modified Michelson interferometer shown in Fig. 15.

This interferometer consists of a quartz wedge used as a beamsplitter, a second quartz wedge used for energy compensation, and two normal incident dielectric mirrors. Part of the incident radiation is reflected by the first wedge toward the mirror. The light that passes through the first wedge passes through the second wedge onto the second mirror. After reflecting from each mirror, the two light paths travel back to the first wedge, are combined at the back surface of the first wedge and travel toward the CCD camera array. The second wedge reduces some of the energy of the light rays traveling along that arm to compensate for the extra energy lost in the other arm owing to surface reflections in the first wedge. Tilting the angle of the second wedge changes the amount of energy reflected by its surfaces. The adjustment of this wedge is made when the two delay arms are of equal length and the interference fringes caused by the interaction of light rays from these two arms should have a contrast of 100%. The wedge is tilted until the fringe pattern on the CCD camera has 100% contrast.

Once proper setup is achieved, the mirror on one arm is moved to change the amount of path difference encountered by light rays in each arm. The contrast of the interference is measured at each mirror position giving a plot of fringe contrast versus path length difference. The results of this measurement for the 5th harmonic wavelength are shown in Figs. 16 and 17. Fig. 16 shows the result with the injection seeder off and Fig. 17 with the seeder on. Making the assumption that the contrast vs. path difference curve is Gaussian shaped and making a least squares fit gives a coherence length of 0.95mm for the 213nm radiation with the seeder off and 1290mm with the seeder. This result shows the dramatic difference in operating conditions with the seeder on and off. The change in coherence length is more

than three orders of magnitude. Calculating the corresponding spectral linewidth using Eqn. 8 gives 47pm for unseeded and 0.035pm for seeded operation. The unseeded linewidth is larger than the 1-3pm linewidths required by today's all-fused-silica deep-UV lithography lenses. The seeded linewidth is almost 100 times more narrow than required by today's lenses. A narrow spectral linewidth is a positive feature when designing lenses but detrimental to exposure uniformity owing to the tremendous speckle problem associated with such highly coherent laser sources.

Coherence length measurements can measure the linewidth for a single pulse but are incapable of monitoring a shift in the line center from pulse to pulse. It is not enough to have spectrally narrow radiation within each pulse, the line center must remain stable from pulse to pulse so that the integrated exposure is formed with narrow band radiation. To measure the variation in line center from pulse to pulse we have constructed a Fabry-Perot interferometer shown in Fig. 18 to measure the spectral characteristics of an integrated exposure.

Our Pabry-Perot interferometer was constructed from two dielectric mirrors coated for maximum reflection at normal incidence for 213nm radiation. The mirrors were mounted on 5 axis lens positioners with a spacer squeezed between the two mirrors. The free spectral range (spacing between repeated spectral transmission) for this interferometer is given by:[14]

$$FSR = \frac{\lambda_0^2}{2nh\cos\theta}, \qquad 9$$

where n is the refractive index (1.0 for air), h is the mirror spacing, and λ_0 is the vacuum wavelength. A second important parameter of this interferometer is its finesse given by:[14]

$$F = \frac{\pi\sqrt{R}}{1-R}, \qquad 10$$

where R is the mirror reflectivity. The finesse is a measure of the half-width of the peak transmission function. A higher finesse leads to a tighter transmission peak and thus a finer resolution. The finesse is also limited by the flatness of the mirrors used in the

interferometer. The mirrors used in this experiment had a reflectivity of 96% giving a reflectivity limited finesse of 77. This value is unreasonably high and the true finesse is limited by the mirror flatness. The flatness limited finesse is given by:[15]

$$F = \frac{\lambda}{2\Delta l}, \qquad 11$$

where Δl is deviation from perfect mirror flatness. The mirrors used in this experiment are specified to be 1/10 @633nm flat over 1 inch diameter. Only a 1/2 inch diameter portion of the mirror was used so 1/20 flatness can be expected giving a finesse of 7. The resolution of a Fabry-Perot interferometer with finesse, F, and mirror spacing, h, is given by:[15]

$$\Delta\lambda = \frac{\lambda^2}{2hf}. \qquad 12$$

Fig. 19 shows the unseeded integrated linewidth measurement made with the Fabry-Perot for 16 laser pulses integrated onto the CCD detector. The mirror spacing was 0.22m giving a resolution of 14.7pm and a FSR of 103pm. After taking into account the reduction in resolution caused by the limited number of camera pixels between transmission peaks, we obtain a spectral linewidth less than or equal to 41pm. Fig. 20 shows the result for seeded operation. Here the mirror spacing was set to 40mm giving a resolution of 0.08pm and a FSR of 0.56pm. This measurement is also an integrated exposure of 16 laser pulses resulting in an integrated linewidth less than or equal to 0.11pm. The unseeded Fabry-Perot measurement corresponds well with the 47pm value obtained from the Michelson interferometer. The seeded measurement result of 0.11pm is wider than that obtained from the Michelson because of the resolution limits of the Fabry-Perot interferometer. This 0.11pm value is still 10 times more narrow than necessary for today's all-fused-silica lenses while the unseeded linewidth is 10 times too wide for use with these lenses.

4.6 Conclusion

The first generation 213nm source has proven to be a stable and reliable source of 250mW of 213nm radiation. Using the injection seeder, this radiation has a spectral linewidth well within the 1-3pm requirements of monochromatic lenses used in present large field reduction step and repeat exposure tools.

This 213nm source has shown encouraging results and proven itself to be robust with long mean time to failure. The only maintenance down time has been for a cracked BBO crystal and a faulty temperature sensor. The crystal problem was caused by a failure in the AR-coating placed on the output side of the crystal. The replacement crystal was fabricated without a coating on the output face and has been running problem-free for six months, accumulating nearly 10 million laser pulses.

References

1. P.A. Franken, A.E. Hill, C.W. Peters, and G. Weinreich, "Generation of Optical Harmonics," *Phys. Rev. Let.*, vol. 7, no. 4, pp. 118-119, Aug. 1961.

2. J.A. Giordmaine, "Mixing of Light Beams in Crystals," *Phys. Rev. Let.*, vol. 8, no. 1, pp. 19-20, Jan. 1962.

3. P.D. Maker, R.W. Terbune, M. Nisenoff, and C.M. Savage, "Effects of Dispersion and Focusing on the Production of Optical Harmonics," *Phys. Rev. Let.*, vol. 8, no. 1, pp. 21-22, Jan. 1962.

4. C. Chen, "Recent Developements in Barium Borate," *Proc. SPIE Laser and Nonlinear Optical Materials*, vol. 681, pp. 12-19, 1986.

5. C. Chen, B. Wu, G. You, A. Jiang, and Y. Haung, "High Efficiency and Wide-Band Single-Harmonic-Generation Properties of the New Crystal beta-BaB2O4," *Thirteenth Int. Quant. Elec. Conf.*, pp. 20-21, June 1984.

6. C. Chen, B. Wu, A. Jiang, and G. You, "A New-Type Untraviolet SHG Crystal beta-BaB2O4," *Scientia Sinica B*, vol. 28, no. 3, pp. 235-243, March 1985.

7. K. Kato, "Second-Harmonic Generation to 204.8nm in beta-BaB2O4," *IEEE J. of Quant. Elec.*, vol. QE-22, no. 7, pp. 1013-1014, July 1986.

8. K. Miyazaki, H. Sakai, and T. Sato, "Efficient Deep-ultraviolet Generation by Frequency Doubling in beta-BaB2O4 Crystals," *Optics Lett.*, vol. 11, no. 12, pp. 797-799, Dec. 1986.

9. W.L. Glab and J.P. Hessler, "Efficient Generation of 200-nm Light in beta-BaB2O4," *Applied Optics*, vol. 26, no. 16, pp. 3181-3182, Aug. 1987.

10. A. Yariv, in *Quantum Electronics*, John Wiley and Sons, New York, 1975.

11. S.C. Matthews and J.S. Sorce, "Fourth harmonic conversion of 1.06μ in BBO and KD*P," *Proc. SPIE on Nonlinear Optics*, vol. 1120, pp. 137-147, 1990.

12. D. Eimerl, L. Davis, and S. Velsko, "Optical, Mechanical, and Thermal Properties of Barium Borate," *J. Appl. Phys.*, vol. 62, no. 5, pp. 1968-1983, Sept. 1987.

13. M. Okada and S. Ieiri, "Presence of Self-Induced Thermal Effects in Second-Harmonic Generation," *IEEE J. of Quant. Elec.*, pp. 469-470, Sept. 1971.

14. M. Born and E. Wolf, in *Principles of Optics*, Pergamon Press, New York, 1959.

15. F.L. Roesler and J.E. Lawler, in *Applied Optics*, Unpublished, 1987.

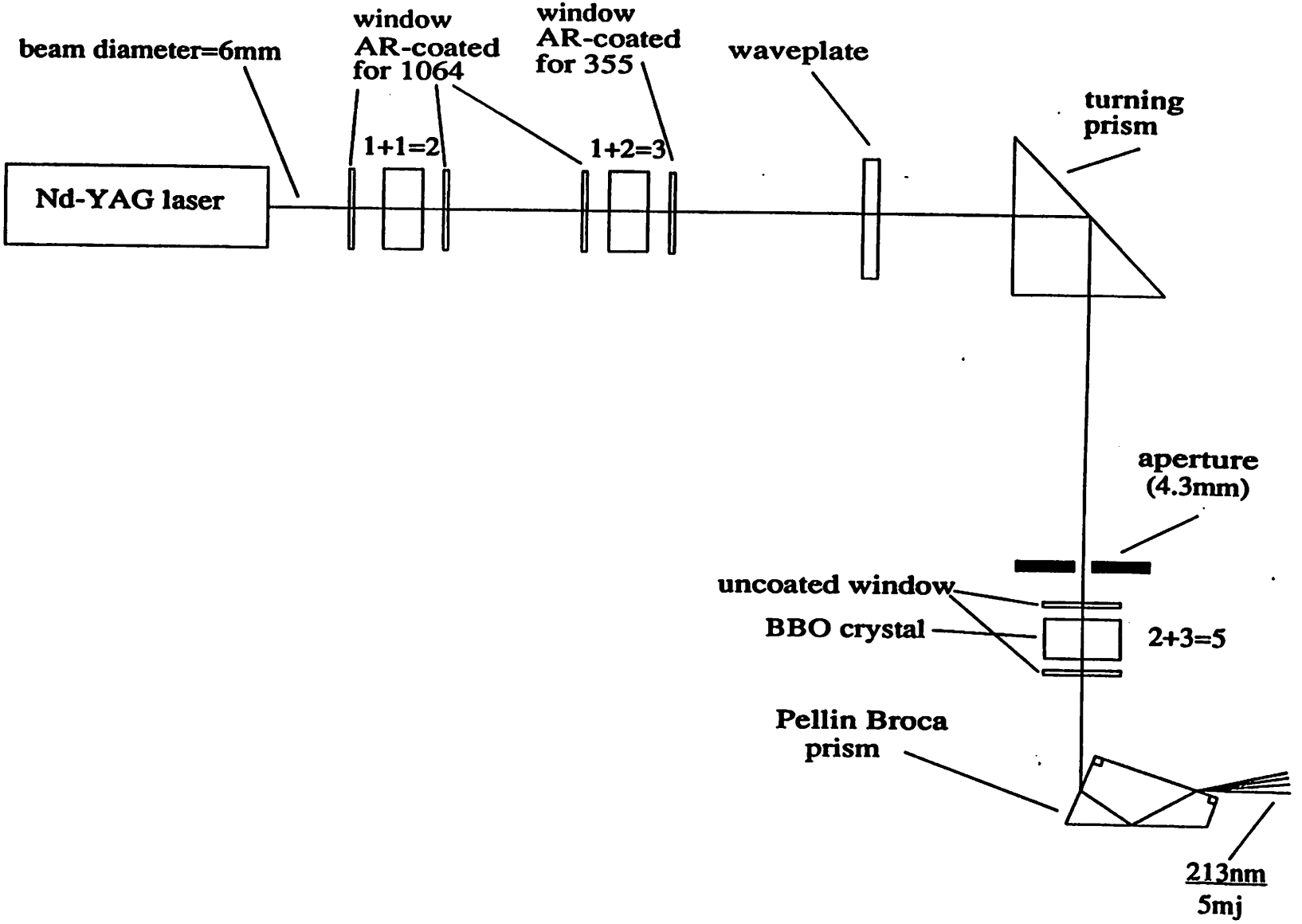

Fig. 1. Orginal configuration for producing 5th harmonic Nd-YAG radiation.

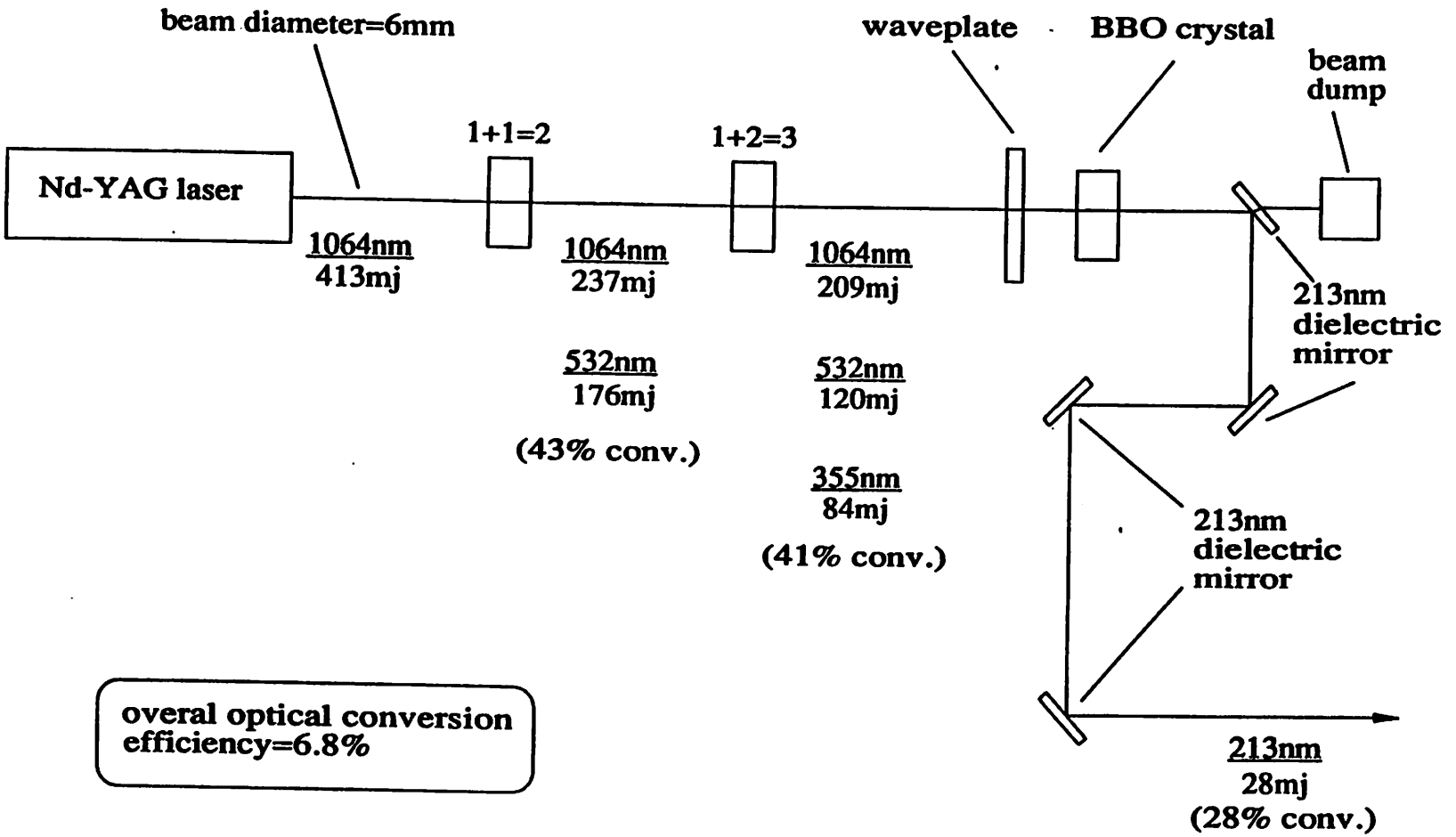

Fig. 2. Final configuation for producing 5th harmonic Nd-YAG radiation.

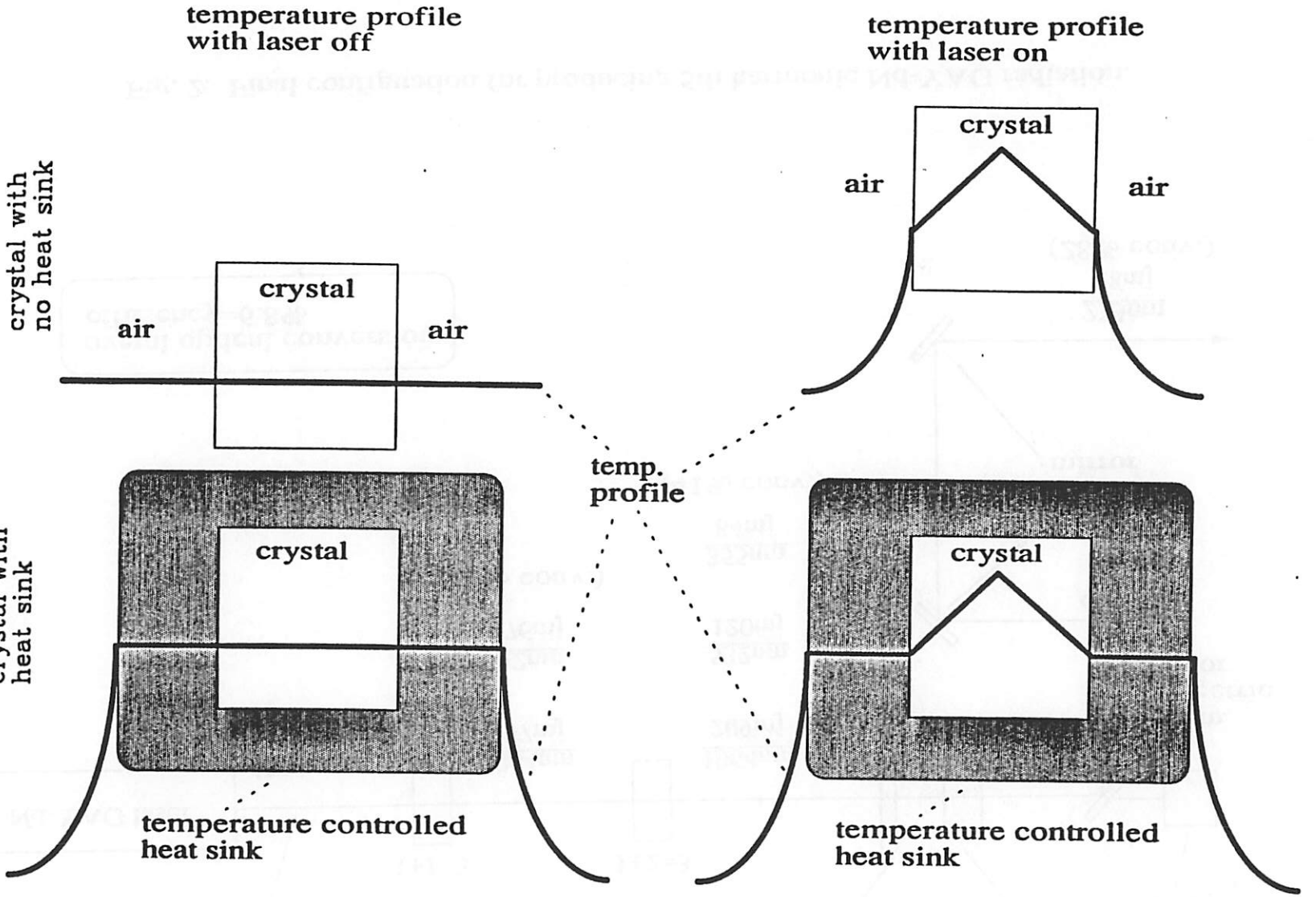

Fig. 3. Temperature profile inside and outside crystal with and without a heat sink.

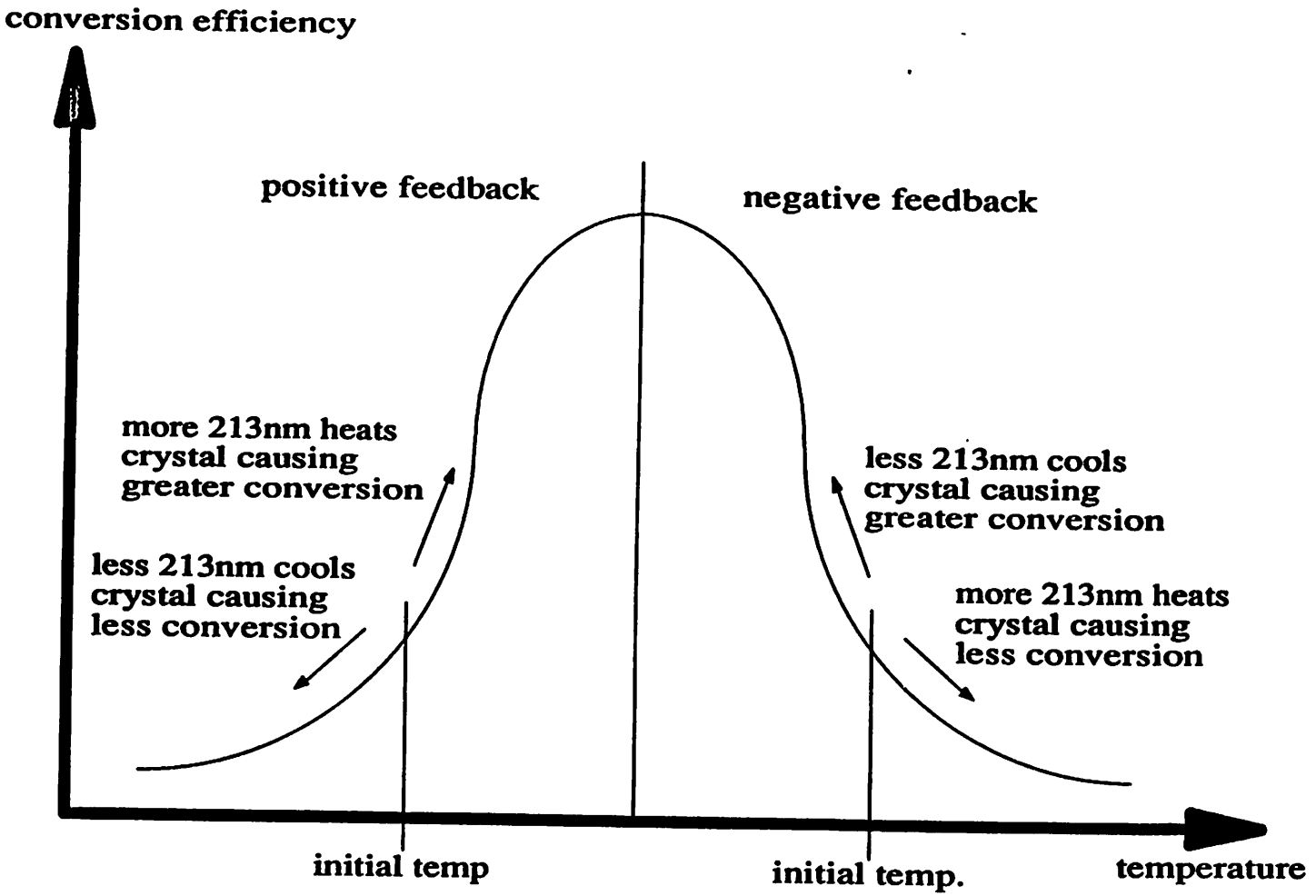

Fig. 4. Schematic representation of conversion efficiency vs. temperature for BBO crystal.

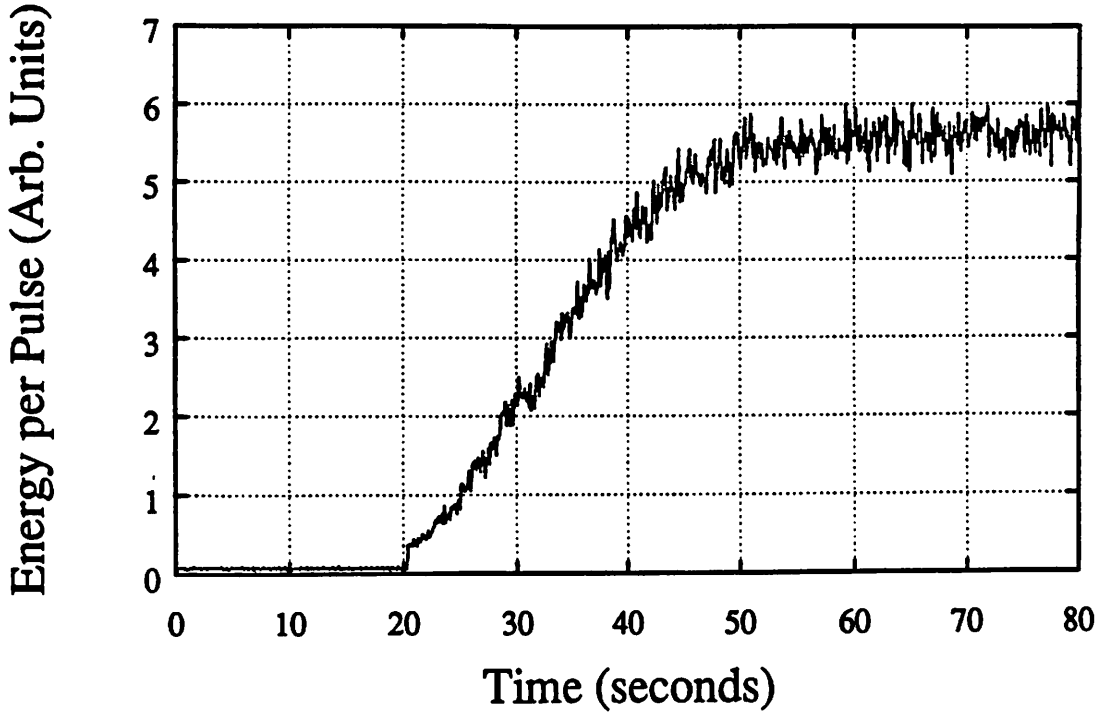

Fig. 5. 213nm output energy vs. time for BBO crystal tuned to positive feedback position.

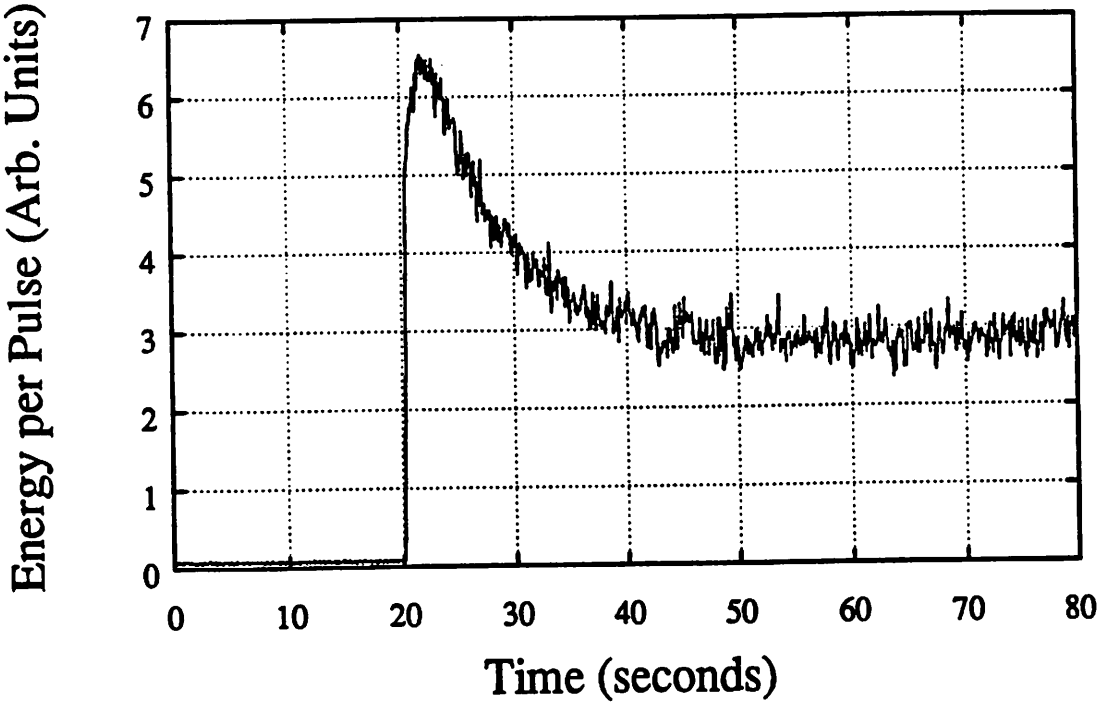

Fig. 6. 213nm output energy vs. time for BBO crystal tuned to negative feedback position.

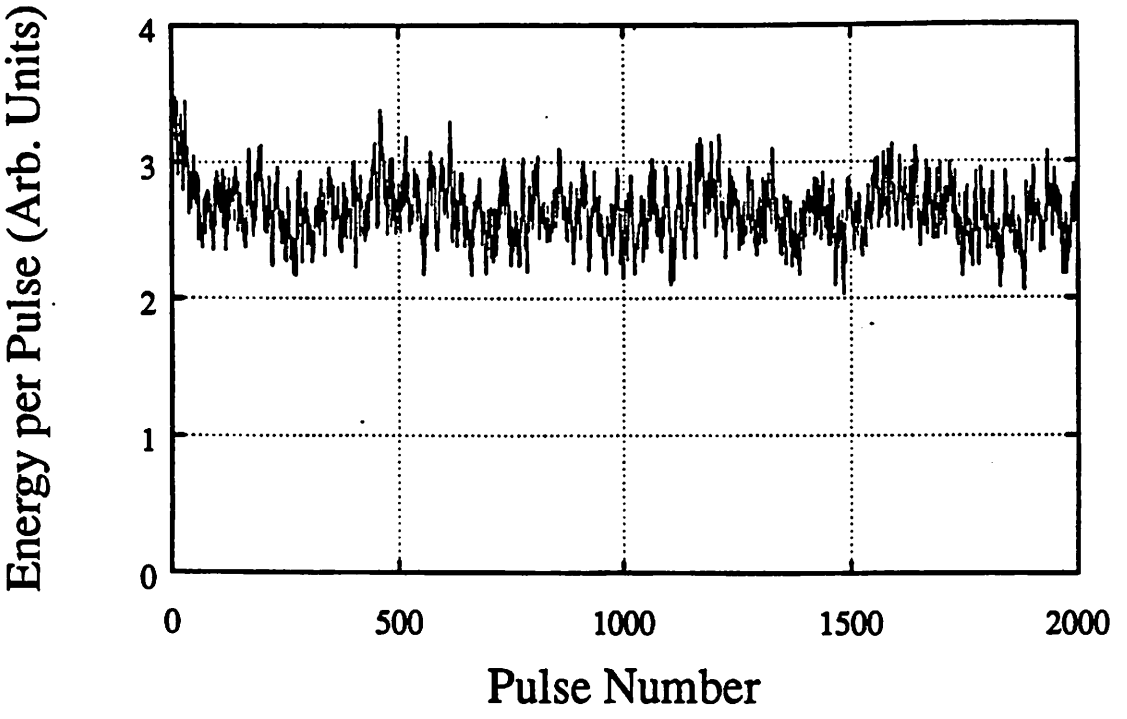

Fig. 7. 213nm pulse energy vs pulse number for 2000 sequential pulses.

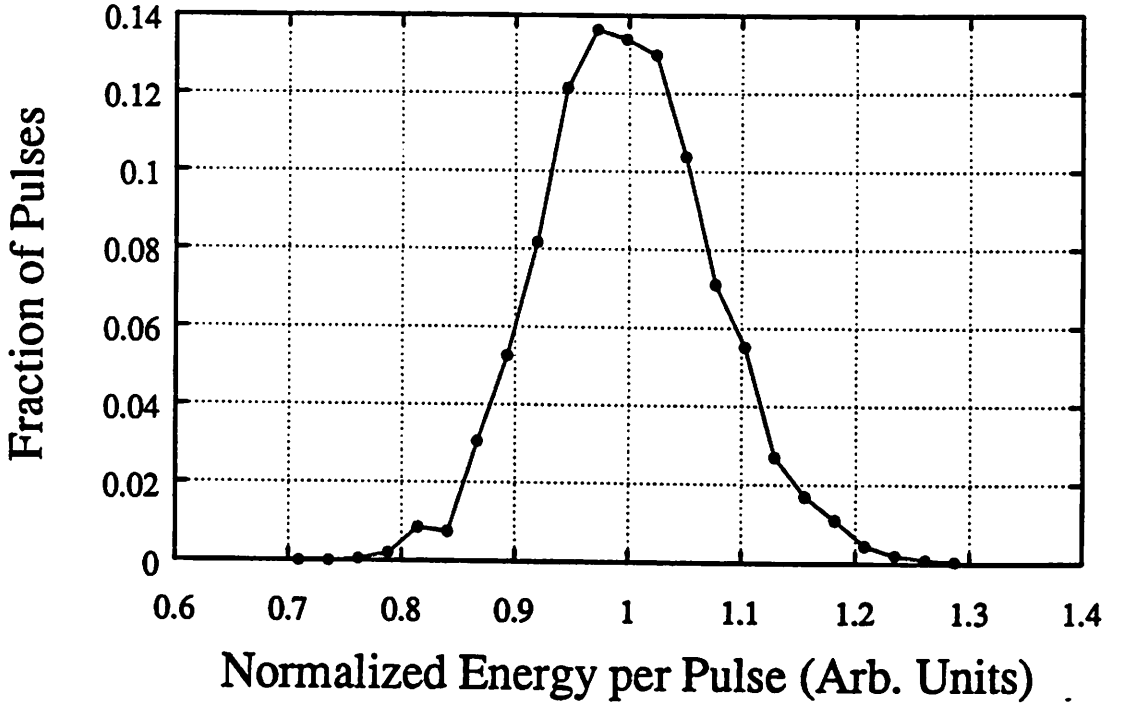

Fig. 8. Histogram of 213nm pulse energy distribution.

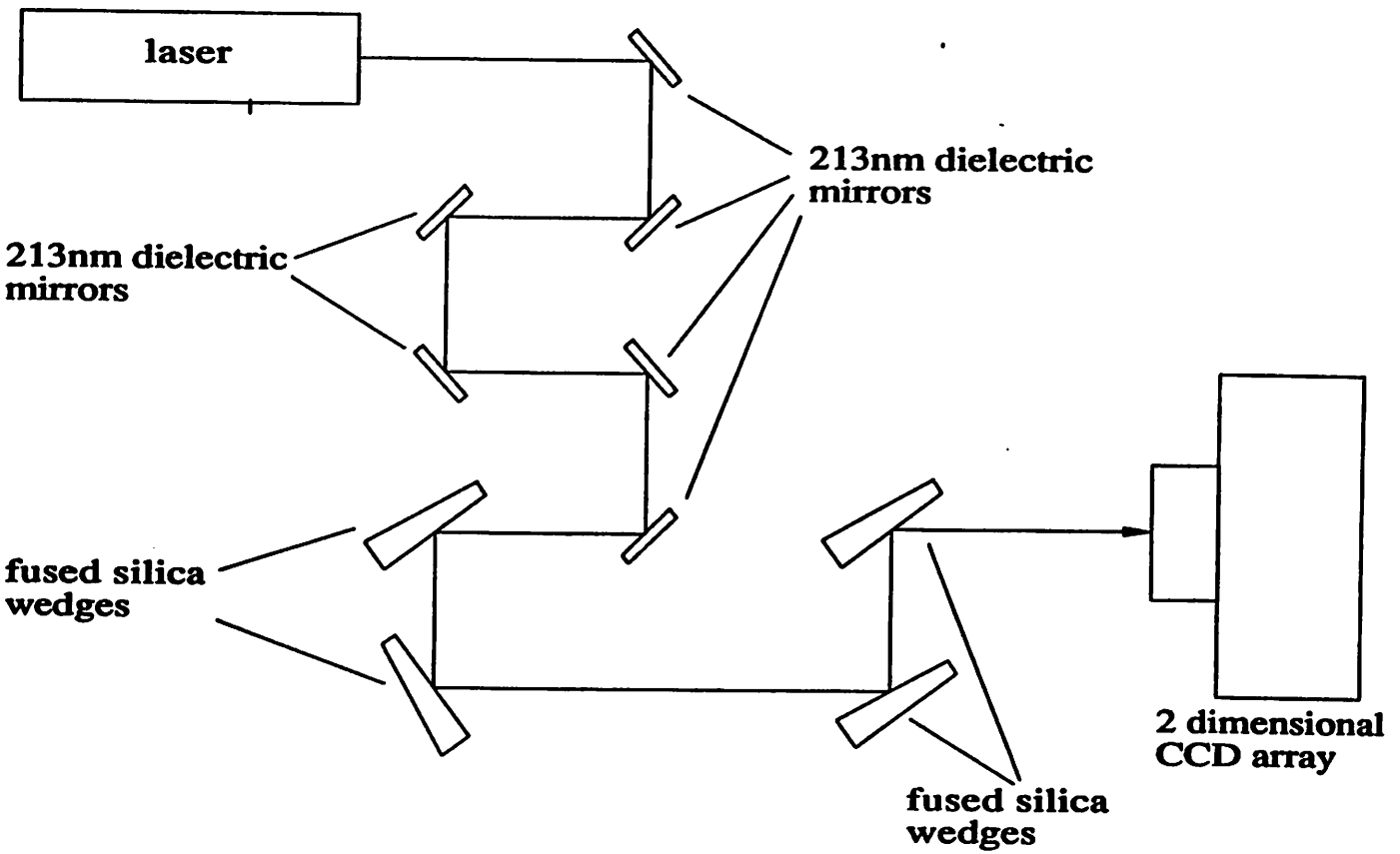

Fig. 9. Setup used to measure 213nm beam profile.

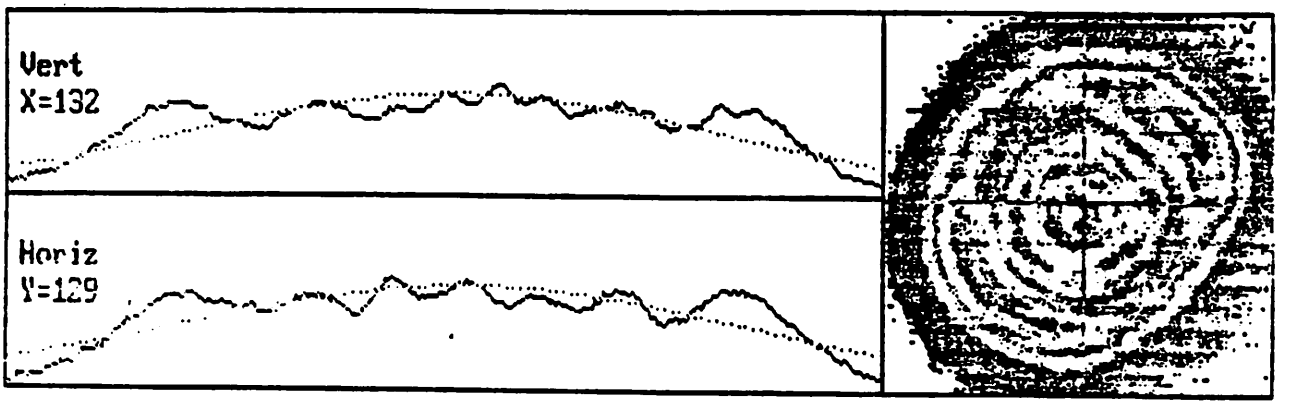

Fig. 10. 1st harmonic (164nm) beam profile.

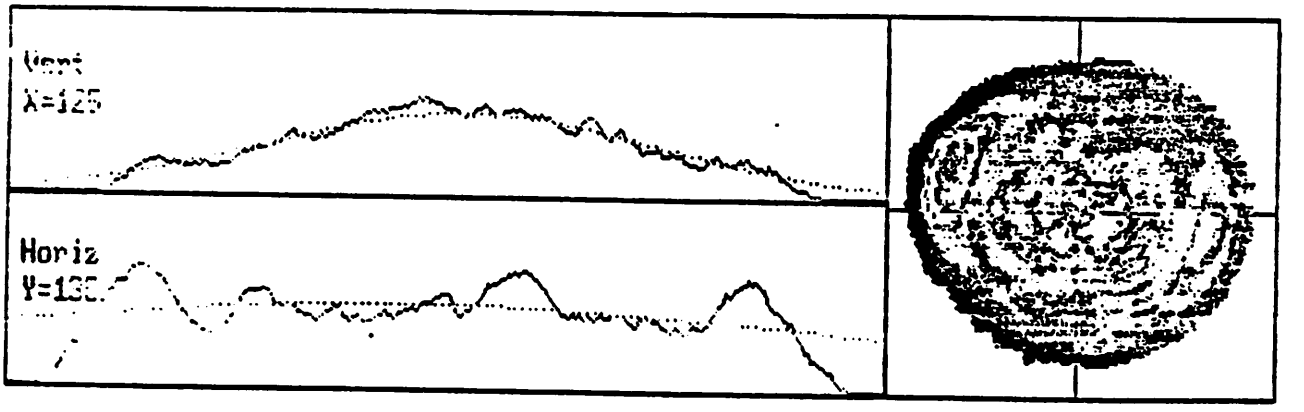

Fig. 11. 2nd harmonic (532nm) beam profile.

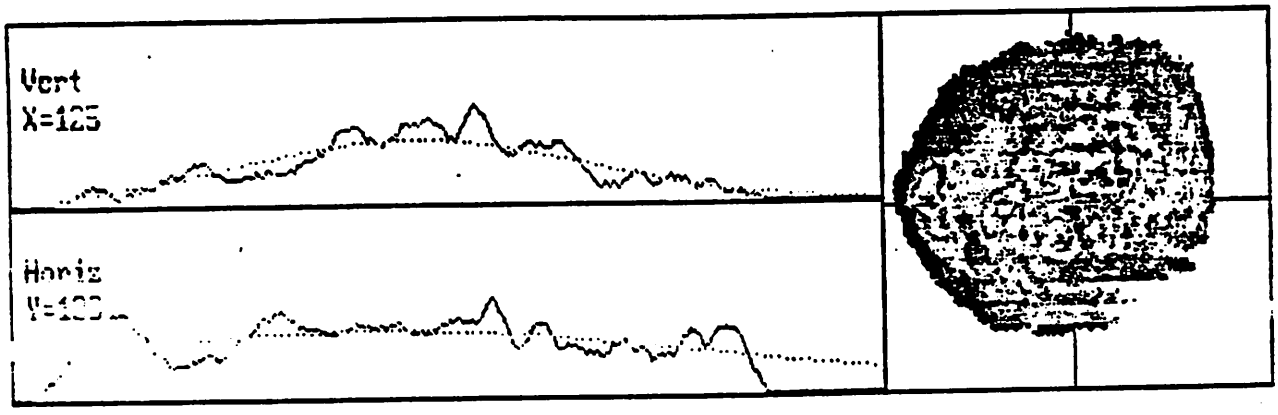

Fig. 12. 3rd harmonic (355nm) beam profile.

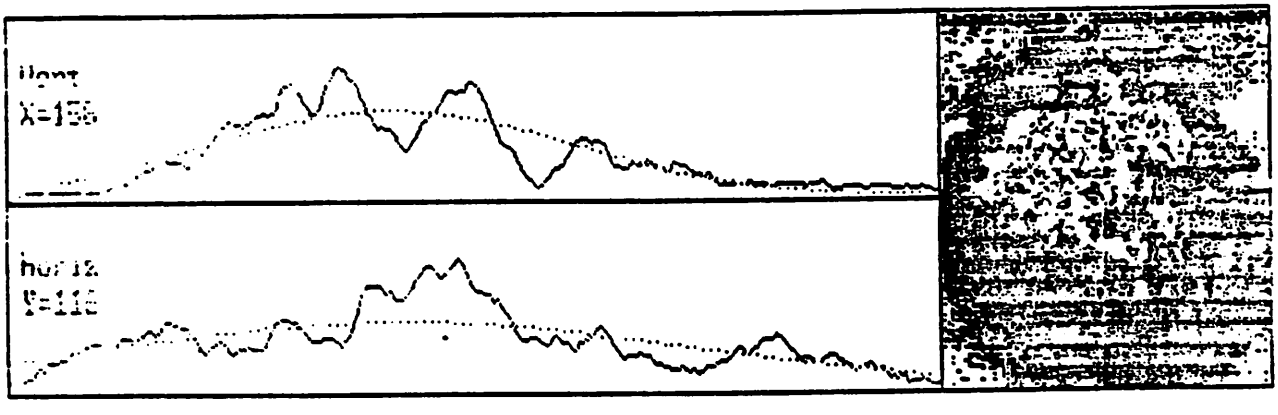

Fig. 13. 5th harmonic (213nm) beam profile.

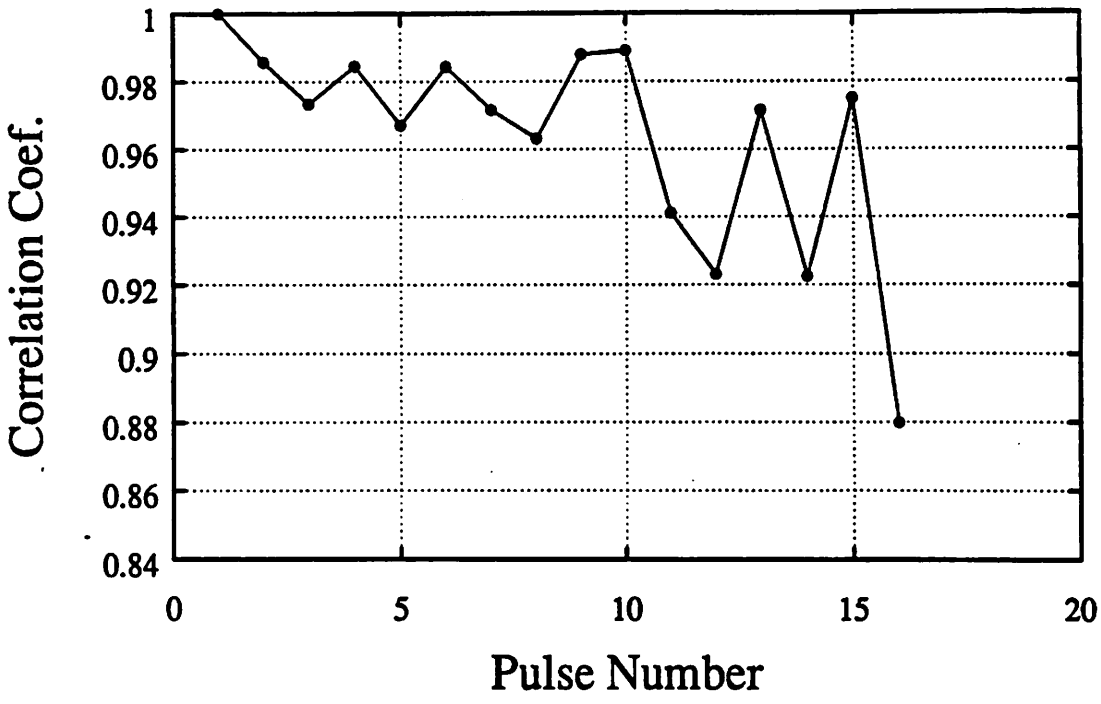

Fig. 14. Correlation coefficient between pulse number 1 and pulse N for N=1 to 16.

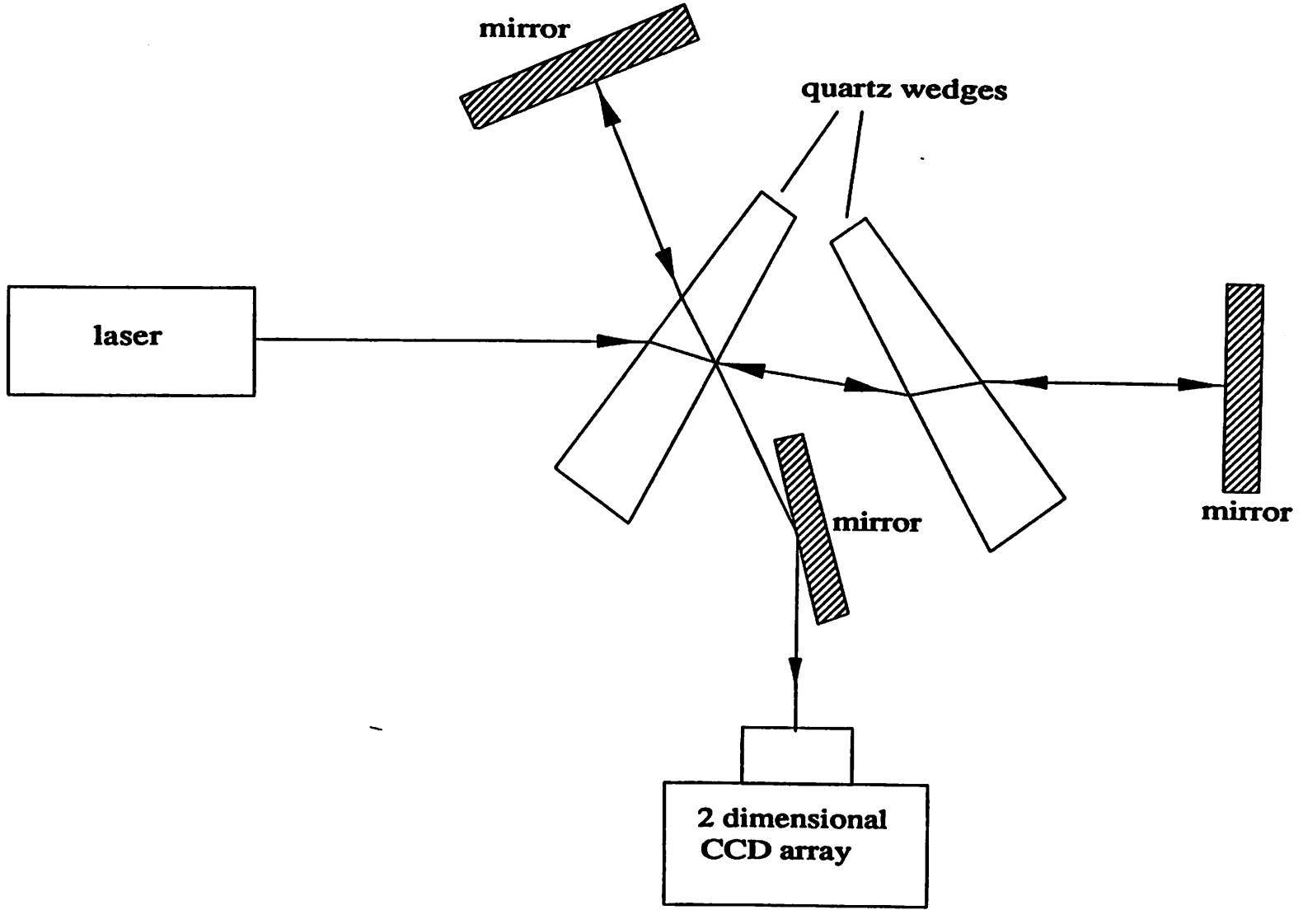

Fig. 15. Modified Michelson interferometer used to measure 213nm coherence length.

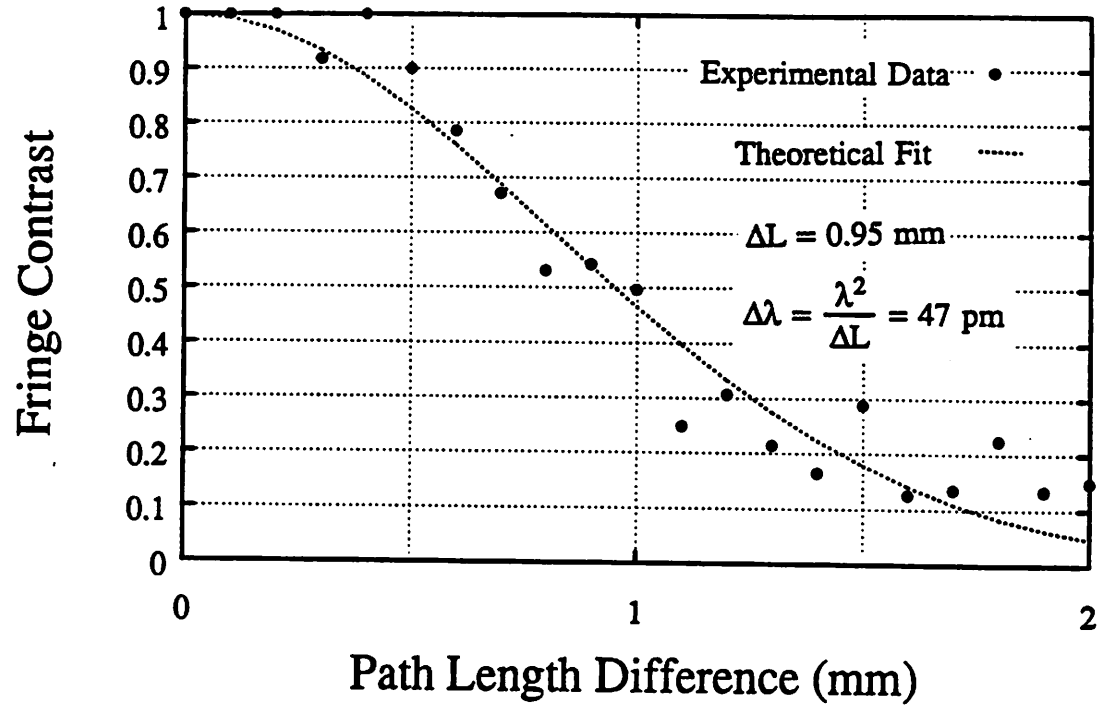

Fig. 16. Contrast vs. path length difference for 213nm radiation (seeder off).

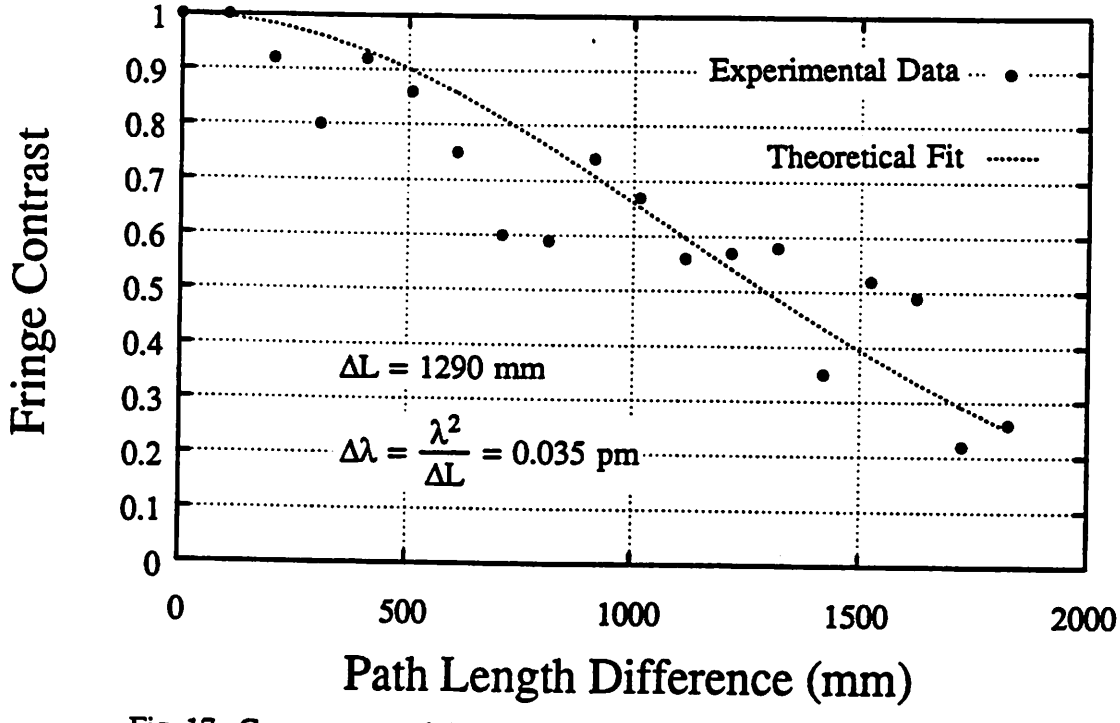

Fig. 17. Contrast vs. path length difference for 213nm radiation (seeder on).

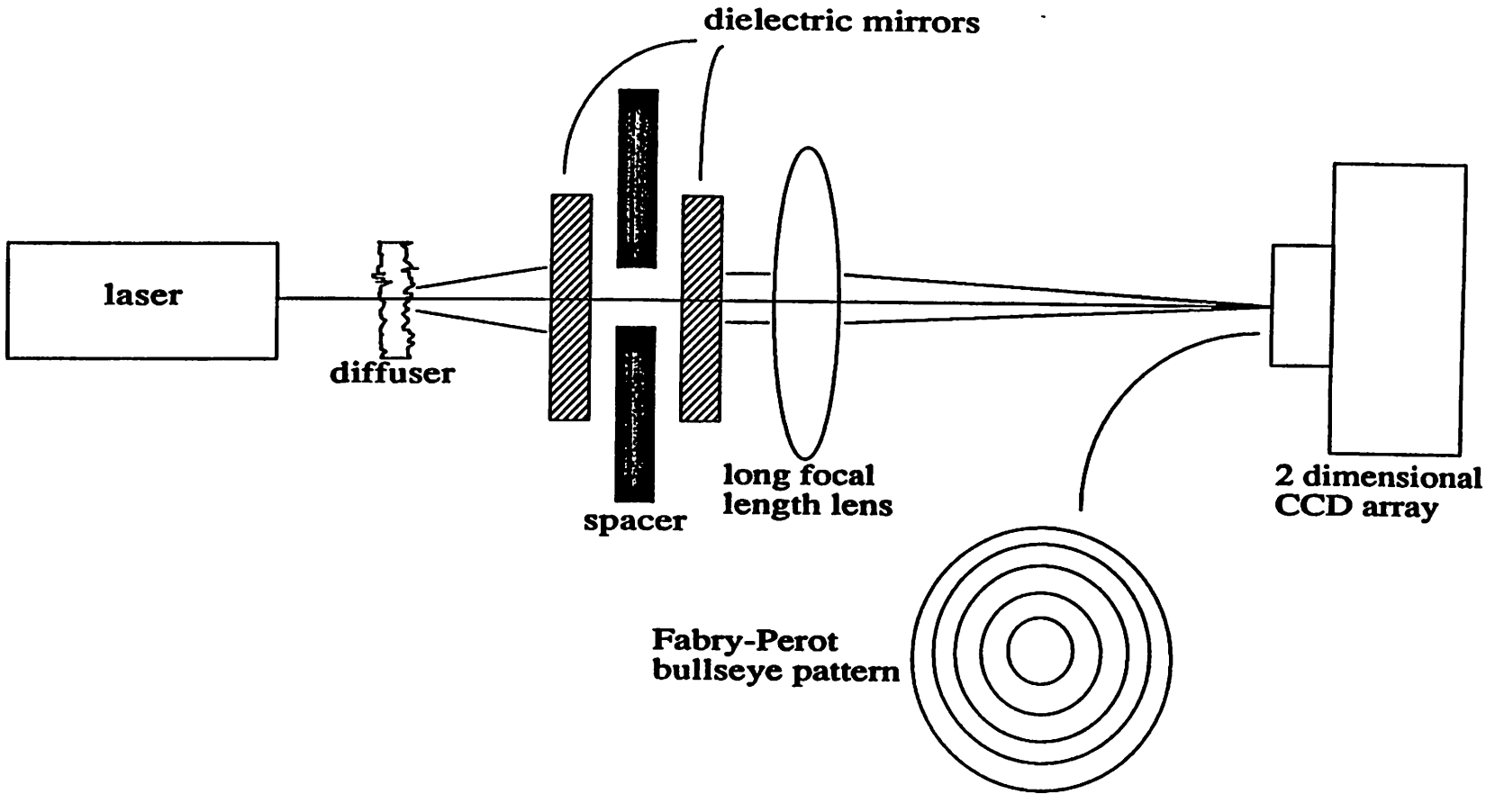

Fig. 18. Fabry-Perot interferometer used to measure 213nm linecenter shift.

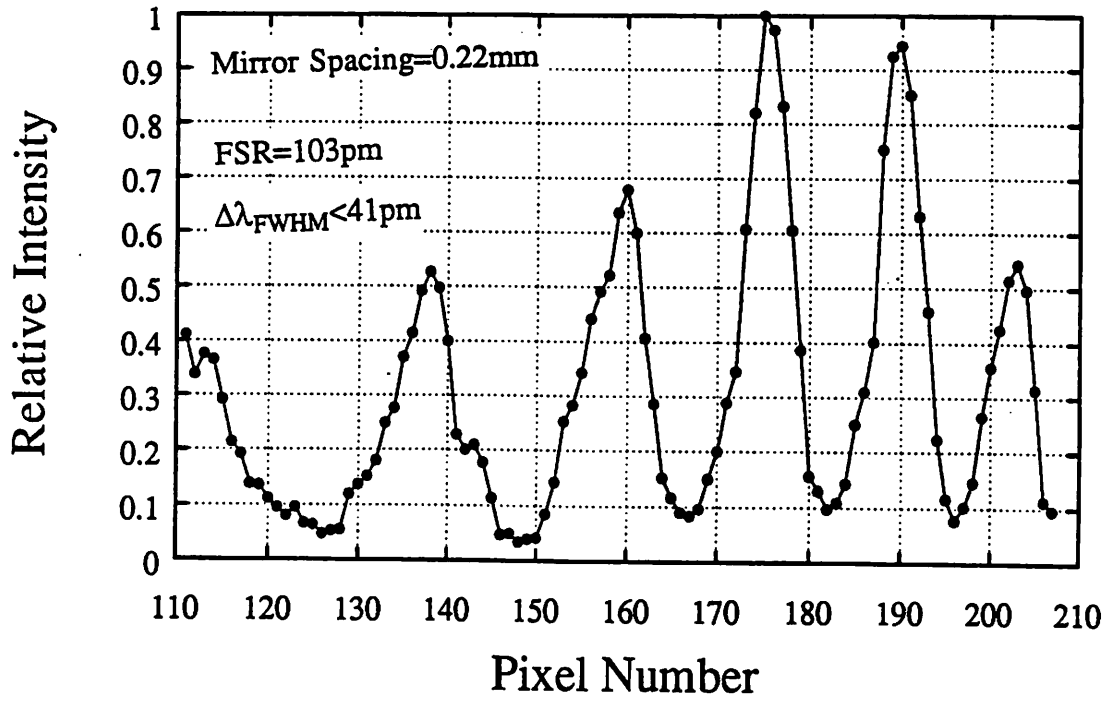

Fig. 19. Pabry-Perot interferometer measurement for 16 pulses of 213nm radiation (seeder off).

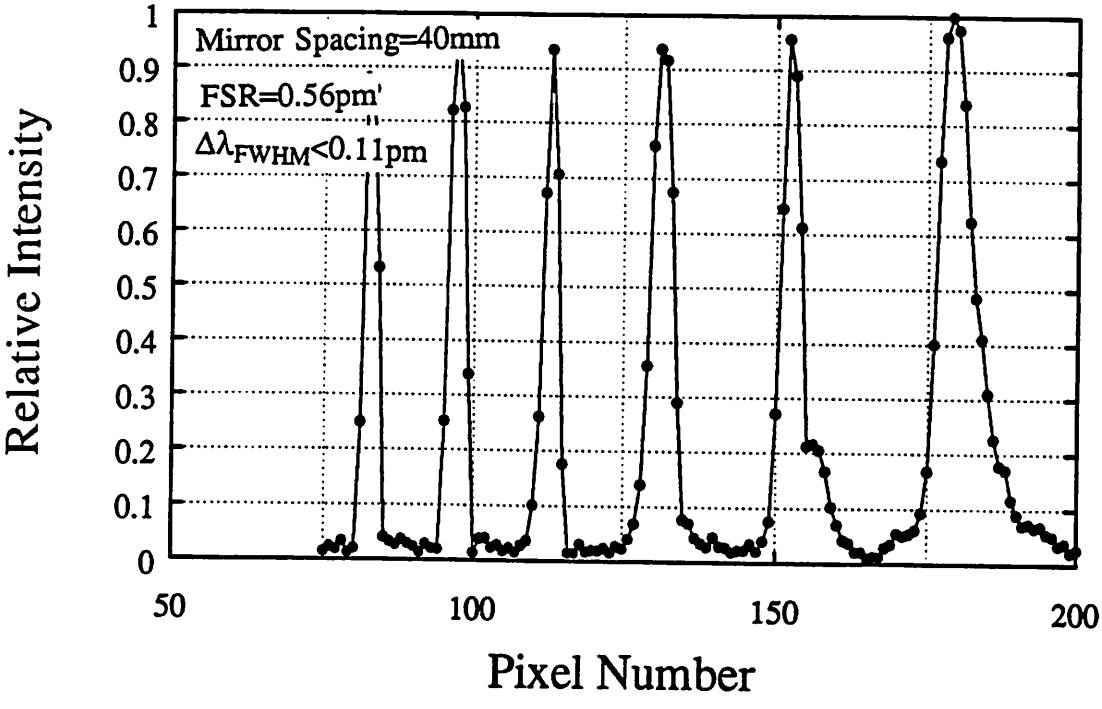

Fig. 20. Pabry-Perot interferometer measurement for 16 pulses of 213nm radiation (seeder on).

Chapter 5
Speckle Reduction via Multiple Rotating Diffusers

Abstract- A simple model for the scattering of coherent light through diffusers has been applied to a moving diffuser "despeckler" to estimate the scattering angles, speckle decorrelation length, and the interaction between multiple diffusers. A Gaussian model for the diffuser thickness variations has been used to derive a relation between the scattering cone of a diffuser and its decorrelation properties. This model is equivalent to a randomized array of lenslets. The lenslet's thickness and diameter correspond to the characteristic heights and widths of the diffuser roughness. This model predicts that a decrease in the decorrelation distance for two closely spaced counter-rotating diffusers is accompanied by an increase in their scattering cone. Simulation and experimental measurements have been used to verify the predictions of this model. Significant speckle decorrelation has been demonstrated for a nanosecond pulsed laser source using moderate diffuser rotation speeds.

5.1 Introduction

It is well known that the speckle related intensity fluctuations in the scattered beams of highly coherent sources may be mitigated by rotating one or more diffusers and averaging the speckle.[1,2] To investigate the required properties of such diffusers we have developed a model for the amount of speckle reduction produced by a single rotating diffuser and by two closely spaced counter-rotating diffusers. One key result obtained in this paper is the trade off between the speckle reduction properties of a diffuser and its scattering characteristics. The greater the speckle reduction, the greater the scattering angle and thus the less total energy collected by a given collection system. We show that with modest rotation speeds (10-30K RPM), counter rotating diffusers can achieve significant speckle averaging even within laser pulses as short as 4ns.

5.2 Diffuser Model

To simplify the analysis of the speckle created by a laser illuminated diffuser we will assume that the speckle has the properties presented in many previous references.[3,4,5,6] The main assumption is that the speckle E-fields possess circular Gaussian statistical properties. This means that the magnitude of the speckle E-field is Gaussian distributed with mean zero and the E-field phase is uniformly distributed over $[0 - 2\pi]$. This assumption leads to negative exponential distributed statistics for the speckle intensity, ($I = EE^*$). An important property of the negative exponential distribution is that its second moment is equal to the square of its first moment:

$$< I^2 > = < I >^2 . \tag{1}$$

A consequence of this property is that the variance of the intensity is equal to the square of the first moment:

$$\mathrm{VAR(I)} = < I >^2 . \tag{2}$$

The negative exponential distribution assumption has been verified for the speckle produced by the diffusers used in this paper. A histogram of the far-field speckle pattern, shown in Figs. 2 and 3, recorded by a two dimensional ccd array (Fig. 1) closely matches that of the negative exponential distribution. Also, Eqns. (1) and (2) have been verified by this measurement.

Ref[1] provides an attractive model for the properties of an ideal diffuser in which the thickness variations, $\delta(x)$, provide a random phase for the transmitted light. The ensemble average of the diffuser thickness variations is assumed Gaussian shaped with mean zero and variance δ_0^2:

$$< \delta(x) > = 0 \ \text{ and } < \delta(x)^2 > = \delta_0^2. \tag{3}$$

The second parameter of the model deals with the lateral autocorrelation of the thickness variations and is also assumed to be Gaussian shaped with e^{-1} width of σ:

$$< \delta(x_1)\delta(x_2) > = \delta_0^2 e^{-\left(\frac{x_1 - x_2}{\sigma}\right)^2}. \quad (4)$$

These parameter definitions are shown in Fig. 4.

5.3 Single Rotating Diffuser

The far-field diffraction pattern created by this ideal diffuser when illuminated by a coherent laser beam is given by the Fraunhofer diffraction formula (ignoring an unimportant phase factor):

$$E_{ff}(u) = \int_{\infty} E_{in}(x) e^{jk_{rel}\delta(x)} e^{-j\frac{k}{z}xu} dx. \quad (5)$$

Where $E_{in}(\cdot)$ is the incident E-field, $k = 2\pi/\lambda$, $k_{rel} = 2\pi(n_{diff} - 1)/\lambda$, x is the position variable at the diffuser, and u is the position variable in the far-field. These coordinate definitions are shown in Fig. 5. The phase shift introduced by the diffuser is defined by $k_{rel}\delta(\cdot)$ instead of $k\delta(\cdot)$ because rays that travel through air instead of diffuser also suffer a phase delay. The factor k_{rel} accounts for the relative phase delay suffered during travel through the diffuser.

If the diffuser is moved a distance Δx, a new speckle pattern is produced. To find the statistics of the far-field intensity we calculate the cross correlation of the E-fields at two points in the far-field plane before and after a shift of the diffuser equal to Δx:

$$< E_{ff}(u_1)E'^{*}_{ff}(u_2) > = < \int_{\infty} E_{in}(x_1) e^{jk_{rel}\delta(x_1)} e^{-j\frac{k}{z}x_1u_1} dx_1 \int_{\infty} E^{*}_{in}(x_2) e^{-jk_{rel}\delta(x_2+\Delta x)} e^{j\frac{k}{z}x_2u_2} dx_2 > . \quad (6)$$

Where $E_{ff}(\cdot)$ is the unshifted E-field and $E'_{ff}(\cdot)$ is the E-field after the diffuser has been shifted. Exchanging the integration with the ensemble average gives:

$$< E_{ff}(u_1)E'^{*}_{ff}(u_2) > = \int_{\infty}\int_{\infty} E_{in}(x_1)E^{*}_{in}(x_2) < e^{jk_{rel}[\delta(x_1)-\delta(x_2+\Delta x)]} > e^{-j\frac{k}{z}[x_1u_1 - x_2u_2]} dx_1 dx_2. \quad (7)$$

By ref[1], the value inside the ensemble average can be approximated as:

$$< e^{jk_{rel}[\delta(x_1)-\delta(x_2+\Delta x)]} > \approx e^{-k_{rel}^2\left(\frac{\delta_0}{\sigma}\right)^2(x_1-x_2-\Delta x)^2}. \quad (8)$$

Substituting into Eqn. (7) gives:

$$< E_{ff}(u_1)E_{ff}^{'*}(u_2) > \approx \int_{\infty}\int_{\infty} E_{in}(x_1)E_{in}^{*}(x_2)e^{-k_{rel}^2\left(\frac{\delta_0}{\sigma}\right)^2(x_1-x_2-\Delta x)^2} e^{-j\frac{k}{z}[x_1u_1-x_2u_2]}dx_1dx_2. \quad (9)$$

Now defining $\Delta x_{21} = x_2 - x_1$ we obtain:

$$< E_{ff}(u_1)E_{ff}^{'*}(u_2) > \approx \int_{\infty} E_{in}(x_1)e^{-j\frac{k}{z}x_1(u_1-u_2)} \times$$

$$\int_{\infty} E_{in}^{*}(x_1+\Delta x_{21})e^{-k_{rel}^2\left(\frac{\delta_0}{\sigma}\right)^2(\Delta x_{21}-\Delta x)^2} e^{j\frac{k}{z}\Delta x_{21}u_2}d\Delta x_{21}dx_1. \quad (10)$$

The first exponential function inside the embedded integral has nonzero value only when $\Delta x_{21} \approx \Delta x$ and is much more narrow than $E_{in}^{*}(\cdot)$. At this point previous references approximate this exponential as a delta function and calculate the integral. This assumption is equivalent the diffuser scattering the incident radiation uniformly in all directions (2π steradians) and all information about the true scattering characteristics of the diffuser are lost. Instead, we assume that $E_{in}^{*}(\cdot)$ is constant in the narrow region where the first exponent is nonzero, take it outside the first integral and evaluate as $E_{in}^{*}(x_1+\Delta x)$. The inside integral can now be calculated giving:

$$< E_{ff}(u_1)E_{ff}^{'*}(u_2) > \approx \frac{\sqrt{\pi}}{k_{rel}\left(\frac{\delta_0}{\sigma}\right)}\exp\left(j\Delta x\frac{k}{z}u_2\right)\exp\left(-\left[\frac{1}{2}\frac{\left(\frac{k}{k_{rel}}\right)}{\left(\frac{\delta_0}{\sigma}\right)}\right]^2\left(\frac{u_2}{z}\right)^2\right)\times$$

$$\int_{\infty} E_{in}(x_1)E_{in}^{*}(x_1+\Delta x)e^{-j\frac{k}{z}x_1(u_1-u_2)}dx_1. \quad (11)$$

To evaluate the remaining integral some assumption about the form of the incident E-field is required. We will assume that the incident beam is Gaussian shaped with radius R_{beam}. If the diffuser shift, Δx, is much less the the radius of the illuminating laser beam, $E_{in}^{*}(x_1 + \Delta x)$ may be replaced with $E_{in}^{*}(x_1)$. This approximation holds for pulse durations below a few hundred nanoseconds, since only a few micrometers of translation can occur in such short times even with high diffuser rotation speeds. Since $E_{in}(\cdot)E_{in}^{*}(\cdot) = I_{in}(\cdot)$, the second integral can be calculated, giving:

$$< E_{ff}(u_1)E_{ff}^{*}(u_2) > \approx \frac{I_0 \pi R_{beam}}{k_{rel}\left(\frac{\delta_0}{\sigma}\right)} \exp\left(j\Delta x \frac{k}{z} u_2\right) \exp\left(-\left[\frac{1}{2}\frac{\left(\frac{k}{k_{rel}}\right)}{\left(\frac{\delta_0}{\sigma}\right)}\right]^2 \left(\frac{u_2}{z}\right)^2\right) \times$$

$$\exp\left(-\left[\frac{1}{2}\left(\frac{R_{beam}}{z}\right)k\right]^2 (u_1 - u_2)^2\right) \tag{12}$$

Eqn. (12) shows that the angular spread, $\left(\frac{u_2}{z}\right)$, of the diffracted energy depends on the parameters of the diffuser, while the autocorrelation of the diffracted E-field (the third exponential) depends on the width of the incident beam and the illuminating wavelength. Evaluating at $u_1 = u_2 = u$ and $\Delta x = 0$ gives the average diffracted intensity versus angle in the far-field created by a single diffuser:

$$< I_{ff}(u) > \approx \frac{I_0 \pi R_{beam}}{k_{rel}\left(\frac{\delta_0}{\sigma}\right)} \exp\left(-\left[\frac{1}{2}\frac{\left(\frac{1}{n_{diff} - 1}\right)}{\left(\frac{\delta_0}{\sigma}\right)}\right]^2 \left(\frac{u}{z}\right)^2\right) \tag{13}$$

Define θ_0 as the e^{-1} width of the diffracted energy, then:

$$\theta_0 = \frac{2\left(\frac{\delta_0}{\sigma}\right)}{\left(\frac{k}{k_{rel}}\right)} = 2\left(\frac{\delta_0}{\sigma}\right)(n_{diff} - 1). \tag{14}$$

Eqn. (14) shows that the spread of the diffracted beam does not depend on the wavelength of the laser. Just as with a simple thin lens, only a dispersion in the refractive index of the diffuser will cause a change of the angular spread with wavelength. Eqn. (14) may be interpreted as the divergence produced by a thin lens of thickness δ_0 and diameter 2σ. Such a lens would have a radius of curvature given by $\sigma^2/2\delta_0$ and therefore a focal length of $\sigma^2/2\delta_0(n-1)$. The angular divergence of a plane wave after passing through a thin lens is half the diameter divided by the focal length. Thus our diffuser model is equivalent to a random array of lenslets with average diameter 2σ and average focal length $\sigma^2/2\delta_0(n-1)$.

. Since it is the scattered intensity and not the E-fields that can be measured, we combine Eqn. (12) with a result from ref[3] which states that the cross correlation of two circular Gaussian distributed intensity fields is given by:

$$< I_{ff}(u_1)I'_{ff}(u_2) > = < I_{ff}(u_1) >< I'_{ff}(u_2) > + | < E_{ff}(u_1)E'^{*}_{ff}(u_2) > |^2. \tag{15}$$

The covariance of $I_{ff}(u_1)$ and $I'_{ff}(u_2)$ is then:

$$\mathrm{COVAR}(I_{ff}(u_1)I'_{ff}(u_2)) = | < E_{ff}(u_1)E'^{*}_{ff}(u_2) > |^2. \tag{16}$$

Substituting Eqn. (12) gives:

$$\mathrm{COVAR}(I_{ff}(u_1)I'_{ff}(u_2)) \approx \left[\frac{I_0 \pi R_{beam}}{k_{rel}\left(\frac{\delta_0}{\sigma}\right)}\right]^2 \exp\left(-2\left[\frac{1}{2}\frac{\left(\frac{k}{k_{rel}}\right)}{\left(\frac{\delta_0}{\sigma}\right)}\right]^2 \left(\frac{u_2}{z}\right)^2\right) \times$$

$$\exp\left(-2\left[\frac{1}{2}\left(\frac{R_{beam}}{z}\right)k\right]^2 (u_1 - u_2)^2\right), \tag{17}$$

which has no dependence on Δx. This result is valid only for diffuser shifts much less than the incident beam width. For shifts greater than the incident beam width, a new portion of the diffuser is illuminated resulting in a different speckle pattern. Our interest is in small diffuser shifts, and thus rotating a single diffuser has little or no effect on the speckle noise

created by a single laser pulse.

5.4 Two Counter Rotating Diffusers

The find the improvement gained from using two closely spaced diffusers we again calculate the cross correlation of the E-fields at two points in the far-field plane:

$$< E_{ff}(r_1)E^{*}_{ff}(r_2) > = \int_{\infty}\int_{\infty} < E_{diff2}(u_1)E^{*}_{diff2}(u_2) >< e^{jk_{rel}[\delta(u_1)-\delta(u_2+\Delta u)]} > \times$$

$$e^{-j\frac{k}{z}[u_1r_1-u_2r_2]}du_1du_2, \qquad (18)$$

where u is the position variable at the second diffuser, r is the position variable in the far-field, $E_{diff2}(\cdot)$ is E-field incident on the second diffuser, and Δu is the relative shift between the two diffusers. These coordinate definitions are shown in Fig. 6. For this case, the E-fields incident on the second diffuser are not deterministic and they must stay inside the ensemble average. These fields are independent of the diffuser thickness variation and thus the ensemble average of the product of the E-fields and diffuser thickness is equal to the product of their separate averages.

Previous references assume that the diffusers are intimately close together and their individual thicknesses can be added together and treated like a single diffuser. However, for practical arrangements, the diffuser separation must be about 1mm or greater, and the assumption of intimate contact is invalid. With a 1mm separation a single scattering center on the first diffuser scattering into a cone of 20 degrees(see Fig. 1) illuminates an area of the second diffuser about 350μm in diameter. Since there are several hundred scattering centers contained within 350μm of a typical diffuser the assumption of intimate contact is inappropriate.

The E-fields incident on the second diffuser are the result of scattering from the first diffuser. Since the second diffuser is close to the first, it is inside both the Fraunhofer and Fresnel regions. A rigorous calculation of the E-fields must be applied to find their ensemble

average. This can be avoided by noting that the form of Eqn. (12) for the ensemble average of two E-fields has an exponential factor proportional to the e^{-1} angle of the cone illuminating the measurement point. When this measurement point approaches the first diffuser (i.e. z becomes small), the cone illuminating the measurement point is no longer $\left(\frac{R_{beam}}{z}\right)$ as in Eqn. (12), but is now proportional to the scattering cone, θ_0. This condition is shown schematicly in Fig. 7. The magnitude of the ensemble average versus position also changes as the sample point approaches the first diffuser. The ensemble average no longer has the exponential shape proportional to $\left(\frac{\delta_0}{\sigma}\right)$ given in Eqn. (12), but is better approximated by the strength of the E-field incident on the first diffuser. Using these two approximations we can write the E-field ensemble average as:

$$< E_{diff2}(u_1)E^*_{diff2}(u_2) > \approx \gamma E_{in}(u_1)E^*_{in}(u_2)e^{-\left[\frac{1}{2}\alpha\theta_0 k\right]^2 (u_1-u_2)^2}, \tag{19}$$

where γ and α are proportionality constants. Substituting the definition of θ_0 from Eqn. (14) gives:

$$< E_{diff2}(u_1)E^*_{diff2}(u_2) > \approx \gamma E_{in}(u_1)E^*_{in}(u_2)e^{-\left[\alpha k_{rel}\left(\frac{\delta_0}{\sigma}\right)\right]^2 (u_1-u_2)^2}. \tag{20}$$

Finally, substituting Eqn. (20) into Eqn. (18) and again using Eqn. (8) gives:

$$< E_{ff}(r_1)E'^*_{ff}(r_2) > \approx \int_{\infty}\int_{\infty} \gamma E_{in}(u_1)E^*_{in}(u_2)e^{-\left[\alpha^2 k_{rel}^2\left(\frac{\delta_0}{\sigma}\right)^2 (u_1-u_2)^2 + k_{rel}^2\left(\frac{\delta_0}{\sigma}\right)^2 (u_1-u_2-\Delta u)^2\right]} \times$$

$$e^{-j\frac{k}{z}[u_1 r_1 - u_2 r_2]} du_1 du_2. \tag{21}$$

Carrying out the integrations and placing in Eqn. (16) yields the final result:

$$\mathrm{COVAR}(I_{ff}(r_1)I'_{ff}(r_2)) \approx \left[\gamma \frac{I_0 \pi R_{beam}}{\sqrt{\alpha^2+1}\, k_{rel}\left(\frac{\delta_0}{\sigma}\right)}\right]^2 \exp\left(-2\left[\sqrt{\frac{\alpha^2}{\alpha^2+1}}\, k_{rel}\left(\frac{\delta_0}{\sigma}\right)\right]^2 \Delta u^2\right) \times$$

$$\exp\left(-2\left[\frac{1}{2}\frac{\left(\frac{k}{k_{rel}}\right)}{\sqrt{\alpha^2+1}\left(\frac{\delta_0}{\sigma}\right)}\right]^2 \left(\frac{r_2}{z}\right)^2\right) \exp\left(-2\left[\frac{1}{2}\left(\frac{R_{beam}}{z}\right)k\right]^2 (r_1 - r_2)^2\right). \qquad (22)$$

From this equation one can see that the angular spread of the doubly diffracted radiation (second exponential) has an e^{-1} width of $\sqrt{\alpha^2+1}\,\theta_0$, which is $\sqrt{\alpha^2+1}$ times that of the single diffuser case. The amount of diffuser shift (Δu) necessary to reduce the covariance by e^{-1} is given by the first exponential in Eqn. (22). This shift distance, defined as ρ_0, is given by:

$$\rho_0 = \frac{\lambda \sqrt{\frac{\alpha^2+1}{2\alpha^2}}}{\pi \theta_0}. \qquad (23)$$

5.5 Noise Reduction for a Single Laser Pulse

In all the previous analysis the variance calculations have been made assuming a single instant in time. To take these results and apply them to the case of a finite duration laser pulse and a continuously moving diffuser, we can make use of a result from statistics:

$$\mathrm{VAR}\left(\int_{\infty} I_{ff}(t)dt\right) = \int_{\infty}\int_{\infty} \mathrm{COVAR}(I_{ff}(t_1)I_{ff}(t_2))dt_1 dt_2, \qquad (24)$$

where in our case the covariance is equal to:

$$\mathrm{COVAR}(I_{ff}(t_1)I_{ff}(t_2)) = \sqrt{< I_{ff}(t_1) >^2 < I_{ff}(t_2) >^2}\, e^{-\left(\frac{1}{\rho_0}\right)^2 [v(t_1 - t_2)]^2}, \qquad (25)$$

where v is the diffuser velocity. Assuming a Gaussian shaped pulse in time, the function

$< I_{ff}(t) >$ can be written:

$$< I_{ff}(t) > = < I_{ff}(0) > e^{-\left(\frac{1}{\tau_{pulse}}\right)^2 t^2}. \tag{26}$$

Combining Eqns. (24)-(26) and calculating the integral gives:

$$VAR\left(\int_{\infty} I_{ff}(t)dt\right) = < I_{ff}(0) >^2 \pi\tau_{pulse}^2 \left[\frac{\left(\frac{\rho_0}{v}\right)}{\sqrt{\left(\frac{\rho_0}{v}\right)^2 + \tau_{pulse}^2}}\right]. \tag{27}$$

Taking the square root of Eqn. (27) and dividing by $< I_{ff}(0) > \sqrt{\pi}\tau_{pulse}$ gives the normalized RMS noise of the far-field speckle pattern for a single laser pulse:

$$RMS_{norm} = \left(1 + \tau_{pulse}^2 \left(\frac{v}{\rho_0}\right)^2\right)^{\frac{1}{4}}. \tag{28}$$

If the diffuser velocity is small ($v \approx 0$) this equation approaches $RMS_{norm} = 1$ as it should for a stationary diffuser and a single laser pulse. If the pulse duration becomes large compared to $\left(\frac{\rho_0}{v}\right)$ this equation becomes proportional to $\frac{1}{\sqrt{\tau_{pulse}}}$. This result is consistent with ref[6]. In our application $\left(\frac{\rho_0}{v}\right)$ and τ_{pulse} are of the same order.

5.6 Simulation

To find a value for the parameter α used as the proportionality constant in the near-field ensemble average estimate, we wrote a computer simulation that solves the full Huygens-Fresnel diffraction formula for the E-field scattering form the first diffuser onto the second:[7]

$$E_{diff2}(u) = \int_{\infty} E_{in}(x) \frac{1}{j\lambda} \frac{e^{jkr_{01}}}{r_{01}} \cos(\bar{n}, \bar{r}_{01})dx. \tag{29}$$

In this formula, $\bar{n}$ is the normal to the first diffuser surface at the source point and $\bar{r}_{01}$ is the

vector from the source point to the sample point (see Fig. 8.). The FORTRAN code used to calculate the E-field is as follows:

```
      do 20 i=-numpix,numpix
            eir=zero
            eii=zero
            x2=real(i)*delx2
            x1=real(-numpix)*delx1
            do 10 i2=-numpix,numpix
                  r=(x2-x1)
                  r=r*r
                  r=r+zdiff2
                  cosnr=zdiff/r
                  r=sqrt(r)
                  kr=k*r
                  coskr=cosnr*cos(kr)
                  eir=eir+eor(i2)*coskr
                  eii=eii+eoi(i2)*coskr
                  sinkr=cosnr*sin(kr)
                  eir=eir-eoi(i2)*sinkr
                  eii=eii+eor(i2)*sinkr
                  x1=c1+delx1
10          continue
            ei(i)=cmplx(eii/lambda,-eir/lambda)
20          continue
```

The difficulty with running this code is that the computation time for the above routine grows as the square of the number of points used in the simulation. This N^2 growth makes it impractical to run this simulation for many cases because the computation time for each case is several hours. To simulate our diffusers with proper resolution we had to use 65,536 points to describe the diffuser surface. Even with optimized code, the program took 16 hours on an IBM RISC system/6000 to calculate the far-field intensity.

After simulating various wavelengths and diffuser parameters, the predicted scattering angle was found to be twice as wide for two diffusers as it was for one diffuser. This would give a value for α of $\sqrt{3}$ in Eqn. (22). Using this value of α in Eqn. (20) gives an e^{-1} width for the E-field ensemble average at the second diffuser of $0.37\frac{\lambda}{\theta_0}$, where θ_0 is in radians. This is similar in form to the Rayleigh resolution criteria.[8] The Rayleigh criteria states that the minimum resolvable feature is proportional to the illuminating wavelength and inversely

proportional to the cone of angles forming the illumination.

5.7 Experiment

To further verify the α parameter and the other predictions made by the analytical model, we fabricated several diffusers and measured their scattering properties under coherent illumination. The diffusers used in the experimental measurements were produced by grinding one side of a 100mm diameter quartz wafer with 10μm silicon-carbide grit. The scattering characteristics of these diffusers were measured at three wavelengths to confirm the wavelength predictions in the analytical model. The three laser wavelengths used were: 633nm (HeNe laser), 442nm (HeCd laser), and 213nm (quintupled Nd-YAG laser). The intensity versus angle measurements were made using a large area silicon photodiode with the diffuser illuminated by a chopped laser signal shown in Fig. 9. The output from the photodiode and the chopper reference signal were then combined by a lock-in amplifier. The large detector area of the photodiode performs a local spatial average, thus removing the fine structure of the speckle and leaving only the average change in intensity versus far-field angle.

The results for both simulation and experiment are shown in Figs. 10 and 11. Making a Gaussian fit to both the single diffuser and double diffuser case shows that the double diffuser scattering cone is twice as wide as the single diffuser. This experimental result agrees with the simulation result of the previous section. Also shown in Figs. 10 and 11 are the analytical results using this value for α. The Gaussian fit to the measurement made at 633nm for a single diffuser was used as the value for θ_0. All the other analytical plots were derived from this value and the equations in the previous sections.

To test the validity of Eqn. (22) for the amount of decorrelation with relative diffuser shift we mounted one diffuser on an interferometer stage and made static measurements of the speckle correlation versus diffuser translation. The far-field intensity measurement was

made by a photo-multiplier tube (PMT) mounted behind a 5μm diameter pinhole. The illuminating laser was again chopped and the PMT signal was combined with the chopper reference by a lock-in amplifier. The experimental setup is shown in Fig. 12. An important parameter in this setup was the spacing between the two diffusers. We attempted to keep the spacing less than 1mm, but this was difficult to measure. To make the measurements insensitive to the diffuser spacing, the laser beam was expanded to a 3mm radius. In this way the diffuser spacing was guaranteed to be much less than the laser beam radius as required by Eqn. (19).

Fig. 13 shows the results of these correlation measurements. The top two graphs show the experiment, simulation, and analytical results for 633nm and 442nm. The bottom graph shows only the simulation and analytical result for 213nm. We were unable to measure the quintupled Nd-YAG laser because its beam profile changed significantly from pulse to pulse. It was impossible to separate the decorrelation effects owing to a shift of the diffusers from those caused by the changing beam profile. Again the analytic plots shown on these graphs were derived using only the value for θ_0 from Fig. 10a and the results from Eqn. (22).

Fig. 13c shows that a promising amount of decorrelation can occur with a relative diffuser shift much less than a micrometer. To test the true effectiveness of this method, we mounted two diffusers on small DC motors, placed them face to face, rotated them counter to each other, and measured the far-field speckle noise created by a 4.2ns quintupled Nd-YAG laser pulse. The setup for this measurement is shown in Fig. 14. The relative diffuser velocity for a given rotation speed is simply:

$$v = 2(2\pi R_{disk})\frac{RPM}{60}, \tag{30}$$

where R_{disk} is the diffuser radius (50mm), RPM = rotations per minute, and the first factor of two is required because the diffusers are both rotating but in opposite directions. With our simple motors we were able to rotate the diffusers up to 15K RPM. Fig. 15 shows the results of this measurement along with the analytic prediction from Eqn. (28). Again, the diffuser

parameters used in Eqn. (28) were those derived from Fig. 10a. The analytic model predicts a 50% reduction in the far-field speckle noise for a rotation speed of 30K RPM using the diffusers fabricated for these experiments.

5.8 Conclusions

Eqn. (23) shows that there is a trade off between the scattering angle of the diffuser and the decorrelation shift distance. As one tries to decrease the shift distance by increasing the roughness of the diffusers, the diffusers scatter the laser energy into angles further from the optical axis. Thus there is an "optimum" diffuser, one that scatters the light into a cone just filling the pupil of the collection optics. Beyond this, one must trade efficiency for further reductions in the decorrelation distance. For the diffusers used in this paper, 86% of the energy was scattered inside a numerical aperture of 0.5 (+/-30 degrees). Rotating at 30K RPM these diffusers would reduce the single pulse speckle noise by 50% and reduce the required pulse count needed to produce 1% illumination uniformity from 10,000 to 2,500. If the θ_0 value of such diffusers could be increased by a factor of two, the amount of energy inside an NA=0.5 would be decreased to 58%, and the single pulse speckle noise would be 38% requiring only 1,400 pulses to produce 1% uniform illumination.

References

1. E. Shroder, "Elimination of Granulation in Laser Beam Projections by Means of Moving Diffusers," *Optics Comm.*, vol. 3, no. 1, pp. 68-72, March 1971.

2. S. Lowenthal and D. Joyeux, "Speckle Removal by a Slowly Moving Diffuser Associated with a Motionless Diffuser," *J. Opt. Soc. Am.*, vol. 61, no. 7, pp. 847-851, July 1971.

3. J.W. Goodman, "Statistical Properties of Laser Speckle Patterns," in *Laser Speckle and Related Phenomena*, ed. J.C. Dainty, pp. 9-75, Springer-Verlag, Berlin, 1975.

4. M.G. Miller, A.M. Schneiferman, and P.F. Kellen, "Second-order Statistics of Laser-Speckle Patterns," *J. Opt. Soc. Am.*, vol. 65, no. 7, pp. 779-785, July 1975.

5. K.A. O'Donnell, "Speckle Statistics of Doubly Scattered Light," *J. Opt. Soc. Am.*, vol. 72, no. 11, pp. 1459-1463, Nov. 1982.

6. N. George, "About Speckle," *SPIE Int. Conf. on Speckle*, vol. 556, pp. 8-27, Jan. 1985.

7. J.W. Goodman, in *Itroduction to Fourier Optics*, McGraw-Hill, New York, 1968.

8. M. Born and E. Wolf, in *Principles of Optics*, Pergamon Press, New York, 1959.

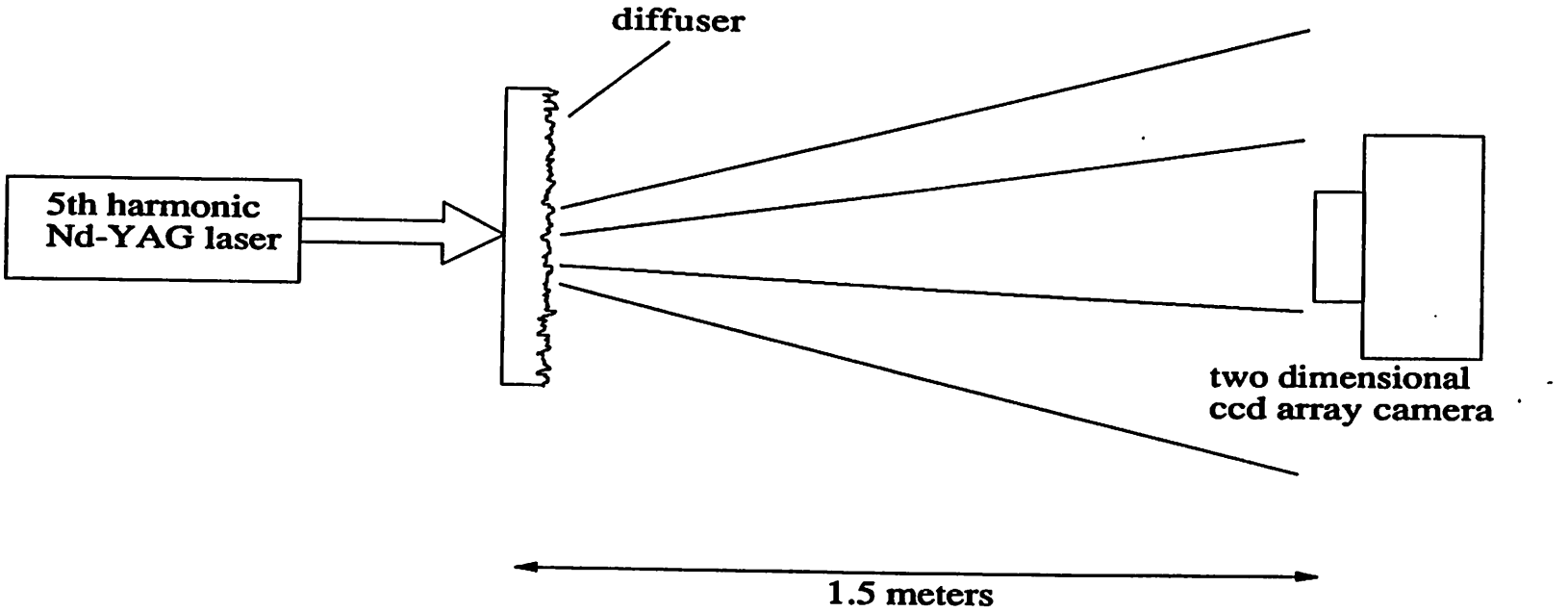

Fig. 1 Setup used to verify the negative exponential statistics of the far-field speckle.

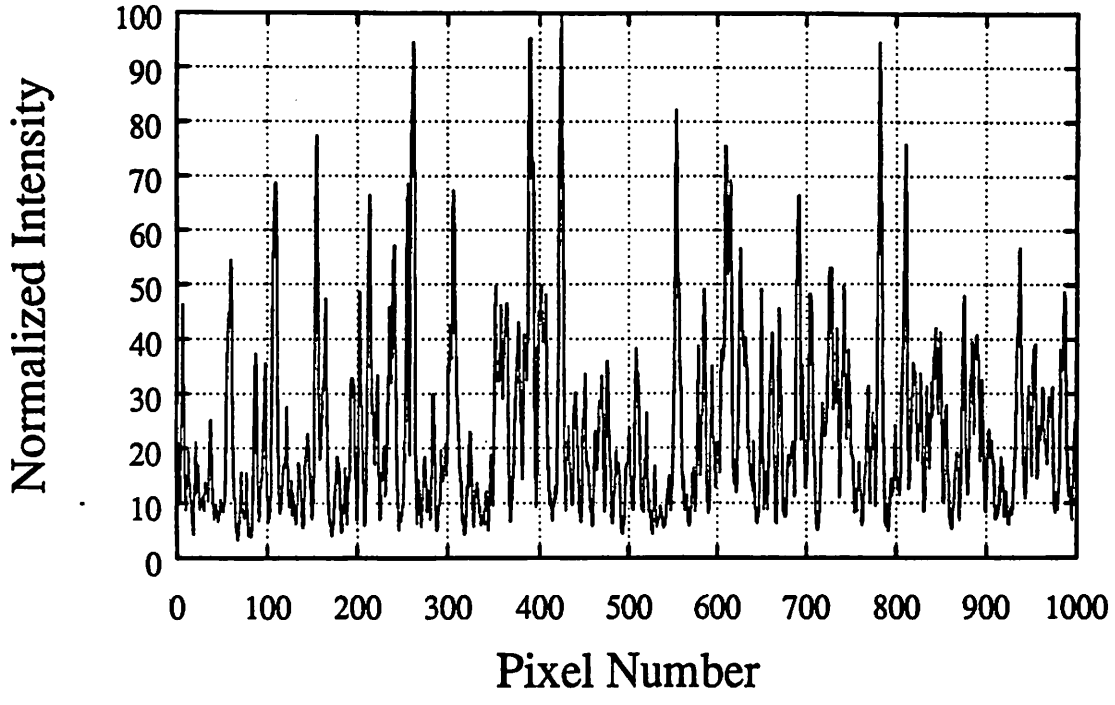

Fig. 2. Intensity vs. pixel number for far-field speckle measurement.

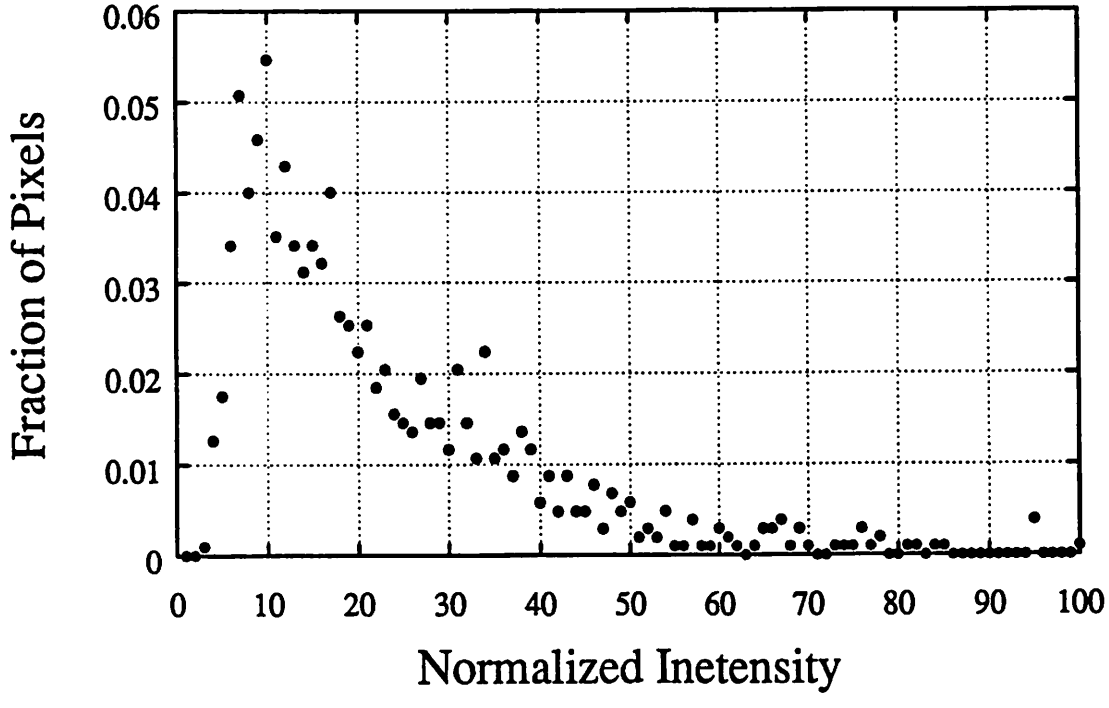

Fig. 3. Histogram of far-field speckle intensity from Fig. 2.

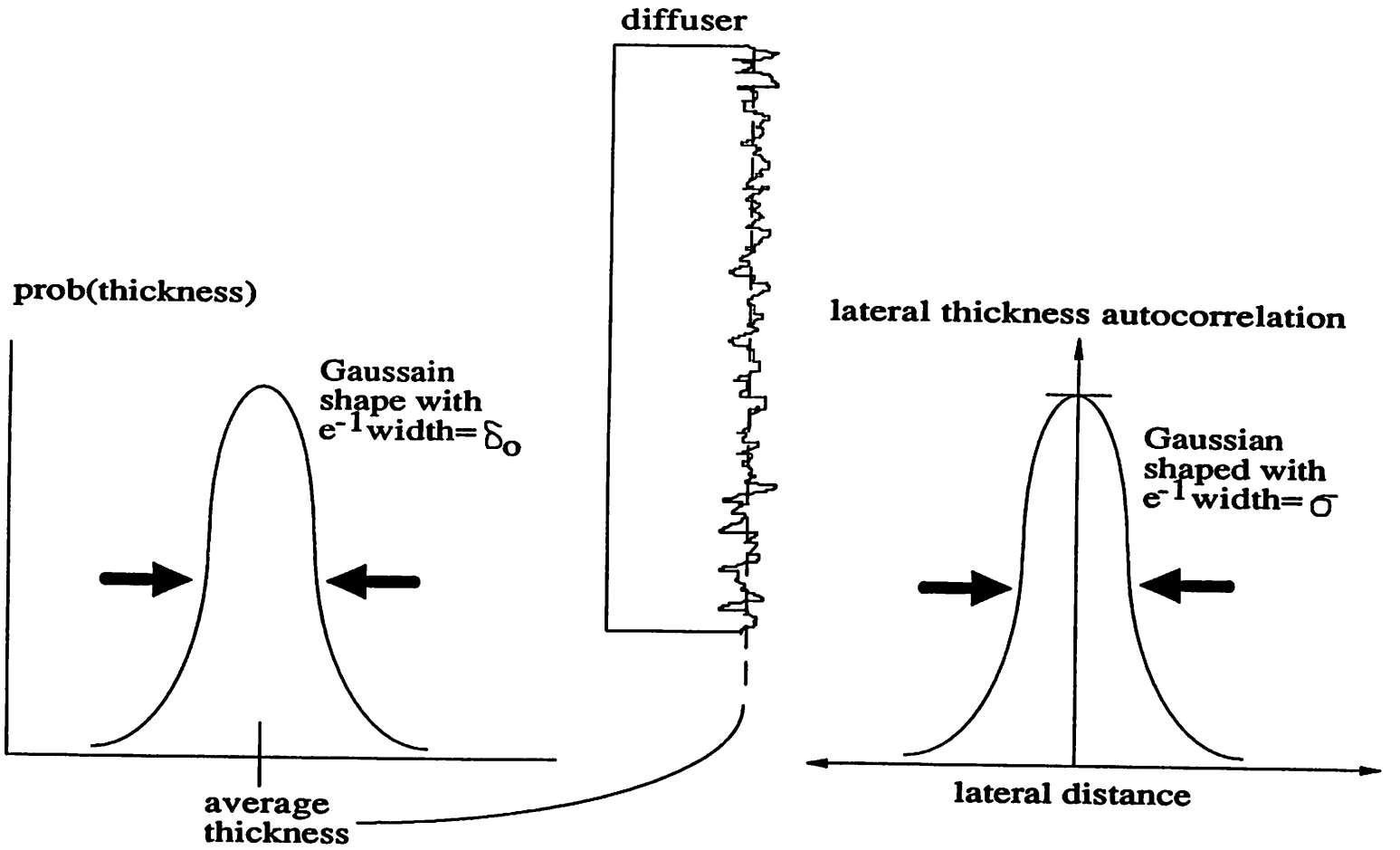

Fig. 4 Parameters used for diffuser thickness model.

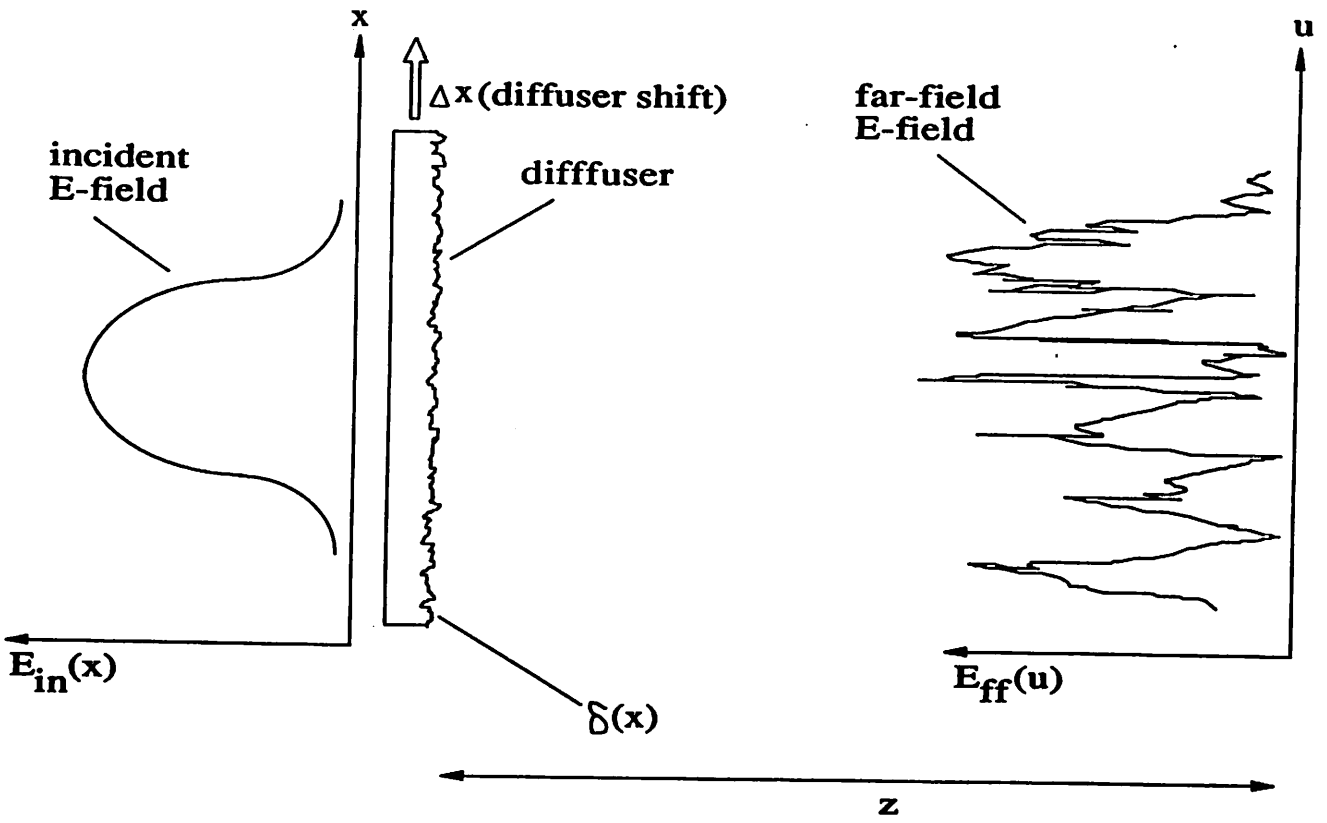

Fig. 5. Coordinate definitions for single rotating diffuser analysis.

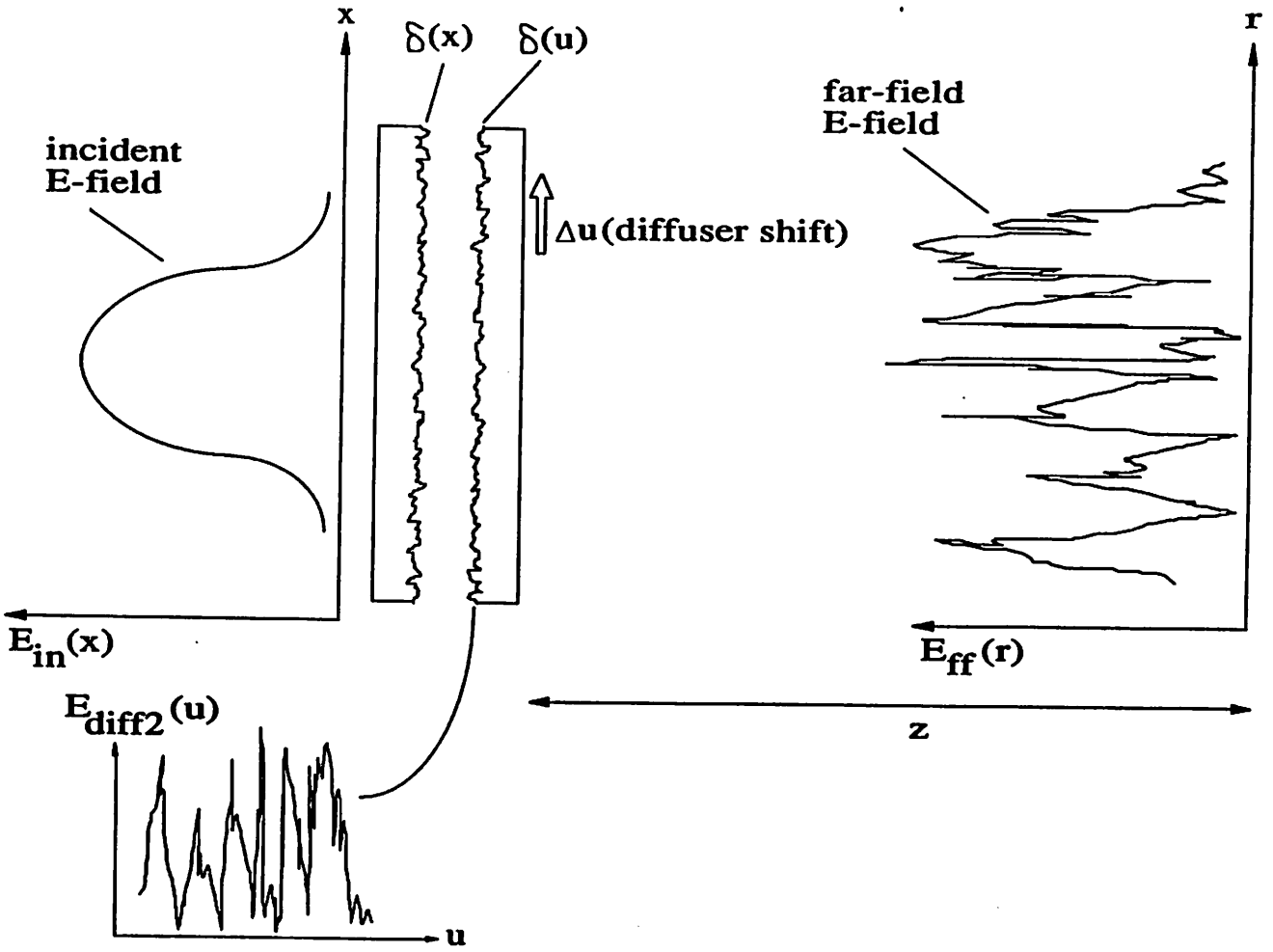

Fig. 6. Coordinate definitions for counter rotating diffuser analysis.

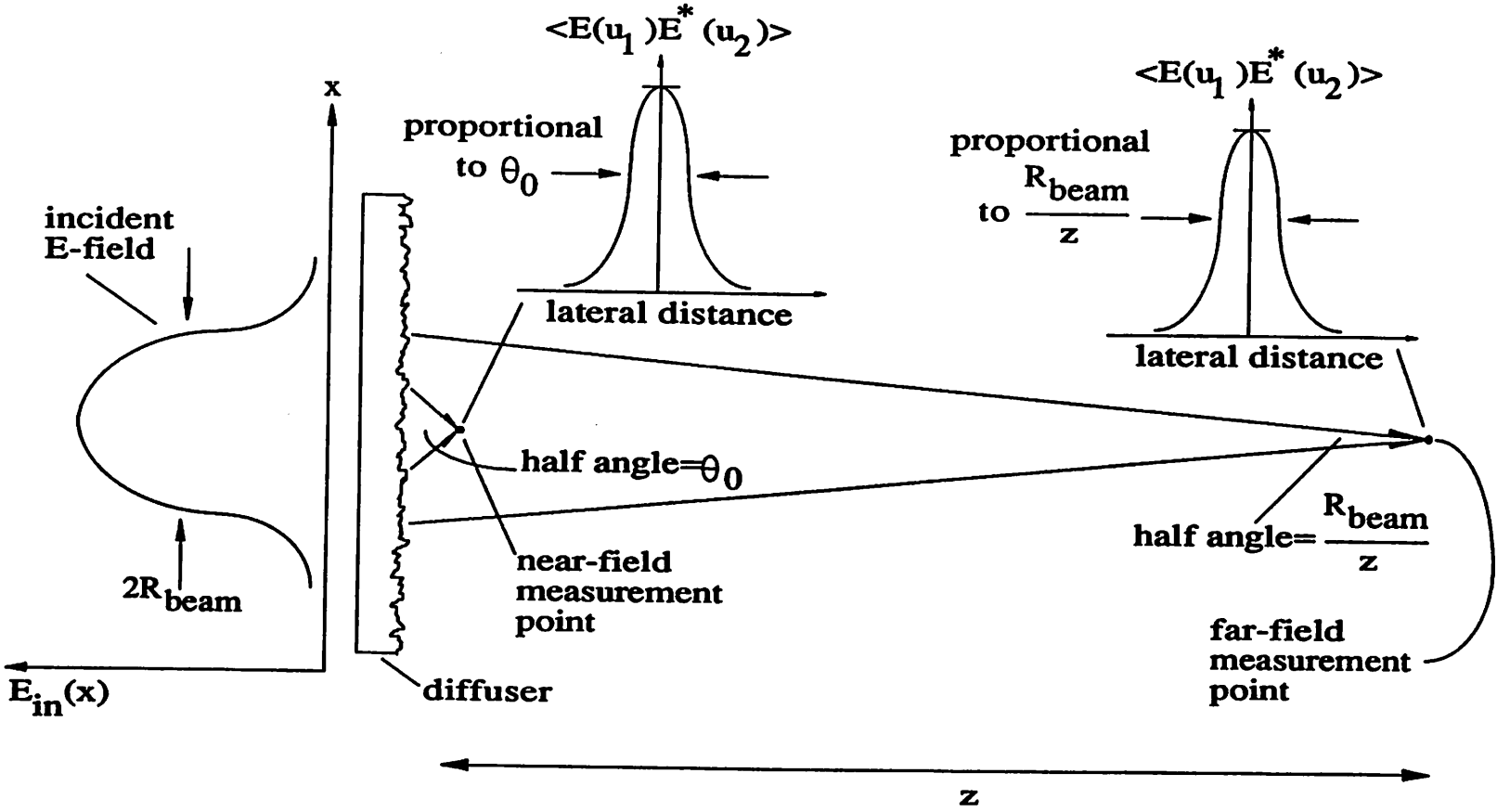

Fig. 7. Estimate for near-field ensemble average.

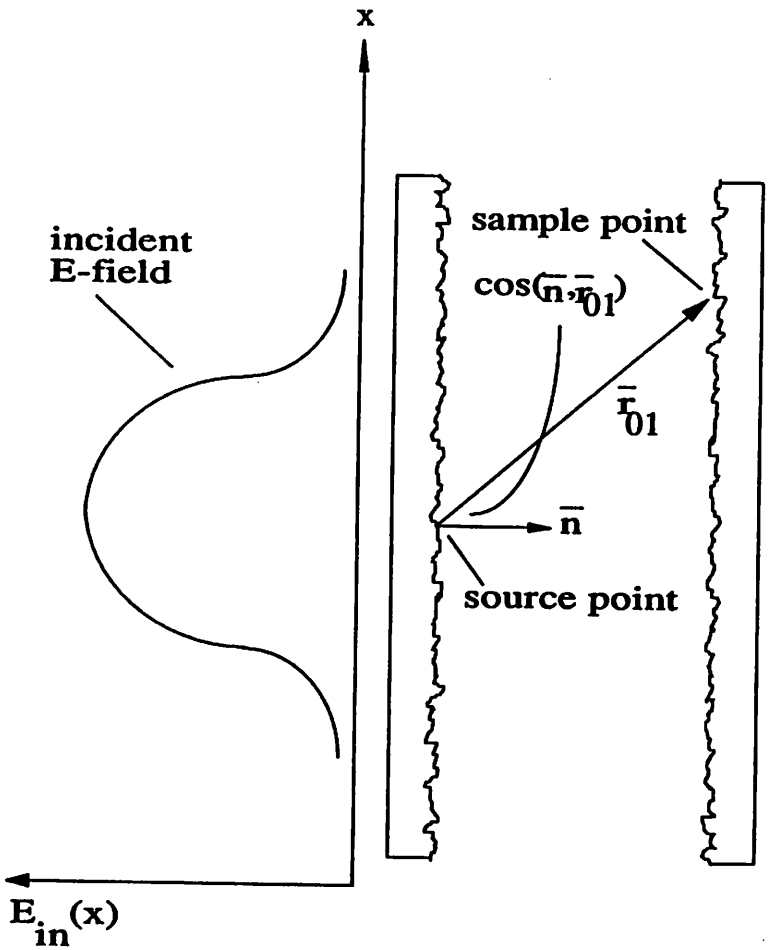

Fig. 8 Parameter definitions for Huygens-Fresnel diffraction formula.

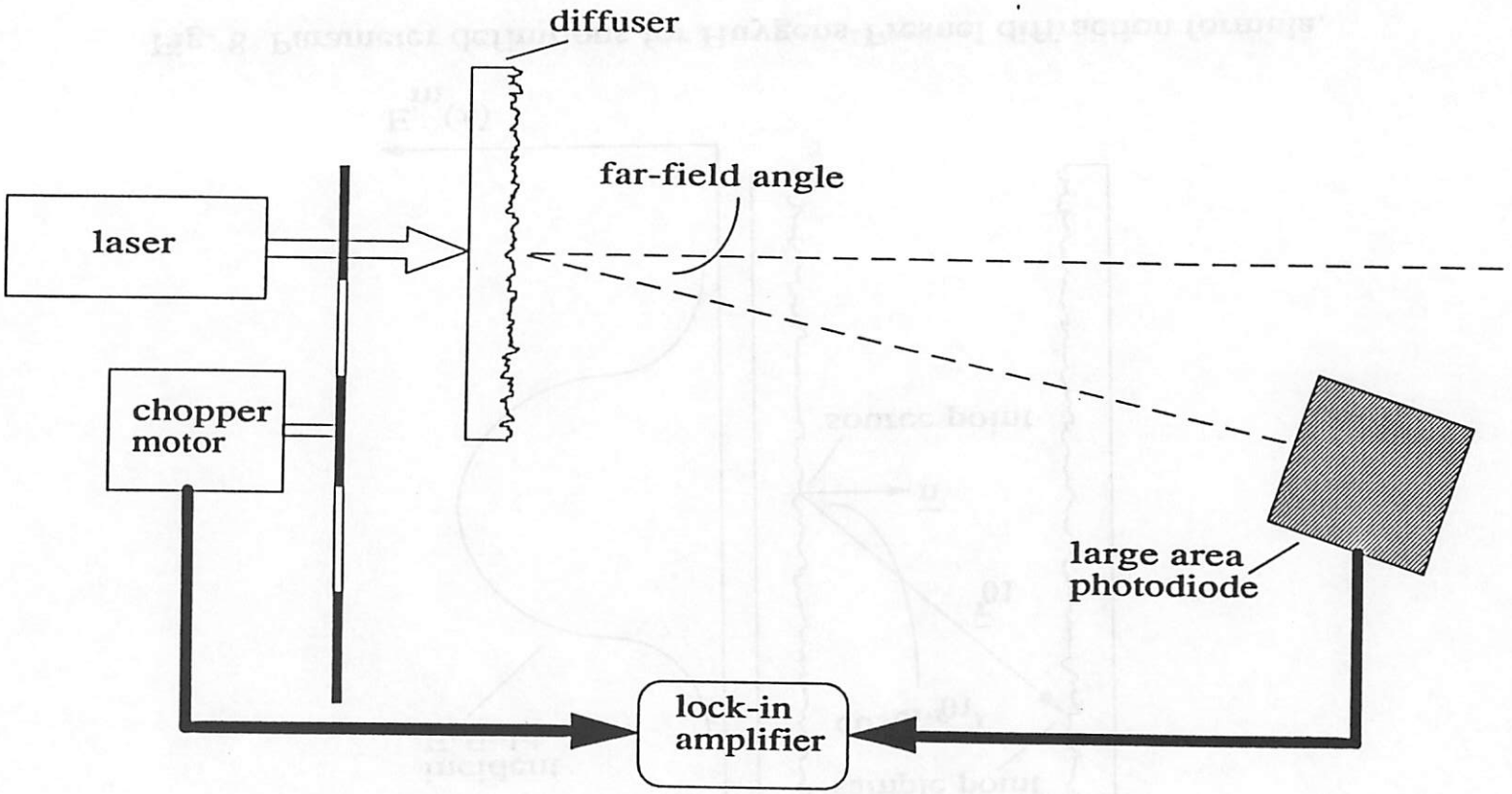

Fig. 9. Measurement setup for far-field scattering.

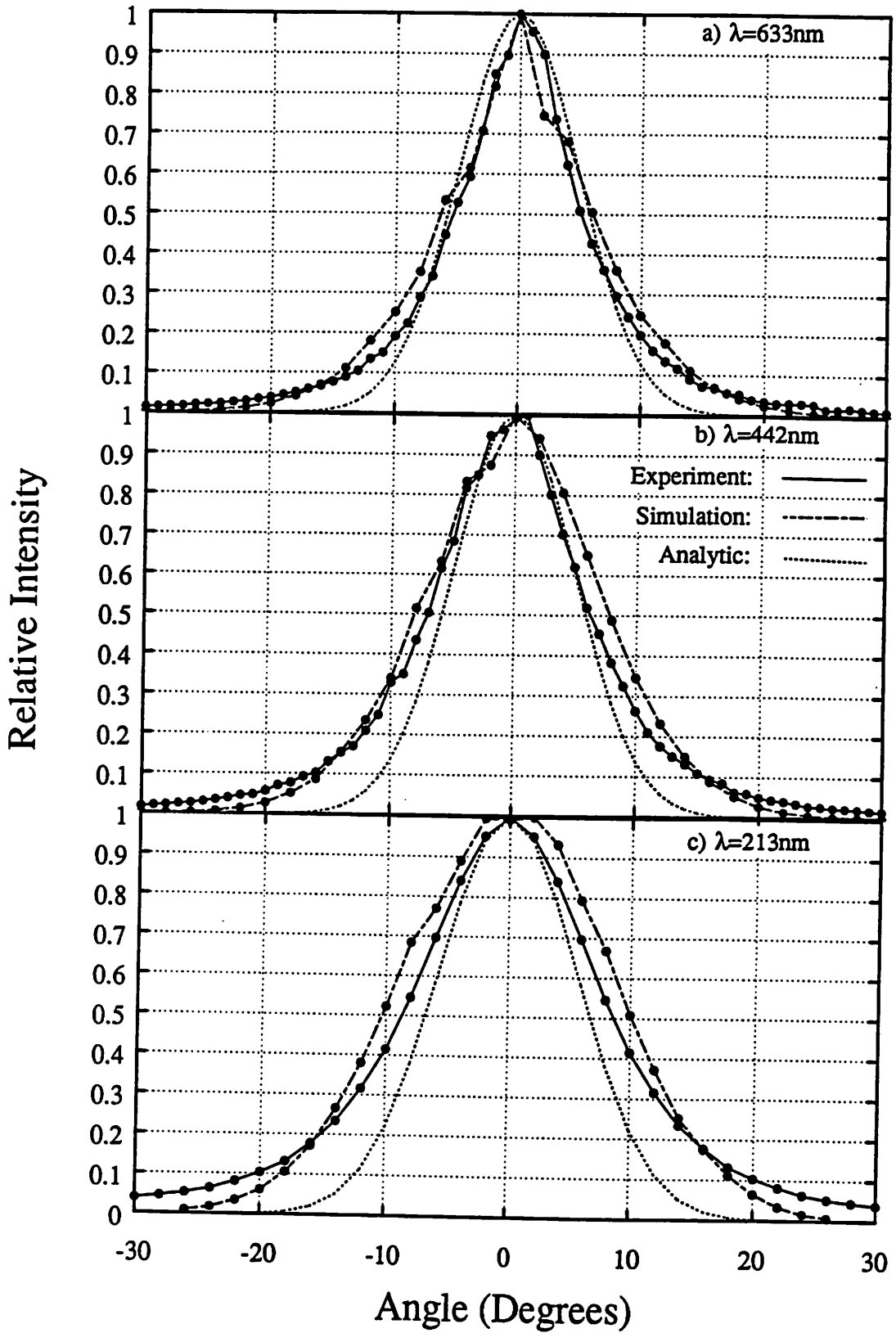

Fig. 10. Scattered Intensity vs. far-field angle for a single diffuser.

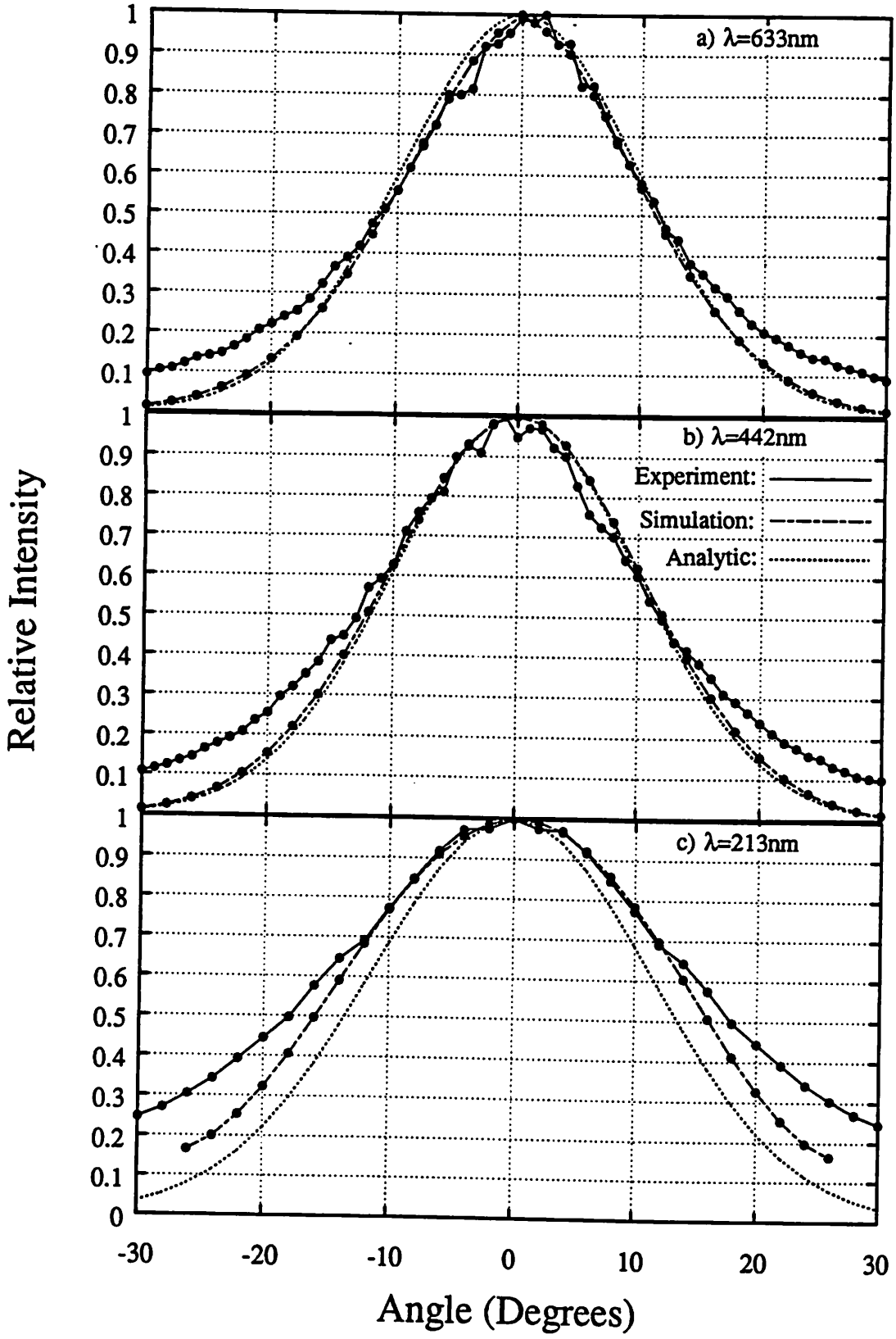

Fig. 11. Scattered Intensity vs. far-field angle for two closely spaced diffusers.

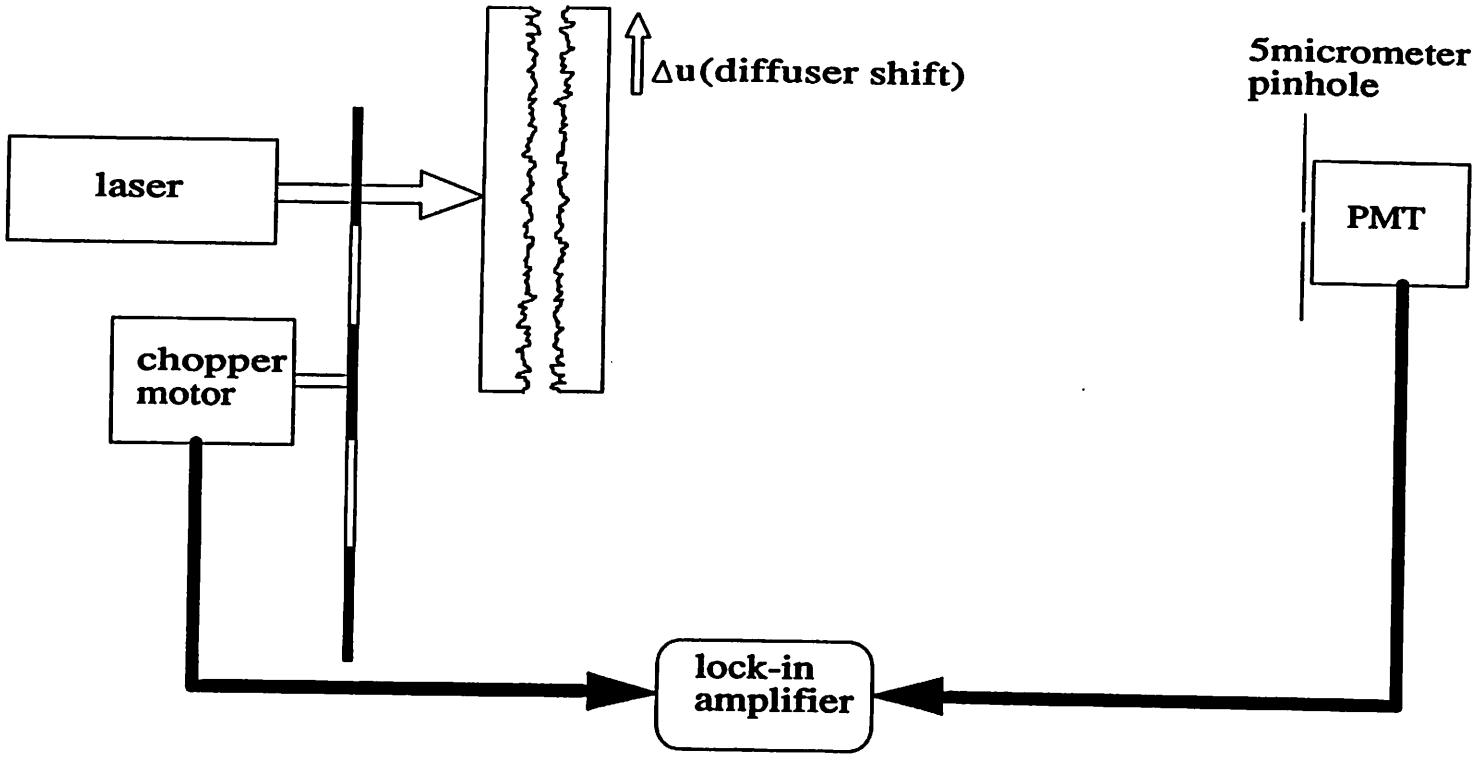

Fig. 12. Experiment to measure lateral decorrelation distance.

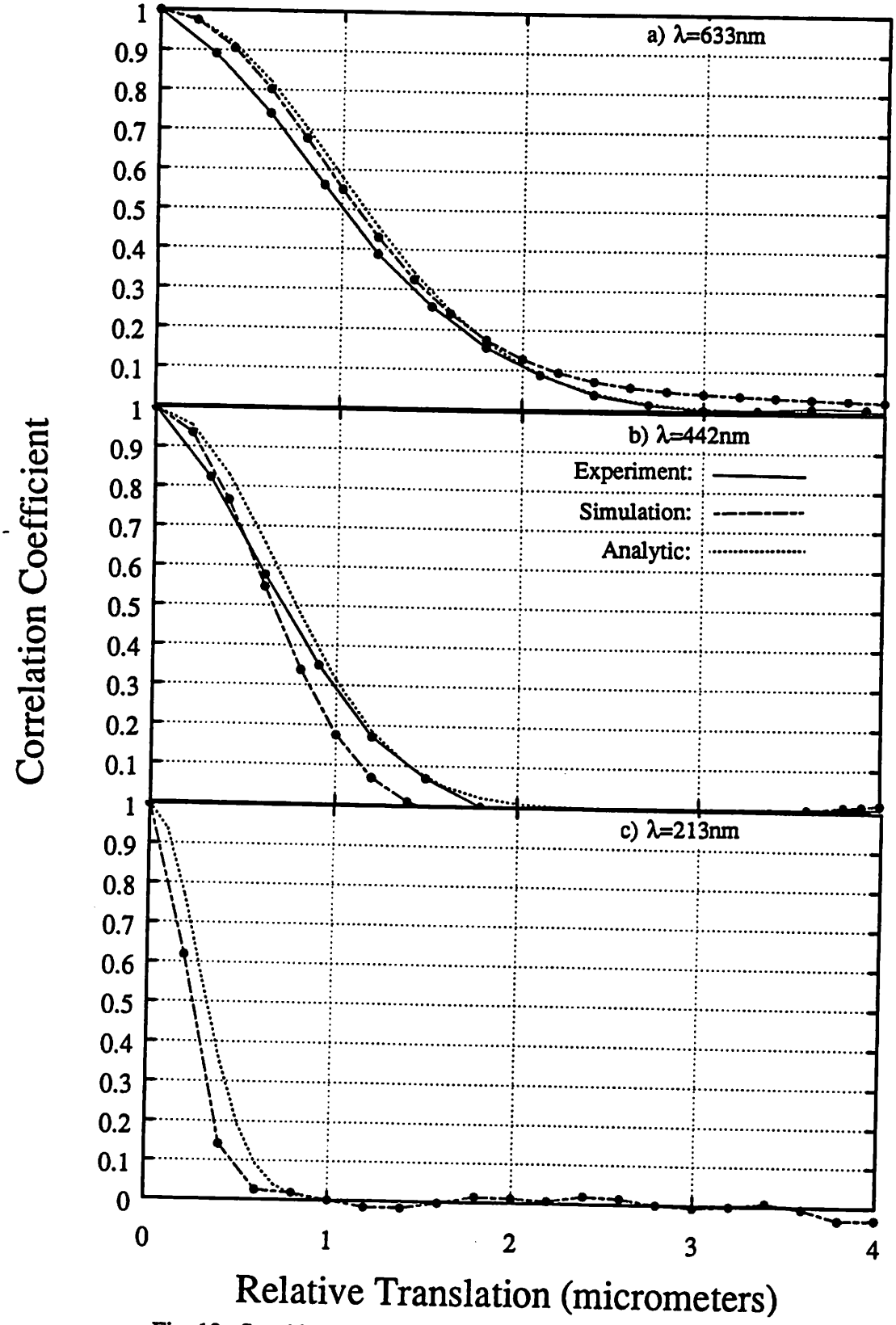

Fig. 13. Speckle correlation coefficient vs. relative diffuser translation.

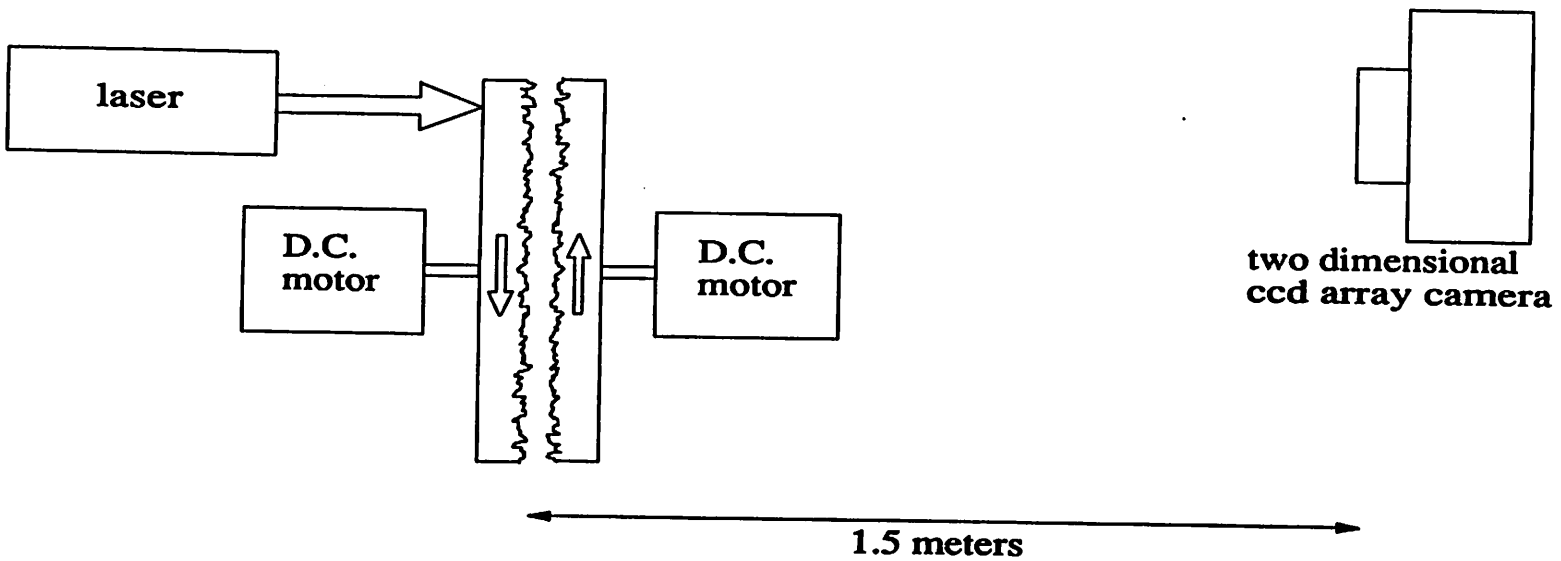

Fig. 14. Experimental setup to measure speckle contrast vs. rotation speed.

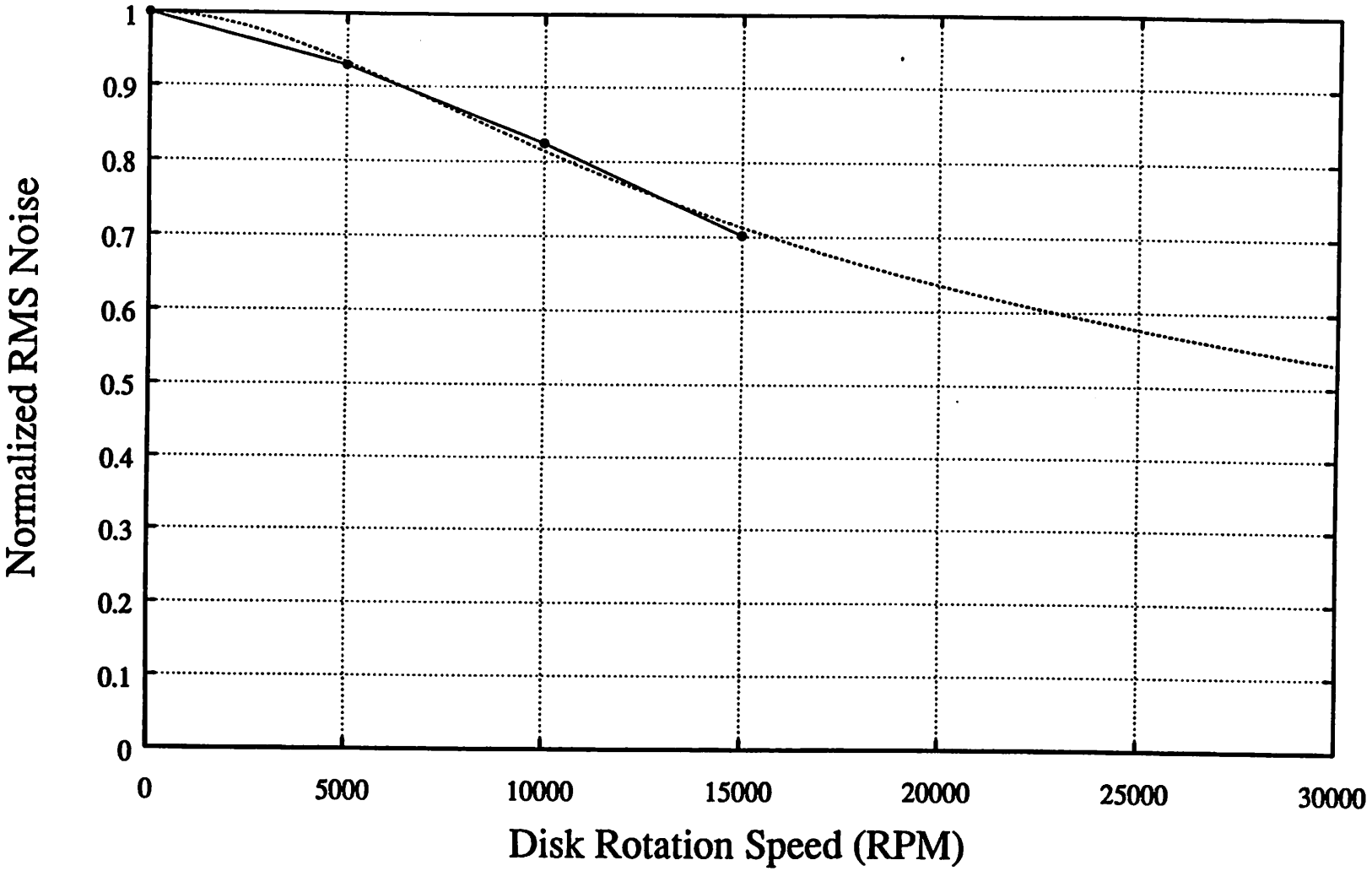

Fig. 15. Single pulse RMS speckle noise vs. diffuser rotation speed.

Chapter 6
Speckle Reduction via Multiple Pulse Generation

Abstract- A novel scheme has been developed to reduce the speckle contrast produced by highly coherent pulsed lasers. The scheme produces multiple sub-pulses from a single main pulse, each delayed by more than the coherence length. Since each sub-pulse is delayed by more than the coherence length they will not interfere when recombined by a diffuser or any other scattering optic. The contrast of the speckle pattern produced by illuminating a diffuser with these sub-pulses will be reduced by a factor of $1/\sqrt{(N)}$, where N is the number of sub-pulses. This multiple pulse generation scheme is compact, simple to fabricate, and exhibits high throughput.

6.1 Introduction

The most straightforward method of producing speckle free illumination from a highly coherent laser source such as the quintupled Nd-YAG laser is to move or rotate some element in the illumination system while integrating many pulses to form the total exposure. This same affect can be achieved by moving the incident laser beam across the diffuser.[1] For the laser scanning method to be affective, the scanning laser spot must be a small fraction of the total diffuser area. As the scattered laser energy is accumulated, the resulting integrated intensity has the same low speckle contrast properties as that from a diffuser illuminated by spatially incoherent light. For this scanning method to have any effect on the number of pulses needed from a pulsed laser source for uniform exposure, significant scanning motion must occur during each laser pulse. For the 4.2ns pulse duration of the quintupled Nd-YAG laser, this is a daunting prospect.

The equivalent of physically scanning the laser beam can be accomplished with no moving parts by splitting the original laser pulse into several sub-pulses, delaying each by an

amount equal to the pulse duration, and having each delayed sub-pulse illuminate a different portion of the diffuser. In this way, the diffuser is illuminated at different positions during different times, exactly as required by the the scanning spot method.

6.2 Previous Multiple Pulse Generation Schemes

The earliest published schemes to multiply the number of pulses from a laser source were designed for communication systems. The information carrying capacity of a communication system based on a pulsed light source is limited to a bit rate equal to the laser pulse rate. Most pulsed laser sources work at much less than 50% duty cycle and thus a significant increase in bandwidth can be achieved by filling the dead time between pulses. Though these pulse multiplication schemes were originally designed to increase pulse rates from hundreds of MHz to the GHz range used in communications systems, they still apply to the KHz pulse rates of today's lithography sources. Several examples are discussed below.

The system shown in Fig. 1 was first proposed by Rubinstein in 1969.[2] This system uses a birefringent material to split the incident laser beam into two equal parts, with one part propagating at an angle to the incident optical axis. On exiting from the birefringent material both beams are traveling parallel to the optic axis but are displaced in a direction transverse to the optic axis. Use of additional birefringent materials will further split these sub-pulses into still smaller fractions each displaced from each other.

After the desired number of pulses is produced, each spatially separated pulse is then directed down a delay line. Each delay is different in length resulting in a relative propagation delay between each sub-pulse. The pulses are then recombined by the inverse arrangement of birefringent elements. Since this system was originally designed for communications, Fig. 1 shows an optical modulator placed in each delay arm used to impress information onto each subpulse. For use in lithography, there would be no need for these modulators, leading to a more simple optical design.

The major disadvantage of this system is its reliance on large high quality birefringent materials. In the the deep-UV, and especially at 213nm, few birefringent materials are known that possess adequate transparency for use as a high throughput component. Calcite is one candidate for it has published transmission down to 213nm.[3] There is an issue of transmission lifetime for this material since there is measurable absorption at 213nm and the material would have to transmit several watts of 213nm power. Another possible material would be crystalline quartz, but its birefringence is weak. Use of a weakly birefringent material would require the use of large components to produce the required beam translation.

Another pulse multiplying system designed for use in communications was proposed by De Lange.[4] A schematic of this system is shown in Fig. 2. Like the Rubinstein system, the incident beam is split into two equal parts by the first optical component. In this system the splitting is performed by a beamsplitter coated to achieve 50% reflection and 50% transmission. One sub-pulse is then delayed by a pulse length and directed onto another 50% beamsplitter. At this second beamsplitter, both sub-pulses are split each into equal parts, creating four equal sub-pulses. These stages are then cascaded until the desired number of pulses are created. Each cascaded section must produce twice as much optical delay as the previous section to prevent overlapping of the newly created sub-pulses. The final section rotates the polarization of all the sub-pulses in one arm and then uses a polarization sensitive beamsplitter to recombine all the sub-pulses.

This system has advantages over the first in that it relies less heavily on special optical materials. Each beamsplitter is easily fabricated using dielectric stacks deposited on fused silica for high transmission at 213nm. The final polization rotator and beamsplitter would be a challenge to fabricate for 213nm but it is expected that such long life optics can be made available. The multiplication factor of each sub-unit in this system is two, that is there are twice as many pulses exiting each sub-unit as there are entering. The size of each sub-unit also grows geometrically since the time delay in each unit must be twice that of the previous. For any more than just a few cascaded stages the length of the later time delays can become

impractical. With our present 213nm laser system, the pulse length of 4.2ns would require the first stage to be 1.3 meters long, the second 2.6 meters and so on. Such large path delays, even with folding mirrors, can be difficult to construct.

A third example of a multiple pulse generator designed for communications was first proposed by Herriott.[5] This system is shown in Fig. 3. It consists of two concentric curved mirrors the first of which is fully reflecting while the second possess a graded reflecting-transmitting surface. As the laser beam bounces back and forth between the two mirrors, the partial transmittance of the second mirror allows a portion of the laser pulse to pass through and be reflected by a flat mirror. For our purposes, we can ignore the modulators placed in front of each flat mirror. Since our intention is for maximum transmission of each sub-pulse, these modulators would be absent in a lithographic version of this system. After reflecting off the flat mirrors, the sub-pulses than trace their way back along the same path between the two curved mirrors to finally exit through the aperture in the first mirror. A quarter-wave plate and Wollaston prism arrangement allow for extraction of the sub-pulses as they travel back toward the laser source.

There are two major disadvantages of this system for use as a high throughput multiple pulse generator. The first is the heavy reliance on the graded reflecting-transmitting mirror. This mirror would be difficult to fabricate for our 213nm wavelength and its nonoptimum characteristics would greatly reduce the performance of the system as a whole. The second and more fundamental drawback of this system is the unavoidable loss of energy incurred when each of the sub-pulses travels back through the graded reflecting-transmitting mirror. This energy loss will be severe. Since the graded mirror will have only a small transmission for light rays incident on each flat mirror, its transmission for the light rays retracing their path will also be low, leading to large energy losses.

An early multiple pulse generator specifically designed for speckle reduction was purposed by Scully.[6] The system, shown in Fig. 4., consists of two polarization sensative

beamsplitters and a delay path. The laser beam is made incident on the first beamsplitter such that its polarization is 45 degrees to the beamsplitter axis. The beamsplitter then separates the laser pulse into two equal parts, one of which is delayed by an amount equal to the pulse duration. The sub-pulses are then recombined by the second beamsplitter. Though the literature describing this system does not mention the possibility, cascading these components is possible by rotating the each successive beamsplitter pair by 45 degrees. The delay line in the following sections would also have to be doubled just as in the previously described systems.

This multiple pulse generation scheme is much the same in form and function as the system proposed by De Lange, so the same general drawbacks apply. The extensive use of the polarization sensitive beamsplitters is a additional level of fabrication difficulty. The need for a 45 degree rotation in the optics for each successive stage also adds to the difficulty in aligning a practical system.

A final multiple pulse generator example is shown in Fig. 5. This system was first proposed by by Taback.[7] The system consists of an integrating sphere coupled to optical fibers of various lengths. The laser source is made incident on the integrating sphere which, through multiple scattering events, produces equal illumination of each fiber. The fibers are fabricated in lengths that differ by a pulse duration thus producing the necessary optical delay.

This system has a simple arrangement and is straightforward to fabricate and align. Unfortunately, this system would be highly inefficient because of the material properties required for the fibers and the integrating sphere. The diffuse reflecting paint used inside the integrating sphere must have nearly 100% reflectivity, since the efficiency of integrating spheres decreases dramatically as the reflectivity of the inside surface decreases. Fig. 6 shows the relation between sphere efficiency and surface reflectivity using the theory developed by Geobel.[8] The throughput of an integrating sphere is given by:

$$\tau = \frac{f_e \rho}{1 - \rho(1 - f_j)}, \tag{1}$$

where f_e is the ratio of exit port area to total inside surface area, f_j is the ratio of both the exit and entrance port areas to the inside surface area, and ρ is the inside surface reflectivity. For the graph in Fig. 6 the entrance and exist ports were assumed equal and that they constitute 10% of the total sphere surface area. Currently available surface materials have a specified reflectivity of 92% at 250nm. At 213nm this value would be much less leading to a low throughput for any integrating sphere used for 213nm lithography.

The optical fibers used in this system also present challenging material requirements. The length of the fibers would have to be several pulse durations, 1.3 meters for present 213nm source. Though fused silica fibers are available, such long fiber lengths would result in high losses.

6.3 Novel Polarization and Delay Scheme

Fig. 7 shows the basic lay out for a single stage of a novel polarization and delay scheme. Each stage consists of one beamsplitter, one normal incidence mirror, and two 45 degree mirrors. All the mirrors are dielectric coated on their front surface for maximum reflection. The beamsplitter has one surface anti-reflection (AR) coated and the other surface coated for partial reflectance-transmittance. We will define the reflectance of the beamsplitter as R_s for the S-polarization and R_p for the P-polarization. Likewise for the transmittance: $(1 - R_s)$ for the S-polarization and $(1 - R_p)$ for the P-polarization.

The stage is aligned such that the laser source is incident with its energy in the P-polarized state. A fraction equal to R_p of the incident energy will be reflected by the beamsplitter while $(1 - R_p)$ will pass through the beamsplitter and then on to the 45 degree mirrors. The two 45 degree mirrors are arranged so that they translate the beam up and over, changing both its direction of travel as well as its polarization relative to its direction of

travel. This portion of the beam is then incident on the normal mirror, directing it back toward to beamsplitter.

After making a full traversal of the delay arm, the pulse encounters the beamsplitter again, but this time in the S-polarization state, and thus R_s will be reflected while $(1-R_s)$ will be transmitted and travel along the same path as the original reflected fraction. At this point there remains $(1-R_p)R_s$ of the original laser pulse energy inside the delay arm. This energy is again rotated by the two 45 degree mirrors and travels via the normal mirror back once again to the beamsplitter. The polarization has now returned to the P state and thus the beamsplitter will transmit $(1-R_p)$ of this energy.

Three individual pulses have now been created by this stage, two with P-polarization and one with S-polarization. Assuming zero losses inside the delay arm, these three pulses will have the following fractions of the original pulse energy:

$$\text{sub}-\text{pulse \#1 (P}-\text{polarized): } R_p$$

$$\text{sub}-\text{pulse \#2 (S}-\text{polarized): } (1-R_p)(1-R_s)$$

$$\text{sub}-\text{pulse \#3 (P}-\text{polarized): } (1-R_p)R_s(1-R_p).$$

Idealy we would like these three sub-pulses to be equal. Since there are three separate quantities and only two independent variables, R_p and R_s, we can only hope to minimize the difference between the three sub-pulses. Fig. 8 is a contour plot of the difference from the mean of the three sub-pulse intensities as the values of R_p and R_s range from zero to one. The minimum difference is obtained with a value of $R_p = 0.29$ and $R_s = 0.59$. Fig. 9 shows the laser pulse intensity versus time at the output of a single multiplier stage using $R_p = 0.29$ and $R_s = 0.59$. This intensity versus time plot was calculated using a recursive subroutine that is general enough to handle all the non-idealities of this system such as energy loss in the arm, misalignment of the mirrors, and imperfect beamsplitter properties. This pulse train is used as the input to the speckle calculation program described in chapter 5. The resulting

RMS speckle noise produced is 51%, down from 100% for a single pulse. This reduction in speckle contrast is equivalent to 3.8 individual pulses.

There is a technology issue involved in achieving such polarization dependent reflectivities from the beamsplitter. Traditional dielectric stack beamsplitters are fabricated using two dissimilar optical materials for the alternating layers. To achieve the desired reflectivities for both polarizations, a beamsplitter operating at 45 degrees may not be practical or even desirable. Though Fig. 7 shows the beamsplitter at a 45 degree angle to the incident beam, this system could be aligned at any angle of incidence. The only drawback would be the need for a larger clear aperture for the beamsplitter as it is used at higher angles of incidence.

Several beamsplitters that were purchased for other experiments had a specified reflectivity of 50% at 45 degrees for randomly polarized light. The actual measured reflectivities were $R_p = 0.24$ and $R_s = 0.76$. Fig. 10 shows the calculated sub-pulse heights using these values for R_p and R_s. There is considerable variation in the heights of each sub-pulse, but using this pulse train in the speckle calculation program produces a speckle noise of 58%, only 7% worse than that produced using the optimum beamsplitter.

Two verify this speckle reduction scheme experimentally, we fabricated a single stage of this polarization and delay scheme using the 213nm laser source. Since the pulse duration for our 213nm source is 4.2ns, the delay arm was made 4.5 feet long to introduce a delay of 4.5ns (speed of light $\approx$ 1 foot/ns). The normal incidence mirror was tilted slightly so that each sub-pulse exited the system at a slightly different angle. A lens was used to convert these differences in angle into differences in position by placing a diffuser at the back focal plane of the lens. In this way three separate illumination spots were created at the diffuser, each producing an uncorrelated speckle pattern. The resulting far-field RMS speckle noise was 63%, nearly the predicted value. System energy losses such as nonperfect mirrors and no AR-coating on the beamsplitter can easily account for the difference from the predicted

value.

6.4 Cascading Polarization and Delay Stages

The cascading of several polarization and delay stages is relatively straightforward. Because each stage produces three sub-pulses instead of just two, each successive delay arm must be made three times longer than the preceding stage. This extra length may seem at first as a disadvantage, but the polarization and delay scheme produces more pulses on a per length basis than any comparable system. The delay arm in the polarization and delay method increases as $\log_3(N)$, where N is the number of sub-pulses. Previous schemes that cascade several stages all have delay arms that increase as $\log_2(N)$. A further advantage of the polarization and delay scheme is that each successive pulse alternates in polarization so that the delay arm need be only one half of the pulse duration. This reduction in arm length is due to the fact that sub-pulses with similar polarization state are separated by two round trips of the delay arm whereas in all other schemes similar pulses are separated by only a single round trip.

To optimize the performance of two or more cascaded stages, the beamsplitter reflectivities must be chosen using similar criteria as that used for a single stage. Writing out the theoretical intensity for each sub-pulse becomes cumbersome for two or more stages and thus we will resort to the recursive computer program mentioned previously to calculate each sub-pulse as the reflectance values of the beamsplitters vary over their range. The optimum beamsplitter values for two cascaded stages are:

$R_{p1} = 0.29$

$R_{s1} = 0.53$

$R_{p2} = 0.33$

$R_{s2} = 0.72.$

The resulting pulse intensity versus time is shown in Fig. 11. Using this pulse train as the input to the speckle program of chapter 5 produces a far-field RMS noise of 33.9%, equivalent to 8.7 individual pulses.

If one could accept a small loss in speckle reduction capability, the delay arm in the second stage could be reduced to only two pulse lengths instead of three. Using $R_{p1} = 0.29$, $R_{s1} = 0.53$ and $R_{s1} = 0.33$, and $R_{s2} = 0.72$ for the beamsplitter parameters and a second stage delay of only two pulse widths produces the pulse train shown in Fig. 12. The far-field RMS noise produced by this pulse train is 36.1%, equivalent to 7.6 pulses. This is a small reduction in speckle mitigation ability and allows for a more compact system.

One final feature of this pulse generation system is the ability to implement the entire system in a single piece of fused silica. For a laser source with coherence lengths or pulse durations of only a few inches, this system could be implemented in a reasonable sized piece of fused silica. The two 45 degree mirrors could be replaced by total internal reflection at the inside surfaces of the fused silica cube. The normal incidence mirror could be replaced by two total internal reflections aligned in a manner similar to a corner cube. The entire system alignment would then consist of positioning the cube properly relative to the incident laser beam.

6.5 Conclusions

Producing multiple sub-pulses from a single laser pulse is an effective and practical method of reducing a the speckle noise, and thus the number of pulses needed to produce a

uniform exposure. Using two stages of the polarization and delay system results in a single pulse speckle noise of only 33.9% which reduces the required integrated pulse count for 1% uniform illumination from 10,000 to only 1,150.

Though the path lengths used in each delay arm of such pulse multipliers can be long for laser sources such as our current quintupled Nd-YAG, proper design of the radiation properties of the laser source can lead to dramatically reduced path lengths. The pulse duration, and hence the required delay arm length, is an important design issue of the second generation quintupled Nd-YAG laser source. Since pulse duration and spectral linewidth are inversely related in Fourier transform limited laser systems such as ours, one must weight the advantages gained by reducing the pulse duration against the possible decreased lens performance owing to broader spectral width.

References

1. D.J. Cronin and A.E. Smith, "Dynamic Coherent Optical System," *Opt. Eng.* , vol. 12, no. 2, pp. 50-55, 1973.

2. C.B. Rubinstein, "Optical pulse Generator," *U.S. Patent #3,430,048*, Feb. 1969.

3. Melles Griot, in *Optics Guide 3*, 1985.

4. O.E. De Lange and et. al., "Optical Pulse Multiplier," *U.S. Patent #3,447,856*, June 1969.

5. D.R. Herriott and H.J. Schulte, "Optical Pulse Generator," *U.S. Patent #3,501,222*, March 1970.

6. C.N Scully, "Laser Target Speckle Eliminator," *U.S. Patent #4,511,220*, April 1985.

7. I. Taback, "Speckle Reduction Apparatus," *Applied Optics*, vol. 28, no. 22, p. 4947, Nov. 1989.

8. D.G. Goebel, "Gemalized Integrating-sphere Theory," *Appl. Opt.*, vol. 6, p. 125, 1967.

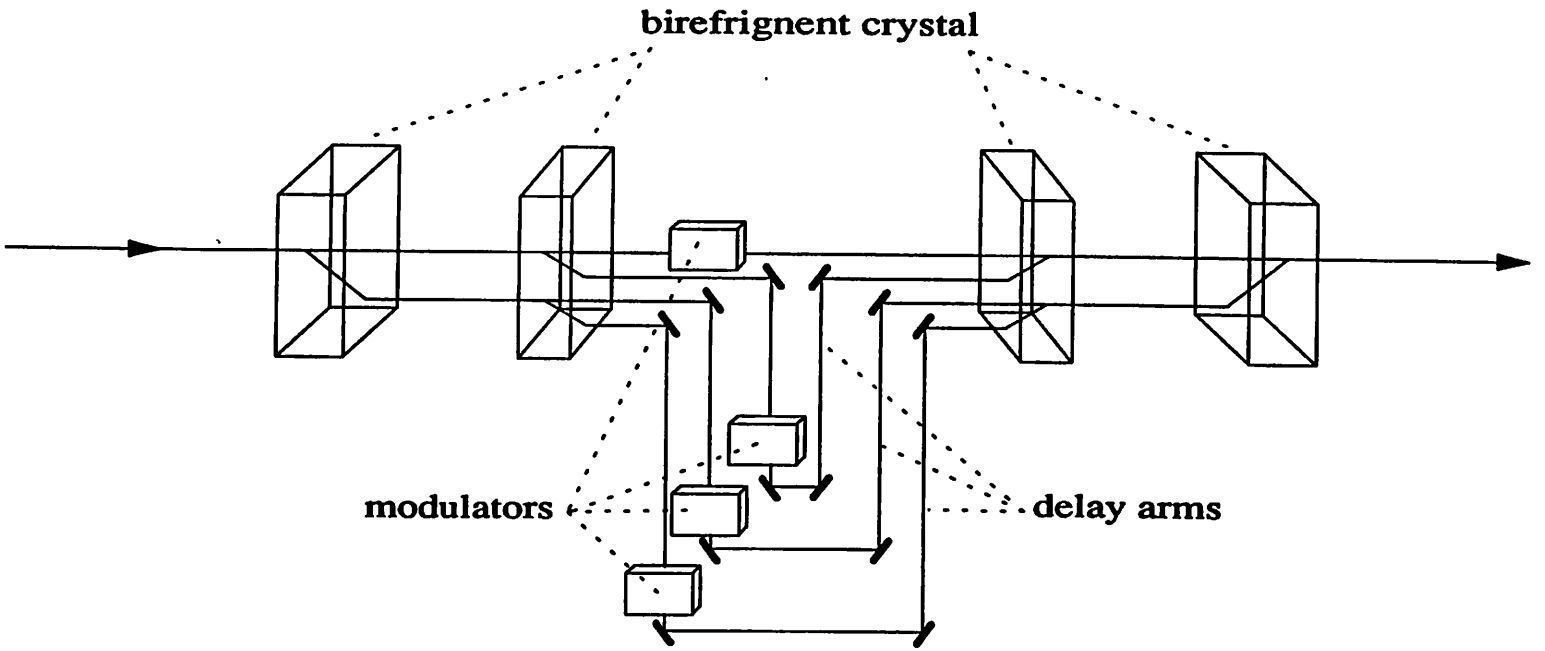

Fig. 1. Multiple pulse generation scheme proposed by Rubinstein in 1969.

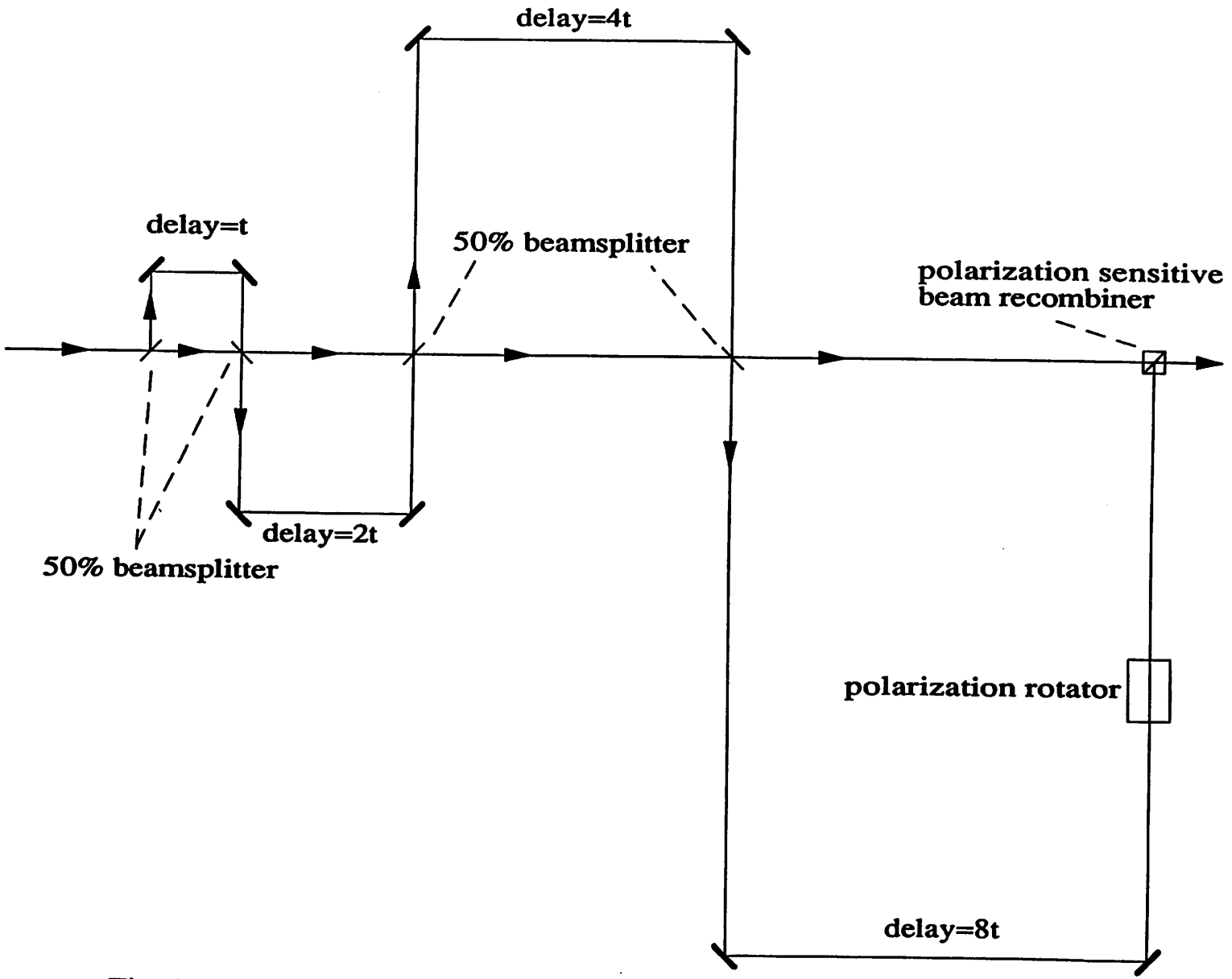

Fig. 2. Multiple pulse generation scheme proposed by De Lange in 1969.

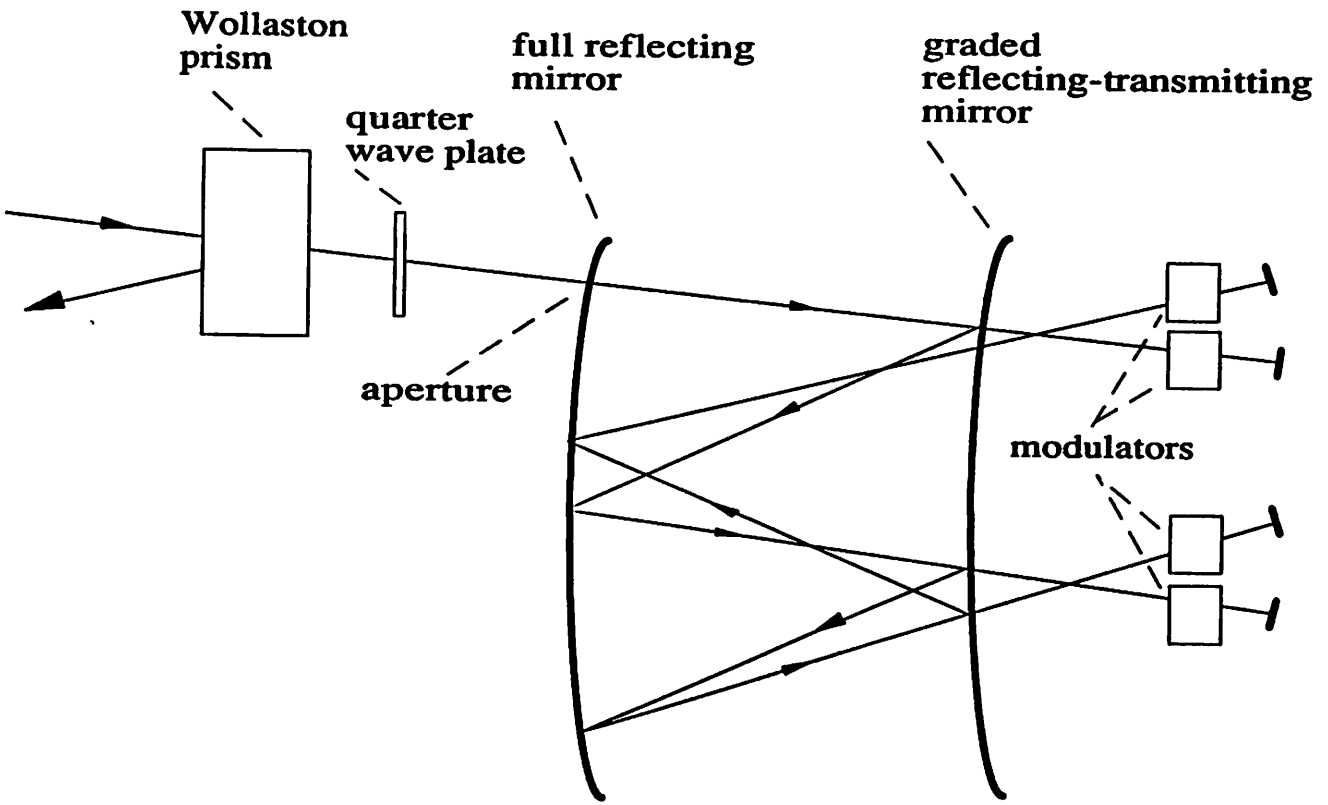

Fig. 3. Multiple pulse generation scheme proposed by Herriott in 1970.

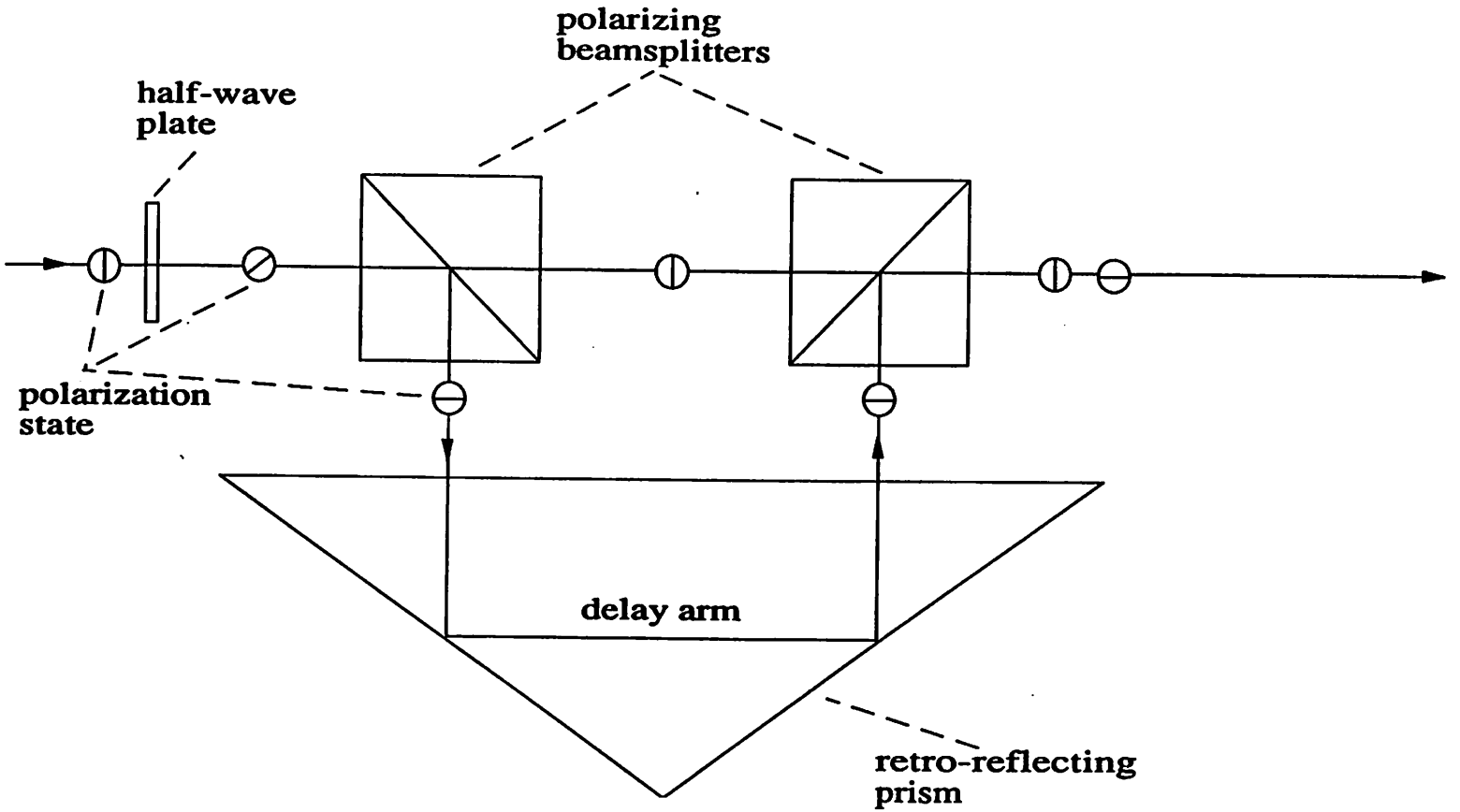

Fig. 4. Speckle reduction scheme proposed by Scully in 1985.

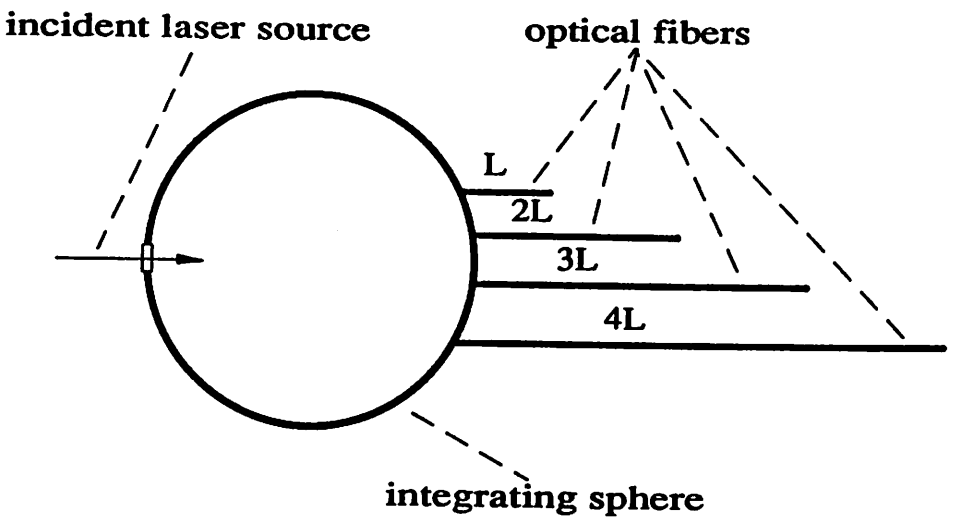

Fig. 5. Speckle suppression apparatus proposed by Taback in 1989.

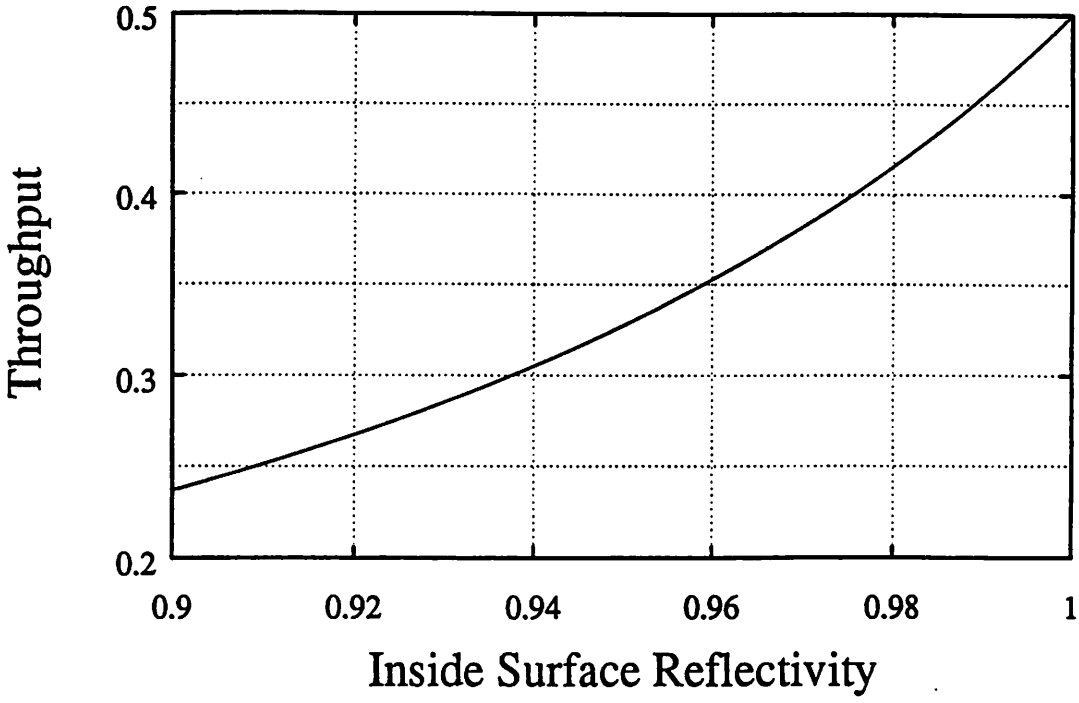

Fig. 6. Integrating sphere efficiency vs. reflectivity of diffuse reflector.

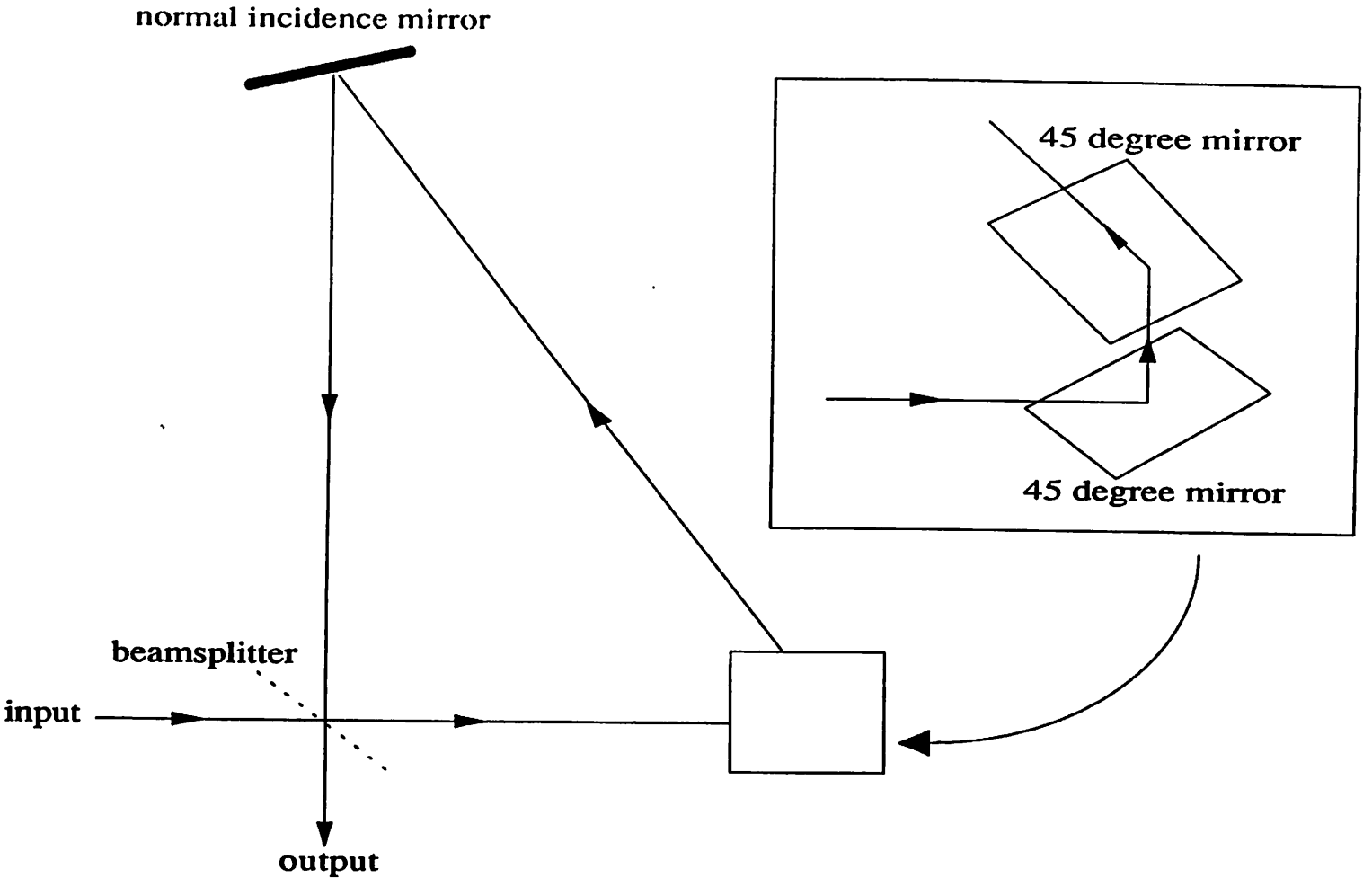

Fig. 7. Schematic layout of the polarization and delay multiple pulse generation system.

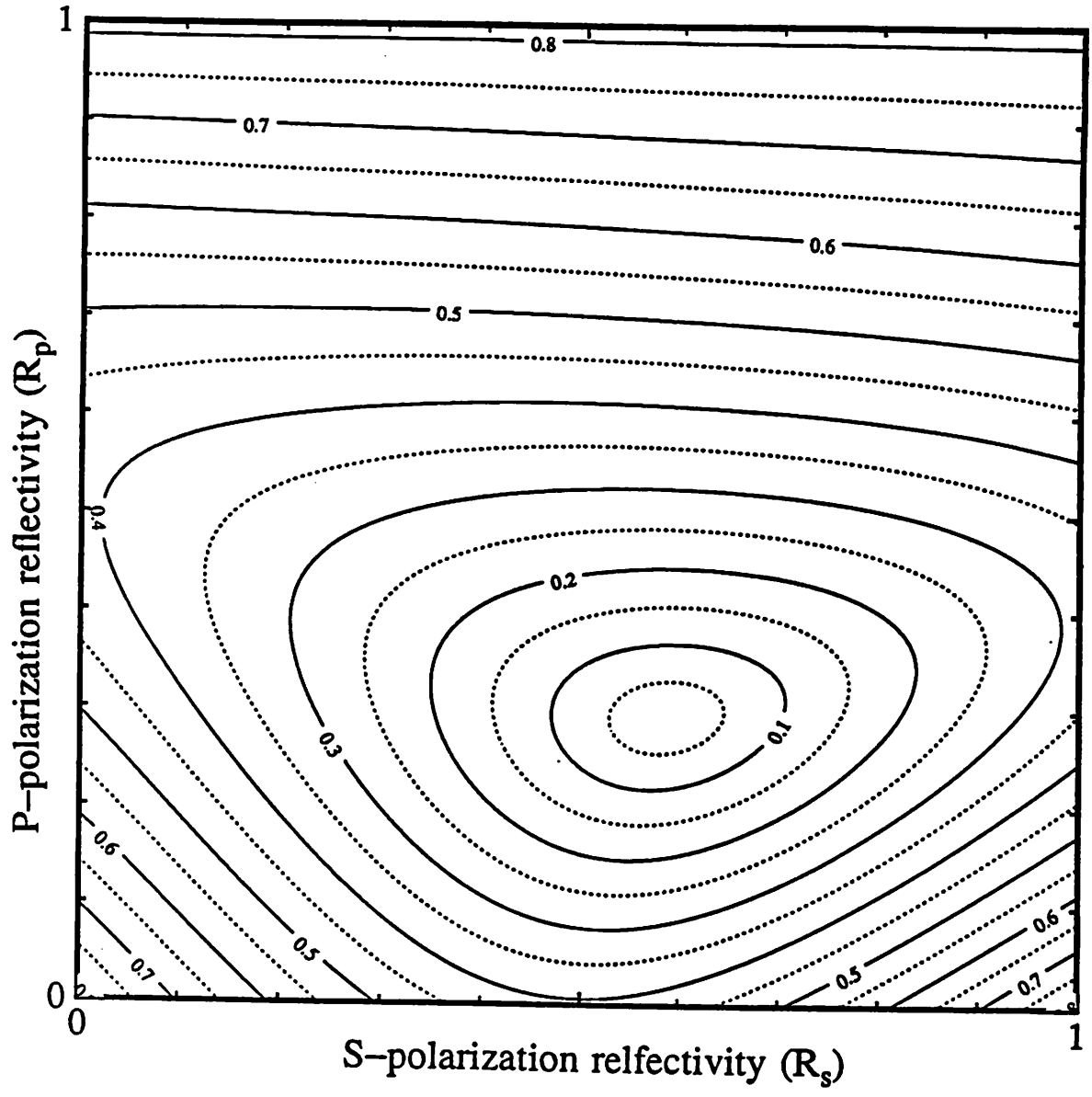

Fig. 8. Difference from mean of the three sub-pulses as R_p and R_s range from zero to one.

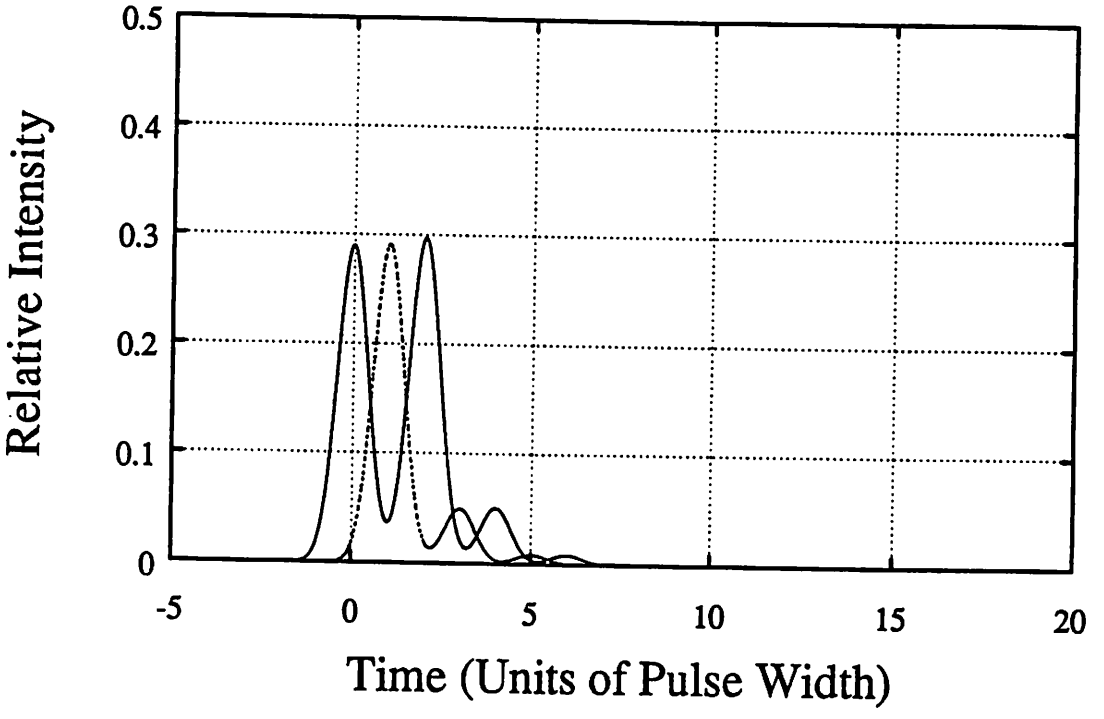

Fig. 9. Laser pulse intensity vs. time for a single stage of the polarization and delay system using $R_p = 0.29$ and $R_s = 0.59$.

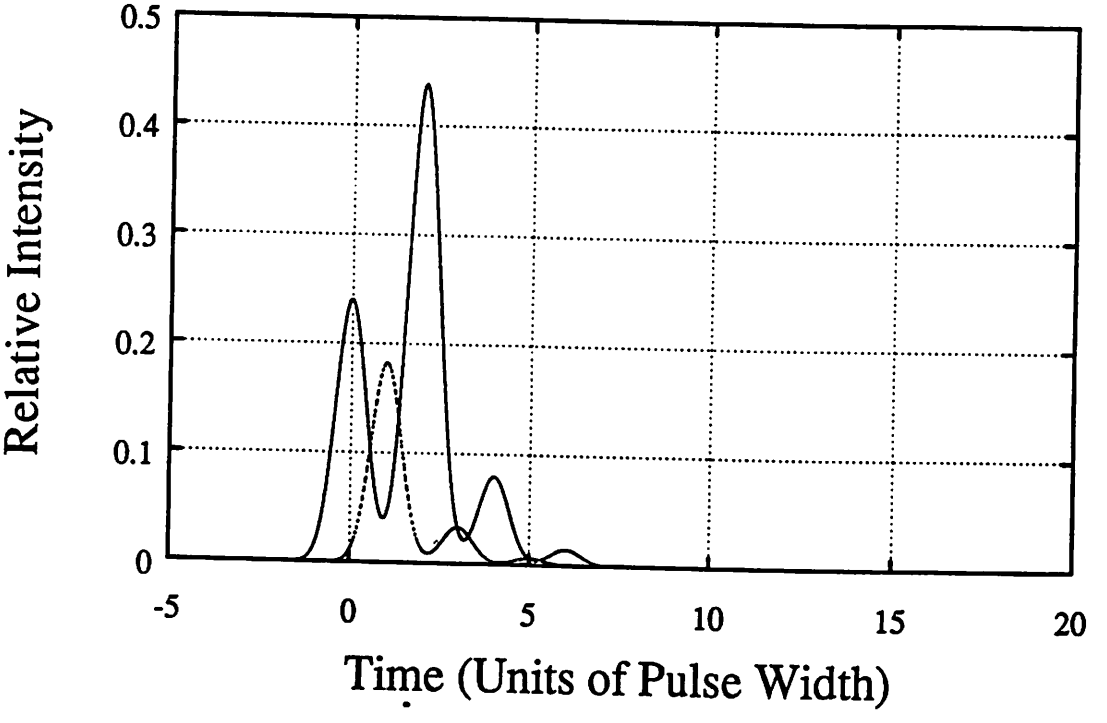

Fig. 10. Laser pulse intensity vs. time for a single stage of the polarization and delay system using $R_p = 0.24$ and $R_s = 0.76$.

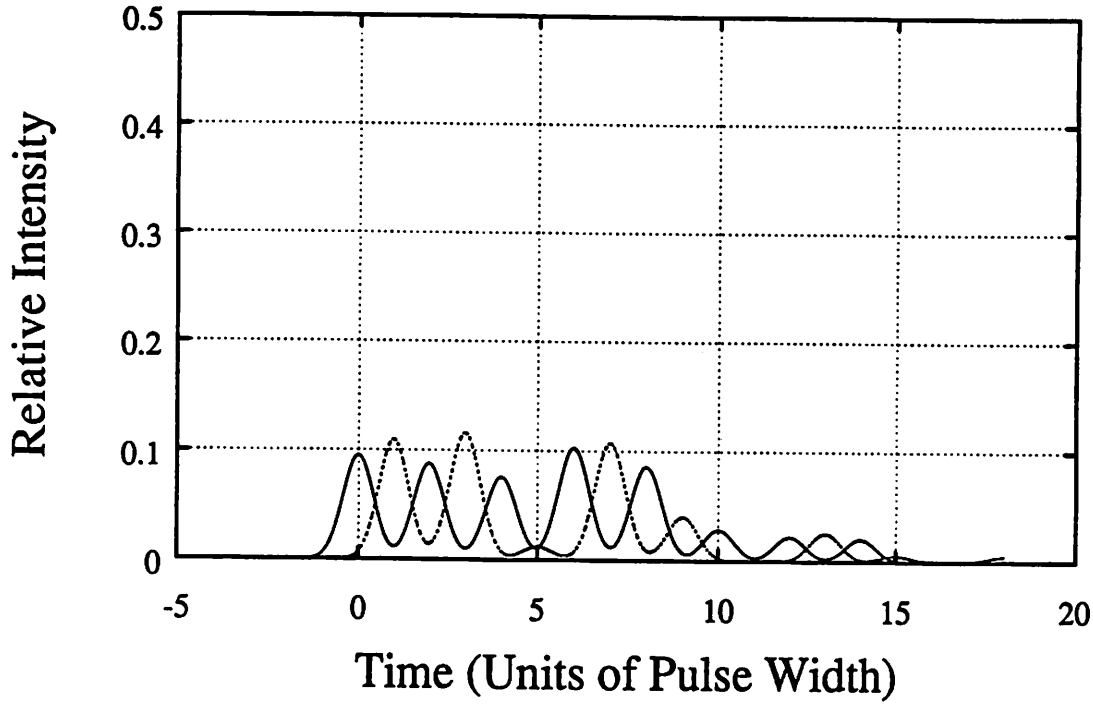

Fig. 11. Laser pulse intensity vs. time for two stages of the polarization and delay system using $R_{p1} = 0.29$, $R_{s1} = 0.53$, $R_{p2} = 0.33$, and $R_{s2} = 0.72$.

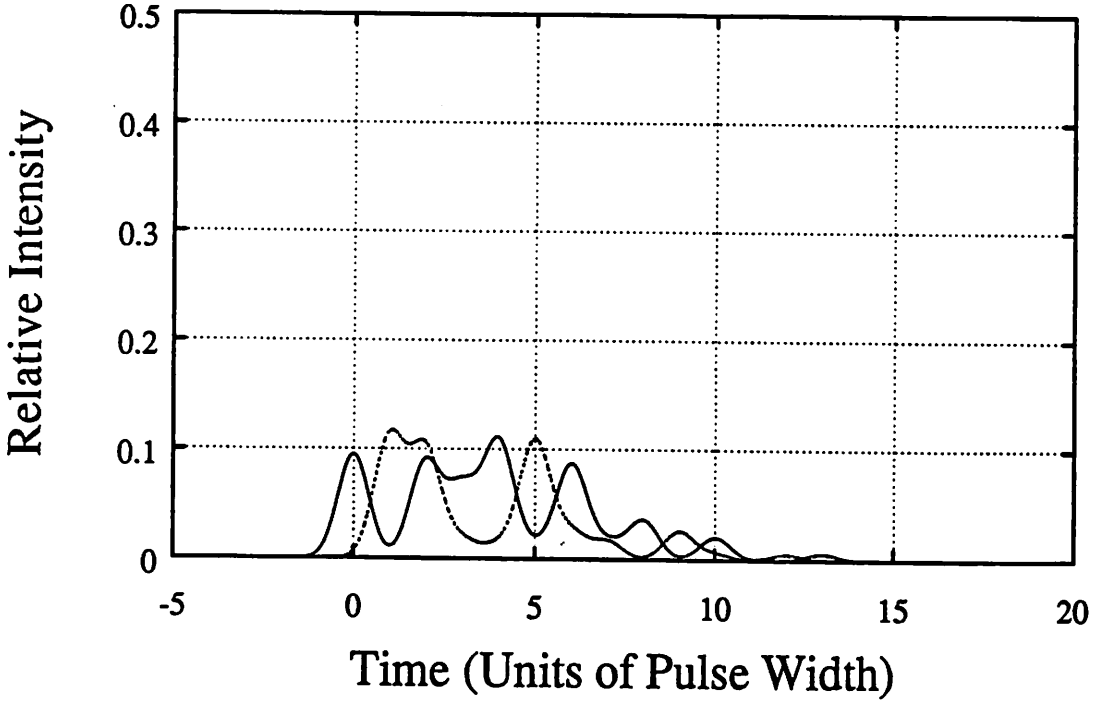

Fig. 12 Laser pulse intensity vs. time for two stages of the polarization and delay system with the second stage delay equal to two pulse widths.

Chapter 7
213nm Lithography

Abstract- 213nm lithography has been demonstrated using a 0.25W quintupled Nd-YAG laser source and two high numerical aperture objectives. O.25μm line/space patterns were resolved with an all-reflective Schwarzschild objective (NA=0.65) over a 100μm diameter field. An all-refractive objective (NA=0.6) has produced 0.2μm equal line/space patterns over a 950μm diameter field.

The images were formed in a 0.58μm layer of PMMA using MIBK and MEK developer systems. Speckle-free images were produced with as few as 300 laser pulses, demonstrating that highly coherent pulsed lasers are viable sources for deep-UV lithography.

7.1 Introduction

Each attempt to decrease the exposure wavelength used in microlithography is accompanied by new challenges in lens design and construction. In the deep-UV region, only fused silica is sufficiently transparent and possessing of the appropriate mechanical and chemical properties to be a useful material for lens construction. With only a single type of lens material one cannot design a color corrected lens. Single-material lenses must be illuminated with light sources that produce a spectral linewidth determined by the dispersion of fused silica and the lens focal length. The maximum permissible spectral linewidth is given by:[1]

$$\Delta\lambda = \frac{(n-1)\lambda}{f(1+m)(\frac{\delta n}{\delta\lambda})NA^2}, \qquad (1)$$

where $\Delta\lambda$ is the FWHM of the spectral linewidth, n is the refractive index, f is the focal length, m is the lens magnification, and NA is the lens numerical aperture.

Applying this formula to the 213nm BOLD objective, which has a focal length of 21.44mm and a reduction ratio of 1:20, gives a spectral linewidth of 24pm.[2] The 47pm bandwidth of the unseeded 5th harmonic Nd-YAG is too wide for this lens. The seeded bandwidth of 0.035pm is well within these requirements. The all reflective Schwarzschild objective exhibits no dispersion so it will function equally well for both seeded and unseeded operation. The Schwarzschild allows one to observe differences between seeded and unseeded operation without the effect of a change in lens performance. The 1:74 magnification of this lens is an additional advantage because it makes for large features on the mask, thus easing mask fabrication tolerances. The disadvantage of all-reflective optics in general is the small field size over which the image is free from aberrations.

7.2 Schwarzschild Objective

The Schwarzschild objective used in these experiments is a 0.65NA, 1:74 reduction ratio lens with a focal length of 2.6mm. The corrected field is small, only 240 μm in diameter. This lens also contains a 12.5% central obscuration at the entrance pupil. The setup used to print images with this objective is shown in Fig. 1.

The mask is illuminated by the far-field scattering of two diffusers in series. This double diffuser configuration is not meant for speckle contrast reduction as described in chapter 5. The first diffuser improves the uniformity of the radiation incident on the second diffuser. Since the second diffuser is imaged into the entrance pupil of the Schwarzschild objective, this diffuser should be illuminated uniformly to produce uniform pupil filling. The aperture placed against the second diffuser controls the amount of partial coherence, σ. An image of the second diffuser is formed immediately after the dielectric mirror by relay lens #1. This image of the diffuser is then imaged by the field lens through the mask into the entrance pupil of the Schwarzschild objective.

This Schwarzschild objective system was intended only for temporary use and thus an elaborate focus positioning scheme was considered too time consuming and expensive to construct. Instead, we took advantage of the all reflective property of this objective, that is if best focus is found at one wavelength then best focus for all wavelengths has been found. A HeNe laser was folded into the optical path through the dielectric mirror to produce a focus signal. The HeNe laser light is scattered by the diffuser shown in Fig. 1. This diffuser is imaged by relay lens #2 to a point near the intermediate image of the 213nm diffuser just after the dielectric mirror. The image positions for the 633nm diffuser and the 213nm diffuser do not exactly correspond since the field lens has a shorter effective focal length for the 213nm radiation. To form an image of the 633nm diffuser in the entrance pupil, the intermediate image of the 633nm diffuser must be formed further away from the mask and field lens. There is no partial coherence adjustment for the 633nm illumination. Since the HeNe laser beam is only 420 μm in diameter and is imaged nearly 1:1 into the entrance pupil, the fill factor for the 633nm illumination is zero.

After passing through the mask and being imaged by the objective onto the wafer, the 633nm radiation is recollected by the objective and reimaged onto the mask. The light that passes back through the mask is deflected by a beamsplitter and detected with a photomultipler tube (PMT). Only when the wafer is in the best focus plane will the the reflected light be reimaged properly back through the mask and onto the PMT. We thus have a focus signal that is a maximum when the wafer is at best focus. This reimaged intensity is small and is overwhelmed by the unwanted reflections from the field lens and the mask. To help separate the desired signal from these unwanted reflections, a chopper motor was placed after the mask to modulate the light passing through the objective. Combining the chopper motor signal and the PMT signal with a lock-in amplifier eliminates the undesired signals from the field lens and mask reflections.

The only disadvantage of this lock-in amplifier scheme is the reduced dynamic range of the PMT due the the large DC signal from the unwanted reflections. To further improve

the signal to background ratio an aluminum coated wafer is used instead of a bare silicon wafer. The improvement in reflected 633nm signal can be seen in Fig. 2. This figure is a plot of reflectivity versus wavelength of an aluminum coated wafer as compared to bare silicon. There is a 2.5 times increase in reflectivity at 633nm but almost no increase at 213nm. Coating the wafer improves the 633nm focus signal with little or no increase in standing wave ratio at the 213nm exposure wavelength.

A plot of the focus signal versus wafer position is shown in Fig. 3. The mask used for this measurement was equal lines and spaces of 74μm on the mask corresponding to 1.0μm on the wafer. This is close to the diffraction limited line/space dimension for the 633nm wavelength and the 0.65 numerical aperture given by λ/NA =0.974μm. The Modulation Transfer Function (MTF) should be a step function owing to the near zero fill factor. The MTF should be equal to unity for line/space patterns larger than 0.974μm and zero for line/space patterns smaller than 0.974μm. When the wafer is far from the best focus position the signal for the PMT should be about half of the peak value. Energy from the out of focus image will pass through the 50% duty cycle mask onto to the PMT, producing a signal equal to half of the value at best focus. After subtracting the background signal, the FWHM of the focus signal is about 1.2 μm. This corresponds well to the 1.1μm width predicted by the following depth of focus equation:

$$DF = \frac{(0.5P)^2}{\sqrt{2}\lambda}, \tag{2}$$

where DF is depth of focus, P is period of the line/space pattern, and λ is wavelength. Eqn. (2) is the depth of focus equation for microscope systems used in the confocal arrangement.[3,4]

A hand turned micrometer stage has insufficient resolution to position the wafer with the small depth of focus shown in Fig. 3. Fig. 4 shows the arrangement used to hold the wafer and lens in position. The micrometer screw on the wafer stage could not repeatably

position the wafer for maximum focus signal. To improve wafer placement, a large squeeze bottle was placed behind the wafer stage and inflated with pressurized air. Inflating and deflating the bottle changed the pressure on the post holding the wafer thus changing the amount of deflection of the post toward or away from the Schwarzschild objective. This simple system allowed us to position the wafer with submicrometer precision.

The results of images printed with this system will be presented in section 7.5 .

7.3 213nm BOLD Objective

The BOLD objective designed and built by GCA/Tropel is one in a series of micro-objectives for use with various deep-UV radiation sources. This objective is a small field, (1mm diameter) high numerical aperture, (NA=0.6) all-fused silica refractive optic intended for experimental investigation of new radiation sources and photoresist systems. The objective itself consists of 6 individual fused silica elements. This objective is much less complicated than the more typical 20 to 30 element lenses used in large field (several centimeter diameter) imaging systems. Table 1 lists the relevant specifications for this objective.

GCA/Tropel does not have the capability to make interferometric measurements at 213nm, so a 257nm source was used and only on-axis tests were performed. The results of the interferometric testing is shown are Fig. 5. Fig. 5 is a plot of wavefront aberration versus numerical aperture. The edges of the diagram correspond to NA=0.60. The total included range of the wavefront distortion is 0.195 fringes at 257nm. Converting 0.195 fringes at 257nm to 213nm gives 0.235 fringes, or 0.118 of a wave of distortion, almost a tenth of a wave at 213nm. A tenth-wave of wavefront distortion or less is considered diffraction limited performance. Since only the on-axis field position was measured, adjustments for coma and astigmatism are not independent. Two of the six elements can be adjusted to correct for coma and astigmatism and this has been done on a best effort basis, but without interferometric measurements at 213nm one cannot be completely sure that these aberrations have

been minimized over the entire field.

To illustrate the potential performance of this lens using the 213nm exposure wavelength, a set of SAMPLE[5] simulation runs are shown in Figs. 6 and 7. These plots show the aerial image intensity contrast versus line/space spatial frequency for various amounts of defocus. Fig. 6 is the result using $\sigma = 0.5$ and Fig. 7 is the result with $\sigma = 1.0$. As Fig. 6 shows, a image contrast of greater than 90% can be obtained for line/space pairs down to 0.2μm if best focus can be achieved. With $\sigma = 1.0$, 50% image contrast is maintained down to 0.137μm line/space patterns.

The layout for the imaging system using the BOLD objective is shown in Fig. 8. This system is similar to that used with the Schwarzschild objective. The major differences are the absence of the HeNe focus system and the addition of the 3 mirror speckle reduction scheme described in chapter 6. Since the BOLD objective is a refractive optic best focus at 633nm will not correspond to best focus at 213nm, thus rendering the HeNe focus system useless. To assist in finding best conjugate position, this objective is supplied with three stainless steel balls mounted on the image side of the lens such that their vertices describe the best wafer side conjugate position. Pressing a wafer against these balls positions the surface of the wafer in the best conjugate position on the image side. To show the narrow tolerance required in the placement of these balls, Fig. 9 shows the Strehl ratio versus axial displacement of the mask position. A displacement from optimum of +/-4.6mm reduces the Strehl ratio from 96% to 80%. A mask displacement of +/-4.6mm corresponds to +/-11.5μm of wafer displacement. If the balls are positioned incorrectly during fabrication of the lens, the Strehl ratio of the image is irreparably reduced.

To assist in finding the best focus position for the mask, a confocal focusing system similar to the 633nm scheme for the Schwarzschild was constructed employing the 213nm radiation. Separating the desired signal from the unwanted mask and field lens reflections is a much greater challenge when using the pulsed 213nm source instead of the continuous

633nm source. Since the 213nm laser is pulsed, the simple scheme of using a chopper motor after the mask will not work. One can not easily modulate a pulsed laser source with a pulse duration of 4.2ns. To overcome this difficulty we constructed a shutter system that opens during every other laser pulse. With this shutter positioned between the mask and objective, the focus signal reflected by wafer is modulated at 5Hz while all unwanted reflections were modulated at the 10Hz repetition rate of the laser. We could then use the lock-in amplifier to separate the two signals producing a DC voltage proportional to the desired focus signal. One difficulty with this method is that the 5hz and 10hz signals are both low frequency and close together in the frequency spectrum. The obtain a high degree of separation between the two signals, an integration time of 3 seconds or more was required. This long integration time was also required to reduce signal fluctuation caused by variation in the incident laser pulse. The output from the quintupled Nd-YAG laser exhibits a +/-20% variation from pulse to pulse. Averaging the pulses during one integration time reduces this variation by a factor of $1/\sqrt{15} = 0.26$, reducing the signal variation to +/-5%.

Fig. 10 shows the layout of the mask used for measuring the focus signal versus mask position. The dimensions shown are those that would print on the wafer, the actual mask dimensions are 20 times larger. A clear area duty cycle of less than 50% was chosen to reduce the background signal generated when the mask is far from best focus. The mask has a 1.2μm pitch that should produce a 1.19μm wide FWHM focus signal according to Eqn. 2. The measured focus signal, shown in Fig. 11, has a signal width of 1.2μm FWHM, and corresponds well to the predicted value.

Fig. 8 also shows a pellicle beamsplitter between the mask and the objective. This beamsplitter deflects a portion of the energy returning from the lens onto a CCD array camera. The camera is placed at a position conjugate to the wafer plane so that the intensity at the wafer plane can be monitored by the camera. This arrangement allows us to adjust field uniformity in real time without having to use clear area exposures in photoresist. Figs. 12 and 13 show the wafer field intensity at the center and edge of the field. These

measurements show a field uniformity of 10% RMS and 15% TIR. One disadvantage of using a pellicle beamsplitter is the variation in reflectance versus incident angle owing to the thin film interference effect. This variation is the cause for some of the nonuniformity seen in Figs. 12 and 13. Clear field exposures in resist show the uniformity to be better than 5% TIR over the whole field. A second example of the use of the beamsplitter and camera arrangement is shown in Fig. 14. This is a picture of the field intensity with a mask in place. Unfortunately, the line/space features on the camera face are 3 to 7 times smaller than the pixel size of the CCD array. Another 10X magnification is needed for the camera to fully resolve the aerial images at the wafer plane. This 10X magnification would lead to a 100X reduction in the illumination intensity on the CCD array. With the present system there is insufficient intensity to properly illuminate the CCD array after a 100X intensity reduction.

A vacuum chuck mounted on an air piston presses the wafer against the focus balls. This arrangement is shown in Fig. 15. The vacuum chuck is needed to prevent any bowing that would occur if a bare wafer was pushed up against the focus balls by the air piston. The air piston itself is positioned directly under the optic axis of the objective and is fed by a 20psi source through a large volume squeeze bottle. The squeeze bottle acts like a capacitive load preventing the instantaneous application of the full 20psi to the air piston. If the full 20psi of air pressure were applied the piston too quickly, the wafer chuck would strike the focus balls with great force, possibly causing damage to the wafer or the balls. To test the repeatability of wafer placement, Fig. 16 shows the focus signal versus time as the air pressure to the piston is repeatedly applied and removed. The focus signal after each up and down motion of the wafer chuck is repeatable to +/-5% which corresponds to +/-0.1μm.

7.4 PMMA as a 213nm Photoresist

Polymethylmethacrylate (PMMA) has been suggested as a candidate deep-UV resist.[6] This resist possesses adequate transparency in the deep-UV and is sensative to exposures between 100mJ/cm^2 to 1000mj/cm^2. The developer chemistries for PMMA are many and

varied[7] and all use wet develop techniques (as opposed to silylation, plasma etching, etc). These properties make PMMA ideal for initial imaging studies because of its ease of use and quick turn around time.

The transmission properties of a 1.1μm thick sample of 950K PMMA are shown in Fig. 17. This sample was spin cast onto a fused silica wafer from a mixture of 6% solids dissolved in chlorobenzene. PMMA is nearly transparent to all wavelengths above 250nm. This helps explain why PMMA has such low sensitivity at the KrF excimer wavelength of 248nm. Since there is little absorption at 248nm there is little interaction between the radiation and the resist leading to exposure sensativities in the several J/cm^2 range. Below 250nm the absorption of PMMA increases until it reaches a peak at 210nm. At 213nm this sample of PMMA has 46% transmission corresponding to an optical density of $\alpha = 0.67\mu m^{-1}$. This value agrees with previously measured values for PMMA.[8] This amount of absorption is enough to make the resist sensative to 213nm radiation while being transparent enough to allow nearly uniform exposure throughout the volume of the resist.

Fig. 18 shows a SAMPLE simulation of the 213nm intensity through the depth of a 1μm thick resist film on bare silicon. The decrease in average intensity with depth in this figure is less than what would be expected from a material with $\alpha = 0.67\mu m^{-1}$. The less than expected decrease is caused by the nearly 100% reflection at the resist/silicon boundary. The intensity near this boundary is almost twice what it would be without the reflection from the silicon. This high reflectivity also accounts for the 80% contrast standing waves in the intensity profile. If an anti-reflection coating is applied to the silicon, the standing waves will be reduced at the expense of uniformity of average intensity through the depth of the resist. Fig. 19 shows a SAMPLE simulation of this situation. A 1000 angstrom layer of hard baked G-line resist (AZ2400) has been placed between the PMMA and the silicon, greatly reducing the standing wave contrast, but also degrading the uniformity of intensity through the resist depth. The reduction in resist/silicon interface reflection has been verified

by measuring reflectivity versus wavelength for PMMA on bare silicon (Fig. 20) and a layered stack consisting of PMMA/AZ2400/Si (Fig. 21).

The optical bleaching properties of PMMA at 213nm are shown in Fig. 22. Fig. 22 is a plot of 213nm transmission versus integrated dose for a 1μm thick sample of 950K PMMA. With increasing dose the resist darkens with a e^{-1} value of 255.6mJ. This darkening may be evidence of crosslinking similar to that experienced with the chemically amplified 248nm resists.[9] The per pulse energy density used for this measurement was about 0.1mJ/cm^2, well below the threshold for any suspected nonlinear process.

Damage to PMMA caused by high pulse energies has been observed previously.[6,10] Single pulse ablation experiments have been performed using PMMA and an ArF (193nm) excimer laser source.[11] At 213nm, previous workers have measured the ablation threshold for PMMA to be 1MW/cm^2 .[12] This peak intensity corresponds to 4.2mJ/cm^2 per pulse for our 5th harmonic Nd-YAG laser. Fig. 23 shows an SEM profile of 1μm lines and spaces in PMMA after exposure but before development. This exposure was performed with the Schwarzschild system, which with its high reduction ratio (74X) can easily produce average pulse energies above 10mJ/cm^2.

Reducing the average energy density per pulse below the PMMA ablation threshold is insufficient to avoid photoablation. Because of the high speckle contrast formed by each 213nm pulse (see chapter 4), there will be points within the field with 10 times the average energy density. Thus to prevent resist photoablation damage we must reduce the average energy density per pulse to less than 0.1mJ/cm^2.

We have investigated two PMMA developer chemistries. One developer system based on Methyl Isobutyl Ketone (MIBK) exhibited moderate contrast but low sensitivity. A plot of thickness remaining versus dose for this developer is shown in Fig. 24. This developer exhibited a small top loss of 700 angstroms in the unexposed regions. Also shown in Fig. 24 are the results of SAMPLE simulations using a developer model proposed by Greeneich.[7]

The model is an empirical formula of the form:

$$R = R_0 + \frac{\beta}{M_f^{\alpha}}, \tag{3}$$

where R is the development rate, R_0 is the unexposed development rate, M_f is the fragmented molecular weight, and β and α are fitting parameters. The relation between exposure and fragmented molecular weight is also given by Greeneich:

$$M_f = \frac{M_n}{1+\gamma D}, \tag{4}$$

where M_n is the unexposed molecular weight, D is the absorbed dose, and γ is proportional to chain scission efficiency. Combining Eqn. (3) and (4) gives:

$$R(D) = R_0 + \frac{\beta}{\left[\frac{M_n}{1+\gamma D}\right]^{\alpha}}. \tag{5}$$

Using this developer model in SAMPLE to calculate the thickness remaining versus dose gives a reasonable fit to the measured data in Fig. 24. The values for the developer parameters are as follows:

$$R_0 = 3.99 \times 10^{-5}\ \mu\text{m/sec}$$

$$\alpha = 0.941$$

$$\gamma = 8.54 \times 10^{-4}\ (\text{UCB units})^{-1}$$

$$\beta = 191\ \mu\text{m/sec}$$

With this developer model in SAMPLE, we can predict the resist profiles expected from the Schwarzschild and BOLD imaging systems using this developer chemistry. Figs. 25 and 26 show 0.5μm and 0.2μm line/space patterns in 5800 angstrom thick PMMA on bare silicon. Intense standing waves degrade resist performance, as expected. These simulated profiles may be compared to the actual profiles shown in Fig. 32. Figs. 27 and 28 show the

same simulation conditions except a 1000 angstrom layer of AZ2400 has been placed between the PMMA and the silicon as an AR-coating. The standing wave effects are greatly reduced but the side wall angles are still poor owing to the poor resist contrast and decrease in intensity near the bottom of the resist (Fig. 19).

Two problems with the MIBK developer prompted us to investigate a second PMMA developer system. The first problem was the high standing wave effects. If we used a developer with a higher development rate in the unexposed regions the standing wave effect would be less severe. The second and most significant problem with the MIBK developer is the high dose-to-clear. Exposure times greater than 10 minutes are needed to accumulate the required dose while maintaining the per pulse energy below the ablation threshold.

We found about a 10X reduction in the dose to clear with a developer consisting of 2 parts Methyl Ethyl Ketone (MEK) to 1 part denatured ethanol. The measured and simulated thickness versus dose values using this developer are shown in Fig. 29. The fitted parameters are as follows:

$$R_0 = 4.40 \times 10^{-3}\ \mu\text{m/sec}$$

$$\alpha = 1.1$$

$$\gamma = 6.00 \times 10^{-3}\ (\text{UCB units})^{-1}$$

$$\beta = 2840\ \mu\text{m/sec}$$

One disadvantage of this developer system is a large amount of top loss in the unexposed areas. In our experiments, the PMMA was initially 5800 angstroms thick and only 2800 angstroms remained after the develop step. The high develop rate for unexposed areas helps to reduce the standing wave effect.

This developer left a haze on the wafer if the developer was rinsed off in DI water or simply blown dry. To overcome this hazing problem we do a pure denatured ethanol rinse between the develop and DI rinse steps. The procedure is as follows:

1) Spin coat 950K PMMA 4% solids for 45sec at 1000rpm.

2) Bake for 90sec at 160 degrees Celsius.

3) Expose to 213nm radiation.

4) Mix developer: 2 parts MEK to 1 part denatured ethanol.

5) Shake up developer in the bottle (IMPORTANT!).

6) Immersion develop for 60sec with slow agitation.

7) Immerse in 100% denatured ethanol with ultrasonic agitation for 60sec.

8) Rinse with DI water

SAMPLE simulations for images formed using this developer system are shown in Figs. 30 and 31. No AR-coating is used in these simulations so the image intensity posses a high standing wave ratio. Little standing wave effects are evident in the developed resist profiles. As expected, the high unexposed develop rate helped to alleviate the standing wave problem. There is, unfortunately, no improvement in side wall angle over the MIBK developer, most likely owing to the low contrast of the MEK:ethanol developer system.

7.5 Schwarzschild Imaging Results

The resist images shown in Fig. 32 show the resolution capabilities of the Schwarzschild objective. These images were formed using 3000 pulses from the 213nm laser and developed using the MIBK developer system. During the exposure, the second diffuser in Fig. 1 was rotated so that the speckle intensity variations would integrate to a uniform exposure. Using 3000 pulses results in an RMS intensity variation of $100\%/\sqrt{3000} = 1.8\%$. This low speckle noise contrast makes the resist images speckle free. Figs. 33 and 34 show the nonuniformities that result when the diffuser is not rotated during the exposure. Fig. 33 was exposed on the Schwarzschild system with 1000 pulses with a rotating diffuser, while Fig. 34 was exposed under identical conditions except the diffuser was stationary during exposure. Side wall roughness is the most noticeable difference

between the two figures. The side wall is the point at which the intensity has its greatest slope from light to dark. It is in this region that the nonuniform illumination caused by speckle will most strongly manifest itself. There are also areas of resist remaining in the regions of highest dose. This is caused by a strong null or zero point in the speckle illumination roughness allowing little or no radiation into this region.

7.6 BOLD Imaging Results

The performance of the BOLD objective was also verified using the PMMA resist process. The results from these exposure tests are shown in Figs. 35 and 36. Fig. 35 shows SEM profiles of equal line/space patterns with dimensions of 0.5μm, 0.4μm, 0.3μm, and 0.25μm. These patterns were developed using the MEK:ethanol developer system. The BOLD objective was set to NA=0.6 and a fill factor of $\sigma = 0.5$ was used for the illumination. These features were all taken from the same die with an exposure dose of 1360 UCB units. UCB units are an arbitrary unit of dose use in this system since it has not been calibrated to an absolute standard, but 1000 UCB units are roughly 400 mJ/cm^2. Since the BOLD exposure system (shown in Fig. 8) employs the 3 mirror speckle reduction scheme described in chapter 6, the number of laser pulses needed for 2% unform dose is reduced from 2500 to 272. A minimum of 300 pulses are used in these exposures, resulting in the smooth edge profiles seen in Figs. 35 and 36.

Fig. 36 demonstrates the performance of the BOLD objective over the field. These 0.2μm line/space patterns were printed in the center of the field and at the edge of the field to a diameter of 0.96mm. This field diameter is greater than the 0.8mm diameter specified for the BOLD objective operating at NA=0.6 (see table 1). These images were also taken from the same die as Fig. 36 with an exposure of 1360 UCB units. Resolving 0.2μm line/space patterns at a field diameter of 0.96mm demonstrates the quality of the 213nm BOLD objective and the high stability and precise focus control of this exposure tool.

7.7 Conclusions and Future Work

Two optical lithography systems have been built to investigate the possibility of 213nm lithography. An all-reflective objective (Schwarzschild) an all-refractive objective (213nm BOLD) both demonstrated near diffraction-limited performance. The Schwarzschild objective possessed a severely limited field (200μm) while the BOLD objective demonstrated diffraction limited performance outside its specified 0.8mm diameter field.

Clearly the greatest room for improvement in the work done so far is in the resist system. PMMA has several fundamental properties that prevent it from being a high contrast sensitive resist for use in 213nm lithography. Its ease of use and ready availability make it suitable for use as a tool to test basic system performance, but high aspect ratio patterns near the resolution limit of the BOLD objective will require an improved resist process.

A second major improvement in the optics would be to add a polarization rotation and filter system to improve the signal to background ratio generated by the PMT in the focus signal system. The polarization scheme is shown in Fig. 37. The output from the 213nm laser is 100% linearly polarized out of the plane of the paper in Fig. 37. After passing through the mask the laser radiation is changed to circular polarization by a quarter-wave plate. After being imaged by the objective, reflecting from the wafer, and passing back through the objective, the radiation is changed from circular to linear polarization by the quarter-wave plate but orthogonal to the incident polarization. This reflected light passes through the mask and is reflected by a beamsplitter coated from maximum reflection of the returning polarization and minimum reflection for the original polarization. The unwanted reflections from the field lens and mask will still possess the original polarization and thus will be rejected by the beam splitter, leaving only the desired radiation to reach the PMT.

A further refinement of this system would be to place a lens between the beamsplitter and the PMT to form an image of the mask in front of the PMT. The focus pattern could be placed in the center and four corners of the mask so that a focus signal from different regions

of the field could be monitored by blocking the undesired areas at the image formed in front of the PMT. This scheme would require the beamsplitter to have a high optical quality surface polish to allow proper imaging of the mask.

One final comment about the present system is the size of the field illuminated by the present illuminator. The encouraging results obtained so far at the edges of the field warrant a further investigation of this lens' performance for greater field sizes. The limiting factor for field size in the current system in the diameter of the field lens. Increasing this lens diameter from 1 inch to 1.5 inch would allow field sizes up to 1.6mm diameter. It is expected that the lens performance would degrade this far outside the specified field diameter of 0.8mm and it would be interesting to measure this degradation.

References

1. J.H. Bruning and W.G. Oldham, "A Compact Optical Imaging System for Resist Process and Lithography Research," *SPIE proc. of Optical/Laser Microlith.*, vol. 992, pp. 471-475, 1988.

2. GCA/Tropel, "213nm BOLD Specifications," *Sales Literature*, Nov. 1990.

3. E.A. Ash, in *Scanned Image Microscopy*, Academic Press, San Francisco, 1980.

4. T. Wilson and C.J.R. Sheppard, in *Theory and Practice of Scanning Optical Microscopy*, Academic Press, London, 1984.

5. W.G. Oldham, S.N. Nandgaonkar, A.R. Neureuther, and M. O'Toole, "A General Simulator for VLSI Lithography," *IEEE Trans. Elec. Dev.*, vol. ED26, pp. 717-722, 1979.

6. P. Van Pelt, "Processing of Deep-ultraviolet (UV) Resists," *SPIE proc. of Semi. Microlith.*, vol. 275, pp. 150-154, 1981.

7. J.S. Greeneich, "Developer Characteristics of Poly-(Methyl Methacrylate) Electron Resist," *J. Electrochem. Soc.*, vol. 122, no. 7, pp. 970-976, July 1975.

8. H.R. Philipp, H.S. Cole, Y.S. Liu, and T.A. Sitnik, "Optical Absorption of some Polymers in the Region of 240-170nm," *Appl. Phys. Lett.*, vol. 2, no. 13, pp. 192-194, Jan. 1986.

9. R.A. Ferguson, C.A. Spence, E.A. Reichmanis, L.F. Thompson, and A.R. Neureuther, "Investigation of the Exposure and Bake of a Positive Acting Resist with Chemical Amplication," *SPIE Proc. in Resist Tech. and Proc. VII*, vol. 1262, pp. 412-424, 1990.

10. A.L. Bogdanov, V.A. Nikitaev, A.A. Polyakov, and V.E. Tukish, "Image Formation Mechanism in Polymetylmetarilate (PMMA)-metractilic acid(MMA)-antracene Positive Photoresist Exposed by Pulsed Laser and Kinetics of its Development," *SPIE Proc. in Resist Tech. and Proc. VII*, vol. 1262, pp. 425-431, 1990.

11. F.N. Goodal and R.A. Moody, "Reduction Photolithography by Ablation at Wavelength 193nm," *Opt. Comm.*, vol. 57, no. 4, pp. 227-229, March 1986.

12. G.M. Davis and M.C. Gower, "Excimer Laser Lithography: Intensity-Dependent Resist Damage," *IEEE Elec. Dev. Let*, vol. EDL-7, no. 9, pp. 543-545, Sept. 1986.

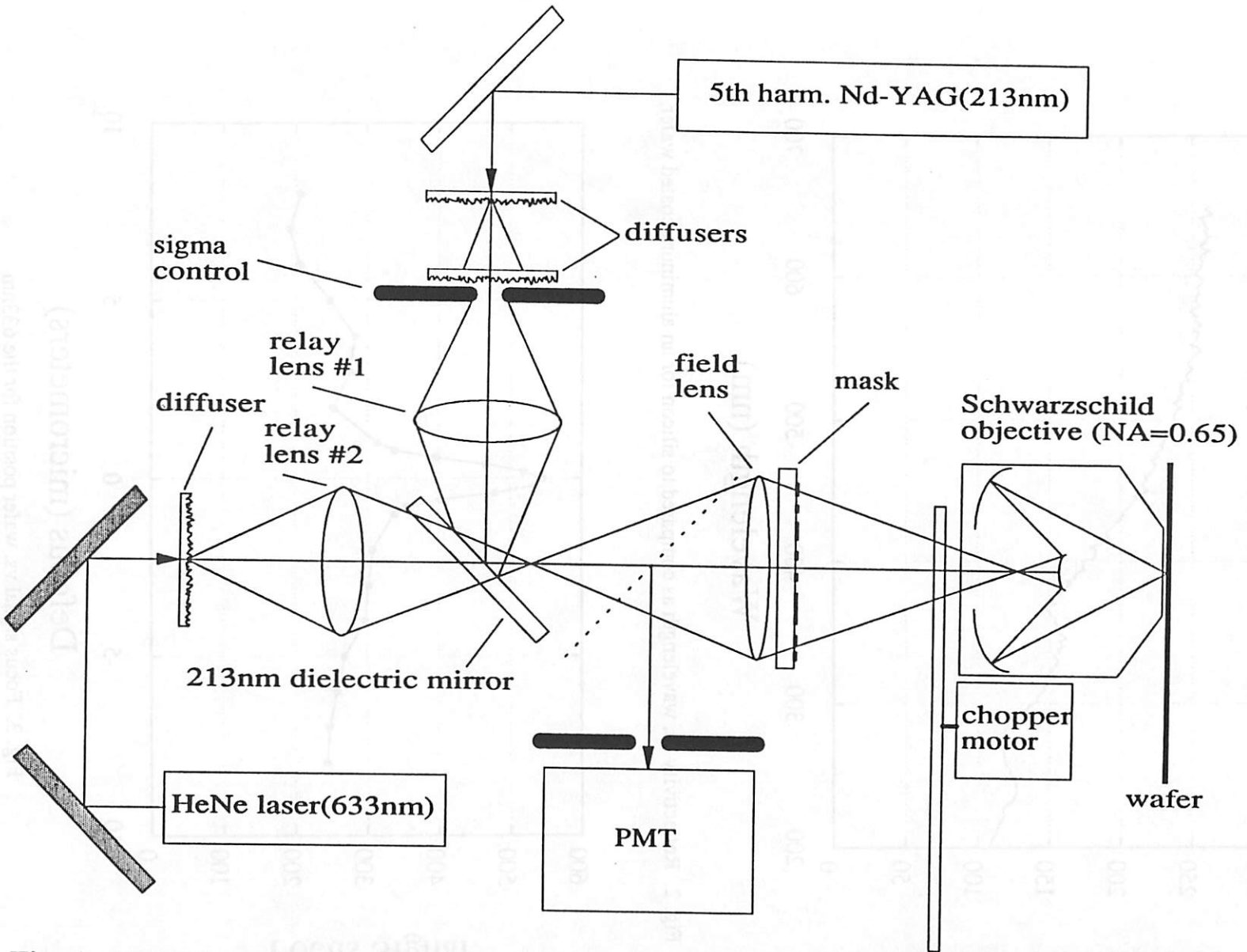

Fig. 1. Optical system for imaging with a Schwarzschild objective and 213nm radiation.

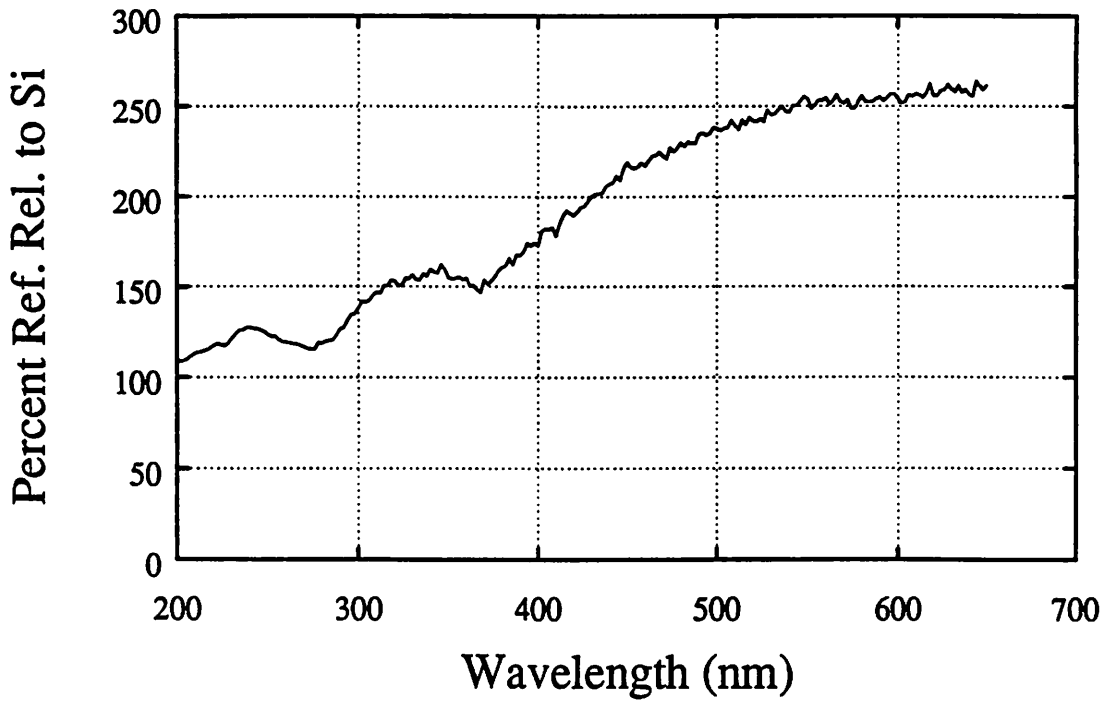

Fig. 2. Reflectivity vs. wavelength as compared to silicon for an aluminum coated wafer.

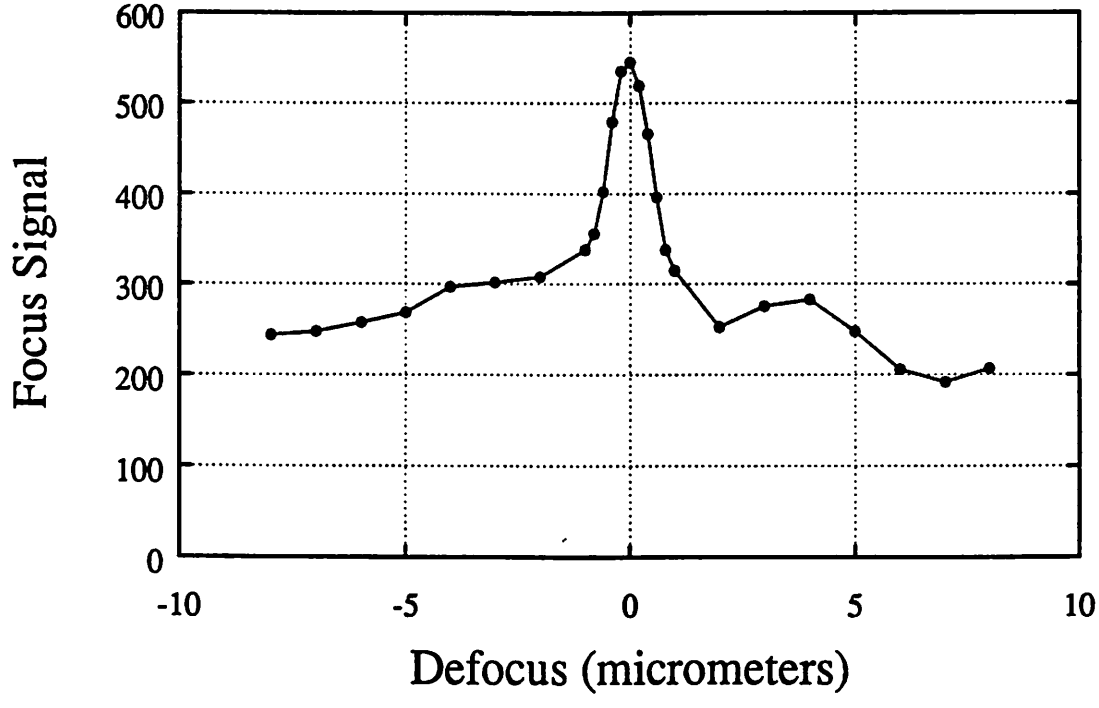

Fig. 3. Focus signal vs. wafer position for the 633nm focus system used with the Schwarzschild objective.

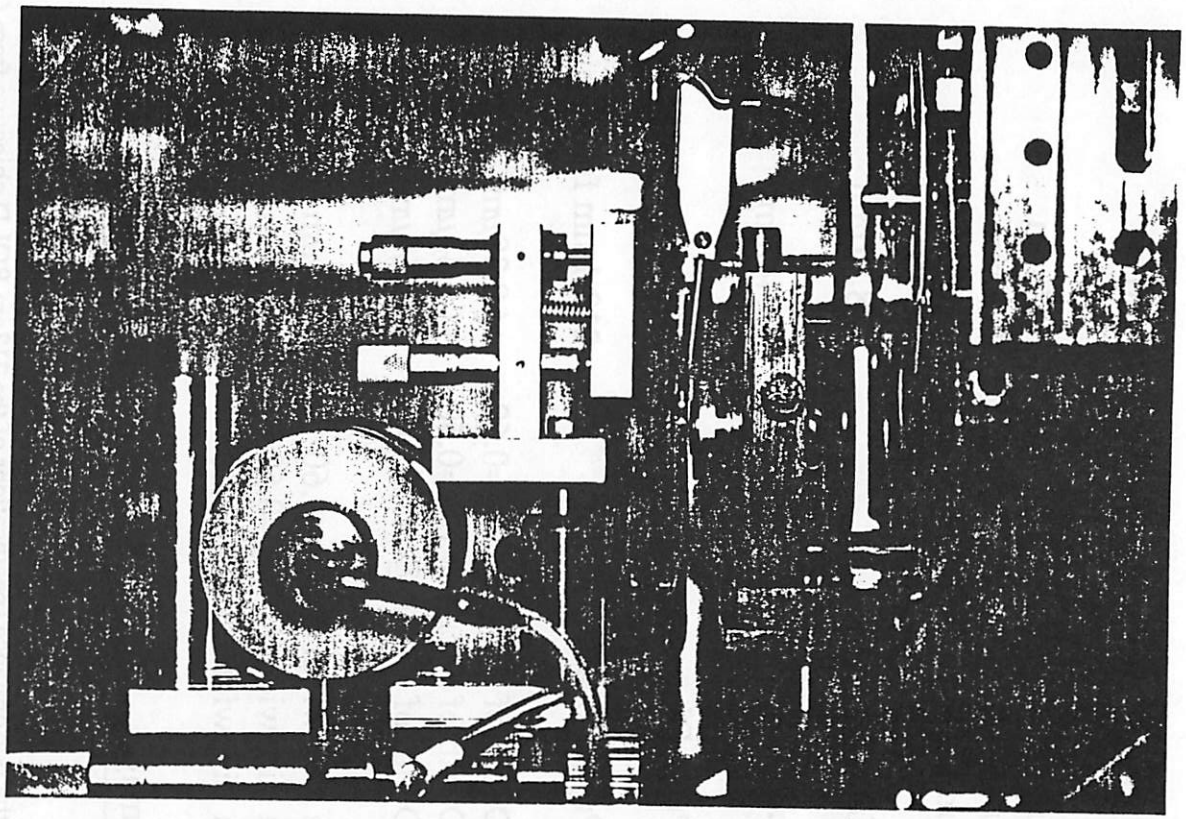

Fig. 4. Photograph of wafer chuck and objective for the Schwarzschild system.

213nm BOLD Objective Specifications	
Wavelength	213nm
Reduction Ratio	1:20
Image Diameter @ NA=0.60	0.80mm
Image Diameter @ NA=0.50	1.00mm
Image Diameter @ NA=0.40	1.10mm
Object to Image Distance	308.51mm
Effective Focal Length	12.44mm
Entrance Pupil Diameter	13.9mm
Entrance Pupil Location	213.1mm from object
Rayleigh Depth of Focus @ NA=0.60	+/-0.30μm
Rayleigh Depth of Focus @ NA=0.50	+/-0.43μm
Rayleigh Depth of Focus @ NA=0.40	+/-0.67μm
Production Linewidth @ NA=0.60	0.284μm
Production Linewidth @ NA=0.50	0.341μm
Production Linewidth @ NA=0.40	0.426μm
Vertex to Image	>2.5mm

Table 1. Listing of the performance specifications of the 213nm BOLD objective from GCA/Tropel.

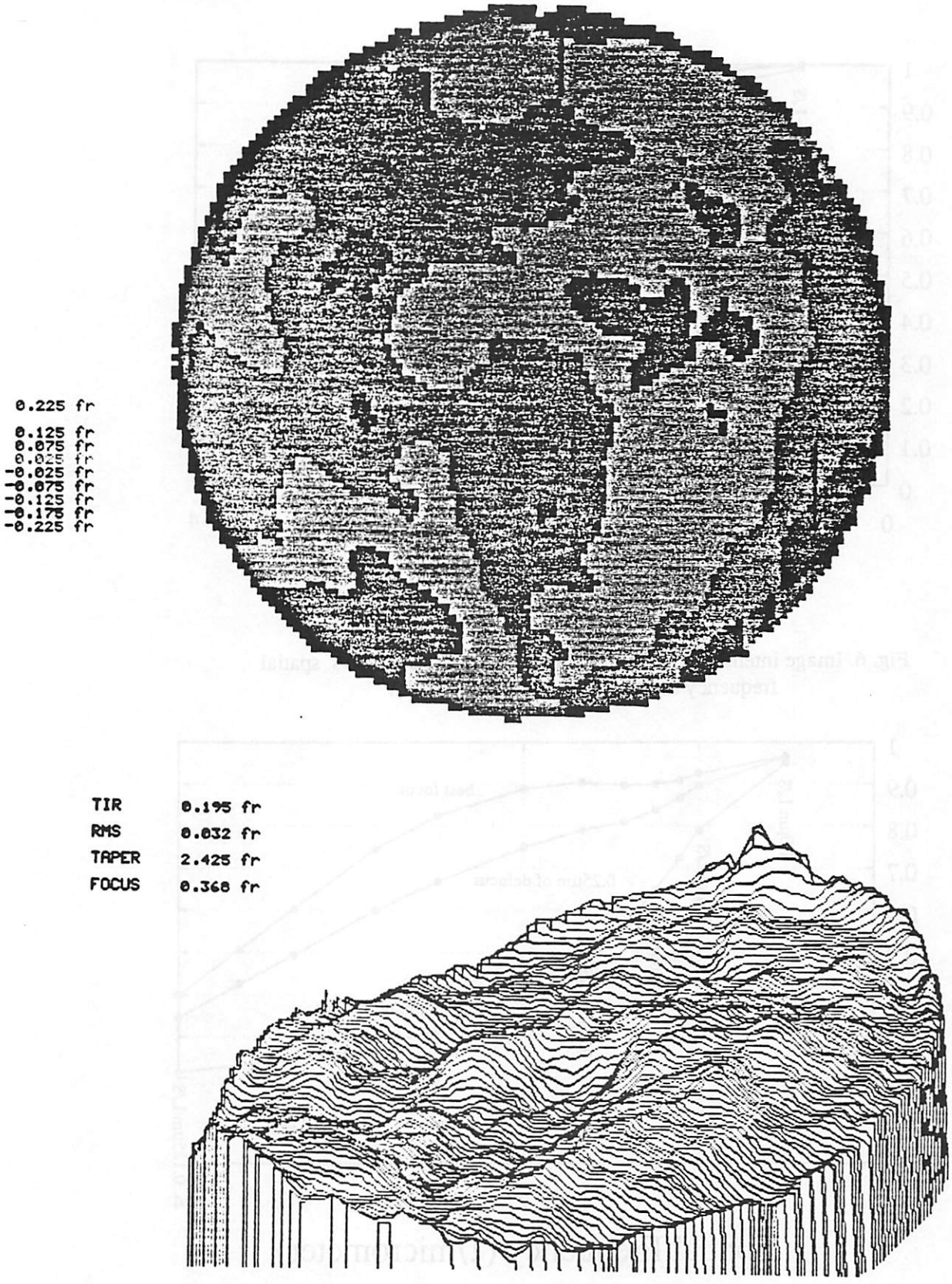

Fig. 5. Plot of wavefront aberration versus numerical aperture for the 213nm BOLD objective (measured with 257nm radiation).

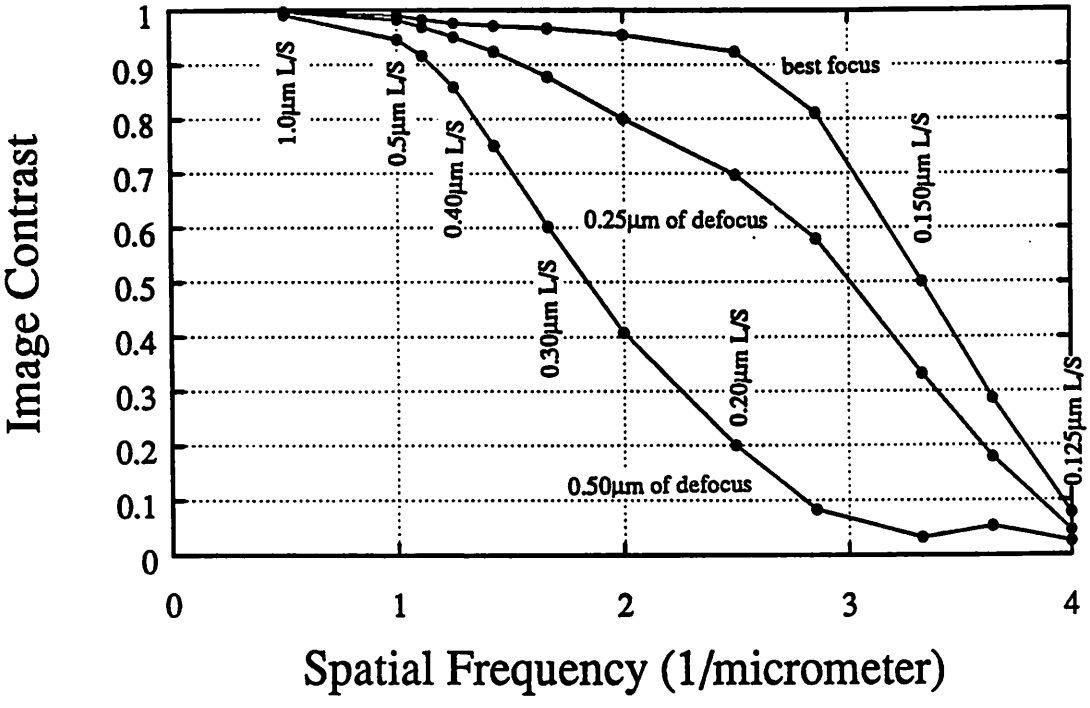

Fig. 6. Image intensity contrast for equal line/space patterns vs. spatial frequency for 3 values of defocus (σ=0.5).

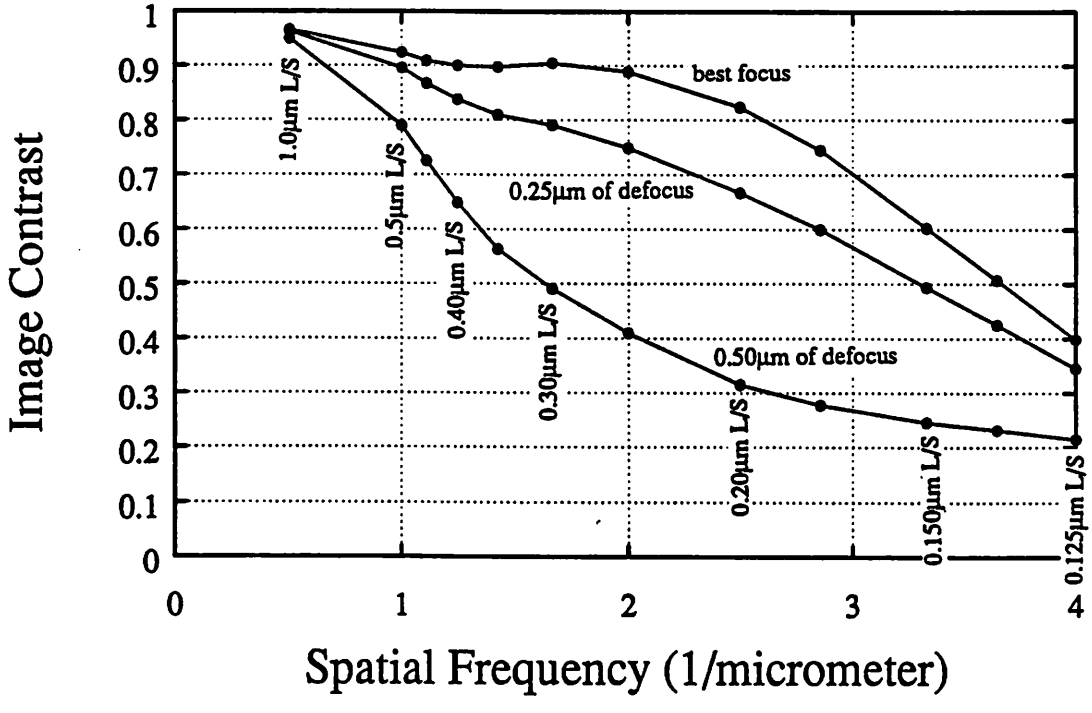

Fig. 7. Image intensity contrast for equal line/space patterns vs. spatial frequency for 3 values of defocus (σ=1.0).

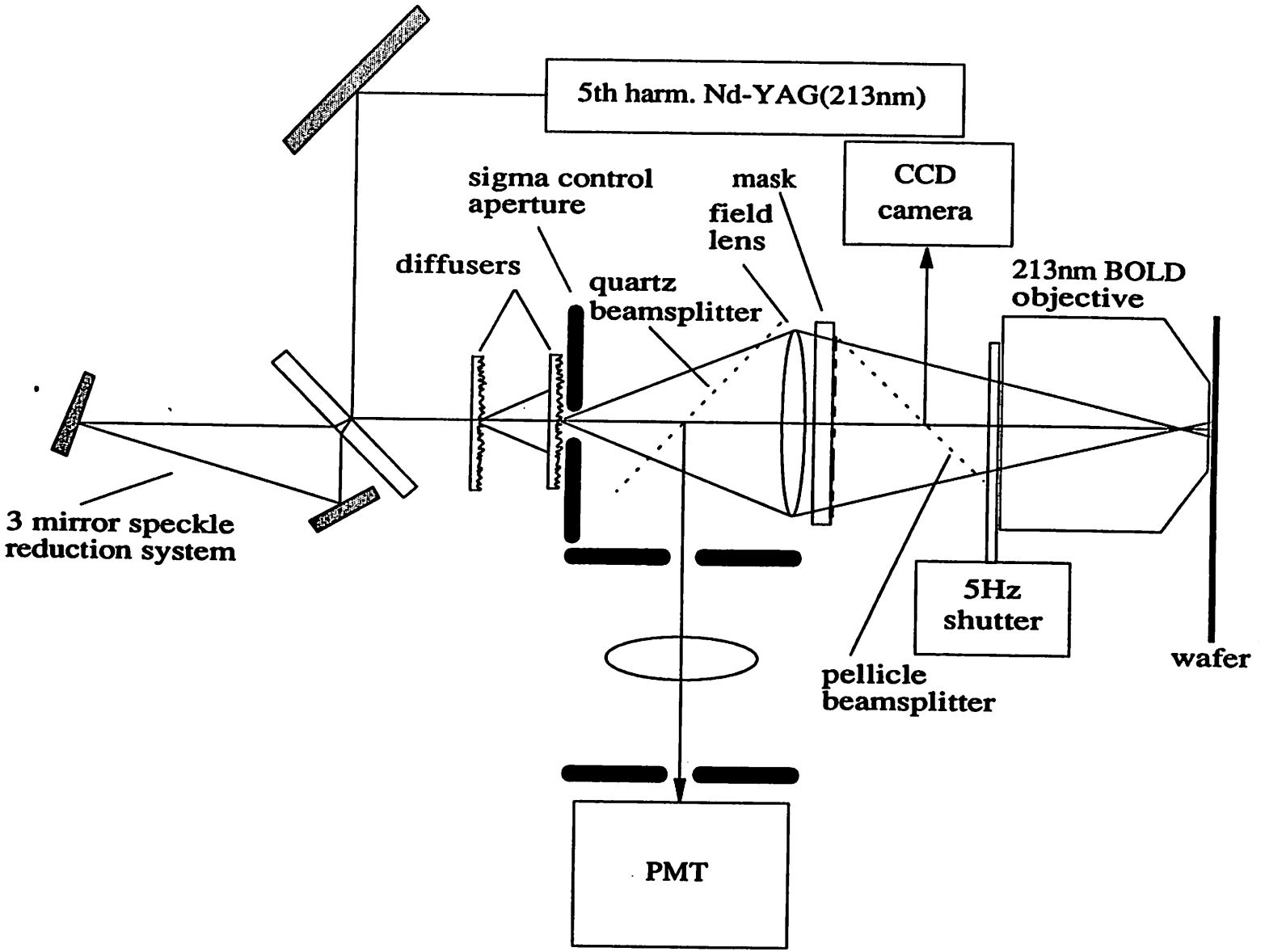

Fig. 8. Optical layout for the imaging system using the 213nm BOLD objective.

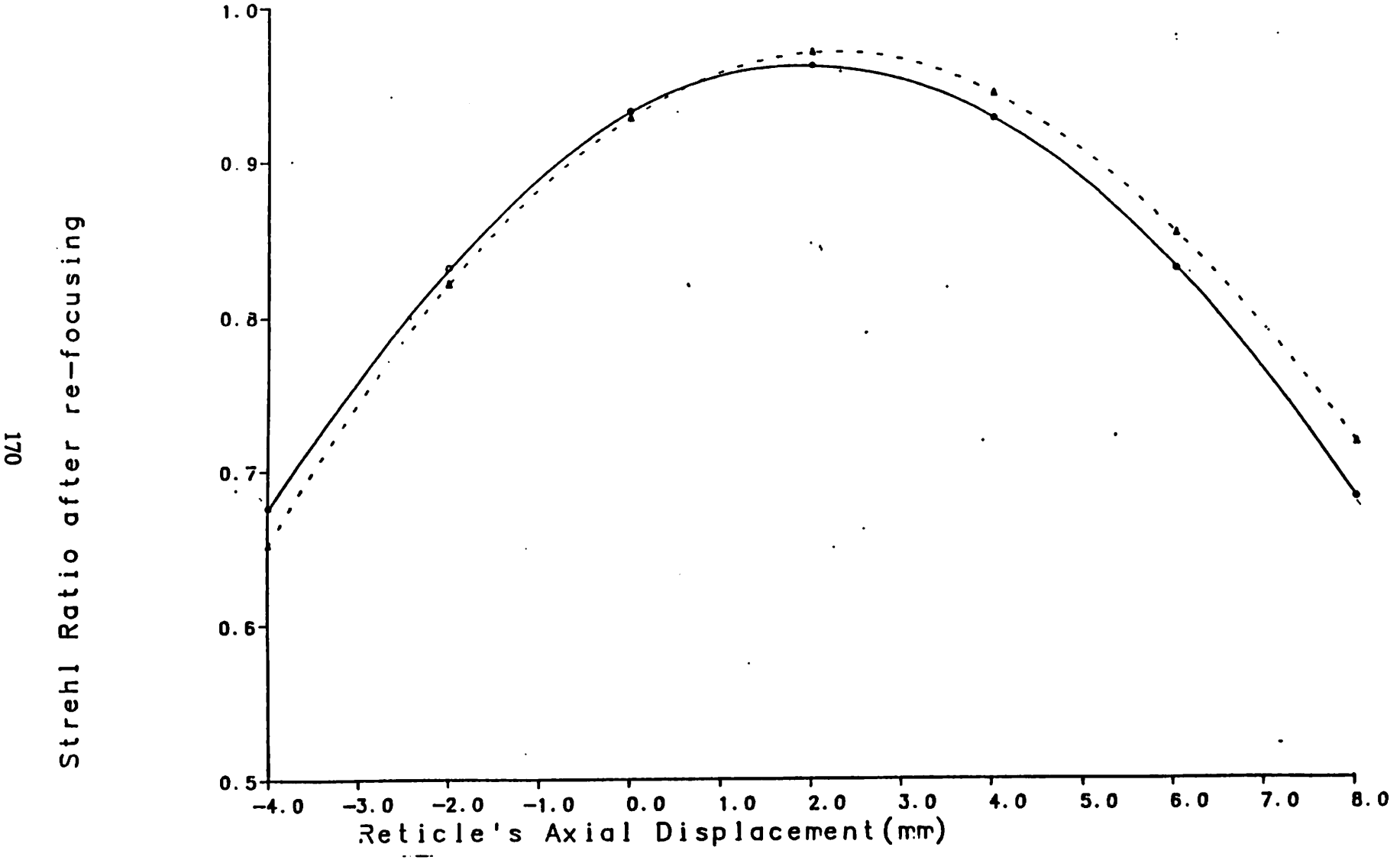

Fig. 9. Plot of Strehl vs. reticle position for the 248nm BOLD objective.

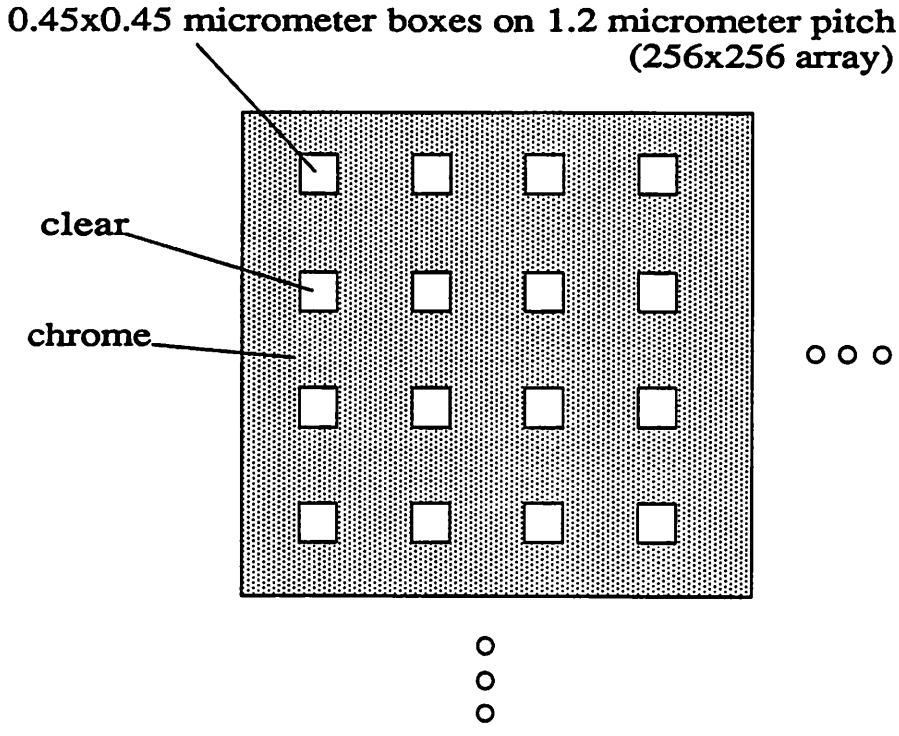

Fig. 10. Mask layout and dimensions for producing the focus signal.

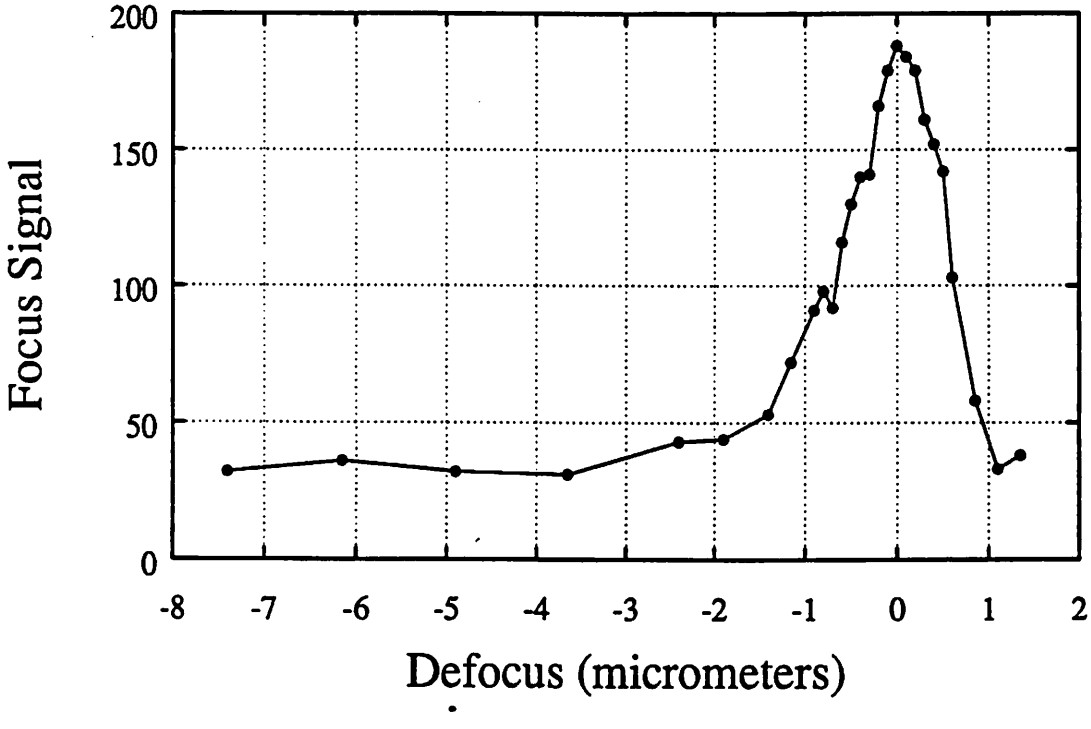

Fig. 11. Measured focus signal versus wafer position (converted from mask position) for BOLD focus system.

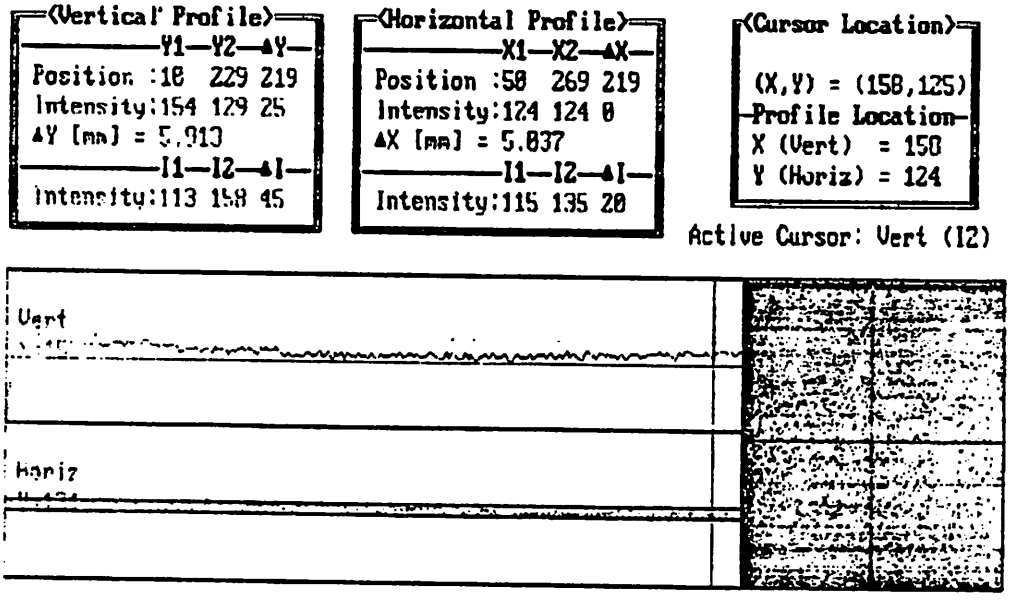

Fig. 12. Illumination uniformity at the center of the field as measured by the CCD camera.

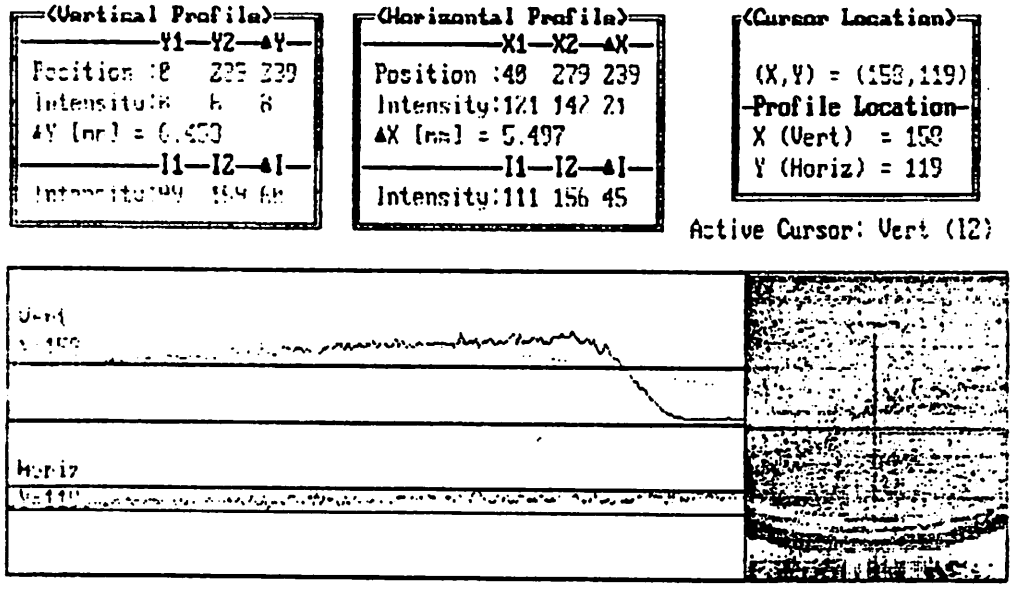

Fig. 13. Illumination uniformity at the edge of the field as measured by the CCD camera.

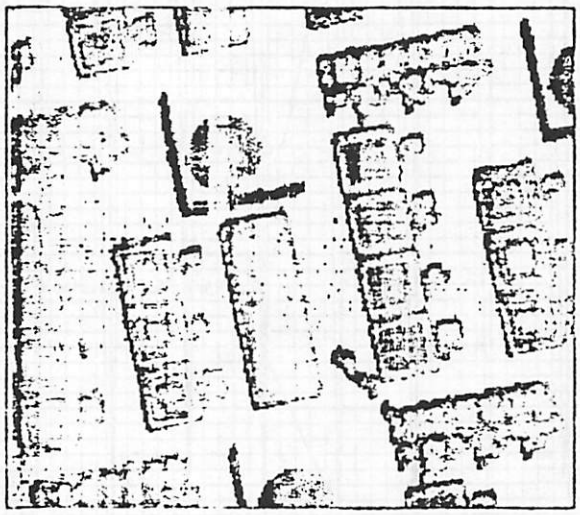

Fig. 14. Field intensity with mask in place as measured by the CCD camera.

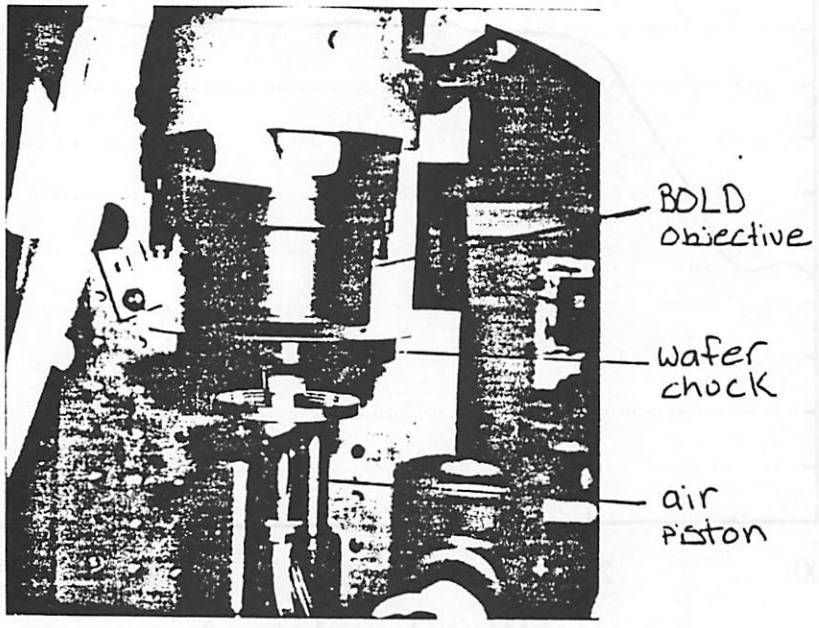

Fig. 15. Photograph of wafer chuck and air piston system.

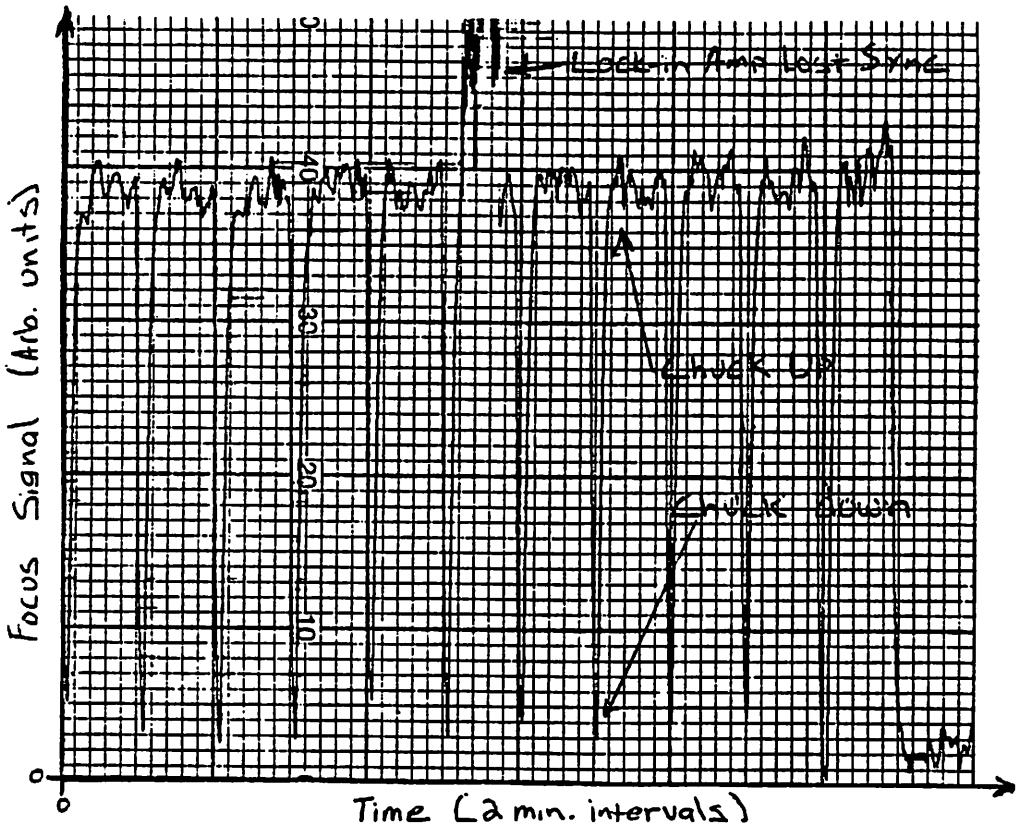

Fig. 16. Focus signal vs. time as the wafer chuck is raised and lowered.

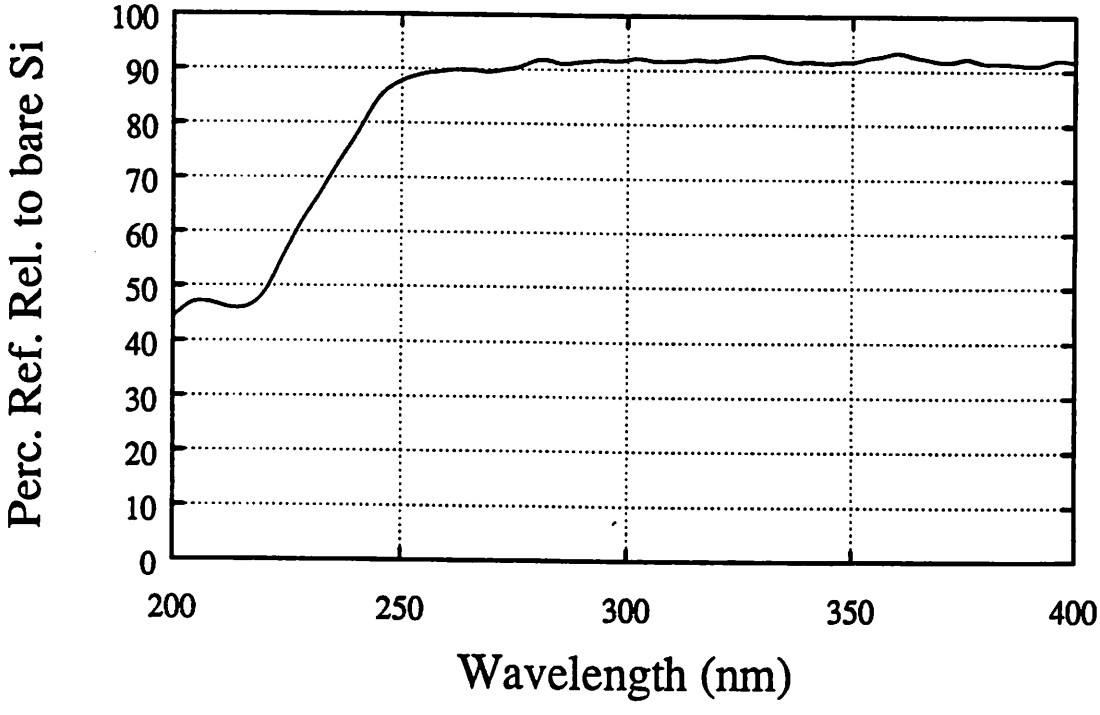

Fig. 17. Transmission vs. wavelength for a 1.1μm thick sample of 950K PMMA.

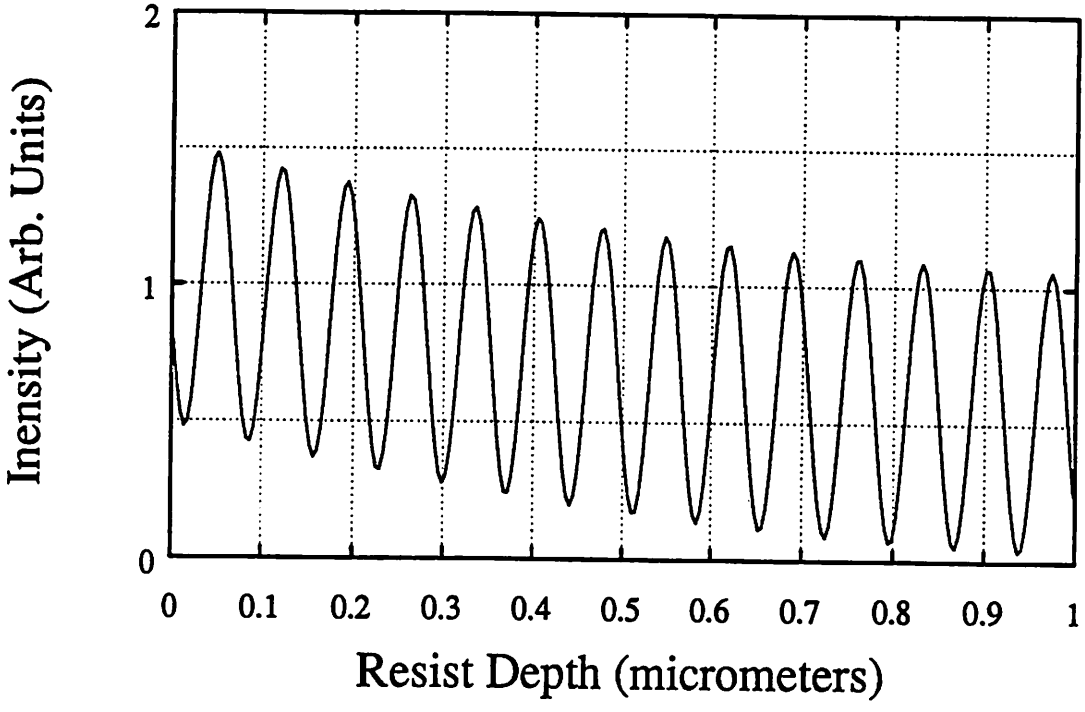

Fig. 18. SAMPLE simulation of intensity vs. depth in resist for PMMA on silicon.

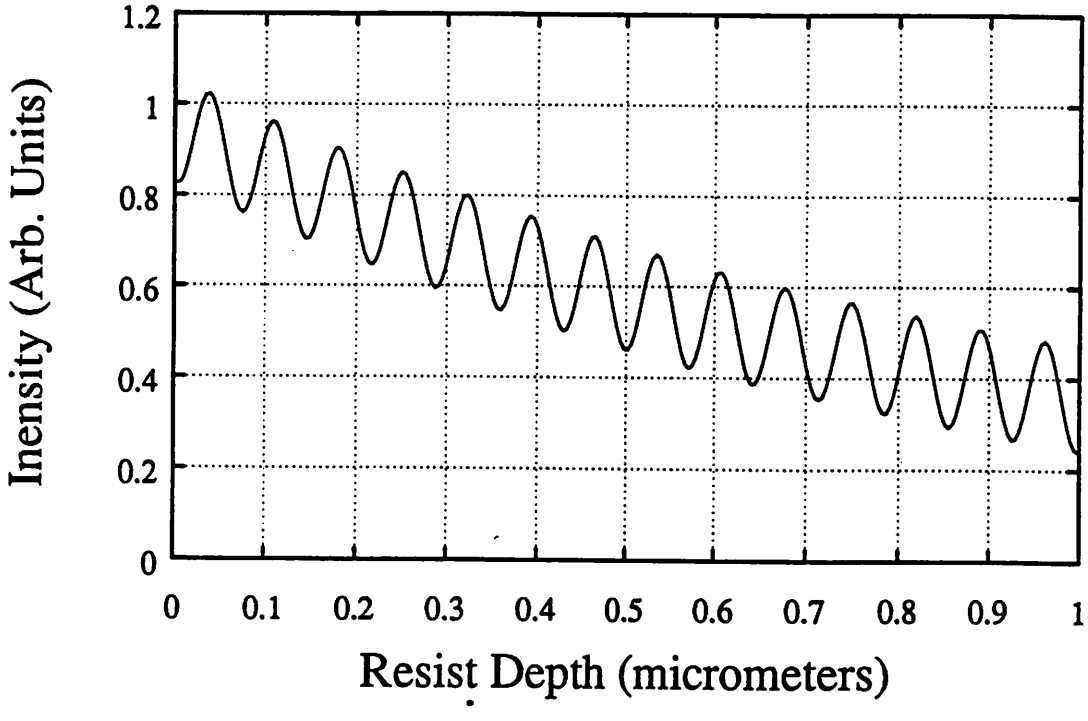

Fig. 19. SAMPLE simulation of intensity vs. depth in resists for PMMA/AZ2400/Si stack.

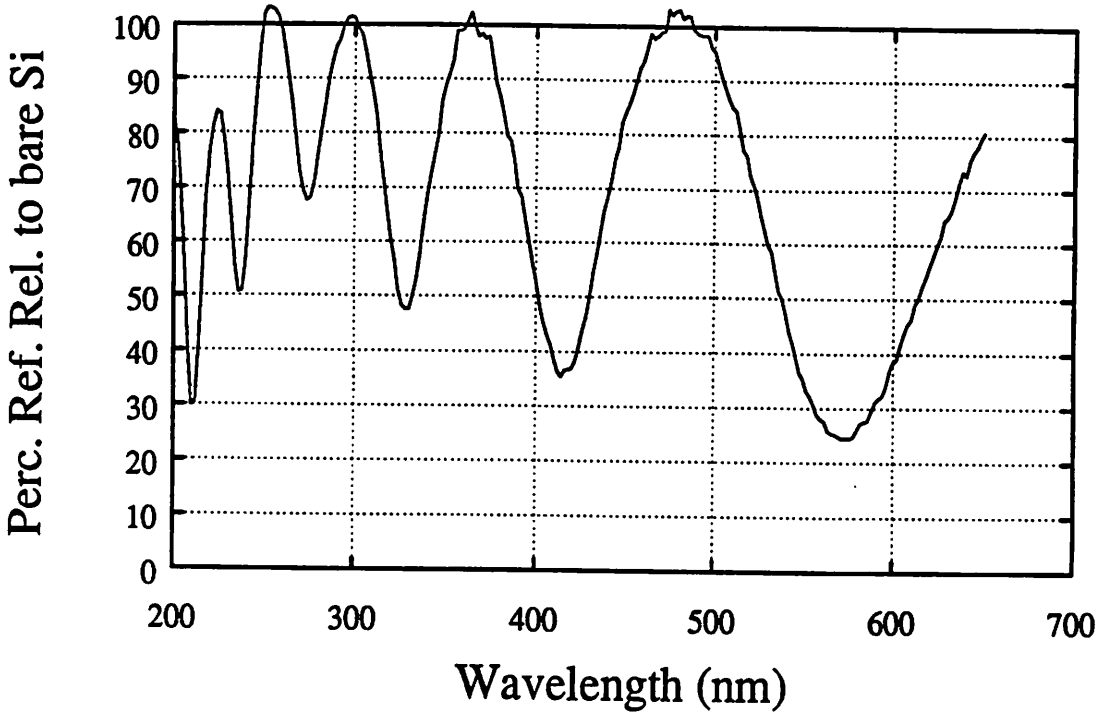

Fig. 20. Measured reflectivity vs. wavelength for PMMA on silicon.

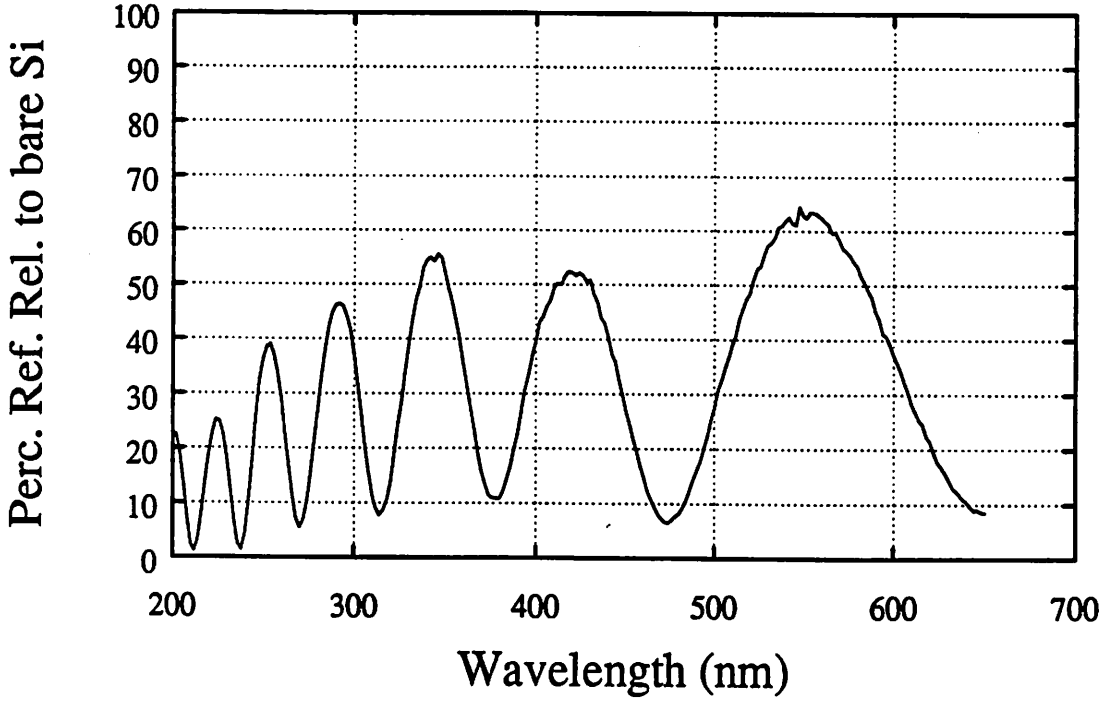

Fig. 21. Measured reflectivity vs. wavelength for PMMA/AZ2400/Si.

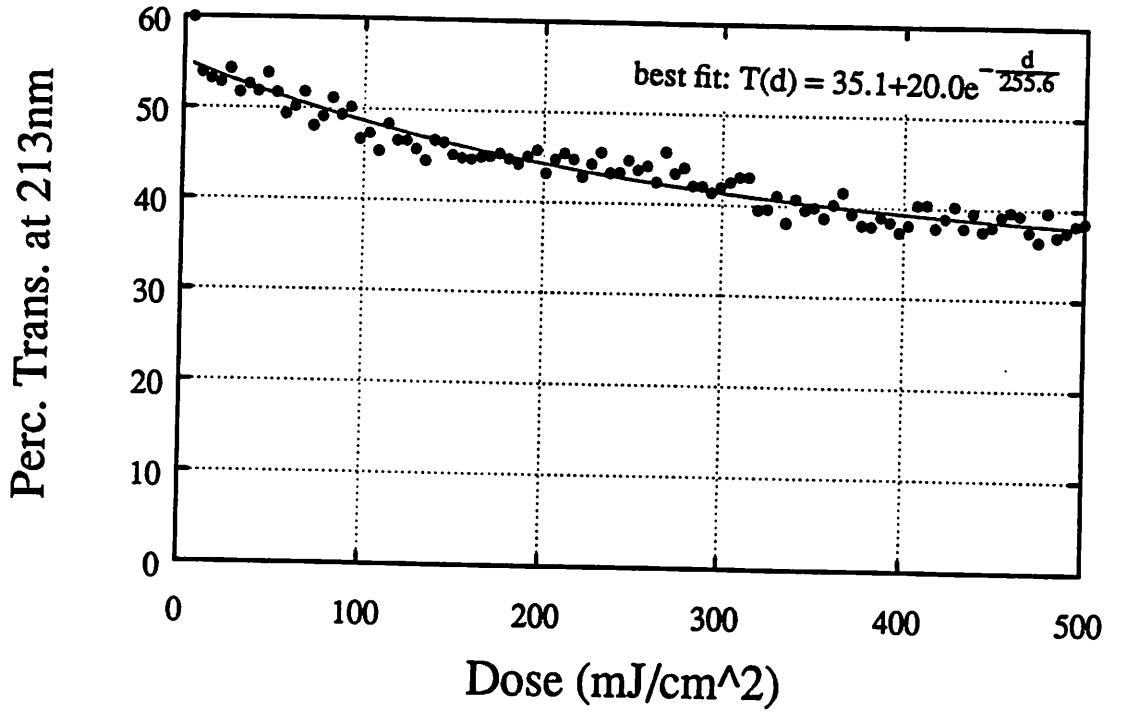

Fig. 22. Measured transmission at 213nm vs. dose for a 1.1μm thick sample of 950K PMMA.

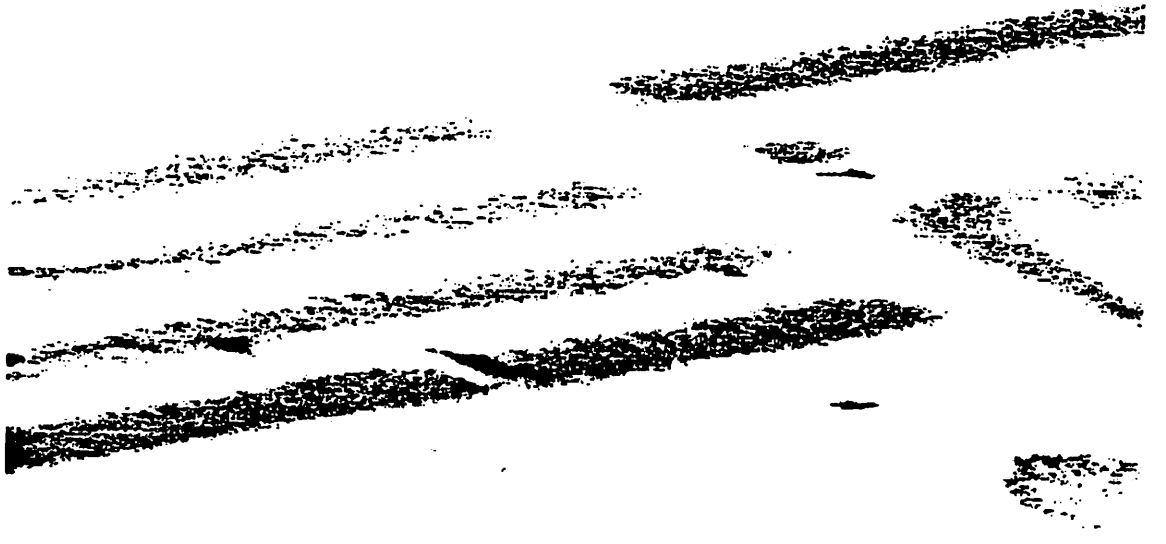

Fig. 23. SEM photograph of 1μm line/space patterns in ablated PMMA.

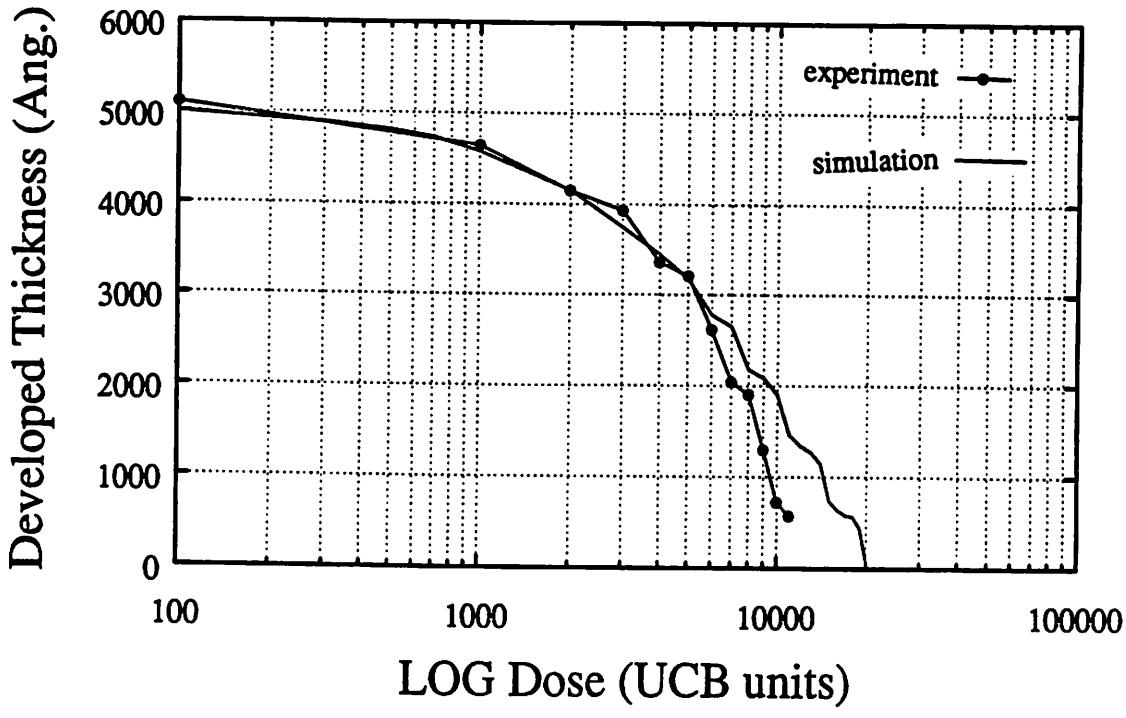

Fig. 24. Thickness remaining vs. dose for 5800 angstroms of 950K PMMA exposed with 213nm radiation and developed in pure MIBK.

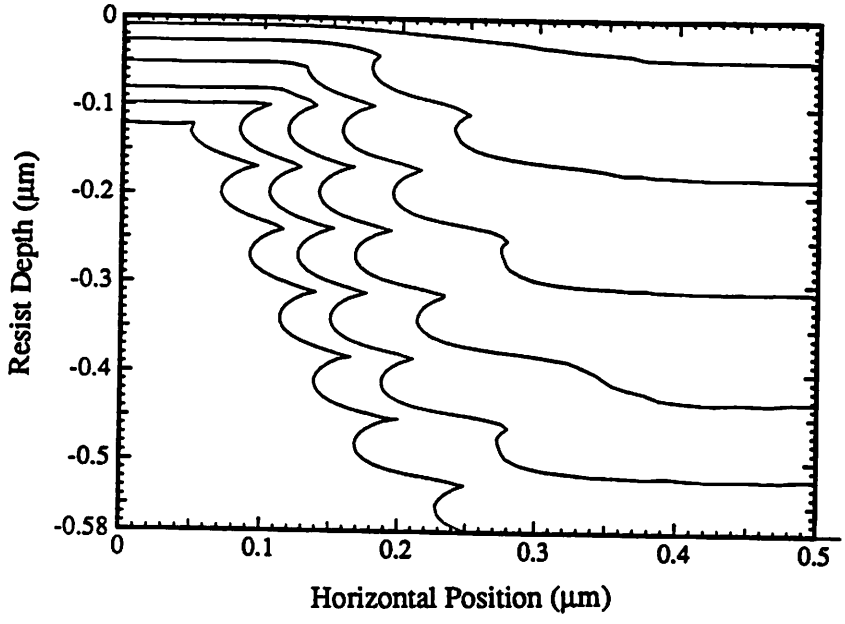

Fig. 25. SAMPLE simulation of 0.5μm L/S with PMMA on bare silicon developed in pure MIBK.

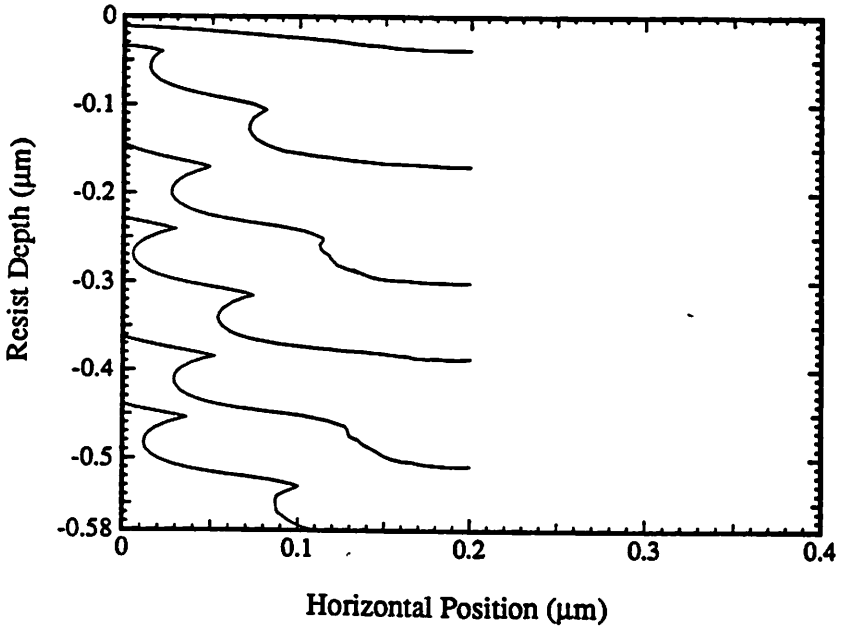

Fig. 26. SAMPLE simulation of 0.2μm L/S with PMMA on bare silicon developed in pure MIBK.

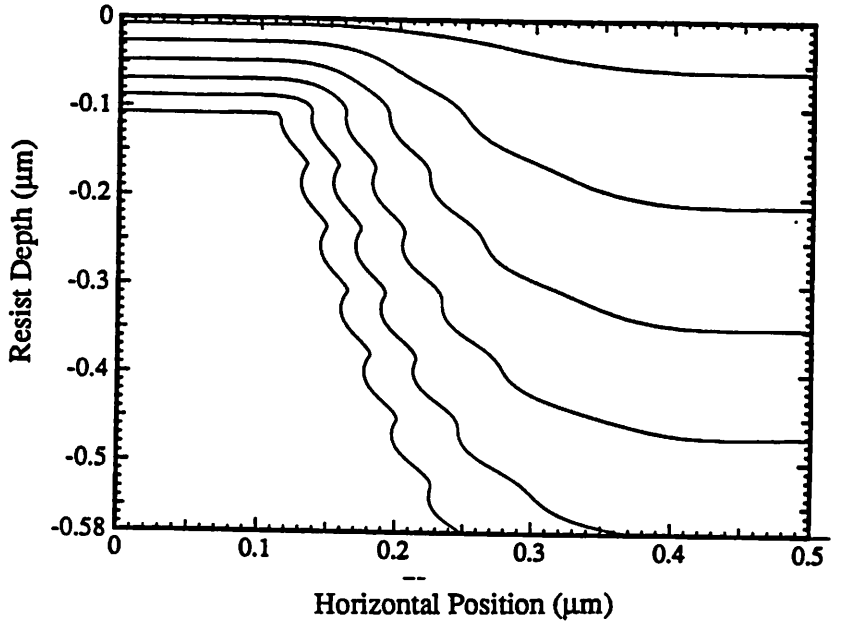

Fig. 27. SAMPLE simulation of 0.5μm L/S with PMMA/AZ2400/Si developed in pure MIBK.

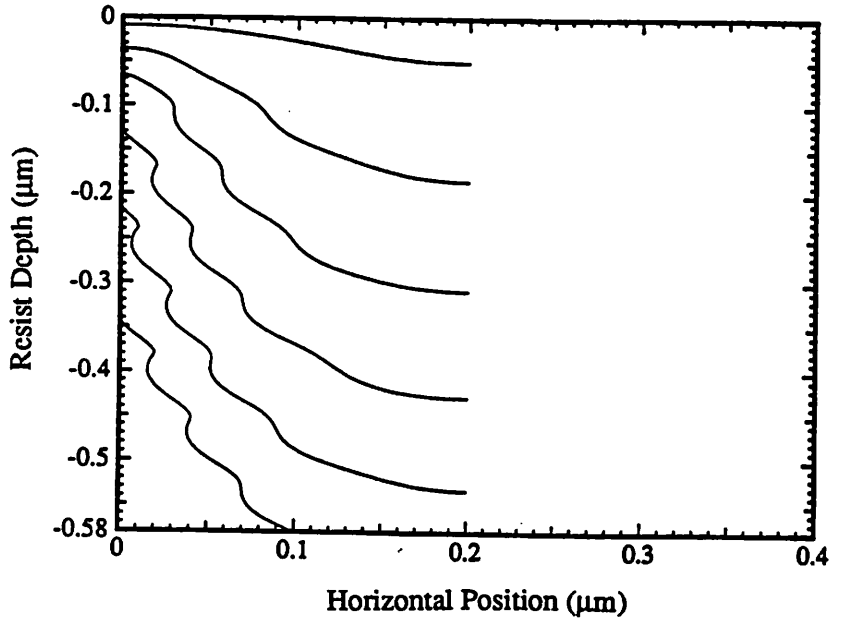

Fig. 28. SAMPLE simulation of 0.2μm L/S with PMMA/AZ2400/Si developed in pure MIBK.

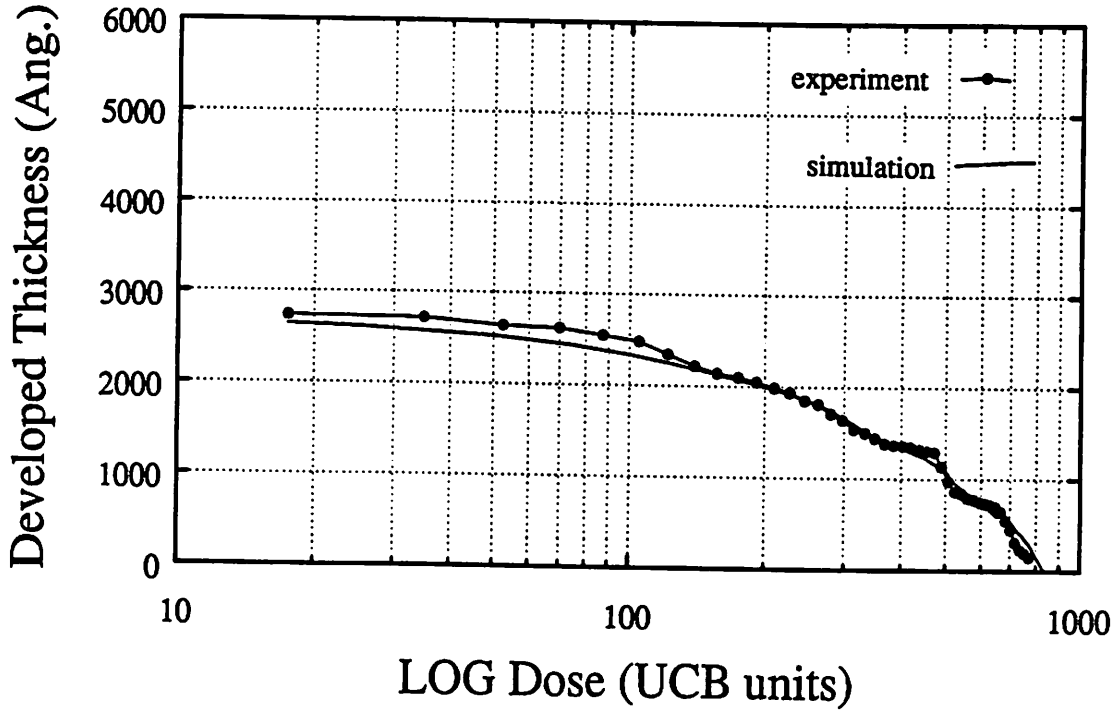

Fig. 29. Thickness remaining vs. dose for 5800 angstroms of 950K PMMA exposed with 213nm radiation and developed in 2:1 MEK:ethanol.

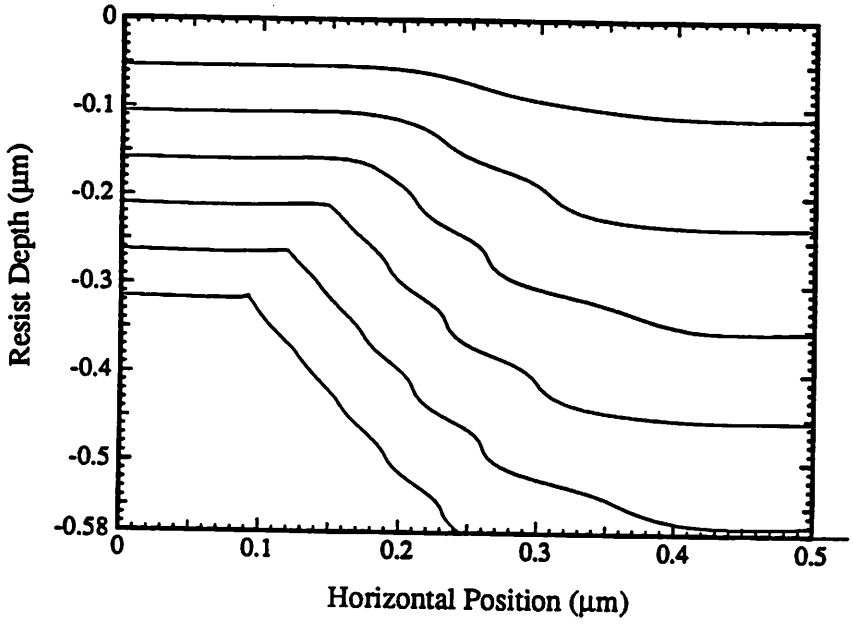

Fig. 30. SAMPLE simulation of 0.5μm L/S with PMMA on bare silicon developed in 2:1 MEK:ethanol.

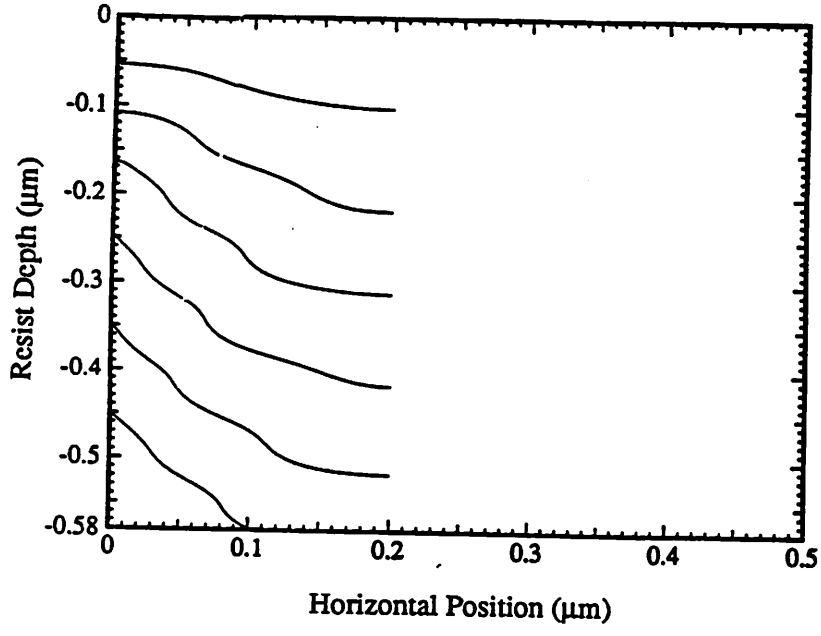

Fig. 31. SAMPLE simulation of 0.2μm L/S with PMMA on bare silicon developed in 2:1 MEK:ethanol.

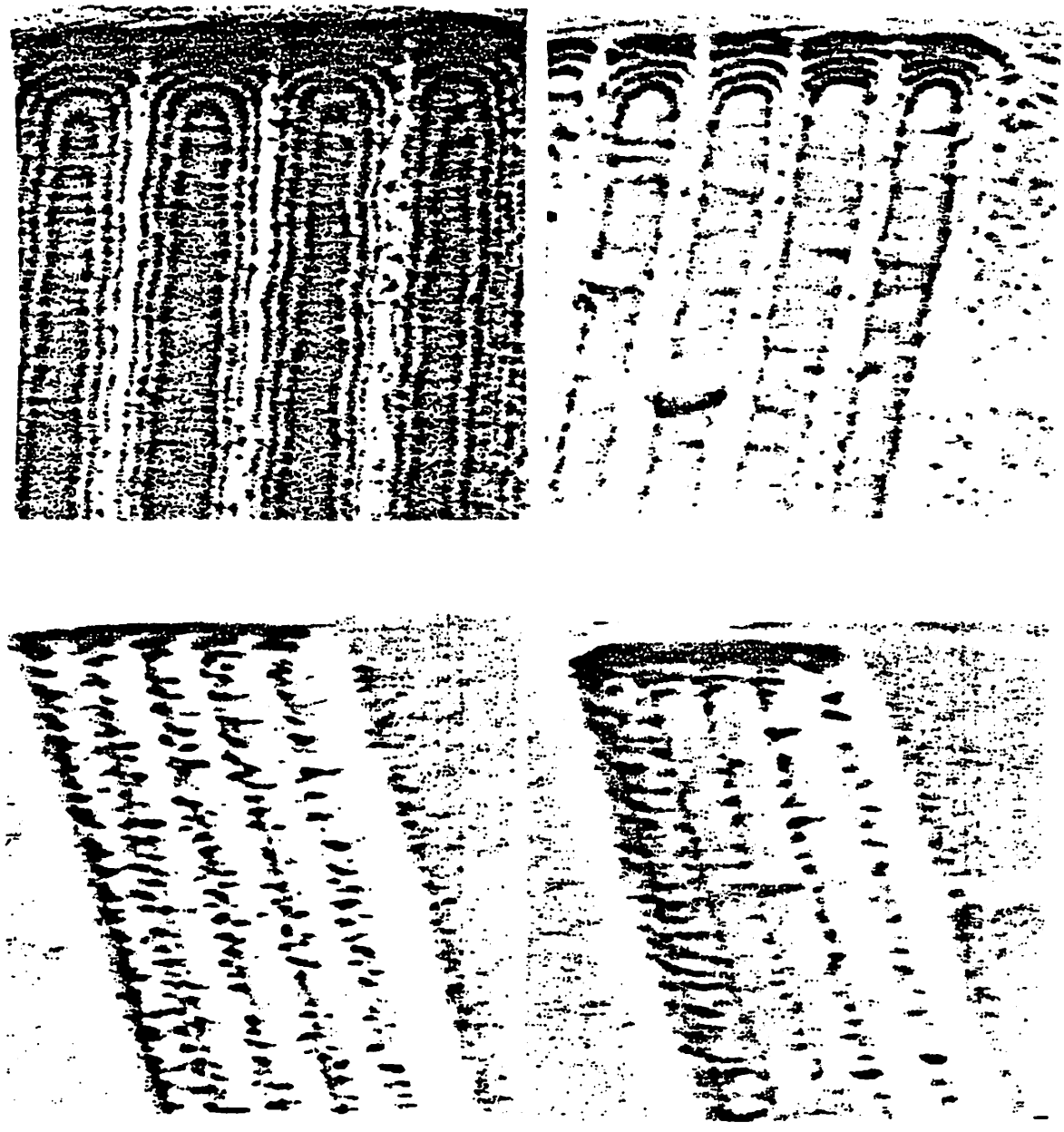

Fig. 32. Line/space features printed in PMMA with the Schwarzschild objective.
Feature sizes: 0.4μm (upper, left), 0.3μm (upper, right),
0.25μm (lower, left), and 0.2μm (lower, left).

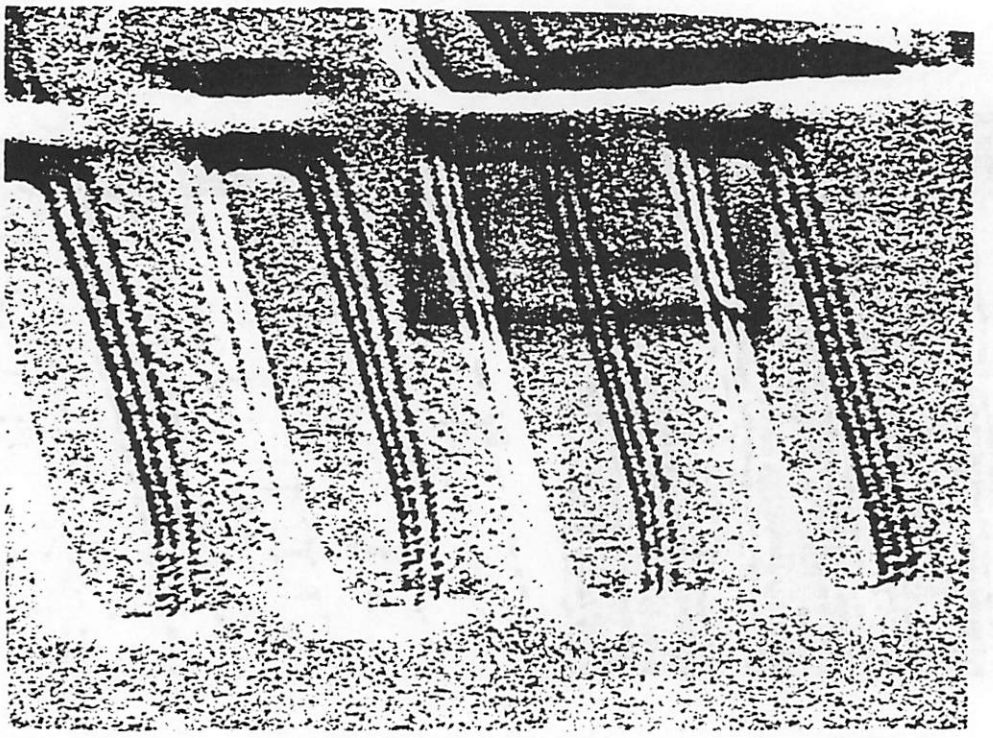

Fig. 33. 1μm line/space patterns printed with rotating diffuser.

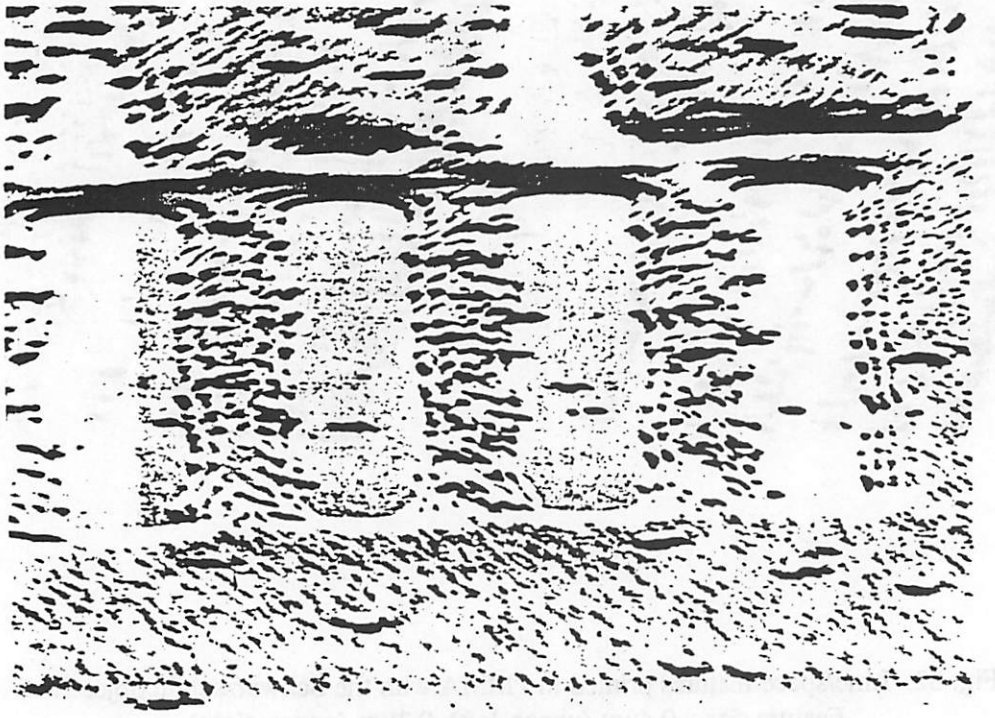

Fig. 34. 1μm line/space patterns printed with stationary diffuser.

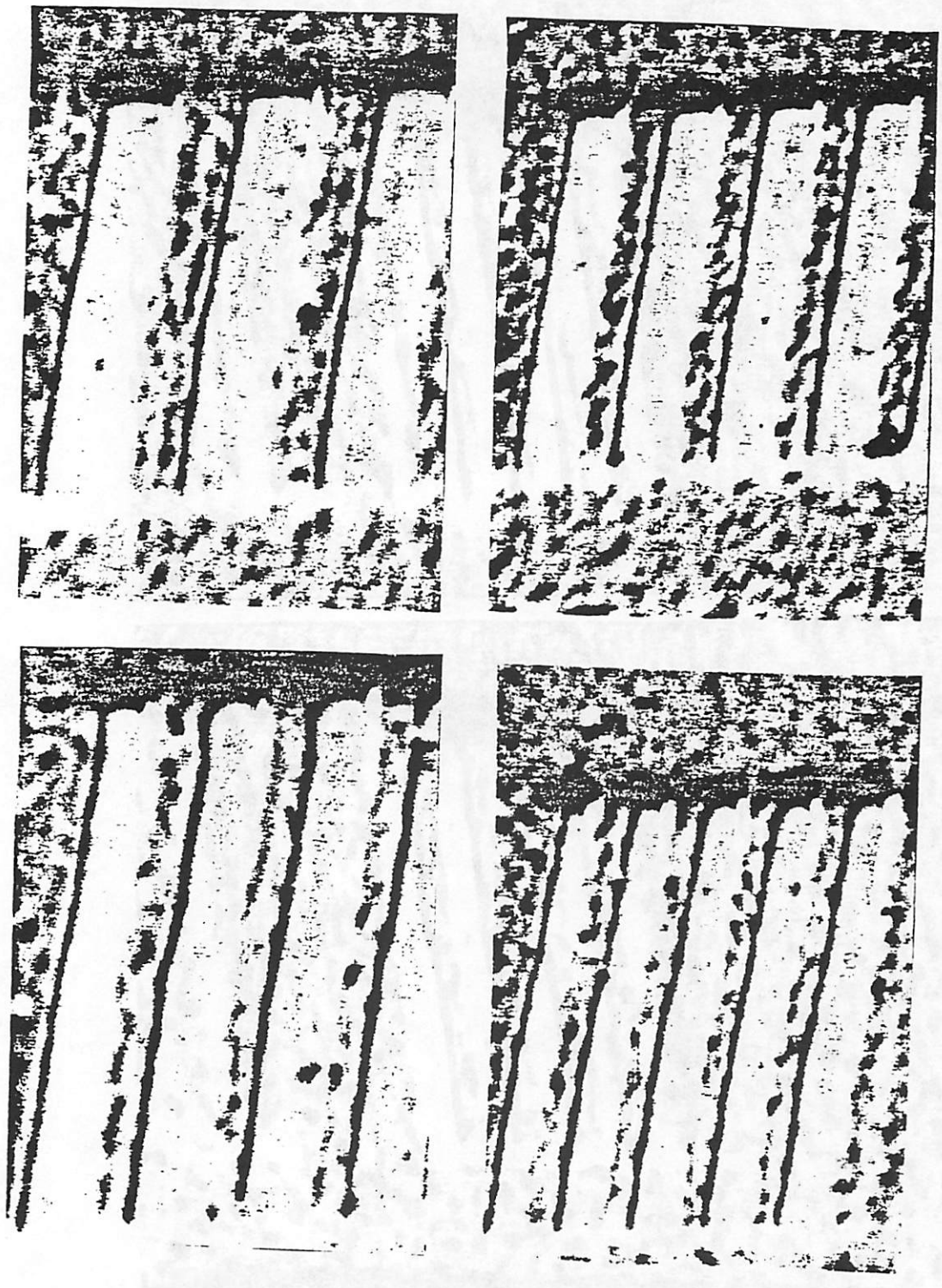

Fig. 35. Line/space features printed in PMMA with the 213nm BOLD objective.
Feature sizes: 0.5μm (upper, left), 0.4μm (upper, right),
0.3μm (lower, left), and 0.25μm (lower, left).

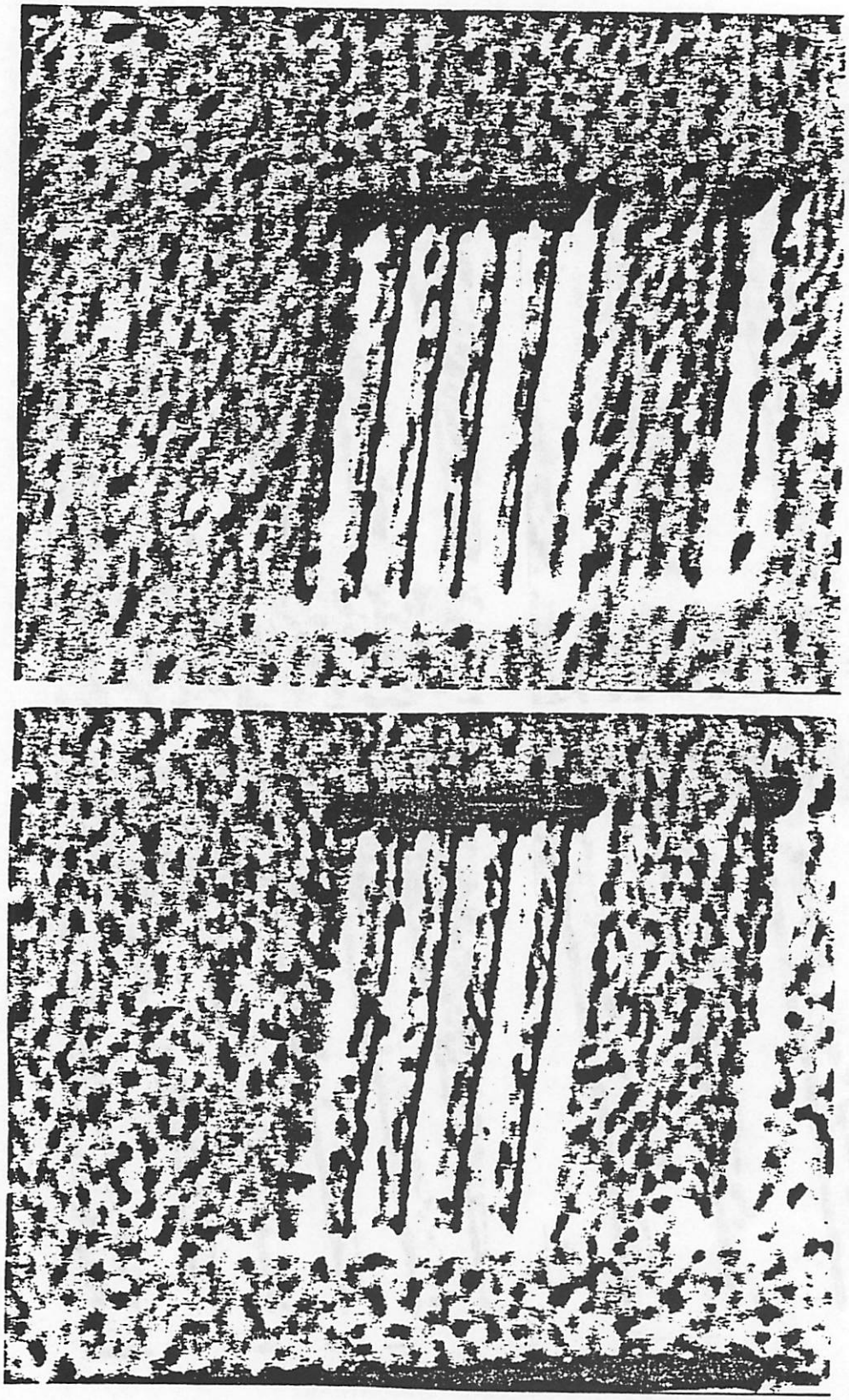

Fig. 36. 0.2μm line/space features printed in PMMA with the 213nm BOLD objective. The upper picture is at the center of the field and the lower is at a diameter of 0.96mm.

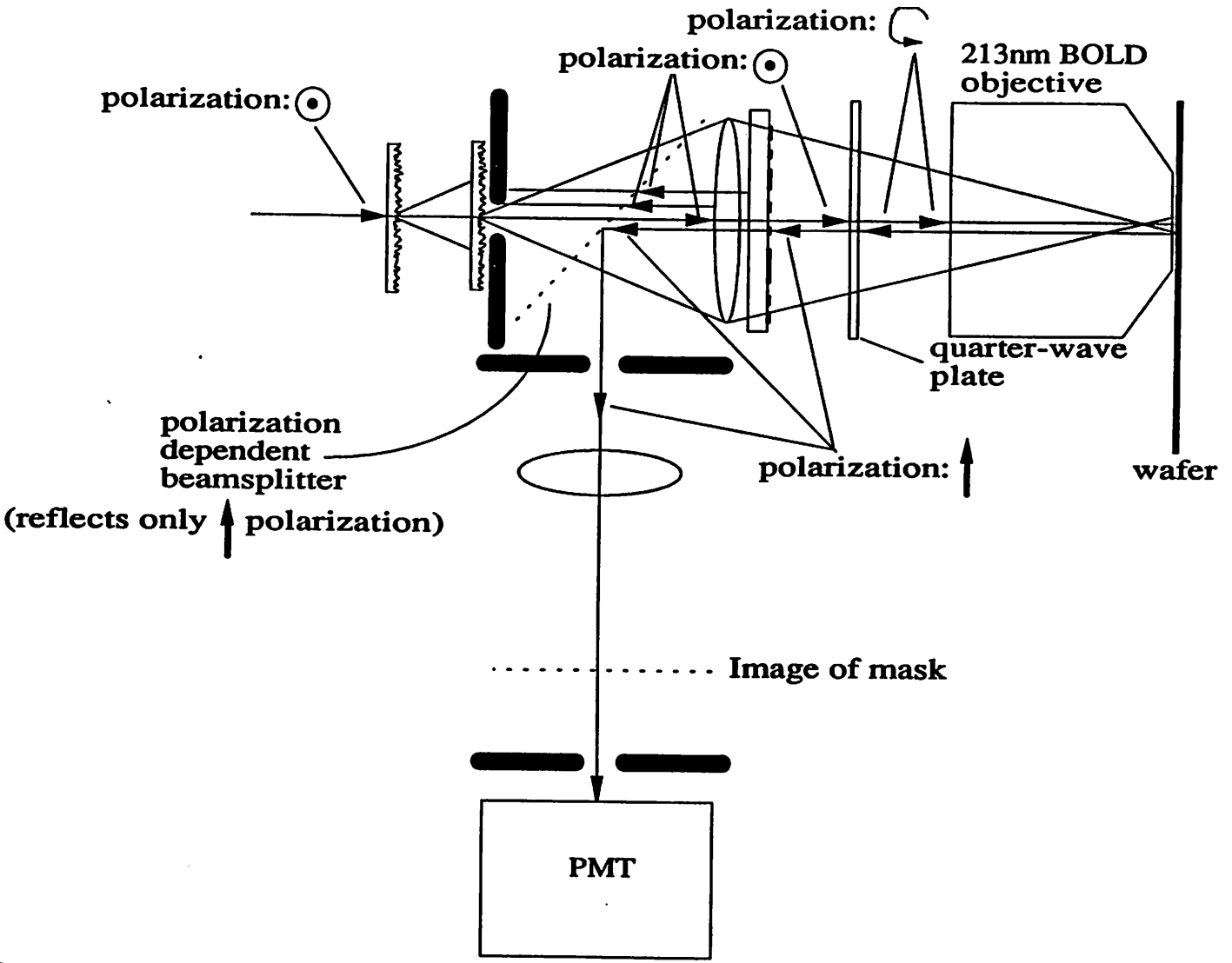

Fig. 37. Improved focus sugnal system using polarization to reject unwanted reflections.

Chapter 8
Conclusions and Future Work

8.1 Conclusions

This thesis has investigated the some of the issues involved with using pulsed lasers as sources for deep-UV lithography. Two very different laser sources were used in this investigation, a KrF excimer laser (248nm) and a quintupled Nd-YAG laser (213nm). The emphasis on the excimer source was long term material lifetime testing, while the work involving the Nd-YAG source centered on producing the 213nm radiation and conditioning it so as to be useful for microlithography.

A large body of work exists pertaining to KrF excimer lithography. Excimer lithography has become in recent years a well established tool with excimer steppers available from several stepper manufactures. Our hope in chapters 2 and 3 was to add to this body of knowledge with information which will help refine this field in the important area of materials aging. Use of pellicles to protect deep-UV masks is a well accepted practice and the many available candidate pellicles needed to be tested under consistent and controlled conditions. A clearly superior pellicle material has emerged from these tests narrowing the field for more extensive testing.

The work on optical fluids was motivated by the lack of detailed information on the optical properties of fluids in the deep-UV. Traditional glues and gels used in the visible region are opaque in the deep-UV and the variety of replacement materials is severly limited. Though fluids are less convenient to work with than glues or gels, they are the only alternative found so far which have adequate transmission in the deep-UV. The refractive index values obtained for these fluids are insufficiently precise for careful optical design but these initial measurements can be used to select a few promising candidates in the refractive index

region of interest.

Clearly, the materials testing performed with the KrF excimer laser should be repeated using the Quintupled Nd-YAG laser. To accumulate useful exposure doses in reasonable times will require a 213nm source with at least 10 times the average power as the current 213nm source. The speckle reduction schemes described in chapters 5 and 6 as well as the exposure system described in chapter 7 will also benefit enormously from a source which can produce several watts of 213nm power.

This thesis will conclude with the following section which describes a possible design for a 4W 213nm laser source. Certain portions of this design rely on technology not demonstrated by the current 213nm source. Conservative estimates have been made of the specifications for these components. The specifications used are within the values quoted to us by several suppliers and manufactures.

8.2 Second Generation 5th Harmonic Source

The key to building a high average power 213nm source is to increase in the pulse repetition rate above the 10Hz of the current system. Further increases in the pulse energy are possible but not by the factor of 20 over the current system needed to produce 4W of 213nm radiation in the second generation system. In fact, scaling back the energy per pulse and increasing the repetition rate by a greater factor offers many advantages, such as greater speckle reduction capability, greater dose control, and a reduction in the nonlinear aging of materials.

If the laser pulse duration is kept constant and the nonlinear crystal parameters are held constant, a small reduction in the 1064nm energy leads to a large decrease in 213nm output. The decrease in 213nm is proportional to the 5th power of the decrease in the 1064nm energy, as shown shown in the following equations:

$$P(2\omega) = \gamma_{11}(\omega)^2, \qquad 1$$

$$P(3\omega) = \gamma_{12} P(\omega) P(2\omega), \quad 2$$

and

$$P(5\omega) = \gamma_{23} P(2\omega) P(3\omega). \quad 3$$

Thus:

$$P(5\omega) = \gamma_{11} \gamma_{12} \gamma_{23} P(\omega)^5. \quad 4$$

Eqn. 4 shows that only small changes in the 1064nm energy lead to significant changes in the 213nm energy.

Since Eqns. 1 through 4 are based on the peak power at each wavelength, reducing the pulse duration while reducing the reducing the pulse energy will keep the peak power constant and thus the conversion efficiencies will remain the same. One cannot reduce the pulse duration indefinitely because of the inverse relationship between pulse duration and spectral linewidth. Fig. 1. shows the relation between pulse duration and linewidth for Fourier transform limited 213nm radiation. The current 213nm source is Fourier transform limited when operated in seeded mode. No laser can operate below the line labeled laser limit without violating the duality laws between frequency and time. The current 213nm source has a pulse duration of 4.2ns which corresponds to a spectral linewidth of 0.035pm. Unseeded, the current source operates well above the Fourier transform limit.

To obtain the full performance of today's all fused silica lens, the laser must operate with a linewidth below approximately 1pm. This sets an upper limit on the range within which the second generation source may operate (designated by the hashed region). Due to current equipment constraints, an operating point for the second generation source has been chosen with a pulse duration of 0.44ns ($1.0/\sqrt{5}$) giving a spectral linewidth of 0.34pm. This linewidth is safely within the lens requirements and leads to a coherence length of 13.4cm. This coherence length makes for a much more compact 3 mirror speckle reduction system (chapter 6). No longer must the delay arm be 1.2m long, now only 13.4cm is needed to fully

separate the delayed pulses. Reducing the 213nm pulse width from 4.2ns to 0.44ns requires a reduction in the 1064nm pulse width from 9.4ns to 1.0ns. Standard pulse carving techniques can attain this 1.0ns pulse width. To maintain peak powers similar to the current source, the pulse energy can be reduced by a factor of 9.4.

The proposed second generation 213nm source is shown in Fig. 2. This system is designed to produce 4mJ per pulse of 213nm radiation at repetition rate of 1000Hz, giving an average 213nm power of 4W. The system layout is very similar to the current system with an oscillator/amplifier configuration feeding the 5th harmonic conversion. The additional component in this diagram is the pulse carver placed between the oscillator and the amplifier. The pulse carver reduces the pulse duration from 9.4ns to 1ns prior to amplification.[1] The energies shown are calculated backward from the 213nm pulse energy. To maintain the same 7% overall 5th harmonic conversion efficiency demonstrated to the current system, 44mJ per pulse is required at 1064nm. The amplifier, with its saturation limited gain of 5, requires an input pulse energy of 8.8mJ. The energy input to the carver must be a factor of 9.4 higher than the output because of the reduction in pulse duration. This leads 82.7mJ per pulse from the oscillator at a 1000Hz repetition rate or 82.7W average power.

The average powers shown in this system are much higher than the current 213nm source. If flashlamps were used to pump the Nd-YAG rods, thermal gradients and lensing would degrade the cavity Q so severly as to make such higher average powers impossible with flashlamp pumping. Fortunately an alternative exists in laser diode pumping. The output from laser diodes in narrow band and can be tuned to match the absorption band of the Nd-YAG rod. This greatly reduces the rod heating and makes several hundred Watt average powers possible.[2]

The pulse carving method is inelegant and inefficient. Other methods of reducing the pulse duration are possible with stimulated Brillouin scattering as one example. Each merits

of each method must be weighed relative to the simplicity and ease of fabrication of the pulse carving method.

Improvements in the 5th harmonic conversion can reduce the required 1064nm pulse energy (see chapter 4) and should also be implemented in the second generation source. Any reduction in the required 1064nm pulse energy would allow an increase in the repetition rate with no additional Nd-YAG rod heating. Repetition rates higher than 1000Hz would further reduce the exposure time required for speckle reduction and thus increase the throughput of any lithography tool illuminated with this 213nm source.

There are no fundamentally new technologies or applications used in this second generation 213nm source. Admittedly, the required performance of several components is near their current state of the art. The pulse carver is one example. A 1ns width pulse carver is available from Medox Electro-optics but represents the limit of this company's current technology.

Of course one could say that any project worth pursuing at the university level should be a bit crazy and push the limits of respectability just a little.

References

1. Medox Electro-optics Inc., "Pockels Cell System Description," in *Product Literature*, 1991.

2. S. Basu and R.L. Byer, "Average Power Limits of Diode-laser-pumped Solid State Lasers," *J. Applied Optics*, pp. 1765-1771, April 1990.

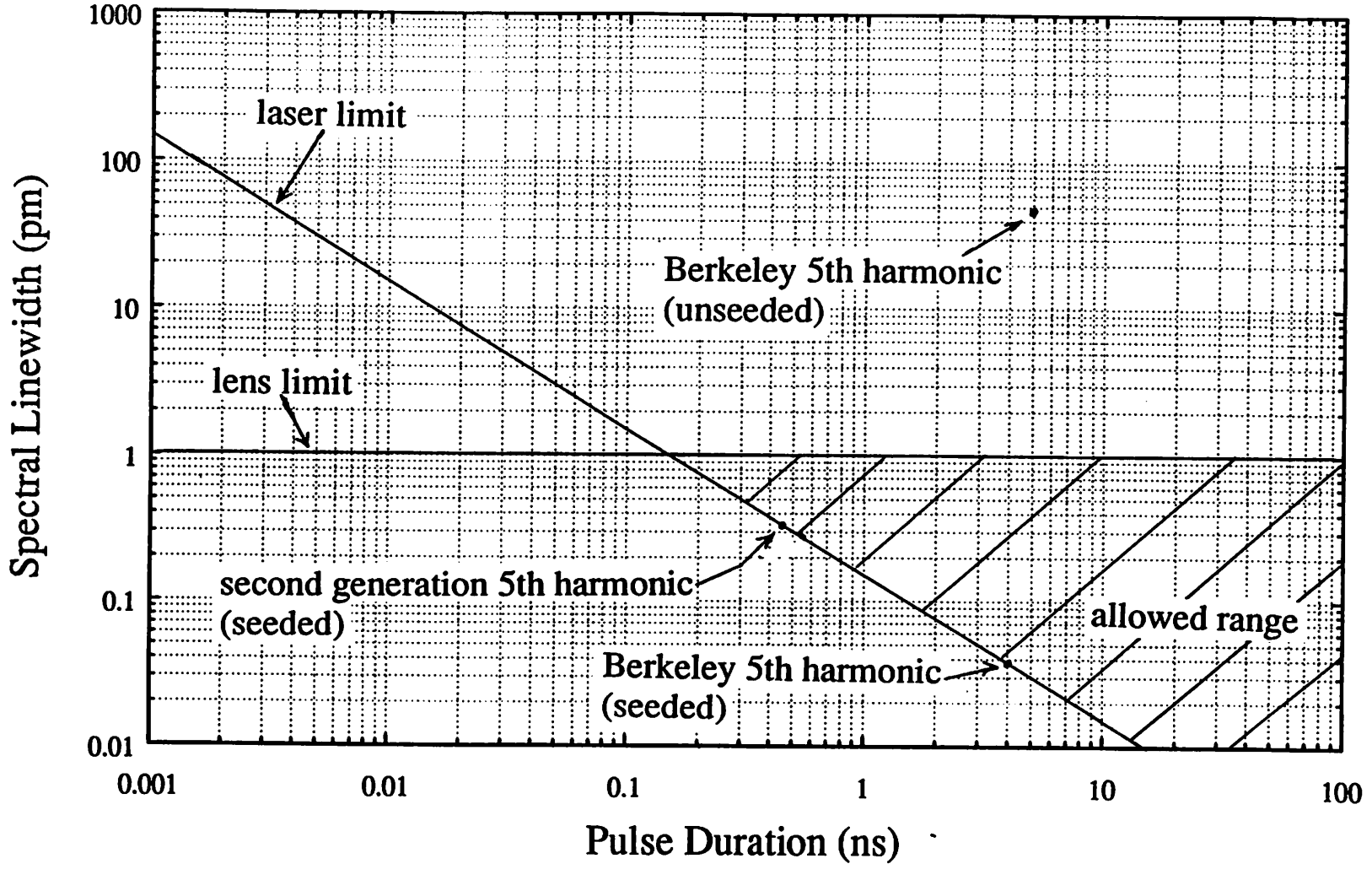

Fig. 1. Relation between pulse duration and spectral linewidth for 213nm laser.

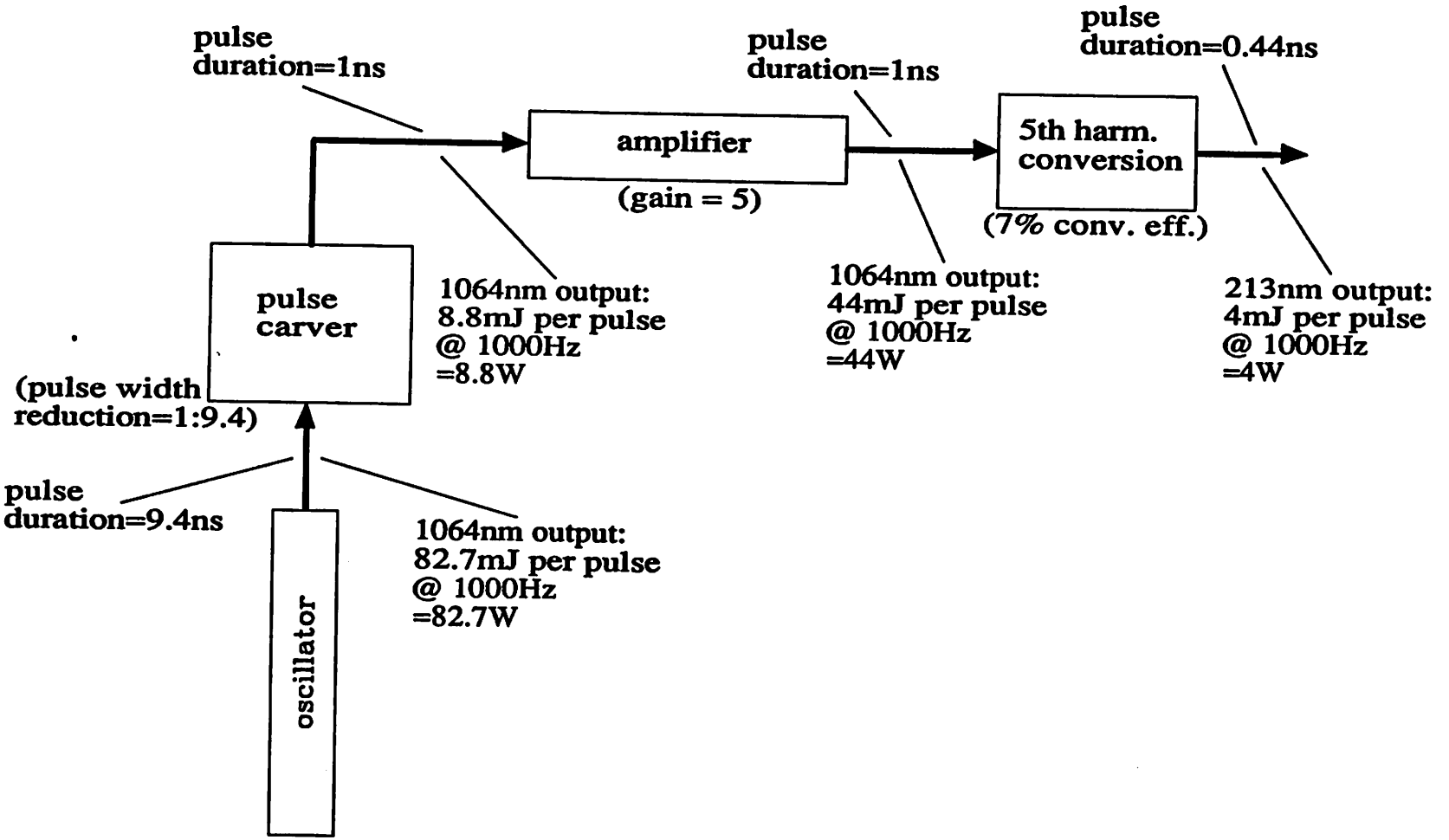

Fig. 2. Layout for proposed second generation 213nm laser source.